Investigating diseases of public health interest using X-ray micro-computed tomography

A thesis submitted to the University of Manchester for the degree of Doctor of Philosophy in the Faculty of Science and Engineering

2019

James D. B. O'Sullivan

School of Natural Sciences

Department of Materials

List of Contents

List of Figures 5

List of Tables 8

List of Abbreviations 9

Abstract 10

Declaration 11

Copyright statement 11

Acknowledgements 12

Preface 13

1. Introduction 16

1.1 The impact and challenges of Neglected Tropical Diseases 16

1.2 The role of microscopy in parasitology 19

1.3 Layout and aims of the dissertation 20

2. Literature Review: Microscopy and its role in understanding parasitic infection 24

2.1 Light Microscopy 24

2.2 Electron Microscopy 26

2.2.1 3D Electron Microscopy 27

2.3 X-ray micro-computed tomography 30

2.3.1 Principles of X-ray micro-computed tomography 30

2.3.2 Comparison of microCT to light and electron microscopy 32

2.3.3 Technical challenges in microCT 34

2.3.4 Correlative imaging 37

2.3.5 Scope and Design of biological microCT studies 38

2.4 Current understanding of *Trichuris muris* and its niche 40

2.4.1 The *Trichuris* life cycle 40

2.4.2 Ultrastructure of the niche 42

2.4.3 Cuticular structure and function 45

2.4.4 Murine immunity to *Trichuris muris* 47

2.4.5 Challenges in *Trichuris* control and research 50

2.5 Current understanding of *Schistosoma mansoni* life cycle and pathology 52

2.5.1 The *Schistosoma* life cycle 52

2.5.2 Schistosome immunopathology 56

2.5.3 Unanswered questions in the pathogenesis of schistosomiasis....57
2.6 Microscopy in assessing efficacy of anthelminthic drugs....60
2.7 Application of microCT to *Trichuris muris* and *Schistosoma mansoni*....62
2.8 Reiteration of doctoral aims....62
3. Methods....64
3.1 Experimental animals....64
3.2 Infections and treatments of mice....64
3.2.1 *Trichuris muris* infection....64
3.2.2 Corticosterone immunosuppression....64
3.2.3 Schistosoma mansoni infection....65
3.2.4 BrDU injection....65
3.3 Preparation of samples for microCT....65
3.3.1 Caecum and proximal colon infected with *T. muris*....65
3.3.2 Livers infected with *S. mansoni*....65
3.3.3 Preparation of *S. mansoni* eggs by density gradient....66
3.4 Micro-computed tomography....66
3.5 Analysis of microCT data....66
3.5.1 Segmentation....66
3.5.2 Epithelial coverage measurements....67
3.5.3 Mucosal thickness measurements....67
3.6 Electron microscopy....71
3.6.1 Fixation, staining and embedding of samples for SBF-SEM....71
3.6.2 Correlative SBF-SEM and TEM....71
3.6.4 Scanning Electron Microscopy....72
3.6.4 Guided Energy Dispersive X-ray Spectroscopy (EDX)....72
3.7 Light microscopy....73
3.7.1 Fixation, embedding and sectioning of samples....73
3.7.2 Immunohistochemistry....73
3.7.3 Morphometry of proliferating cells (pulse chase)....73
3.7.4 Histochemistry....73
3.8 Polymerase chain reaction....74
3.8.1 Primer design....74
3.8.2 Real Time-quantitative Polymerase Chain Reaction....74

3.9 Statistical analyses 75

4. 3D morphology and morphometry of the *Trichuris muris* attachment site using X-ray micro-computed tomography 78

4.1 Introduction 78

4.2 Results 80

4.2.1 Osmium staining of adult worms and surrounding host morphology in C57BL/6 mice 80

4.2.2 Quantification of the integrity of the epithelial tunnel 84

4.2.3 Head morphology and positioning in C57BL/6 mice 86

4.2.4.Head morphology and positioning in a SCID mouse 86

4.2.5 CT measurements of mucosal thickness 90

4.2.6 The influence of corticosterone on immunopathology and head-down behaviour 94

4.3 Discussion 98

4.3.1 Efficacy of micro-computed tomography in imaging the niche of *Trichuris muris* 99

4.3.2 Quantitative measurements of mucosal integrity and pathology 99

4.3.4 Uncertainty in quantitative measurement 100

4.3.5 Observation of novel head-down behaviour 100

4.3.6 The effect of corticosterone on C57BL/6 mice and *Trichuris muris* 102

4.4 Conclusions 103

Supplementary information 104

5. Morphology and prospective function of cuticular inflations of the bacillary band of *Trichuris muris* 106

5.1 Introduction 106

5.2 Results 109

5.2.1 Cuticular inflations develop between 23 and 28 days post-infection 109

5.2.2 Ultrastructure of cuticular inflations from SBF-SEM and TEM 114

5.2.3 Neural organization of sensory apparatus as determined by SBF-SEM and TEM 117

5.2.4 Composition of the cuticular inflations 122

5.2.5 Expression of blister protein homologs in the anterior region of the stichosome 124

5.3 Discussion 126

5.3.1 Development of cuticular inflations 126

5.3.2 Ultrastructure of cuticular inflations 126

5.3.3 Composition of cuticular inflations 127

5.3.4 A prospective role for blister genes in cuticular inflation development? 128
5.4 Conclusion 130
Supplementary information 131
6. 3D characterization of the hepatic and intestinal pathology of *Schistosoma mansoni* 133
6.1 Introduction 133
6.2 Results 135
6.2.1 Visualisation of gross morphology in the *Schistosoma mansoni*–infected liver 135
6.2.2 High-resolution and phase-contrast imaging of calcified eggs 140
6.2.3 Egg egress from the intestine 145
6.3 Discussion 148
6.3.1 DICE-CT allows visualization of *S. mansoni*–induced pathology 148
6.3.2 High-resolution imaging reveals egg calcification in the mouse liver 150
6.3.3 Migration of *S. mansoni* eggs across the small intestine 152
6.4 Conclusions 152
7. Conclusions and areas for further research 155
7.1 Reiteration of dissertation aims 155
7.2 Summary of findings 156
7.3 Implications of microCT study of *Trichuris muris* 157
7.4 Implications of microCT study of *Schistosoma mansoni* 158
7.5 Advances in microCT contrast enhancement: current challenges and future implications 160
7.6 Correlative imaging in the future 163
7.7 Towards reliable and accurate biological morphometry by microCT 164
7.8 General conclusion 167
List of References 169
Appendices 200
Appendix 1: X-ray micro-computed tomography (μCT): an emerging opportunity in parasite imaging 201
Appendix 2: Experimental steering of electron microscopy studies using prior X-ray computed tomography 231
Appendix 3: Matlab code used to measure mucosal thickness 258

Final word count: 76459

List of Figures

1. Introduction 16

1.1 World map showing countries endemic for trichuriasis and schistosomiasis 17

2. Literature Review 24

2.1: Diagrammatic representation of X-ray micro-computed tomography workflow 31

2.2: Life cycle of *Trichuris* in mammalian hosts 41

2.3: Scanning electron micrograph of three worms embedded within the caecal epithelium 43

2.4: The epithelial niche of *Trichuris* spp., with reference to light and electron microscopic observations of the nature of the tunnel 44

2.5: Structures of the bacillary band in *Trichuris* spp. 46

2.6: Lifecycle of the liver fluke *Schistosoma mansoni* during human infection 54

3. Methods 64

3.1: Segmentation workflow for whole organ vasculature (liver) 71

4. 3D morphology and morphometry of the *Trichuris muris* attachment site using X-ray micro-computed tomography 78

4.1: Imaging strategy for imaging caeca from C57BL/6 mice infected with *T. muris* 81

4.2: Osmium tetroxide (OsO_4) optimally stains the worm within the intra-epithelial niche 82

4.3: Worm and host gut morphology in 2D slices 83

4.4: Segmented worm and mucosa from a C57BL/6 mouse showing the breaks in the epithelium covering the tunnel 85

4.5: Variable positioning of the anterior stichosome at day 35 post-infection in a C57BL/6 mouse 87

4.6: Worm head morphology in a SCID mouse reveals a worm traversing a crypt at 35 days post-infection 89

4.7: Three methods were compared for calculating average mucosal thickness of microCT scans of the mouse caecum 91

4.8: Comparison of mucosal thickness measurement models and application of the Avizo influence zones method to compare of mucosal thickness in C57BL/6 and SCID mice 93

4.9: Corticosterone-treated mice exhibit accelerated epithelial cell proliferation in comparison to vehicle controls, in conjunction with a reduction in head-down behaviour in parasitizing worms 96

Supplementary 4.1: Backscattered Electron Micrograph (BSEM) of the worm stichocyte reveals a highly membranous composition 104

5. Morphology and prospective function of cuticular inflations on the bacillary band of *Trichuris muris* 106

5.1: Developmental time course of cuticular inflations during days 21 – 28 post - infection 110

5.2: Developmental time-course of cuticular inflations in female worms as visualised by SEM 111

5.3: A variety of cuticular inflation morphologies are evident at day 25 post-infection 113

5.4: Correlative workflow allowing ultrastructural investigation of the cuticular inflations 115

5.5: SBF-SEM showing the internal morphology of cuticular inflations 116

5.6: A cell under the cuticular inflation has a high concentration of mitochondria 118

5.7: Transmission Electron Microscopy (TEM) of the internal composition of the cuticular inflations
..... 119

5.8: SBF-SEM and TEM showing the organisation of sensory cells within the bacillary pores 120

5.9: Illustration of neural organisation of the sensory processes in bacillary cells as observed by SBF-SEM 121

5.10: Picrosirius red staining of paraffin-embedded worms 123

5.11: RT-qPCR showing expression of collagen-processing genes during the development of cuticular inflations in *T. muris* 125

6. 3D characterisation of the hepatic and intestinal granulomas of *Schistosoma mansoni* 133

6.1: Diffusible Iodine Contrast Enhanced MicroCT of the gross morphology and architecture of the liver and lobes 136

6.2: Scans of the liver right lobe showing morphology at 8 weeks post-infection with *S. mansoni* 137

6.3: Segmentation of vasculature showing reduced vasculature morphology over the course of infection 139

6.4: High resolution microCT of dried liver tissue showing fine vascular and egg morphology 140

6.5: High resolution microCT showing differences in egg density in between week 8 and week 16 post-infection 141

6.6: X-ray guided BSEM and EDX analyses confirms calcification of eggs within the liver . 143

6.7: MicroCT of agar-embedded eggs from a week 8 post-infection liver of a mouse 144

6.8: Schematic workflow showing the process by which microCT is used to guide histological sectioning targeting *S. mansoni* eggs traversing the mouse ileum 146

6.9: Correlative microCT and histology of eggs at various points during their migration across the small intestine wall 147

List of Tables

2. Literature review 24

2.1 Comparison of different imaging modalities used in the biological sciences 25

2.2 Strain- and dose-dependent differences in susceptibility to chronic *T. muris* infection 49

3. Methods 64

3.1 Micro-computed tomography parameters for scans in the results chapters 69

3.2 Data analysis workflow for segmentation and measurement of liver pathology 70

3.3 Data analysis workflow for segmentation and morphometry of *T. muris* infection of the caecum 70

3.4 Forward and reverse primer design for blister-gene homologs in *Trichuris muris* 75

5. Morphology and prospective function of cuticular inflations on the bacillary band of *Trichuris muris* 106

Supplementary 5.1 Names, reference URLs and % similarity of C. elegans blister genes and their homologs in T. muris 131

List of Abbreviations

APC	Antigen-Presenting Cell
BSEM	Back-scattered Electron Microscopy
BSF	Biological Services Facility
CLEM	Correlative Light and Electron Microscopy
CMM	Coordinate Measuring Machine
CNS	Central Nervous System
CT	Computed Tomography
DALY	Disability-Adjusted Life Year
EDX	Energy Dispersive X-ray spectroscopy
EM	Electron Microscopy
FBP	Filtered Back Projection
FIB	Focussed Ion Beam
FIB-SEM	Focussed Ion Beam Scanning Electron Microscopy
HMDS	Hexameythyldisylazane
H&E	Haematoxylin and Eosin
IBD	Inflammatory Bowel Disease
IHC	Immunohistochemistry
I_2E	Ethanoic iodine
MDA	Mass Drug Administration
MicroCT	X-ray micro-computed tomography
MSS-SEM	Microtome Serial Sectioning Scanning Electron Microscopy
NBF	Neutral-Buffered Formalin
NTD	Neglected Tropical Disease
RER	Rough Endoplasmic Reticulum
RT-qPCR	Real Time quantitative Polymerase Chain Reaction
PFA	Paraformaldehyde
PFIB	Plasma Focussed Ion Beam
PI	Post-infection
PTA	Phosphotungstic Acid
SBF-SEM	Serial Block Face Scanning Electron Microscopy
SCID	Severe Combined Immunodeficient
SEM	Scanning Electron Microscopy
ssTEM	Serial Sectionning Transmission Electron Microscopy
STH	Soil-Transmitted Helminth
TB	Tuberculosis
TEM	Transmission Electron Microscopy
Th1	T-helper 1
Th2	T-helper 2
VEGF	Vascular Endothelial Growth Factor
XRM	X-ray Microscopy

Abstract

Trichuris spp. and *Schistosoma* spp. are parasitic helminths and causative agents of trichuriasis and schistosomiasis, which affect hundreds of thousands of people worldwide and are significant public health burdens. Using rodent models, microscopy has been a key research tool in understanding the life cycles of these parasites and mechanisms of disease. However, parasites are difficult to find within tissues using sectioning, and 2D microscopy inadequately characterises their complex 3D attachment sites. X-ray micro-computed tomography (microCT) is a relatively new technique in biological research, and allows non-destructive 3D imaging of sample morphology at histological resolutions. This dissertation aimed to exploit the 3D imaging capabilities of microCT to provide novel insights into challenging biological questions surrounding the mouse models of human trichuriasis and schistosomiasis, namely *Trichuris muris* and *Schistosoma mansoni*. In order to achieve this, specialised sample preparation, imaging and data analysis workflows were conceived in order to develop and fully exploit the 3D imaging opportunities provided by microCT in the two parasites.

Trichuris is a nematode which lives in a highly specialised intracellular “tunnel” made through the epithelial cells of the caecum and proximal colon. At high-levels of infection, *Trichuris* may cause severe colitis-like symptoms, anaemia and growth retardation. In order to develop new therapies, a greater understanding of the maintenance and formation of the *T. muris* attachment site is required. 3D MicroCT was used to image the attachment site *in toto* at histological resolutions. Newly optimised staining of the tissue using osmium tetroxide provided contrast between the worm and the host tissue, and facilitated 3D quantification of the tunnel integrity and the inflammatory status of the host. We identified novel tunnel-forming behaviour in *T. muris* which contradicts core assumptions pervading the literature and changes the way in which host-parasite interactions might be perceived to occur. In addition, using microCT to steer electron microscopy provided new structural and compositional information on the enigmatic surface structures which cover the anterior-most portion of the worms’ surface, suggesting a role for collagen-processing proteins in their formation.

Schistosoma mansoni is a vector-borne trematode which lives in the abdominal venules. Schistosome eggs become lodged in systemic organs including the liver and intestine and cause an inflammatory reaction which can cause ascites, colitis-like symptoms and fatal bleeding. However, the manner in which egg-associated blockage and remodelling of liver vasculature contributes to downstream pathology remains poorly investigated. MicroCT was used in order to visualise the development of inflammatory and vascular pathology in the liver during infection, and showed a reduction in vascular branching. Furthermore, total liver inflammation was visualised in 3D, and surprising instances of egg calcification were revealed by a novel correlative imaging approach which used microCT to guide Energy Dispersive X-ray Spectroscopy (EDX). These insights provide an excellent methodological basis from which to quantitatively investigate *S. mansoni* pathology in future.

Overall, the investigations in this dissertation have supplied new insights into the life-cycles and pathologies of *Trichuris* and *Schistosoma* infections. Accompanying these are a range of newly developed and refined imaging techniques which may be useful not only in parasitology, but a range of other biological fields.

Declaration

No portion of the work referred to in this thesis has been submitted in support of an application for another degree or qualification of this or any other university or other institute of learning

Copyright Statement

i. The author of this thesis (including any appendices and/or schedules to this thesis) owns certain copyright or related rights in it (the “Copyright”) and s/he has given The University of Manchester certain rights to use such Copyright, including for administrative purposes.

ii. Copies of this thesis, either in full or in extracts and whether in hard or electronic copy, may be made only in accordance with the Copyright, Designs and Patents Act 1988 (as amended) and regulations issued under it or, where appropriate, in accordance Presentation of Theses Policy You are required to submit your thesis electronically Page 11 of 25 with licensing agreements which the University has from time to time. This page must form part of any such copies made.

iii. The ownership of certain Copyright, patents, designs, trademarks and other intellectual property (the “Intellectual Property”) and any reproductions of copyright works in the thesis, for example graphs and tables (“Reproductions”), which may be described in this thesis, may not be owned by the author and may be owned by third parties. Such Intellectual Property and Reproductions cannot and must not be made available for use without the prior written permission of the owner(s) of the relevant Intellectual Property and/or Reproductions.

iv. Further information on the conditions under which disclosure, publication and commercialisation of this thesis, the Copyright and any Intellectual Property and/or Reproductions described in it may take place is available in the University IP Policy (see http://documents.manchester.ac.uk/DocuInfo.aspx?DocID=2442 0), in any relevant Thesis restriction declarations deposited in the University Library, The University Library’s regulations (see http://www.library.manchester.ac.uk/about/regulations/) and in The University’s policy on Presentation of Theses

Acknowledgements

Foremost, I wish to acknowledge my supervisors, Kathryn, Sheena and Philip. Thank you for giving me the opportunity to undertake this thesis, and for all of your advice, mentorship and enthusiasm.

I feel truly lucky to have been able to carry out a project which I found so interesting, challenging and creative. Thank you to Carl Zeiss AG, who provided the funding that made the work possible.

To my friends in the Else, Cruickshank and Withers labs, especially Gurdeep, Jordie, Hannah, and Sheila: Thank you for your help, support and feedback. I will cherish your friendship and the good times we've had just as much as any of the science. Thank you for making this such a wonderful experience.

To my family: Thank you for always listening, and especially for looking out for me in those last, most challenging months.

I would also like to thank the generous employees of the Lego Store (Arndale Manchester), who kindly provided me with materials for the mounting of samples in chapter 4.

To Carina: thank you for sharing this journey with me. By far my most important discovery happened in April, during my first year.

Many other people throughout the University of Manchester and beyond made this work possible. Their contributions as scientists and friends are too numerous to list here. Thank you all!

Preface

The work contained within this dissertation and the accompanying studentship were funded by an industrial sponsor, Carl Zeiss AG. Zeiss, in their capacity as a manufacturer of X-ray microscopes, wished to oversee a project in which the soft tissue imaging capabilities of micro-computed tomography were expanded and refined. Zeiss microscopes were used for much of the imaging in this work.

After beginning the project, the author optimised imaging protocols in two case studies of soft tissue disease: the parasitic infections schistosomiasis and trichuriasis. After some surprising and interesting insights arose from preliminary data, it was decided that the biological findings relating to these infections should take narrative centre stage. Therefore, the following work is fundamentally biological in its rationale and experimental design. However, to achieve the biological aims, the development of novel imaging methodologies remained essential. These new and useful workflows are described alongside the biological findings.

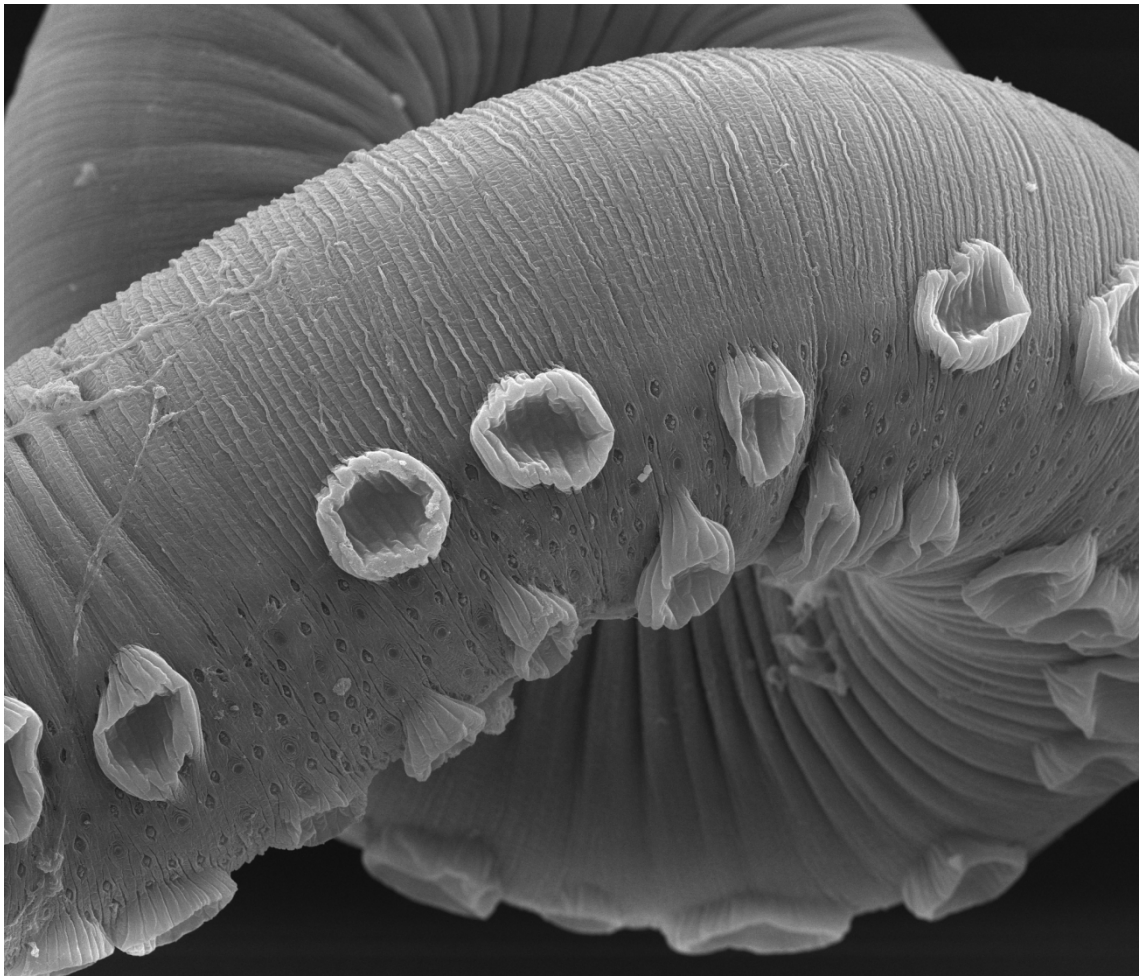

Blank page

1. Introduction

1.1 The impact and challenges of Neglected Tropical Diseases

Neglected Tropical Diseases (NTDs) are infections which exact a devastating economic and human cost in the poorest areas of the developing world (Murray *et al.*, 2015). In all those affected, NTDs are cumulatively estimated to be responsible for over 17 million Disability Adjusted Life Years (DALYs) (Kyu *et al.*, 2018a). Parasitic helminths (from the greek *helmins*, literally “parasitic worm”) cause extensive human morbidity and mortality and represent a significant proportion of NTDs (Pullan *et al.*, 2014). In addition, helminthic infection of farm animals and disrupted agriculture represents a considerable challenge for affected communities (Morgan *et al.*, 2013). Current efforts for control of helminth-caused disease include mass drug administration (MDA), in which community-wide administration of anthelminthic drugs aims to treat and prevent disease (Webster *et al.*, 2014). However, high rates of reinfection, the growing threat of resistance to anthelminthic drugs used for MDA, and the lack of sufficiently efficacious drugs for certain infections (Keiser and Utzinger, 2008) all represent challenges for disease control. Consequently, progress in controlling neglected helminthiases is lagging years behind the targets set by the World Health Assembly for 2020 (Becker *et al.*, 2018). Further research into the lifestyles and pathologies of parasites is required for development of new, more effective therapies and control measures in the future.

Two parasitic diseases that represent considerable burdens to global public health are trichuriasis, caused by the whipworm *Trichuris spp.*, and schistosomiasis, caused by the flatworm *Schistosoma spp.* Trichuriasis and schistosomiasis are estimated to directly affect 500 million and 200 million people respectively (Vos *et al.*, 2017), and maintain sustained transmission (endemicity) throughout South America, Africa, the Middle East and Asia (**Fig. 1.1**) (Gryseels *et al.*, 2006; Pullan *et al.*, 2014). Whilst some aspects of Trichuriasis and schistosomiasis are now well understood, gaps remain in our understanding of parasite lifestyles and pathological impacts on the host. Advances in imaging and biotechnology have increased understanding of other NTDs; for example, the single-celled parasite *Leishmania* is now very well understood because it is amenable to *in vitro* culture within host cells (macrophages), and can be genetically manipulated to allow specific functional studies (e.g. Naderer *et al.*, 2015). As a result, many mechanisms of *Leishmania* survival within its niche

have been characterised (de Menezes *et al.*, 2016). Similar experimental tools remain largely unavailable in helminth parasites due to the complexity of life cycles (Hoffmann *et al.*, 2014). Additionally, highly specialised host-specific niches integrating multiple cell and tissue types preclude *in vitro* culture. While recent approaches based on CRISPR-based transgenic tools show great promise in flatworms (Arunsan *et al.*, 2019; Ittiprasert *et al.*, 2019), such technology is still likely a long way from wide-scale adoption across the range of highly specialised parasites. Therefore, fundamental difficulties remain in the study of both *Trichuris* and *Schistosoma*.

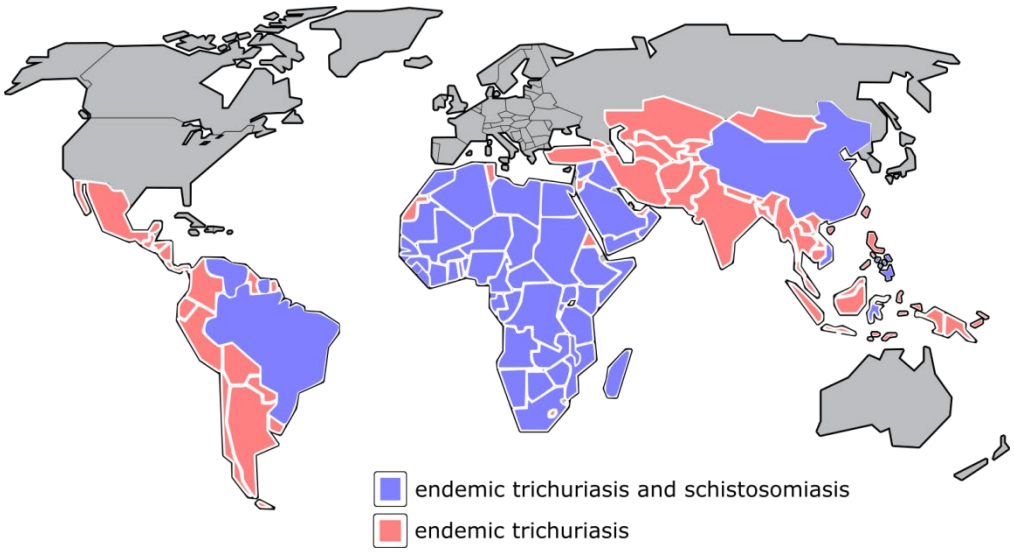

Figure 1.1 World map showing countries endemic for trichuriasis and schistosomiasis. An infection is "endemic" when it sustains a steady state of transmission through the population. Pink countries are endemic for Trichuriasis, and blue countries are endemic for both Trichuriasis and schistosomiasis. In grey countries, infections may be recorded, but disease transmission is not sufficiently maintained to reach a steady state. Data taken from Gryseels et al. (2006) and Pullan et al. (2014).

This dissertation focuses on investigating the lifestyle and pathologies of two challenging parasitological case studies: *Trichuris muris* and *Schistosoma mansoni*. *Trichuris* spp. is a Soil-Transmitted Helminth (STH) which lives at least partly embedded within a tunnel in the host's intestinal epithelium throughout its entire life (for full life-cycle see section 2.4.1). The morbidity induced by heavy infection with *Trichuris* can be especially severe in children, including both anaemia and growth retardation (Kaminsky *et al.*, 2015). Trichuriasis remains a significant public health challenge because the progress of MDA is hindered by poor efficacy of existing drugs (Du *et al.*, 2013), and high levels of reinfection (Jia *et al.*, 2012). The mechanisms underlying host immunity have been well-studied in *Trichuris* (Klementowicz *et al.*, 2012; Hurst and Else, 2013). However, very little is known about the manner in which the tunnel is formed and maintained, as well as mechanisms by which the worm interacts with the host. Moreover, some unique anatomical features of *Trichuris* remain poorly characterised, and their function is not understood. In this thesis, these questions will be answered in *Trichuris muris*, a mouse model of human trichuriasis which continues to supply the majority of our knowledge of *Trichuris* infection.

Schistosoma mansoni is transferred to hosts through water by a snail vector, and as of 2016 was estimated to infect almost 200 million people (Vos *et al.*, 2017). After a tortuous migration through host tissue, adults take refuge in the portal vein and mesenteric venules (for full life-cycle see chapter 2.5.1). However, most fatal pathology is caused by the eggs, which can get swept by the circulation into systemic organs such as the liver, causing an inflammatory response. This inflammation is associated with pulmonary hypertension (Graham *et al.*, 2010), ascites and potentially fatal bleeding (Chofle *et al.*, 2014). In the case of *Schistosoma,* much of the basis of the worm's survival within the host is now understood. However, the mechanisms by which deposition of eggs leads to downstream pathology remain poorly understood. Changes in vascular morphology are known to be risk factors for subsequent disease. However, little attention has been given to how vascular changes are linked to pathology, despite thousands dying each year (Roth *et al.*, 2018). The life cycles and pathologies of *Trichuris* and *Schistosoma* are reviewed more thoroughly in the literature review (chapter 2) of the thesis.

1.2 The role of microscopy in parasitology

Microscopy is an indispensable tool in understanding many parasitic worms, including *Trichuris* spp. and *Schistosoma* spp.. The growing capabilities of microscopy in the 20th and 21st centuries have with them brought new insights into parasite biology. However, technical constraints of microscopic techniques introduce difficulty into parasitological research. For example, using microscopy to visualise tissue morphology almost always involves some kind of sectioning workflow by which the tissue of interest is blindly sectioned and the slices are surveyed to locate features of interest. Therefore, it can be challenging to find parasites in the tissues which they infect as well as analyse the key interactions between parasites and host, many of which may occur at specific parasite attachment sites. Furthermore, the orientation in which tissue is cut may bias the interpretation of morphology due to missing elements which are outside of the plane of view. Indeed, if the 3D morphology of a structure is required to investigate a biological question, characterisation by sectioning approaches becomes exceedingly difficult. Therefore there is a rationale for investigating and developing the use of natively 3D imaging modalities that survey the entire tissue in 3D at sufficient histological resolution.

X-ray micro-computed tomography (microCT) is an imaging modality which is capable of 3D imaging of tissues at near histological resolutions. Data is collected by generating a number of 2D X-ray images taken of the sample across a range of rotational positions (see **appendix 1,** see also section 2.3.1, figure 2.1). The images taken from many different angles are then computationally reconstructed to produce a 3D dataset, based on the absorptive characteristics of the sample. The dataset can be visualised either as 2D slices through virtual sectioning, or alternatively may be rendered in 3D. MicroCT therefore provides an excellent method for viewing the 3D morphology of a sample of interest, without the need for any destructive sectioning processes. MicroCT offers an excellent opportunity to address the aforementioned changes in *Trichuris muris* and *Schistosoma mansoni*. Specifically, a non-destructive 3D imaging process gives the opportunity to look at the morphology and positioning of *T. muris* within its niche as a whole for the very first time. In *S. mansoni*, microCT would allow visualisation of the changes in whole organ vascular morphology and inflammation during

infection. MicroCT may also applied in a “correlative” manner, in which case microCT mapping of a sample may steer subsequent sectioning-based imaging (Burnett *et al.*, 2014). Such a process may be used to facilitate greater efficiency in the imaging of parasite attachment sites which are heterogeneously distributed throughout tissues.

MicroCT is employed in a range of fields (Stock, 2008; Boerckel *et al.*, 2014; Shearer *et al.*, 2016). However, it is still relatively rarely used as an experimental tool in preclinical biological studies when compared to more conventional bright field and fluorescent microscopic approaches, despite similar spatial resolution. Performing experiments using microCT introduces novel methodological challenges; due to the low absorbance of biological soft tissues to X-ray radiation, generating contrast in features of interest can be challenging. However, samples can be prepared in a variety of different ways to maximise the quality of subsequent microCT, including immersion in high-Z elements in staining procedures. Sample preparation must be optimised depending on the nature of the sample and desired results, and there are continuing efforts to improve quality of microCT soft tissue imaging via optimisation of sample preparation (Aslanidi *et al.*, 2013; Pauwels *et al.*, 2013). 3D imaging using microCT represents an excellent opportunity to gain totally novel insights into parasite-host interfaces, and challenge the assumptions pervading the existing literature. However, in order to effectively answer the biological questions which surround soft tissue parasites such as *T. muris* and *S. mansoni*, there is a requirement to develop microCT methodology which facilitates imaging of sufficient quality to observe and quantify morphology.

1.3 Layout and aims of the dissertation

This dissertation is structured as follows: **Chapter 2** contains a review of the literature pertinent to the reader, and outlines the experimental issues addressed. **Chapter 3** describes the experimental methods which were employed in experimental investigation. The main results described in this dissertation are divided into two chapters investigating *Trichuris muris* (**chapters 4 and 5**) and one chapter investigating *Schistosoma mansoni* (**chapter 6**). **Chapter 7** is a general discussion of the outcomes and implications of the dissertation as a whole. The Appendices contain work which, whilst not part of the thesis structure, supplements the rationale and findings. Namely, **appendix 1** is a review and opinion piece publishing in *Parasitology* discussing and demonstrating the potential advantages of using microCT to

investigate parasitological questions. **Appendix 2**, is a methodological paper published in *Ultramicroscopy,* describing the use of microCT to assist steering of subsequent EM. The methodology described was extensively used in **chapter 5**.

The overall aim of this thesis is to exploit the 3D imaging capabilities of X-ray micro-computed tomography to investigate the lifestyles and pathologies of the murine parasites *Schistosoma mansoni* and *Trichuris muris.* MicroCT allows non-destructive 3D imaging of biological tissue *ex vivo* at length scales ranging from whole organs to tissues and cellular morphology. Therefore, it may allow new directions of investigation to be taken which have not previously been possible. For each of **chapters 4-6**, there is also a requirement for developing and employing imaging protocols which allow the biological questions to be addressed. Therefore an accompanying "technical aim" of each chapter is to develop approaches to sample preparation, imaging and data analysis which facilitate achieving the biological aims:

Chapter 4: To characterise spatial positioning of *T. muris* within the epithelial tunnel, as well as the ultrastructural features of *Trichuris* at the attachment site. A more comprehensive understanding of tunnel morphology and would inform understanding of tunnel formation and maintenance. **Technical aims:** To develop an optimised staining imaging protocol allowing the attachment site of the worm to be visualised, and to develop 3D measurements of tunnel integrity and mucosal inflammation.

Chapter 5: To characterise the morphology, structure and composition of *T. muris* surface structures which interact with the host within the epithelial tunnel, in order to better understand the effector mechanisms by which survival in the host is promoted. **Technical aims:** To develop a correlative imaging approach by which microCT-steered EM allows efficient ultrastructural investigation of the cuticular inflations.

Chapter 6: To characterise liver and intestinal pathology of *Schistosoma mansoni*. An understanding of how inflammation leads to change in liver architecture may inform further understanding of how dangerous pathologies are generated. **Technical aims:** To develop optimised staining to visualise changes in egg-induced granulomatous inflammation and vascular pathology throughout infection. To develop a correlative imaging approach by which microCT-steered histology allows efficient investigation of egg traversal across the intestine wall.

The purpose of the literature review in **Chapter 2** is to familiarise the reader with the current state and potential future developments in soft tissue microCT imaging, as well as to summarise the state of existing knowledge on *Schistosoma mansoni* and *Trichuris muris* which are pertinent to the investigations of the thesis. There will be a particular focus on the contributions of microscopy in the study of these parasites, as well as a description of some outstanding problems which need to be addressed, especially those to which micro-computed tomography may make a useful contribution. At the conclusion of the Literature review, the doctoral aims are listed again, with reference to the more detailed information on the parasites provided throughout the chapter.

Blank page

2. Literature Review: Microscopy and its role in understanding parasitic infection

It is difficult to imagine how we could understand the biological world without microscopy, and visualising spatial patterns of morphology and molecular composition underpins much of our knowledge of disease. Parasitology as a biological field is no exception to this rule, and microscopy has been key in investigating parasite life cycles and pathology (Halton, 2004). Multiple types, or modalities, of microscopy are used which have a range of capabilities and strengths. Throughout history the range of research conducted has depended on the capabilities of the microscopes of the time. As imaging has become more sophisticated, new avenues of investigation have been opened. Therefore, there is a growing library of imaging modalities which all can provide different insights into biological tissues, based upon their capabilities and limitations. These will be discussed in the following paragraphs, and are summarised in **table 2.1**.

2.1 Light microscopy

Brightfield light microscopy, as the earliest and crudest form of microscopy, relies on the projection of light through a sample, which attenuates the beam, providing contrast. Bright field microscopy was a key tool in the identification and classification of microbes including helminth parasites, which were often based on the appearance of surface structures and genitalia (Knight, 1984; Oliveros *et al.*, 1998; Feliu *et al.*, 2000; Torres *et al.*, 2011; Steinmann *et al.*, 2015). The subsequent development of histological techniques, in which a sample is sectioned and stained chemically, allowed much more in-depth studies of the parasite interior and pathology the parasite caused. Histochemical stains such as haemotoxylin and eosin (H&E) allow the gross cellular morphology of tissues to be characterised, whilst other stains allow the identification and distribution of non-cellular tissue constituents such as collagen and elastin. These widespread approaches were useful in determining parasite life cycles; for instance, histological surveys of tissue helped characterise the migration route of *S. mansoni* larvae through the systemic organs, as will be discussed further in section 2.5.1 (Wheater and Wilson, 1979). Furthermore, phase contrast light microscopy allowed the visualisation of live cells without chemical contrast enhancement, as it exploited the differential scattering of light by the sample to provide contrast (Zernike, 1942).

Modality		Maximum resolution	3D capability	Destructive?	Morphological imaging	Molecular imaging	References
Light microscopy	**Brightfield Microscopy**	200 nm	N/A	Yes	Standard tool for tissue composition and cellular architecture	Up to 2 labels visualised by immunhiustochemistry	1. Gao *et al.* 2014 2. Girkin et al. 2018 3. Icha *et al.* 2017 4. Huang *et al.* 2009
	Fluorescence microscopy	200 nm (350 nm axial)[1]	Optical sectioning up to several millimetres of depth[2]	No, but phototoxic effects damage tissue structure and reduce fluorescence[3]	Morphology inferred through fluorescently labelled materials	Fluorescent channels allow many concurrent labels to be visualised	
	Superresolution fluorescence microscopy	10 nm (50 nm axial)[4]	Optical sectioning up to several microns of depth[4]		N/A	Single molecules can be fluorescently visualised[4]	
Micro-computed tomography and nanotomography	**Laboratory MicroCT/NanoCT**	65 nm (isotropic)	Centimetres imaging depth. Maximum field of view and resolution are determined by detector size and magnification	No, but X-ray exposure may change tissue properties	Tissue architecture comparable to brightfield microscopy, with less cellular detail	Some limited labelling of proteins with antibodies	5. Kampschulte *et al.* 2016 6. Albers *et al.* 2018 7. Metscher *et al.* 2011
Electron microscopy	**SBF-SEM**	5 nm (25 nm axial)[8]	Automated diamond knife allows maximum depth of 100s of microns	Yes	Ultrastructural morphology including cell membranes and organelles	Some capacity for 3D nano-gold immunostaining[8]	8. Vihinen *et al* . 2013 9. Wei *et al.* 2012 10. Hayworth *et al.* 2006
	FIB-SEM	3 nm (3 nm axial)[9]	Automated Ion beam milling allows superior axial resolution to SBF-SEM, at expense of maximum depth	Yes		N/A	
	TEM	>1 nm	Manual staining, imaging and alignment of individual slices (ssTEM) is error-prone and time-consuming[10]	Yes		Well-established nano-gold EM for subcellular protein localisation	

Table 2.1: Comparison of different imaging modalities used in the biological sciences. Whilst brightfield and fluorescence microscopy offer an excellent view of cellular morphology and molecular composition, morphological insights in 3D are less feasible. Micro-computed tomography offers 3D morphological insights with the greatest imaging depth, at resolutions slightly below what is possible by light microscopy, although with less clear cellular architecture. Electron microscopy exhibits superior resolution capable of visualising cellular ultrastructure, but is limited to small fields of view.

Whilst bright-field microscopy remains a staple of technique of biological research, fluorescence microscopy is ubiquitous. Instead of transmitting light through the sample to be observed through the eyepiece or detector, fluorescent microscopes contain a light source which emits light of a specific wavelength which excites fluorescent molecules within the sample, the signal of which is transmitted to the viewer. The first fluorescence microscope utilised UV light to produce an image based on the autofluorescence of the sample (Heimstadt, 1911). However, the technique only became useful as we know it today through the development of specialised optics (Ploem, 1967), and fluorescent chemical labels (Coons *et al.*, 1941). Through the use of fluorescently labelled antibodies, gene products and RNA labels, spatial patterns of protein expression and transcription can be qualitatively and quantitatively analysed, even in a multiplex manner (Hofman *et al.*, 2019). With no absorption of transmitted light through the tissue, the trade-off is a near absence of gross morphological detail. Immunology as a field has benefitted greatly from fluorescence imaging, as it has allowed the distribution of immune cells to be visualised.

Fluorescent imaging techniques have also been subjected to constant refinement, and more recently have expanded into the domain of 3D imaging. For instance, confocal microscopy, which was initially developed to avoid the deleterious effects of background fluorescence in images, but also facilitates 3D imaging through optical sectioning of the sample (White, 1987; van Meer, 1987). Fluorescence imaging in three dimensions has also been refined further through the development of explicitly 3D techniques designed to image as deeply as possible. Optical coherence tomography is one such technique which capitalises on the existing methods established in tomographic reconstruction (Sharpe *et al.*, 2002) and both light sheet microscopy and multiphoton microscopy are modern approaches which refine the technology present in confocal microscopes to achieve deeper optical sectioning (up to tens of millimetres beneath the sample surface) over a wider field of view which is less damaging to the sample (Pang *et al.*, 2009; Kobat *et al.*, 2009; Stelzer, 2015).

Multiphoton microscopy utilizes excitation with near infrared light (NIR) in order to reduce scattering through the sample, resulting in lower phototoxicity and deeper penetration (Larson, 2011). Light-sheet microscopy achieves a similar outcome using a different approach, by which the directions of illumination and detection are perpendicular to one another (Greger *et al.*, 2007). Therefore, the illuminating laser, which can be shaped into a “sheet” optically, only

excites the fluorophores that are in the desired plan of focus, thus reducing background fluorescence as well as the total dose of light that the sample receives. The increase in depth and reduction in phototoxicity achieved by both multiphoton and light sheet microscopy means that both techniques have the capability for *in vivo* imaging applications. In particular, patterns of fluorescently-labelled gene products in transgenic organisms can be monitored in real time. Alternatively, antibodies may be used to non-invasively label targets of interest. The limitations of this approaches are firstly, the availability of transgenic organisms for study, and secondly that features are not too deep for staining by antibodies, as tissue clearing to increase permeability is not compatible for *in vivo* study.

2.2 Electron Microscopy

Most forms of optical microscopy are constrained by their limit of resolution (that is, the minimum distance between objects such that they can still be distinguished as separate). The diffraction of light through the microscope lens gives rise to a resolution limit which is half the wavelength of light (~200 nm) (Airy, 1835; Abbe, 1873). Indeed, this diffraction limit can be observed in the microscope, in the form of the “Airy disc”, which is the diffraction artefact observable at the resolution limit. Breaking this barrier in resolution occurred upon the first use of electrons for imaging, which followed the discovery that electrons could themselves behave in a wave-like manner (Broglie, 1924; Davisson and Germer, 1928). Some decades following this discovery, technology allowed the first electron microscopes to be constructed which exploited electron beams possessing much smaller wavelengths than visible light. Due to the shorter wavelength of the electron beam, the electron microscope boasts much higher resolutions than light microscopy, and has been instrumental in developing our understanding of the interaction sites between parasites and hosts.

Electron microscopy (EM) can be classified broadly into two groups of techniques, Transmission Electron Microscopy (TEM) and Scanning Electron Microscopy (SEM): TEM is similar to light microscopy as the sample is embedded and sectioned before being subjected to an electron beam. Contrast is generated by the differential scattering and transmission of the electron beam by the atomic electrons and nuclei within the sample (Egerton, 2005), and is enhanced by addition of electron-dense contrast agents including osmium tetroxide, uranyl acetate and Lead

aspartate which allow differentiation between cell membranes and other components of cell ultrastructure. Therefore, whilst light microscopy allowed visualisation of cells and organelles, electron microscopy allowed detailed study of organellar structure which was capitalised on to characterise organelles such as the mitochondria and the endoplasmic reticulum for the first time (Palade, 1952; Palade and Porter, 1954), as well as the working principles behind muscle fibre contraction (Huxley, 1957). SEM involves firing the electron beam at the surface of the sample, and detecting either secondary or backscattered electrons using specialised detectors. Secondary electrons give information about the topology of the sample surface over a large depth-of-field at resolutions approaching 1 nm, and are useful for determining morphology of fine surface structures. This capability has therefore been highly useful in taxonomy of parasites such as *Trichuris*, which is often dependent on small variations in surface morphology (Pfaffenberger and Best, 1989; Lanfredti *et al.*, 1995; Torres *et al.*, 2011). Alternatively, the SEM may detect backscattered electrons. In Back-Scattered Electron Microscopy (BSEM), variations in electron density just below the sample surface are tracked. This property may be exploited in resin-embedded samples in order to give a TEM-like image of cellular ultrastructure (Denk and Horstmann, 2004), although with reduced maximum resolution. Nevertheless, BSEM still has sufficient resolution to provide information on ultrastructural features of parasites, such as the flagellar structure in the African trypanosome (Hughes *et al.*, 2013).

2.2.1 3D Electron Microscopy

Modern electron microscopy continues to develop, and there is a continuing interest in further developing the 3D imaging capabilites of electron microscopy. In particular, several 3D EM techniques are now available which allow the visualisation of cell ultrastructure as a volume. Initially, 3D EM was restricted to painstakingly preparing, imaging and registering Serial TEM sections by eye, in an approach called Serial Sectioning Transmission Electron Microscopy (ssTEM) which was first used to study connectivity between neurons in the brain (Davis and Sterling, 1979; White and Rock, 1981; White *et al.*, 1986). The development of techniques which exploit automated milling of a resin block and serial backscatter SEM of the block surface (blockface) has now superseded serial sectioning TEM due to its comparable resolution and greater ease of sample preparation, image acquisition and alignment. Two methods of 3D electron microscopy exploiting blockface imaging are prevalent today; Serial Blockface

Scanning Electron Microscopy (SBF-SEM), and Focussed Ion Beam Scanning Electron Microscopy (FIB-SEM).

SBF-SEM (aka SBEM) was invented by Denk and Hortmann (Denk and Horstmann, 2004). A sample of interest is prepared by fixation in resin. The mechanical sectioning and imaging of the whole sample is automated and takes place inside of the electron microscope. A diamond or glass microtome slices off the top layer of the sample, and the newly exposed layer of block face is scanned by an electron beam. The microtomes used in SBF-SEM can cut slices off the top of the sample of a minimum thickness of ~25nm, which determines the axial (depth) resolution. SBF-SEM is able to visualise sub-cellular structures, and provided some of the first three dimensional models of the endoplasmic reticulum (Vihinen *et al*., 2013), as well as the intercellular distribution of collagen fibrils in embryonic chick tendon (Kalson *et al.*, 2013). The mapping of synaptic connections, previously the domain of ssTEM, has also received attention from SBF-SEM (Friedrich *et al.*, 2013). Whilst lateral resolution has been shown to be high (~5nm), the limited axial resolution has resulted in some workers supplementing SBF-SEM with electron tomography (Vihinen *et al.*, 2013). A newer technique, called Focussed Ion Beam Scanning Electron Microscopy (FIB-SEM), overcomes the reduction in axial resolution encountered by SBF-SEM. Whilst the working principles are much the same in both techniques, FIB-SEM uses a focussed beam of Gallium ions to ablate layers of the sample between scanning of the blockface, instead of a microtome (Bushby *et al.*, 2011). The use of an ion beam for sectioning has multiple advantages; it avoids artefacts caused by the mechanical stresses of slicing, higher voltages of electron beams can be used which increases lateral resolution, and the Gallium ion beam removes much thinner layers which increases axial resolution (Peddie and Collinson, 2014). One study using FIB-SEM for reconstruction of a whole yeast cell achieved an isotropic resolution of ~3nm^3 (Wei *et al.*, 2012). However, the trade-off is that smaller volumes can be imaged than using SBF-SEM, due to the greater amount of time sectioning with the ion beam takes. The greater axial resolution of FIB-SEM has been useful in the study of protozoan parasites (de Souza and Attias, 2018) and has even been combined with fluorescence microscopy to characterise the molecular and mechanical events during endocytosis in the parasite *Giardia lamblia* (Zumthor *et al.*, 2016).

2.3 X-ray micro-computed tomography

2.3.1 Principles of X-ray micro-computed tomography

X-ray micro-computed tomography (microCT) allows non-destructive 3D imaging of biological soft tissues on a variety of resolutions. In a typical imaging workflow (**Fig. 2.1**), images are produced by illuminating a sample with a focussed beam of X-rays. The X-rays are differentially absorbed by and transmitted though the sample to a detector; the higher the density and atomic number of constituent elements, the higher the absorption of X-rays, giving increased contrast in the projection (image). The 3D aspect of the imaging modality comes from the computed tomographic reconstruction. In this process, many projections are taken from a range of angles around the sample. This may be achieved by having the X-ray source and detector mounted on a gantry which moved around the sample, as in many medical CT scanners, or by having the sample itself mounted on a rotating stage. The projections are then computationally reconstructed to produce the 3D data, through either filtered back-projection (FBP) (Wells *et al.*, 1992) or Iterative reconstruction. 3D datasets may then be viewed as either cross-sectional slices, or as a rendered 3D volume, and are amenable to further digital labelling (segmentation) (Maire and Withers, 2014) which facilitates downstream quantitative methods.

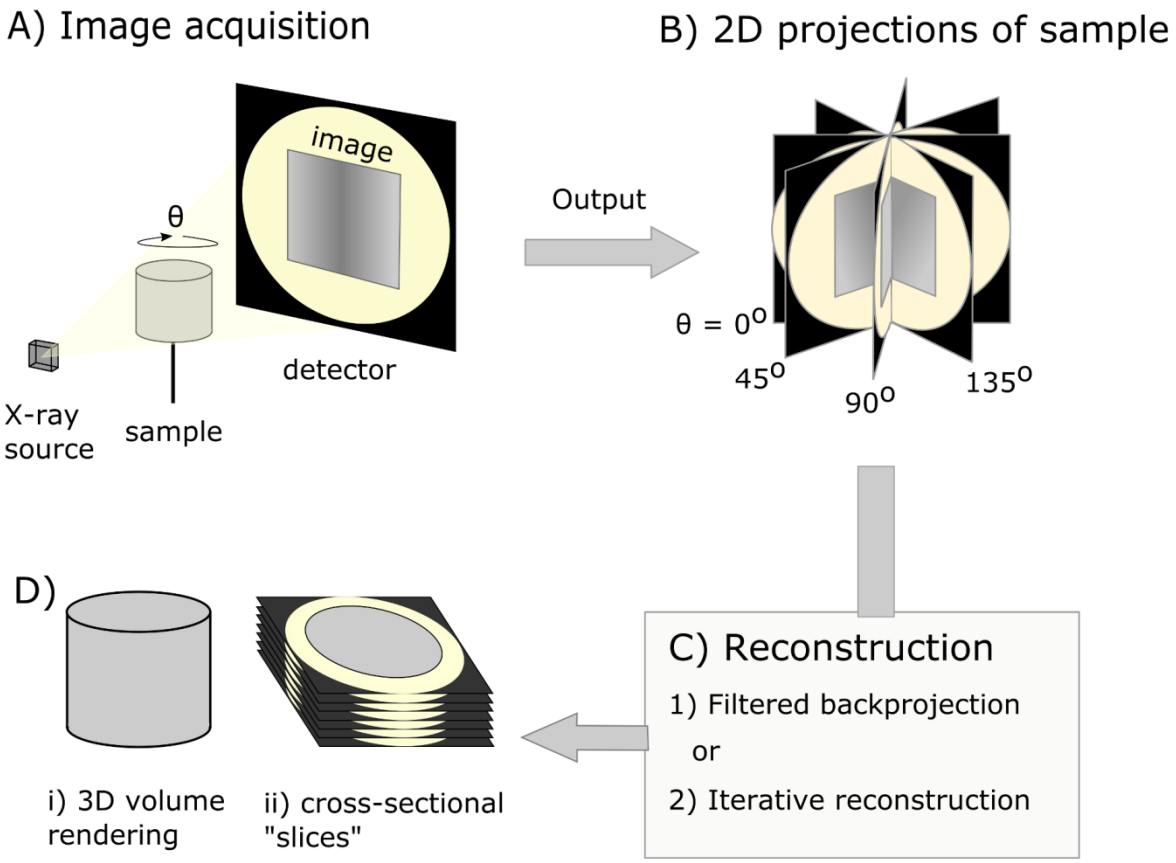

Figure 2.1: Diagrammatic representation of X-ray micro-computed tomography workflow. **A**) Basic illustration of tomographic apparatus, including the X-ray source, detector and sample. Projection images are made as the sample is rotated at increments through θ. **B**) The raw output of the tomogram is a series of projections of the sample taken at different angles. **C**) Projections are digitally "reconstructed"; two commonly used approaches are filtered backprojection and iterative reconstruction. Reconstruction algorithms output a dataset which is suitable for analysis. **D**) The sample may be viewed in a virtual environment in a variety of ways, including as a 3D rendered volume (**i**). Alternatively, 2D cross-sections, or “slices”, of the sample may be viewed (**ii**). Taken from O’Sullivan et al. (2018)

MicroCT is employed in a variety of fields, from materials science (Stock, 2008) to geology and the biological sciences (Shearer *et al.*, 2016). For biological researchers, the attraction of using microCT is the ability to obtain 3D morphological information, which can be achieved at the expense of slightly inferior spatial resolution when compared to traditional paraffin-based histology (Metscher, 2009a; Busse *et al.*, 2018). In some cases microCT instruments can surpass the resolution limit of light microscopy (Withers, 2007; Kampschulte *et al.*, 2016), however this comes at the expense of a reduced field of view which may not be appropriate for many samples. It is important to differentiate between the gantry-based microCT scanners generally used for *in vivo* imaging at low (~100 μm) resolution, and the higher resolution microCT scanners featuring samples on rotating tables, which are generally capable of the aforementioned histological resolutions. The work in this thesis involves only the use of such "rotating table" scanners to image chemically-fixed biological samples *ex vivo*. Within table based scanners which are referred to by "microCT" in this thesis, a further delineation exists between those which purely exploit geometric magnification of the cone-shaped X-ray beam to achieve higher resolutions (up to 3 μm), as opposed to those which instead exploit micro-focus X-ray tubes, X-ray optics and optical magnification to achieve the highest possible resolutions (<200 nm). Systems which use optical magnification can be referred to as X-ray Microscopes (XRM). However, for the purpose of this thesis, both techniques are grouped under the term "microCT", as is conventionally done throughout the biological literature (Gignac and Kley, 2014).

2.3.2 Comparison of microCT to light and electron microscopy

Light microscopy differs considerably to microCT in the soft-tissue insights it can provide based on fluorescence imaging, which provides more functional information about the sample and its chemical composition. These spatial insights can be pushed through the resolution-limit of light microscopy via the use of advanced image reconstruction algorithms which exploit spatio-temporal behaviour of fluorescent species (fluorophores) in super-resolution (Huang *et al.*, 2009). Furthermore, optical sectioning allows 3D imaging, albeit at anisotropic resolution. However, central to 3D optical sectioning of samples at depths over 100 μm is the need to optically clear the sample by applying detergents and bleach – this treatment allows excitation light to pass to sufficient depths to fluorophores (Muntifering *et al.*, 2018). Clearing techniques may include the use of organic solvents (Renier *et al.*, 2014) or detergents (Hama *et al.*, 2011)

which strip away light-scattering lipids within the sample, including the phospholipid bilayers of cells. Alternatively, hydrophilic reagents may be used which, when infiltrated into the sample, reduce the variations in refractive index in the sample interior which are responsible for scattering and opacity (Richardson and Lichtman, 2015). Optical sectioning without clearing is possible beneath 100 μm depth, facilitating *in vivo* experiments via intravital microcopy (Weigert *et al.*, 2010). However, scattering of light by the tissue prevents deeper imaging (Richardson and Lichtman, 2015), and reduces the effective resolution of features of interest compared to cleared samples (Clendenon *et al.*, 2011). Whilst clearing techniques lead to increased sample transparency and depth of imaging, the loss of sample lipid leads to an almost complete loss of morphological detail. Therefore, whilst resolution of fluorescence microscopy may be superior to microCT, morphological detail in the tissue is lost due to the clearing process. MicroCT on the other hand can achieve greater imaging depths and can determine the tissue morphology inside the sample without the need of clearing, but techniques for molecular localisation are poorly developed.

Use of 3D electron microscopy has grown in recent years (Peddie and Collinson, 2014), and continues to provide ultrastructural insights into tissues. EM resolution is far superior to microCT, and approaches several nanometres for 3D techniques. A trade-off is that small fields of view are required to facilitate these ultra-high magnifications. Therefore, microCT is more suited for tissue morphology rather than organellar morphology. There is a continuing drive to continue expanding the volumes which electron microscopic techniques can probe. For instance, the use of Xenon Plasma Focussed Ion Beams (PFIB) as substitutes for Gallium-based focussed ion beams in FIB-SEM has led to increased speed and volumes of EM imaging (Burnett *et al.*, 2016) albeit orders of magnitude lower than microCT. However, it may be conceivable that in future, as 3D EM volumes continue to increase, insights at the tissue level, such as vascular structure and neural organisation may become more readily addressed using electron microscopy. With this being the case, a current important direction of methodological development, correlative microscopy, has sought to integrate EM and microCT workflows together to increase the ease and efficiency of ultrastructural imaging. These workflows are discussed in more detail in the next section.

2.3.3 Technical challenges in biological MicroCT

A consistent challenge of biological soft tissue imaging is the attainment of sufficient contrast to allow differentiation and quantitative analysis of features within the sample. This is because biological soft tissues are relatively low-density and are mostly composed of light elements including primarily carbon and oxygen, which poorly attenuate X-rays. Two different approaches may be used to gain sufficient contrast in X-ray images despite the low native contrast; phase contrast and staining.

Phase contrast

Phase contrast imaging exploits differential phase shift of X-rays by different “regions” of the sample in order to generate contrast (Momose *et al.*, 1996). Therefore, instead of a 3D map of attenuation, a 3D map of phase shift is produced in the final tomogram. Variation in the refractive index of the sample is responsible for these changes in phase. However, as X-ray detectors can only detect changes in X-ray intensity, imaging of this kind requires the implementation of specialized optics, and/or the use of spatially coherent X-ray beams that allow the phase information to be converted into readily detectable intensity variations. Phase contrast negates the need for staining processes to increase absorptive contrast, allowing tissue to be imaged closer to its native state, without artifacts such as shrinkage. Phase contrast has been effectively used to investigate morphology of brain (Schulz *et al.*, 2010; Lwin *et al.*, 2016), intervertebral discs (Disney *et al.*, 2017) and even in post-mortem pathological investigation (Zamir, 2017). However, due to the specialized illuminating beams and optics required, phase contrast is a less accessible technique compared to staining. Additionally, staining may more easily facilitate imaging of features of interest in certain samples, depending on the specificity of the staining reaction occurring.

Staining

Staining of biological tissue generally involves submerging the fixed tissue of interest within a solution of high-Z ionic composition, for instance iodide. Immersion staining for microCT works on the same principles as its light- and electron microscopic analogues; that differential binding of stain to compositionally heterogeneous elements within a sample allows differential absorption of incident X-rays leading to contrast between different features of interest. Iodine is a commonly used stain in soft-tissue microCT imaging (Gignac and Kley, 2014), in the forms of

aqueous potassium iodide (KI), potassium triiodide (I_2KI aka Lugol's Iodine), and ethanoic Iodine solution (I_2E) (Metscher, 2009a). Stains for electron microscopy require high electron density in order to be attenuating of incident electrons, and these characteristics also make them translatable to microCT sample preparation. EM stains utilised for microCT to date include Osmium tetroxide (Descamps *et al.*, 2014) and Uranyl acetate (Faraj *et al.*, 2009). There is also potential for other less common EM stains to be used. For example, copper sulphate (Tapia *et al.*, 2012), of which only a little is known about its performance as a microCT stain (Pauwels *et al.*, 2013). The common usage of such translatable stains also facilitates correlative workflows incorporating electron microscopy (Eshar *et al.*, 2011; Handschuh *et al.*, 2013). Phosphotungstic Acid (PTA) and Phosphomolybdic Acid (PMA) have also been employed as MicroCT contrast agents (Metscher, 2009a; b; Nierenberger *et al.*, 2015). PTA has been noted to be of particular interest to researchers aiming to visualise collagen, as it binds collagen specifically (Nemetschek *et al.*, 1979). PMA exhibits similar collagen binding behaviour to PTA (Puchtler and Isler, 1958). Antibodies have also been used as contrast agents, the most successful case being use of a peroxidase conjugated antibody to precipitate silver within tissue (Metscher and Müller, 2011). In this way, metal deposition is concentrated around the specific sites of binding, resulting in a tomogram of the target molecule's distribution. The electron-dense gold-labelled antibodies which are used for immunogold molecular imaging in electron microscopy are a further candidate for use in an immunohistochemical approach to microCT, and have now been used successfully in brain tissue (Depannemaecker *et al.*, 2019). A critical consideration in this case is ensuring sufficient concentration of the metal within the tissue to generate sufficient contrast. In this regard, previous attempts at using silver nanoparticles as soft tissue contrast agents have been successful (Zou *et al.*, 2015), suggesting that antibodies bound to other, non-gold metal nanoparticles may prove efficacious new contrast agents.

A central methodological consideration in immersion staining is optimising staining time and stain concentration in order to ensure sufficient penetration of the stain into the tissue without sample shrinkage. Stains which penetrate tissue quickly are often favoured for their ease of use in microCT studies, for example potassium iodide and Mercuric (II) Chloride ($HgCl_2$) (Pauwels *et al.*, 2013). When imaging new and previously uninvestigated samples, researchers may estimate a suitable staining time based on those previously recorded in soft tissue samples (Pauwels *et al.*, 2013). For samples stained with iodine, Gignac et al. (2016) produced a meta-

analysis of staining protocols for samples of a variety of sizes and morphologies, to which researchers may refer to in order to estimate an optimal staining procedure. A more rigorous approach is to run experiments optimising staining prior to the initiation of study. Researchers adopting this approach have longitudinally assessed stain penetration over a single incubation of I_2KI using microCT (Balint *et al.*, 2016), whilst others have used a trial-and-error approach of testing many incubations of different concentrations of I_2KI on the same sample (Aslanidi *et al.*, 2013). However, whilst higher concentrations of staining solutions may be effective in their fast penetration of sample tissue, soft tissue samples are vulnerable to shrinkage when immersed in hypertonic solutions (Vickerton *et al.*, 2013). One approach to avoid such artefacts is the immersion of samples in a graded ethanol series, followed by immersion in ethanoic staining agent (Metscher, 2009a; de Souza e Silva *et al.*, 2015)

The 3D imaging capability of microCT means it is uniquely suited to visualising the vascular morphologies of whole organs (Epah *et al.*, 2018). These networks of vessels have a dense tree-like bifurcating structure. In order to better visualise these, perfusion contrast has been developed as a methodological approach. A whole animal is perfused with a radiopaque compound which fills and creates a cast of blood vessels throughout the body. The composition of the compound may allow the surrounding tissue to be dissolved (using a strong basic solution such as Potassium hydroxide) leaving a rigid cast behind (corrosion casting) (e.g. Mondy *et al.*, 2009, 2013). Previously morphology of such casts has been qualitatively assessed using a light stereomicroscopy (Andrade and Santana, 2010). Alternatively, a variety of propriety and non-propriety “soft” perfusion contrast agents are currently available which require the surrounding tissue to be intact for preservation of the casts’ structure. Microfil is one such example which has found broad uses in a variety of tissue including brain (Ghanavati *et al.*, 2014; Perrien *et al.*, 2016), liver (Masyuk *et al.*, 2003; Den Buijs *et al.*, 2006; Vasquez *et al.*, 2011) and kidney (Vasquez *et al.*, 2011). It consists of a lead chromate and lead sulphate-containing silicone rubber compound to which is added a curing agent shortly before perfusion, and is advertised to shrink minimally. Angiofil and Britevu are competitor products to Microfil which are similarly designed to be perfused into organs which can be scanned intact. Angiofil is a younger fluorescent product and has a smaller body of supporting literature (Grabherr *et al.*, 2008a; b). Its capability to be fluorescently imaged has been exploited to provide estimates of vessel filling by the perfusion agent in a correlative workflow (Schaad *et al.*, 2017). Alternatively,

"homemade" soft perfusion contrast agents continue to be used which are generated using suspensions of radiopaque contrast species such as lead tetroxide (Xiong *et al.*, 2017; Lachant *et al.*, 2019) and barium in mixtures of agarose gel or gelatin (Turkoglu *et al.*, 2014; Liu *et al.*, 2019).

2.3.4 Correlative imaging

Of growing importance is not just imaging using isolated modalities, but combining multiple insights from different techniques in a single workflow. The combination of multiple modalities may serve several purposes. For instance, it may be that producing a large-scale "map" of the sample can help put insights in a clear spatial context for the reader; alternatively there may be a requirement to put biochemical information, e.g. as gained from fluorescence immunohistochemistry, within the morphological context of the tissue. This latter reason is largely the case in Correlative Light and Electron Microscopy (CLEM), for which many workflows have been developed to co-localise fluorescent reporters or exogenous fluorescent labels, such that ultrastructural information can be sought from regions in which specific genes of interest are expressed (Oorschot *et al.*, 2014; Russell *et al.*, 2017). Currently, the forefront of CLEM research is aiming to increase the level of molecular resolution of the techniques closer to immune-gold levels (sub-100 nm) by using super-resolution fluorescence approaches requiring sophisticated image reconstruction (Peddie *et al.*, 2017).

Alternatively, if a sample is highly morphologically complex and internally heterogeneous, microCT may be employed in a workflow to guide subsequent sectioning processes for either light- or electron-microscopic imaging (Handschuh *et al.*, 2013; Starborg *et al.*, 2019). In the case of electron microscopy, microCT can be conveniently carried out during sample preparation, after the sample has been embedded, but before sectioning takes place. The electron-dense stains which are required to introduce to the sample to provide EM contrast perform a similar attenuating role during the microCT scan; in this way, the stain distribution within the sample can be inspected to ensure sufficient penetration has taken place before further time investment in the sample. In addition, high-throughput approaches to scanning which sacrifice resolution for speed may be employed to screen a range of samples for features of interest before sectioning takes place, allowing maximum time and cost efficiency of experimental design. Once an object has been "scouted" by microCT, the precise location to the

desired beginning of an imaging frame may be milled down to and shaped with an ultramicrotome and razor blades, allow site-specific electron microscopy. Such an approach may be extremely useful for EM of parasites such as *T. muris* and *S. mansoni* as they are unpredictably distributed within their host tissues, and could only be made visible using non-destructive micro-computed tomography.

2.3.5 Scope and design of biological microCT studies

In the biological sciences, microCT is now more commonly employed in several specific research areas. Since native X-ray contrast in dense, calcified tissues including bone and teeth is excellent, 3D morphological characterisation using microCT is very commonplace in bone and dental research. High skeletal contrast means that microCT has also lent itself to studies of dental morphology and diseases, as well as other musculoskeletal conditions such as arthritis, but also the dynamics of bone architecture in healthy conditions (van der Linden *et al.*, 2006).

In studies of 3D morphology in soft tissues, a more diverse range of experimental design can be seen, due to the greater effort involved in sample preparation, challenges in sample segmentation and larger diversity of tissue structure and morphology. Therefore, many soft tissue studies focus on methodological developments including staining,(**section 2.3.3**) (Boughner and Cooper, 2019; Hsu *et al.*, 2019; Depannemaecker *et al.*, 2019). For instance, the effects of a variety of stains on a tissue may be observed (Saukko *et al.*, 2019). If a suitable sample preparation protocol is available, studies on specific tissues are then structured in a descriptive manner, in which the known features of the tissue are described as they appear in microCT data, thus demonstrating feasibility of the imaging approach. The key message of such papers is the positive detection and identification of known features (Depannemaecker *et al.*, 2019; Pascolo *et al.*, 2019), sometimes in comparison to histology (Barbone *et al.*, 2018). In additional methodological studies, microCT of soft tissue supplement data collected by more traditional approaches by providing spatial context for molecular localisation by fluorescence microscopy, and approach which has been utilised in the field of evolutionary biology (Rasch *et al.*, 2016; Heude *et al.*, 2018). The key findings of such studies are totally independent from any 3D morphological insights from microCT. In this way, the vast majority of soft tissue microCT studies remain either methodological in nature, or feature the modality in a supplementary setting to complement the main research insights from other imaging techniques.

There is now a growing range of studies in which microCT is the driving force behind the research conclusions. In these cases, the morphometric capabilities of microCT are used to address hypotheses directly, either by quantification and of morphological features of interest not possible through 2D imaging modalities between experimental groups such as mouse strains (De Clercq *et al.*, 2019) or drug treatment groups (Hlushchuk *et al.*, 2019; Lachant *et al.*, 2019). Alternatively a descriptive approach may be taken in which novel morphological features are characterised (Bikis *et al.*, 2018; Quade *et al.*, 2019). A growing range of effective and complex approaches to soft tissue segmentation (Baum *et al.*, 2019; Yan *et al.*, 2019) provides a basis for increasing opportunities of hypothesis-driven microCT research with the power to provide insights beyond those of conventional 2D histology. Critically in this thesis, the field of parasitology features many opportunities for hypothesis-driven research which is driven centrally by 3D morphology and morphometry (O'Sullivan *et al.*, 2018). The next section of this review will therefore describe the current state of knowledge and application of microscopy to the two focal parasites of this thesis, *Trichuris muris* and *Schistosoma mansoni*, and will outline the outstanding questions in their biology which microCT could potentially answer.

Microscopy in *Schistosoma* and *Trichuris* research

Both light and electron microscopy have had key roles in the study of *Trichuris* and *Schistosoma*. The capabilities of these imaging techniques have facilitated insights in a variety of levels, ranging from the structure of the lifecycle, to host-parasite interactions and pathology of disease. The following section covers the existing knowledge of *Schistosoma* and *Trichuris* which are relevant to the subsequent investigations in the thesis, including the role of microscopy, and the potential role of microCT in the study in each.

2.4 Current understanding of *Trichuris muris* and its niche

2.4.1 The *Trichuris* life cycle

Trichuris trichiura, the causative agent of Trichuriasis, is a Soil Transmitted Helminth (STH) estimated to affect nearly half a billion people worldwide (Pullan *et al.*, 2014). Many infected individuals maintain a low-level infection with minimal symptoms, but in vulnerable patients such as children, high burdens of *Trichuris* infection are accompanied by harmful pathology such as anaemia and colitis-like symptoms, which may lead to compromised physical and educational development (Simeon *et al.*, 1995; Gardner *et al.*, 1996; Ahmed *et al.*, 2012). Understanding the life cycle and immunopathology of *Trichuris* is an important aspect of informing control strategy. Most research towards these goals has been undertaken in *Trichuris muris* and its host the mouse *Mus musculus*, which is a convenient and tractable model which reflects many of the events in human infection (Klementowicz *et al.*, 2012). All worms of the *Trichuris* genus share a similar monoxenous life cycle (**Fig. 2.2**), with transmission via the faecal-oral route. After the mammalian host ingests an egg the larvae hatch in the caecum before penetrating and entering the caecal epithelial cells at the base of the crypts of Lieberkühn (Lee and Wright, 1978). From this point onwards, *Trichuris* remains at least partly embedded within the epithelial cells of the host for the rest of its life, living in a unique intraepithelial tunnel of dead cells. Light microscopic investigation of worm embedded within the epithelium has revealed that worms progress through a series of four moults (Panesar, 1989). After the third moult, the tail end of the worm protrudes from the epithelial tunnel, facilitating mating in sexually mature worms. Eggs are laid into the lumen and are passed out into the environment with the faeces.

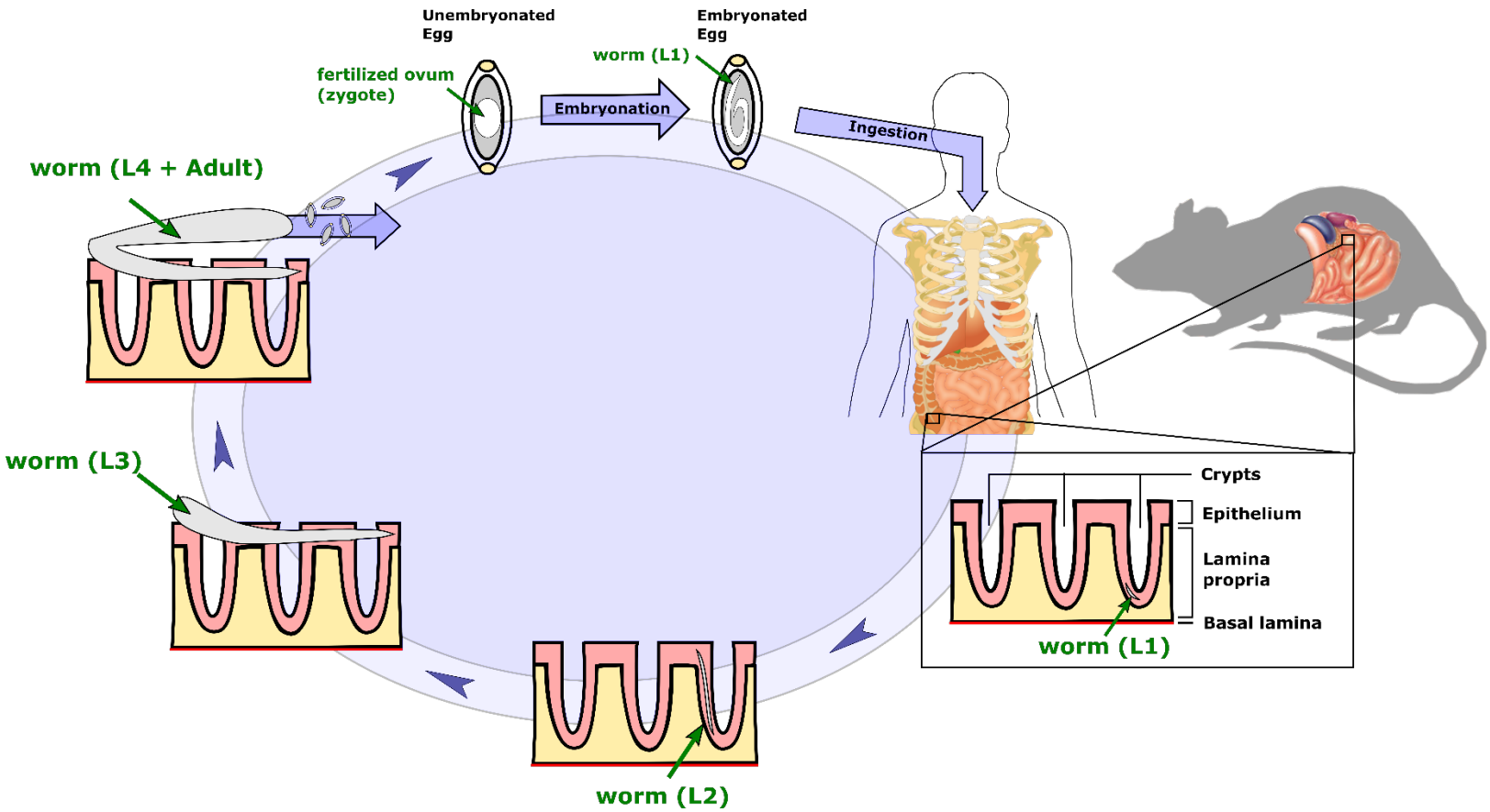

Figure 2.2: Life cycle of *Trichuris* in mammalian hosts. Embryonated eggs are ingested, for instance via contaminated food, and hatch in the caecum. Larval worms penetrate the epithelial cells of the caecum, and from this point on remain at least partly intracellular. During a series of moults, the tail end of the worm hangs outside of the tunnel to facilitate mating and egg-laying, whilst the stichosome remains embedded within a layer of dead epithelial cells.

2.4.2 Ultrastructure of the niche

The niche of *Trichuris* is specialised, and worms grow and maintain the epithelial tunnel whilst simultaneously nourishing themselves and avoiding the immune response of the host. During *Trichuris* infection, the anterior two-thirds of the worm (called the stichosome) remain burrowed within the intestinal epithelium. The stichosome is primarily filled with large, cylindrical cells called stichocytes, but also is the location of the bacillary band, which is a region of many hundreds of pores (bacillary pores) covering the ventral cuticle. The bacillary band is also punctuated by periodic swellings of the cuticle, called the cuticular inflations. The bacillary band and its associated structures remain in close contact with the interior of the host's epithelial cell layer.

Electron microscopy has been widely employed to characterise the intra-epithelial environment of *Trichuris*, as well as the adaptations which allow its survival. SEM of the caecum surface demonstrated the manner in which the worms tunnel through the epithelial cells, and that they are covered by a thin layer of epithelial material (**Fig. 2.3**). TEM of the tunnel interior has uncovered a variety of insights (**Fig. 2.4**) including the worm's syncytial nature, and suggests that the worm continually burrows through the lateral membranes of the epithelial cells (Tilney *et al.*, 2005). Fresh, intact host organelles are seen in the syncytium around the anterior of the worm, whilst disrupted, broken organelles characterise the more posterior regions of the tunnel (Lee and Wright, 1978). Most aspects of tunnel formation remain enigmatic, and the digestive or mechanical degradation of lateral membranes remains uncharacterised. Moreover, there is evidence of remodelling within the tunnel-forming syncytium, as evidenced by the markedly electron-dense remnants of the lateral membranes, as well as a layer of fibrous material appearing to cover the apical surface of the worm (Lee and Wright, 1978). Overall, the host-parasite interactions taking place within the tunnel remain poorly understood, and it is assumed that worms stay at the apical surfaces of the crypts. However, worms exhibit a plethora of surface structures of which not all have been thoroughly investigated. An understanding of the function of these surface structures may assist clarifying the events taking place at the host-parasite interface (Tilney *et al.*, 2005; Hansen *et al.*, 2016).

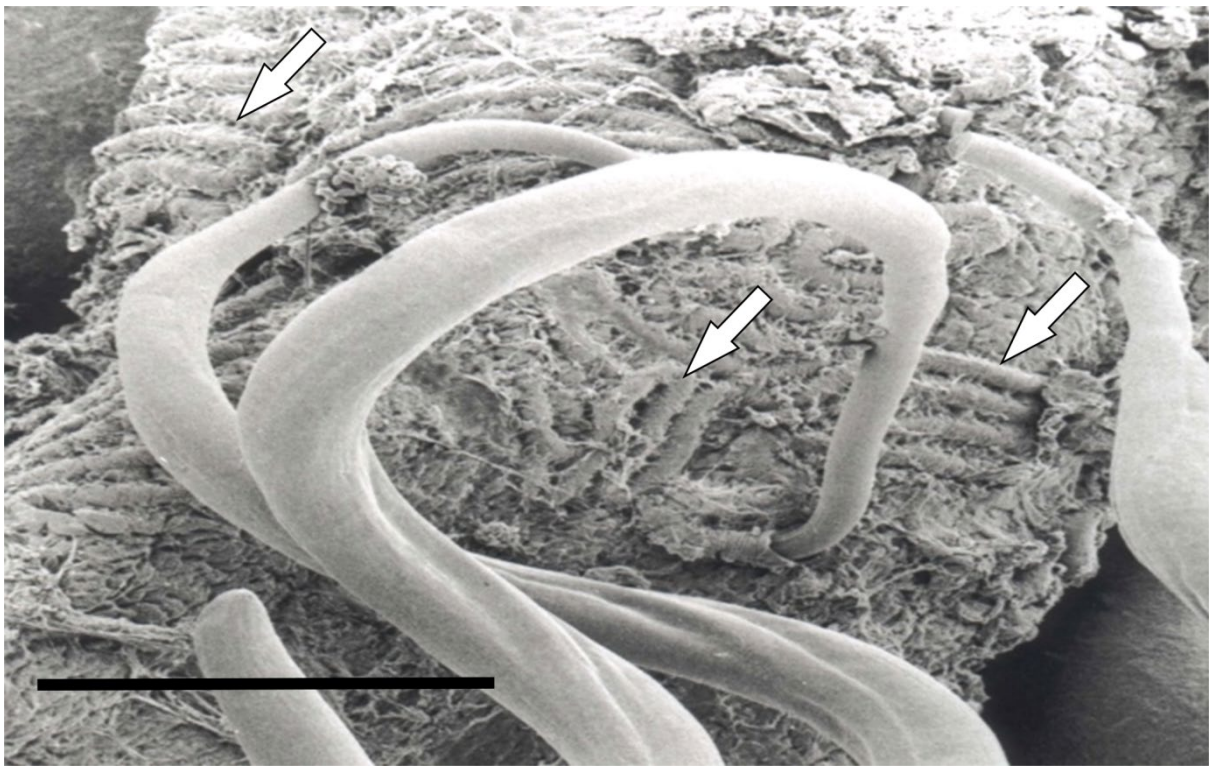

Figure 2.3: Scanning electron micrograph of three worms embedded within the caecal epithelium. The embedded portions of the worms appear as filamentous striations in the epithelial surface overlying the tunnel (arrows), whilst the posteriors of the worms lie free within the caecal lumen. Scalebar = 1 mm. Image generated by the Electron Microscopy Core Facility at the University of Manchester, and adapted from Hurst and Else (2013).

Figure 2.4: The epithelial niche of *Trichuris* spp., with reference to light and electron microscopic observations of the nature of the tunnel. Numbers 1 – 6 indicate observations taken from Lee and Wright (1978), Tilney et al. (2005) and Hutteman et al (2008), which have characterised the niche morphology and ultrastructure.

2.4.3 Cuticular structure and function

All nematodes have a cuticle, which serves as an antagonist for the longitudinal muscles to allow movement, and controls the transfer of substances between the worm and environment. Nematodes share a similar cuticular structure, which has been investigated by TEM (Johnstone, 1994). Above a layer of hypodermal cells lies the basal and median layers, which are collagenous in nature. Above the median layer is the cuticle cortex, which consists mostly of a protein called cuticulin (Fetterer and Rhoads, 1993). Covering the cortex is the epicuticle, a thin layer of lipids and carbohydrates. The cuticle of *Trichuris* is characterised firstly by its insolubility, and also by the folded lamellae of the cortex layer (Wright, 1968a). However, in addition a variety of surface structures punctuate the cuticle, which are thought to be involved in the maintenance of the epithelial niche.

Surface structures

Electron microscopy has been critical not only in providing a view of the intra-epithelial tunnel but has also been useful in clarifying the systematics of the Trichurid family (Pfaffenberger and Best, 1989; Lanfredti *et al.*, 1995; Torres *et al.*, 2011). However, beyond this, EM has provided insight into the nature of enigmatic *Trichuris* surface structures. These ultrastructural studies are not generally specific to *T. muris*, and are distributed through a range of trichurid species including *Trichuris vulpis, Trichuris trichiura, Trichuris myocastoris, Trichuris suis* and *Capillaria hepatica.* In the case of *Trichuris,* it is thus fair to say that our understanding of ultrastructure is a mosaic of genus-level insights, with potential differences between species remaining uncharacterised. The research in this area, whilst split between species, has all specifically focussed on the bacillary band, on the ventral side of the anterior portion of the stichosome (Sheffield, 1963; Wright, 1968b; Lee and Wright, 1978; Tilney *et al.*, 2005). SEM was critical in determining the nature of the bacillary band, which was named on account of the many bacillary pores present in the region (Fig. 2.5). The bacillary pores have been studied in detail using TEM, which has revealed that they are likely heterogeneous in function. The initial observations noted that the bacillary cells underlying the pores exhibited highly folded apical membranes, indicating either an absorptive or secretory role (Wright, 1963, 1968b; Tilney *et al.*, 2005). Additionally, the finger-like processes of sensory neurones are also seen in a subset of bacillary pores (Wright and Chan, 1973).

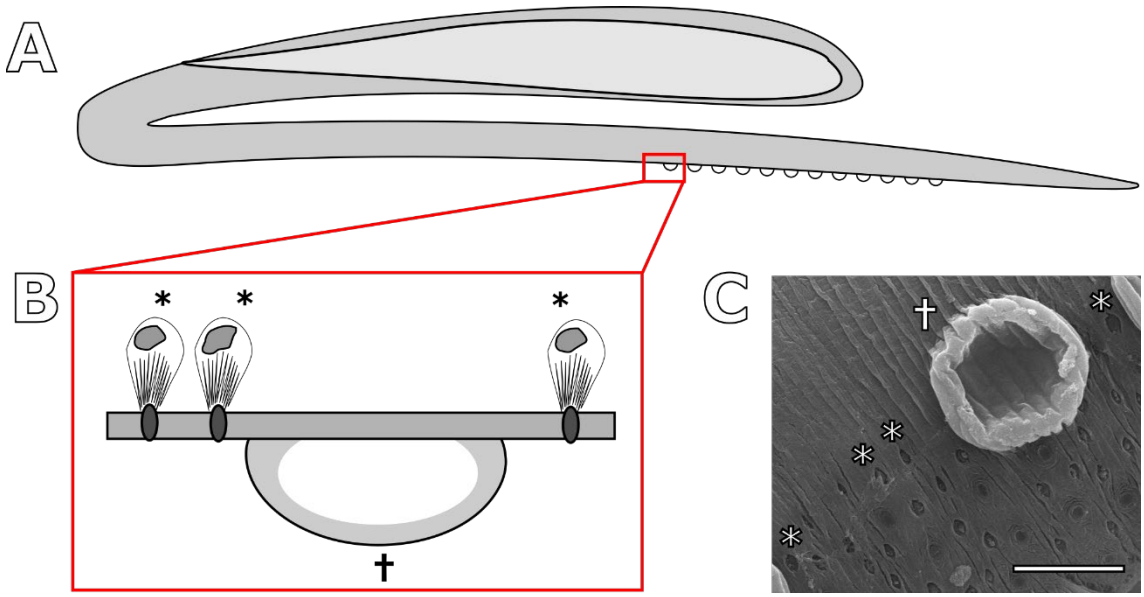

Figure 2.5: Structures of the bacillary band in *Trichuris* spp. A) The bacillary band is present on the worm's anterior-ventral surface in is characterised by the presence of the bacillary pores. **B**) Illustration showing the bacillary cells (*) underlying the bacillary pores. Raised portions of cuticle called the cuticular inflations (†) are also present on the bacillary band. **C**) SEM of *Trichuris muris* showing the bacillary pores (*) and a cuticular inflation (†). Scale bar = 10 µm.

In addition to the bacillary pores, *Trichuris* spp. exhibits cuticular inflations in the bacillary band. Under bright-field illumination and SEM they appear as blister-like formations in the anterior-most region of the bacillary band. The function of these structures is unknown, although some authors have asserted the existence of a secretory role (Hüttemann *et al.*, 2007). The most comprehensive ultrastructural analysis by TEM shows that in *T. vulpis* the inflations are likely fluid-filled, containing a fine anastomosing network with some more electron dense inclusions in the medial layer of cuticle (Wright, 1975), ultimately of unknown composition. A confounding factor in the investigation of the cuticular inflations is that differing external morphologies persist even through more recent SEM studies. In these cases, cuticular inflations either present themselves in a bulbous "inflated" state, or a collapsed, concave state. It has been speculated that these differences in morphology are due to the dehydration and drying processes used to prepare samples for SEM (Wright, 1975; Lopes Torres *et al.*, 2013), despite the fact that both forms are evident through a variety of studies in which all samples were dried (Robles *et al.*,

2014). No functional significance has been ascribed to differences in cuticular inflation shape, which is perhaps unsurprising given that generally their origin, development and function are so poorly characterised. It has however been noted that cuticular inflations bear some similarity to the cuticular bosses in *Gongylonema* spp., which is another nematode with an intra-epithelial niche (the oral mucosa) (Naem *et al.*, 2000).

Greater understanding of the composition and functional significance of *T. muris* surface structures may be important in generating new control strategies, given the likelihood of them having a critical role in supporting the intra-epithelial niche. Since most ultrastructural research took place, *T. muris* has arisen as the most dominant model of trichurid infection of mice in the lab. Therefore, there is now a need to consolidate the existing, multi-species knowledge about the bacillary band from *T. vulpis, T. myocastoris* and *T. suis* into the *T. muris* research landscape. *T. muris* now forms the basis of most of our understanding of immunity and host-parasite interactions during trichuriasis (Klementowicz *et al.*, 2012; Hurst and Else, 2013), but these insights are rarely related to the ultrastructural events happening within the tunnel. In order to accomplish this, newer research should aim to provide and up-to-date view on just how much of the previous ultrastructure research applies particularly to *T. muris.*

2.4.4 Murine immunity to *Trichuris muris*

Understanding of the host immune response to *Trichuris* largely comes from studies of *Trichuris muris* in its mouse host, which closely mirrors the events of a human infection (Klementowicz *et al.*, 2012). The causes of susceptibility and resistance to *Trichuris* infection fundamentally hinge on the T-helper type 1/ type 2 (Th1/Th2) polarity of the immune response (Else and Grencis, 1991). Variable resistance and susceptibility of different mouse strains have been a useful tool in unpicking the Th1/Th2 model and understanding effector mechanisms of worm expulsion. For instance, mouse strains may be susceptible (e.g. AKR or SCID) or resistant (BALB/c) to infection. Furthermore, and critically to the work contained within this thesis, susceptibility is some strains may be dose-dependent (**Table 2.2**). In the C57BL/6 and BALB/c mouse strains, for instance, administering a low dose to mice results in susceptibility to chronic infection, whereas mice given high doses are able to clear infection before adult worms are established (Bancroft *et al.*, 1994).

In early research into mouse immunity to *Trichuris muris*, CD4+ T-cells were identified as key immune drivers, and a paradigm was established in which a Th2 response driven by IL-4 is required to expel worms, with downstream IL-13 also having a key role in worm expulsion (Else *et al.*, 1994; Bancroft *et al.*, 1998, 2000). On the other hand, susceptibility in animals that maintained chronic infections is strongly correlated with a dominant Th1-polarised response primarily characterised by pro-inflammatory IFN-γ (Else *et al.*, 1992) and IL-12-dependent IFN-γ (Bancroft *et al.*, 1997). However, beyond this Th1/Th2 dichotomy a richer and more varied immune response has been identified; for instance, pro-inflammatory TNF-α acts as a regulator of both Th1 and Th2 parasite-specific responses (Hayes *et al.*, 2007). In addition, a range of other cytokines with regulatory roles have also been implicated in induction and maintenance of Th1 and Th2 responses, including IL-10 (Schopf *et al.*, 2002), IL-27 (Bancroft *et al.*, 2004) and IL-18 (Helmby *et al.*, 2001).

Beyond the central role of CD4+ T-cells, researchers have also attempted to unpick the roles of other innate and adaptive cell types in induction and maintenance of the T-helper response throughout infection. The role of dendritic cells has attracted interest, due to their function as Antigen-Presenting Cells (APCs) which are known to prime T-cell Th1/Th2 bias. Dendritic cells promptly mobilise near to the colonic epithelium within the first week of infection in mice which are resistant to *T. muris* infection (Cruickshank *et al.*, 2009), providing a kinetic argument for their role in resistance. However, whilst some subsets of intestinal dendritic cells are essential for clearance of *T. muris* infection (Demiri *et al.*, 2017; Bradford *et al.*, 2018), the presence of others does not seem to be required to clear infection, as evidenced in knockout mice (Mullaly *et al.*, 2011). B-cells have been implicated in resistance, although their role remains somewhat unclear. The μMT mouse strain which lacks B-cells is unable to clear the parasite (Blackwell and Else, 2001), however SCID mice adoptively transferred CD4+ T-cells are perfectly able to clear infection without B cells (Else and Grencis, 1996). B-cells may have a role in maintaining the Th2 response in an antibody- independent manner (Sahputra *et al*. 2019). Basophils and eosinophils are also thought to have a role in promoting the Th2 response during infection via the secretion of cytokines (Perrigoue *et al.*, 2009; Svensson *et al.*, 2011).

Mouse Strain	Infection	Outcome	Reference
AKR	High dose = 200 eggs	susceptibility	Else et al. 1992
	Low dose < 200 eggs	susceptibility	
SCID	High dose = 200 eggs	susceptibility	Else and Grencis 1996
	Low dose < 200 eggs	susceptibility	
C57BL/6	High dose = 200 eggs	resistance	Bancroft et al. 1994
	Low dose <=40 eggs	susceptibility	
BALB/c	High dose = 200 eggs	resistance	Cruickshank et al. 2009
	Low dose <= 20 eggs	susceptibility	

Table 2.2: Strain- and dose-dependent differences in susceptibility to chronic *T. muris* infection.

Downstream of understanding the immune basis of regulation of resistance and susceptibility to *T. muris* infection, another important facet of *T. muris* research has been identifying the effector mechanisms by which worms are expelled in resistant mice. Increased muscle contractility has been associated with expulsion of the parasite, and it has been suggested that type-2 cytokines such as IL-4 and IL-13 may be directly responsible for hypercontractility of smooth muscle (Akiho *et al.*, 2002; Khan *et al.*, 2003). In addition, increased epithelial cell turnover and its regulation by CXCL10 is a key mechanism in expulsion in resistant strains of mice (Cliffe *et al.*, 2005). Moreover, slowing the rate of epithelial cell turnover in a deliberate manner promotes worm survival (Bell and Else, 2011). The mucus barrier has also been shown to have importance in worm expulsion. In particular, MUC5AC production has been associated with resistance to infection (Hasnain *et al.*, 2011). Therefore, a range of potential effector mechanisms have been identified, playing diverse roles in resistance to chronic *T. muris* infection.

Conversely, it is also of interest to researchers to study the conditions which promote chronic infection, in order to achieve a better understanding of how *Trichuris muris* survives within the niche. Going hand-in-hand with this aim is an understanding of the debilitating gut immunopathology, which is driven by the Th1 response. A recent insight is that *T. muris* can actively modulate the host immune response, and prevent the establishment of a resistant Th2 response by secreting a protein throughout development which is likely to bind and inhibit IL-13 (Bancroft *et al.*, 2019). However, once the worm is established, a key feature of chronic

infection is remodelling of the intestinal epithelium. There is a marked IFN-γ crypt hyperplasia, which is characterised by increased intestinal epithelial cell proliferation and increased crypt length (Artis *et al.*, 1999). Interestingly, and perhaps counter-intuitively, the inflammatory cytokines IFN-γ and TNF-α are also associated with increased levels of apoptosis at the base of the crypts during chronic infection (Cliffe *et al.*, 2007) . Regulation of apoptosis and cell shedding in the crypt may be of further interest in characterising the survival of *T. muris* during chronicity, as it is already known to be a very tightly regulated process, which includes the input of the microbiome (Bullen *et al.*, 2006; Zaborin *et al.*, 2017).

2.4.5 Challenges in *Trichuris* control and research

One of the largest challenges in control of *Trichuris* is the poor efficacy of existing anthelminthic drugs. Commonly used anthelminthics include albendazole and mebendazole, which are much less effective in treating *Trichuris* infection than other STH infections (Keiser and Utzinger, 2008). Even when albendazole and mebendazole are used in combination, efficacy in expelling adult worms can be beneath 50% (Speich *et al.*, 2015), although trials of large-scale combination therapy continue (Patel *et al.*, 2019). Authors of drug efficacy studies have never speculated as to why effectiveness of anthelminthics is so poor, and therefore fresh hypotheses are required to start investigations in this issue. A starting point may involve a better understanding of several aspects of the *Trichuris* life-cycle. Drugs such as albendazole and mebendazole specifically target polymerisation of tubulin within worm intestinal epithelial cells (Lacey, 1990). However, since the bacillary band may have a more important role in some forms of nutrient uptake than the worm's intestine (Hansen *et al.*, 2016), drugs targeting the intestine may perform sub-optimally. This may explain why they are less efficacious in Trichuris than in *Ascaris lumbricoides*, another STH which feeds conventionally through an intestinal canal. Moreover, the overlying epithelium of the syncytial tunnel may prevent access of drugs to the worm itself, and some such as albendazole already exhibit poor penetrance of the intestinal epithelium (Jung *et al.*, 1998). An important goal in ongoing *Trichuris* research is to continue to identify new anthelminthic therapies to supplement ongoing control efforts (Geary, 2012). To support such an effort, new targets for drugs must be identified, i.e. nematode-specific proteins which are critical to the survival of *Trichuris* in its niche. Genomics approaches are assisting in this area (Foth *et al.*, 2014), but a greater understanding of the worm life-style, including tunnel formation and maintenance, is required. Moreover, there is a requirement for tools to quantify

the integrity of the epithelial tunnel, both to understand the poor performance of extant drugs and potentially to assess that of newer therapies.

In order to understand the intra-epithelial tunnel, new approaches to visualisation are required, by which the positioning of worm structures in the tunnel interior, and the worm's path through the host tissues can be characterised. Such experiments have not been possible in the past, as paraffin-based sectioning can capture only small snapshots of the worm at an orientation which may provide a sub-optimal view of the tissue. Moreover, 3D fluorescence microscopy approaches are complicated by the lack of transgenic worms and poor antibody penetration into uncleared intestine which precludes intravital imaging. MicroCT provides an excellent opportunity to non-destructively visualise the niche of *T. muris in toto*, showing both the orientation of the parasite and any preferential path it may take through the tissue. In addition, study of larval worms may reveal the earliest events in tunnel formation, which have yet to be described beyond microscopic observations. In addition, finding out more about the nature of surface structures and their potential roles in host-parasite interactions may also be productive in suggesting new targets for therapy. Cuticular inflations represent an important part of this process, as they are the least well understood structure on the surface, and may have a specific role in maintaining the worms' intra-epithelial lifestyle. However, again new imaging approaches are required, which are able to facilitate capturing many of these sparsely-distributed structures. A correlative imaging workflow, which could efficiently capture the inflations within the frame of imaging of a secondary modality, could be a productive avenue for the next set of insights characterising *Trichuris* lifestyle and pathology

2.5 Current understanding of *Schistosoma mansoni* life cycle and pathology

2.5.1 The *Schistosoma* life-cycle

Schistosomiasis (as known as Bilharzia) is a disease caused by the flatworm genus *Schistosoma* (McManus *et al.*, 2018), which estimated to directly affect almost 200 million people worldwide (Vos *et al.*, 2017). There are several different species of *Schistosoma* which cause acute and chronic disease in humans, including *S. japonicum, S. haematobium* and *S. mansoni*. During their lifecycle (**Fig 2.6**) *Schistosoma spp.* are always transmitted to the definitive host through the aquatic environment, in which snails such as *Biomphalaria* spp. act as the intermediate host/vector. Snails release infective cercariae into the surrounding water which penetrate the skin of the host. From this point, the larvae undergo an extensive migration through the host systemic circulation. Transit through these tissues and the accompanying Th1 inflammatory response to the larvae constitutes the acute phase of infection, which includes swimmers itch and Katayama fever (Verbrugge *et al.*, 2004; Ross *et al.*, 2007). Eventually the larvae reach the abdominal vasculature. Here, the different Schistosome species take up residence in different abdominal compartments and mature to adulthood. *S. mansoni* for instance takes residence in the mesenteric veins draining the small and large intestines as well as the portal vein at 5 weeks post-infection, whilst *S. haematobium* instead localises to the vasculature surrounding the bladder. The flukes mature to adulthood and mate in this environment. In *S. mansoni,* propagation of eggs in the environment to continue the life cycle is achieved by traversal across the intestinal wall into the lumen where they pass out via the faecal route. A pre-requisite for this process is adhesion of the egg to the correct region of vasculature to allow traversal (Costain *et al.*, 2018).

Harmful pathologies in schistosomiasis result from the inflammatory response of the host to eggs which become trapped within tissues (the egg granuloma). The burden of schistosomiasis pathology is significant, with almost 10,000 estimated deaths occurring in 2017, with over 1 million Disability-Adjusted Life Years (DALYs) in affected individuals (Vos *et al.*, 2017; Roth *et al.*, 2018). All *Schistosoma* species can produce morbidity including anaemia and poor child development, due to the inflammatory burden on the host (Friedman *et al.*, 2005; King and Dangerfield-Cha, 2008). However, site-specific pathology also occurs based on the migration route of eggs during the life cycle. For example, retention of eggs in the intestinal wall can result

in intestinal bleeding and diarrhoea (Mohamed *et al.*, 1990). *S. haematobium* is responsible for urogenital schistosomiasis, in which eggs trapped in the bladder lining cause discomfort, increased risk of bacterial infection and renal dysfunction (Khalaf *et al.*, 2012). In addition, eggs may be swept by the circulation to a variety of systemic organs, where they become lodged and clearance is not guaranteed. Eggs of *S. japonicum* can affect the Central Nervous System (CNS), where they can cause symptoms such as headache, epilepsy, muscle pain and paralysis (Ross *et al.*, 2012). Some of the most severe pathology can be due to the hepatosplenic form of disease, in which eggs deposited in the liver lead to ascites (accumulation of fluid within the peritoneal cavity), and potentially fatal bleeding of the oesophagus (Richter *et al.*, 1998).

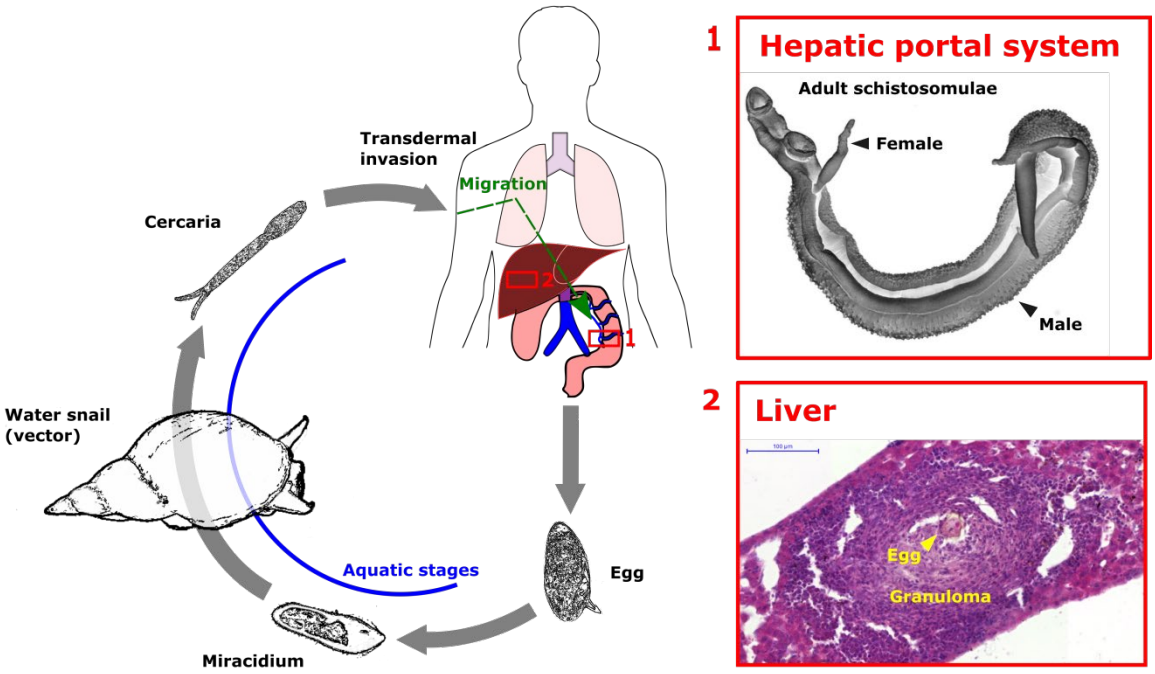

Figure 2.6: Lifecycle of the liver fluke *Schistosoma mansoni* during human infection. In aquatic environments, schistosome eggs hatch, producing miracidia, which infect the water snail vector of the disease. Cercariae are released by the snails and are motile in the aqueous environment. Infective cercariae enter the human host via the skin. After migration across the dermis, they migrate intravascularly to the hepatic portal system via the lungs and systemic circulation. Maturation to adulthood occurs within the mesenteric venules of the colon and the portal vasculature (1). Eggs laid by adults can be swept back by the flow of blood into the systemic circulation and may become lodged in the liver. Here, they cause a damaging inflammatory response called a granuloma (2), the downstream pathophysiological effects of which may include fatal oesophageal varices. Additionally, eggs may migrate to the lumen of the colon, from where they are then shed in the faeces.

Although *S. haematobium* is the most common and burdensome schistosome infecting humans (Medina *et al.*, 2008), *Schistosoma mansoni* is the most-studied schistosome in regard to its lifecycle and generation of pathology. The experimental focus on *S. mansoni* exists because unlike the majority of schistosome species, the life cycle, including some degree of hepatic pathology, is completely recapitulated in both rodents and humans (Loker, 1983). Microscopy played a key role in the identification of the *S. mansoni* migration route around the body, and histological techniques was used to measure the duration of migration of cercariae through the skin (Miller and Wilson, 1978; Wilson and Lawson, 1980). Further histology then revealed that cercariae were present in a variety of systemic organs including the spleen, kidney and brain following their exit from the lungs, which bolstered previously made suggestions that parasites migrated from the lungs to the liver via the systemic circulation (Wheater and Wilson, 1979). Greater clarity in the migration route of *S. mansoni* was achieved by the subsequent employment of X-ray imaging. Autoradiographic tracking, which involved labelling parasites with the gamma-emitting isotope [^{75}Se]-methionine, allowed larvae to be visualised within whole tissues exposed to an X-ray film. This approach allowed accurate assessment of the numbers of schistosomes within the skin, as well as the systemic and splanchic organs post-infection (Georgi, 1982; Georgi *et al.*, 1983).

During the developing saga of schistosome migration, further study by TEM revealed associated ultrastructural events within the larvae. For instance, upon migration across the skin, Crabtree and Wilson (1985) noticed an associated emptying and disappearance of the parasites' acetabular gland, which suggested it as the source of lytic enzymes key to facilitating the transit of larvae across the skin. *Schistosoma* has evolved to survive in an extremely hostile environment, the blood, which, like all tissues, is subject to constant immune surveillance. TEM revealed there was a constant turnover of the membranocalyx, the exterior most surface of the invading worms tegument, and this turnover was speculated to constitute an immune avoidance strategy (Wilson and Barnes, 1977). Further TEM investigation of the larval tegument revealed accumulation of intramembranous particles shortly after infection. This corresponds with a stage when the live worms are non-immunogenic. Collectively this research led to the currently accepted model of immune avoidance by which *Schistosoma* avoids the immune system by acquiring host antigens and integrating them into its own tegument. SEM revealed that spines coving the middle of the parasite disappeared after the parasites had transited into the lung.

This observation lead to the speculation that the spines are functionally significant in relation to the locomotion of larvae through the blood vessels, in which larvae are proposed to move in an inchworm-like fashion (Crabtree and Wilson, 1980).

2.5.2 Schistosome Immunopathology

The thorough characterisation of the worm lifecycle and migration during most of the 20th century has now been superseded by greater focus on the development of egg-induced immunopathology. In *S. mansoni* infection, eggs which are distributed ectopically (that is, in any organ apart from, the intestine) induce a host inflammatory response which leads to the chronic pathology in both humans and mice. The schistosome egg is a metabolically active entity which, when embedded within the host tissue, elicits a strong type 2 immune response by secreting an antigenic mixture which includes toxins (Vella *et al.*, 1992). The egg becomes a focus of granulomatous inflammation, a highly organised infiltrate consisting of a variety of cell types, the formation of which is mainly regulated by CD4+ T Cells (Mathew and Boros, 1986). The Th2 granuloma is additionally characterised by inclusion of alternatively activated (M2) macrophages, basophils and eosinophils (Pearce and MacDonald, 2002). The maintenance of the granuloma is of critical importance to both the parasite and the host, as the parasite requires the granuloma to aid migration across to the gut lumen (Secor *et al.*, 1997). Without the induction of the granuloma, the host dies from the toxicity of the eggs (Brunet *et al.*, 1997). As the egg granuloma matures, the strong type-2 polarity of the inflammatory environment promotes fibrosis through the production of arginase. Additionally, angiogenesis and vascular remodelling are both stimulated by the presence of the granuloma (Andrade and Santana, 2010).

So far, murine insights into the nature of egg granuloma of *S. mansoni* have been somewhat transferrable to humans, insofar as humans suffering from chronic schistosomiasis exhibit elevated type 2 cytokine responses (Williams *et al.*, 1994; Araújo *et al.*, 1996). However, murine and human infections differ significantly in terms of the downstream pathological consequences of granulomatous inflammation and fibrosis (Fallon, 2000), especially in the liver. In humans, only 5-10% of patients develop severe chronic hepatosplenic schistosomiasis (Warren, 1978). In human hepatospenic schistosomiasis, pre-sinusoidal deposition of eggs results in a characteristic perivascular fibrosis called Symmer's pipestem fibrosis, which is associated with

portal hypertension. Portal hypertension is itself a risk factor in the formation of many downstream pathologies including ascites (Michielsen, 1996), and potentially fatal oesophageal varices (Chofle *et al.*, 2014). In addition, increased portal hypertension can lead to portocaval shunting, in which eggs may be swept back through the right ventricle into the pulmonary circulation (Andrade and Sadigursky, 1982). The deposition of eggs in the pulmonary circulation, and the associated granulomatous inflammation may lead to the further development of pulmonary arterial hypertension (PAH), at which point patients are at an increased risk of fatal right ventricular failure. Overall, this sequence of events is very different to what occurs in the mouse. Indeed, whilst most human schistosomiasis sufferers live with the disease for many years, mice infected with a normal experimental dose of cercariae (>30) exhibit 100% fatality by the 16th week of infection. Moreover, hepatic fibrosis in the humans is largely focussed around major blood vessels (perivascular fibrosis), whereas in mice fibrosis is distributed more diffusely throughout the parenchyma. Whilst mice do exhibit some degree of reversible perivascular fibrosis over a range of infection doses (Andrade, 1987; Andrade and Cheever, 1993), it has been debated whether these truly reflect the reality of human pipestem fibrosis which is irreversible and develops over many years. Ultimately, it seems likely that extensive fibrosis in the liver and remodelling of vasculature would lead to portal hypertension and consequently some risk of internal bleeding. However, the events leading towards death in *S. mansoni*-infected mice remain poorly characterised.

2.5.3 Unanswered questions in the pathogenesis of schistosomiasis

Something of a mystery is also the role of angiogenesis which is correlated both with granuloma formation and granuloma regression post-chemotherapy (Andrade *et al.*, 2006; Andrade and Santana, 2010). In mice, Vascular Endothelial Growth Factor (VEGF) has a key role in the formation of granulomas, with decreased granuloma dry weight evident upon its neutralisation with anti-VEGF antibody (Appleton *et al.*, 1996). However, in chronic infection in mice, vascular occlusion of sinusoids by eggs also occurs in parallel to periportal fibrosis (Silva *et al.*, 2006). The relative roles of angiogenesis, occlusion and remodelling of the liver sinusoids in the production of downstream pathology has remained largely uninvestigated quantitatively, perhaps due to a lack of tools to investigate such phenomena at the scale of the smallest vessels. Such work is certainly needed, in light of work suggesting pipestem fibrosis is probably not the direct cause of portal hypertension, which may instead be attributable to lesions

surrounding the smaller hepatic vessels (Andrade and Cheever, 1971; Warren, 1972; De Cock, 1986). Factors such as vessel tortuosity are known to correlate with systemic hypertension (Cheung *et al.*, 2011), and 3D imaging and quantification tools represent an opportunity to investigate such parameters in detail. Overall, there is still a lack of a unifying hypothesis which links together the response to egg antigen, pulmonary hypertension and pulmonary vasculopathy (Graham *et al.*, 2010). Currently, we know about the immunomodulation of the granuloma, and that there is an upstream effect of gross vascular remodelling which is characteristic of serious disease. However, clarification is needed on the mechanisms by which egg granulomas drive vascular remodelling. It may be that understanding these issues may lead to increase knowledge of the etiology of disease and potential for therapy. However, new tools are required which will allow concurrent characterisation of vascular topology at the micro and macro scale, whilst allowing for characterisation of the state of granulomatous information within the liver.

Another area of investigation in the pathogenesis of schistosomiasis is the role of periportal inflammation on the function of the hepatic lymphatic system. The presence of egg granulomas has been confirmed within the spaces of Disse in the liver (Grimaud and Borojevic, 1977). The spaces of Disse contain blood plasma and allow the transfer of proteins and plasma components between the hepatocytes and the sinusoids. Lymphatic circulation has an important role in the regulation of blood pressure, and therefore lymphatic blockage by eggs may be hypothesised to have a role in portal hypertension. Additionally it is already established that lymphatic dysfunction can be responsible for the formation of ascites (Chung and Iwakiri, 2013), a characteristic pathology of hepatosplenic schistosomiasis. Lymphangiogenesis (the proliferation and branching of new lymphatic vessels) remains an unexplored but potentially fruitful area of investigation in the context of chronic schistosomiasis, given its derivation from, and close functional partnership with a well-characterised vascular network (Adams and Alitalo, 2007). Indeed, a more involved role for lymphatics in *S. mansoni* pathology than has previously been appreciated has already been suggested by the anti-lymphangiogenic effects of praziquantel, an effective treatment for schistosomiasis (Abd El-Aal *et al.*, 2017).

Whilst development of fatal pathology associated with hepatic schistosomiasis is of greatest concern to clinicians, human schistosomiasis patients can develop a range of other pathologies associated with the egg granuloma (for a more comprehensive overview, see Barsoum *et al.*,

2013). Intestinal schistosomiasis accounts for a significant amount of the disease morbidity in endemic regions (Booth *et al.*, 2007). In these cases, *S. mansoni* eggs which are traversing the intestinal wall become trapped during transit. Often the trapped eggs will become calcified, and therefore the situation can be diagnosed using Computed Tomography or ultrasonography (Sah *et al.*, 2015; Rodrigues *et al.*, 2016). It is speculated that the calcified eggs are necrotic centres, and the healing-associated fibrosis which occurs around them is responsible for chronic morbidity, which includes colitis-like symptoms including inflammation and ulceration, alongside colonic polyposis, all of which are associated with diarrhoea. Calcification of infectious agents within tissue is already established as a cause of pathology in other infections. For instance, larval tapeworms encysted in host muscle or brain may die and form calcified lesions (Nash *et al.*, 2004), and the granulomas caused by the bacteria that cause tuberculosis can become calcified over time (Keisuke Uchida, 2013). However, the regulation of this type of necrotic calcification of tissue resident infectious agents is poorly understood. Additionally, the presence of eggs is correlated with development of colorectal tumours in both *S. mansoni* (H Salim *et al.*, 2010; Herman *et al.*, 2017) and *S. japonicum* (Matsuda *et al.*, 1999). Intestinal schistosomiasis is less well understood than hepatic schistosomiasis, in part due to the fact that the mechanisms of successful trans-enteric migration and expulsion are not fully understood (Schwartz and Fallon, 2018; Costain *et al.*, 2018). However, in mice, it is clear that the intestinal granuloma differs in composition compared to the hepatic granuloma, and notably contains a higher proportion of alternatively activated macrophages, and less eosinophils, B-cells and T-cells (Weinstock and Boros, 1983). Furthermore, in *S. mansoni*, calcification off eggs within the granuloma seems to uniquely occur in the intestine, and has not to our knowledge been recorded in the liver.

Overall in schistosome research there is a persisting requirement to relate the various contributions of the egg granuloma to the vascular morphology of the liver in a more quantitative manner than has previously been attempted. Currently this has not been thoroughly investigated, as no quantitative tools exist, and the corrosion casting of vasculature which has been used previously does not put the vascular changes in the context of the surrounding vascular tissue, nor characterise vascular changes on the smallest scale such as angiogenesis. MicroCT workflows involving segmentation to digitally label vasculature within an intact sample represent an excellent opportunity to investigate this question. Additionally, gut pathology, which

is difficult to characterise because of the random distribution of eggs through the small intestine, may be made easier by guiding histological techniques with a microCT map of the sample.

2.6 Microscopy in assessing efficacy of anthelminthic drugs

The ability of light and electron microscopy to resolve surface and internal structures of interest facilitates not just investigation of their function, but also assessment of their integrity. In the context of both *Trichuris* and *Schistosoma*, such assessment has supplemented a range of existing methods of measuring the efficacy of potential new anthelmintic agents. *In vivo* efficacy of drugs against helminth targets can be assessed by observing changes in the number of eggs passed in the faeces (Keiser *et al.*, 2013; Speich *et al.*, 2015), and more recently ultrasound imaging has been proposed as a new approach to visualise the burden of parasites within the body as non-invasively as possible (Gorgas *et al.*, 2017). Such approaches build upon the previously existing approach of measuring parasite mass post-mortem (Hemphill *et al.*, 2014).

In vivo tests of drug efficacy may be followed by *ex vivo* trials, which are useful in demonstrating the direct action of a compound on a target helminth of interest. Recent work has generated high throughput approaches to assess worm motility in response to anthelminthics using video cameras (Partridge *et al.*, 2017, 2018). However, historically EM has more often been employed for such *ex vivo* testing. Parasites are isolated before immersion in a solution of the candidate anthelminthic, before fixation and further preparation for microscopy. SEM can then allow unusual topology of the parasite cuticle and underlying tegument to be identified. In *Schistosoma* spp. there is an abundance of studies conducted in this manner, which note a variety of effects including bursting and/or erosion of surface structures, as well as protrusion and wrinkling of the tegument. Such SEM observations were first made upon exposure of *S. mansoni* to a combination of Praziquantel and host antibodies (Modha *et al.*, 1990), but also upon exposure to Luteolin (Wangchuk *et al.*, 2016), Miltefosine (Eissa *et al.*, 2011a; b), Mefloquine (Manneck *et al.*, 2011) and Sesquiterpenes (de Oliveira *et al.*, 2017). Likewise, exposure to Luteolin induced cuticular damage including swelling of the bacillary glands in *Trichuris*. Inspecting thin sections by TEM arguably provides a more informative approach in assessing anthelminthic efficacy, due to visualisation of sub-surface ultrastructure. For instance, in a trial of Hinokitiol on the cercarial stage of *Schistosoma mansoni*, Chisty et al. (2004) note tegumental thinning, outward migration of cytoplasmic granules and accumulation of

membranous bodies. *Schistosoma mansoni* extracted from mice treated with artemether similarly demonstrate ectopic vacuoles and a disrupted basement membrane under TEM inspection (Shuhua *et al.*, 2002), and degeneration of the reproductive organs has also been used as a measure of the anthelmintic activity of perhexiline (Guidi *et al.*, 2016). It is perhaps unsurprising that studies couple SEM and TEM observations of worms to combine the distinct structural insights provided by both. For example SEM study of adult *S. mansoni* treated with primaquine show tegumental sloughing and peeling, whilst TEM reveals disruption of tegumental ultrastructure and associated accumulation of vacuoles (Kamel and Bayaumy, 2017).

Electron microscopic assessment of remains a common approach of assessing drug efficacy. However, researchers continue to develop new assays; for example, coloured dyes and light microscopy can be employed to assess parasite surface integrity in terms of its permeability. When a non-parasitic model helminth, *Caenorhabditis elegans*, is incubated in a medium containing (prospectively anthelminthic) cysteine protease and Neutral red dye, diffusion of dye into the parasite is indicative of damaged, permeabilised cuticle, thus confirming anthelminthic activity (Phiri *et al.*, 2017). In future, there may be further room for the development of electron microscopic approaches to testing drug efficacy. It is worth noting that a 3D EM approach could allow visualisation of tegumental and cuticular ultrastructure, with simultaneous assessment of parasite surface topology by the tracking relevant structures through the Z-axis. Registering disruption of surface morphology with underlying ultrastructural disruption may provide more information relating the action of prospective drugs. Additionally, combining 3D EM approaches such as Focussed Ion Beam-SEM and SBF-SEM with microCT imaging of parasites embedded within tissue in a correlative workflow would facilitate putting changes in tegumental integrity in the context of the surrounding host tissue in *in vivo* trials.

2.7 Application of microCT to *Trichuris muris* and *Schistosoma mansoni*

Whilst microCT has so far been sparingly applied to parasitological problems, the potential research domains which could be addressed by this imaging approach has been broadly discussed recently (O'Sullivan *et al.*, 2018) (**Appendix 1**). However, the capabilities of microCT also offer solutions to specific problems in *Trichuris* and *Schistosoma* research.

In *Trichuris muris*, 3D morphological imaging could allow the interior of the epithelial tunnel to be imaged for the very first time, thus testing the assumptions about worm positioning within the niche that have pervaded the literature so far. Additionally, the use of a correlative workflow to direct sectioning for electron microscopy could allow more efficient imaging of enigmatic surface structures such as the cuticular inflations. Similarly in *Schistosoma mansoni*, microCT could allow qualitative and quantitative observations of innately 3D morphology such as the portal vasculature which goes beyond what has currently been achieved in previous studies.

2.8 Reiteration of doctoral aims

Despite the imaging techniques currently available, much remains unknown about the life cycles and pathologies of parasitic helminths, including *T. muris* and *S. mansoni*. MicroCT could provide answers to some of these issues. However in order to do this the efficacy of microCT must be assessed and optimised in the context of these particular soft tissue systems. This may include improvements to sample processing and preparation, along with image analysis and data handling. Therefore, the aims of the entire thesis may be expressed as follows:

To address unanswered questions about the lifecycles and pathologies of Trichuriasis and schistosomiasis by developing and exploiting the 3D soft-tissue imaging capabilities of X-ray micro-computed tomography.

For each chapter of results, there is therefore a pair of more refined aims which first address the biological questions about the parasites' life cycles and/or pathology and secondly address the development and appraisal of soft tissue imaging protocols to satisfy the biological aims. These may be summarised for each chapter as follows.

Chapter 4: To characterise spatial positioning of *T. muris* within the epithelial tunnel, as well as the ultrastructural features of *Trichuris* at the attachment site. A more comprehensive understanding of tunnel morphology and would inform understanding of tunnel formation and maintenance. **Technical aims:** To develop an optimised staining imaging protocol allowing the attachment site of the worm to be visualised, and to develop 3D measurements of tunnel integrity and mucosal inflammation.

Chapter 5: To characterise the morphology, structure and composition of *T. muris* surface structures which interact with the host within the epithelial tunnel, in order to better understand the effector mechanisms by which survival in the host is promoted. **Technical aims:** To develop a correlative imaging approach by which microCT-steered EM allows efficient ultrastructural investigation of the cuticular inflations.

Chapter 6: To characterise liver and intestinal pathology of *Schistosoma mansoni*. An understanding of how inflammation leads to change in liver architecture may inform further understanding of how dangerous pathologies are generated. **Technical aims:** To develop optimised staining to visualise changes in egg-induced granulomatous inflammation and vascular pathology throughout infection. To develop a correlative imaging approach by which microCT-steered histology allows efficient investigation of egg traversal across the intestine wall.

3. Methods

3.1 Experimental Animals

All experiments involving animals were undertaken under the authorities of Home Office personal and project licenses, as per the specifications in the Animals (Scientific Procedures) Act 1986. Severe Combined Immuno-deficient (SCID) mice were bred within the Biological Services Facility (BSF) of the University of Manchester.C57BL/6 and BALB/c mice were purchased from Envigo (Huntingdon, UK). All animals were kept in specific pathogen free conditions at the University of Manchester BSF, on a 12 hour light/dark cycle. All gavage and injection procedures were carried out in the morning between 9:00 and 11:00 to control for circadian effects.

3.2 Infections and treatments of mice

3.2.1 *Trichuris muris* infection

Eggs from the E isolate of *T. muris* were obtained in the following manner: SCID mice were given 200 infective eggs by oral gavage. At 42 days post-infection (PI), mice were culled, and adult worms were extracted from caecum and proximal colon. Isolated worms were incubated for 24 hours in RPMI-1640 medium (Gibco, UK), in a 37^{o}C incubator (with no atmospheric gas control). At 4 hours and 24 hours during incubation, eggs were removed from the media bathing worms, filtered in a 70 micron nylon strainer to remove debris and suspended in milliQ water. *T. muris* for SEM, SBF-SEM and qPCR were generated using by infecting SCID mice with a dose of 200 infective eggs by oral gavage. At day 35 PI the caecum was dissected and the worms were carefully removed using forceps.

Experiments in **chapter 4** required low dose infections of SCID, C57BL/6 and BALB/c mice (Envigo, UK). In these cases, 40 eggs were individually counted into each oral gavage bolus regardless of infectivity.

3.2.2 Corticosterone immunosuppression

Corticosterone has immunosuppressive effects in mice (Schwab, 2004), and was therefore used was in experiments where the goal was to produce an immune-suppressed phenotype (**chapter 4**). Mice were injected subcutaneously at 50mg/kg with a suspension of

corticosterone in PBS (Cambridge Biosciences, UK), or a PBS sham at 7, 9 and 13 days after infection (Caratti *et al.*, 2019).

3.2.3 Schistosoma mansoni infection

For studies of *S. mansoni*, mice were infected with 40 cercariae percutaneously by the tail exposure method, and were weighed regularly. Mice were euthanised 8 weeks or 14 weeks after infection. The liver was carefully dissected and placed in neutral buffered formalin for 48 hours before transferring to 70% ethanol for storage.

3.2.4 BrDU injection

Mice received an intraperitoneal injection (10ml/kg) of BrDU labelling reagent (no. 00-0103, Invitrogen, Camarillo CA) either 12 hours or 40 minutes before culling.

3.3 Preparation of samples for microCT

3.3.1 Caecum and proximal colon infected with *T. muris*

Regions of the caecum and proximal colon were removed after culling of mice. These samples were fixed in Karnovsky's fixative for 24 hours, and stored in 4% PFA in 0.1M HEPES until further processing. Prior to processing, samples were washed in ddH_2O before incubation in 1% aqueous OsO_4 for one hour, before graded dehydration to 100% ethanol. Subsequently, samples were critical point dried and mounted for scanning.

3.3.2 Livers infected with *S. mansoni*

The liver was dissected and fixed in Neutral Buffered Formalin for 48 hours, before storage in 70% ethanol. In cases where the whole liver was imaged, the liver was stained in a 1% solution of ethanoic Iodine (I_2E) for 72 hours, before being mounted in a plastic tube with a reservoir of ethanol to avoid sample shrinkage. When single lobes were imaged, they were first rehydrated in distilled water, stained in 1% aqueous I_2KI and pre-embedded in agar-gelatin to facilitate correct orientation during subsequent embedding and sectioning (Jones and Calabresi, 2007). These pre-embedded samples were mounted within plastic tubes during imaging.

In order to achieve higher resolution imaging of liver architecture, small 2-3 mm fragments of liver were isolated. These samples were not stained, and were instead simply dehydrated

through graded ethanol and dried using Hexamethyldisilazane (HMDS) before mounting for imaging.

3.3.3 Preparation of *S. mansoni* eggs by density gradient

Livers were dissected from *S. mansoni*-infected livers 8 weeks post-infection. The livers were homogenised in saline, in Tissuelyser II (Qiagen, Manchester) at low speed to ensure disintegration of tissue. Tissue debris was removed by pouring the homogenate through a 200 µm nylon mesh filter, to give a suspension of *S. mansoni* eggs in saline.

10^6 *S. mansoni* eggs were purified from infected mouse liver 8 weeks post-infection and suspended in 1.7% w/v aqueous NaCl. The egg suspension was carefully layered onto a 20% percoll solution in a falcon tube, and centrifuged at 500G for 6 mins in order to remove tissue debris. The pellet of eggs was resuspended in saline, and carefully layers onto a 40% percoll solution and centrifuged as before. Less dense, immature eggs were retained within the saline layer, and were fixed in 4% aqueous Paraformaldehyde (PFA). The pellet of eggs was resuspended in saline, and carefully layered onto a 50% percoll solution and centrifuged as before. The resulting pellet of higher density, mature eggs were resuspended in 4% $PFA_{(aq)}$ to fix.

3.4 Micro-computed tomography

A wide range of micro-computed tomography was employed throughout the thesis, requiring a variety of different parameters. The pertinent information for all experiments is outlined in **Table 3.1.** For HMDS-dried liver samples in chapter 6, phase contrast by propagation-based imaging was achieved by moving both the source and detector a minimum of 200 mm away from the sample before imaging. Projections from all scans were reconstructed using Filtered Backprojection (FBP).

3.5 Analysis of microCT data

3.5.1 Segmentation

All microCT data were visualised and analysed within AVIZO versions 9.3 – 2019.1 and Matlab R2016a (under research license). The requirements of analytic workflows varied based on sample type and desired output. For instance, in liver samples (**chapter 6**), segmentation of

vasculature and granulomata were key, and thus a sequence of thresholding steps were undertaken in order to pick out each piece of morphology (**Table 2.2**). For liver vasculature in particular, a more sophisticated approach was taken (**Fig. 2.2**). In the case of caecum samples containing *T. muris* (**chapter 4**), using a watershed approach gave a satisfactory initial rough segmentation which separated the worm, mucosa and submucosa (**Table 2.3**). Due to local areas of low contrast, in almost all cases some manual alterations of the segmentation were then required to provide the final segmentation.

3.5.2 Epithelial coverage measurements

For measurements of epithelial coverage (**chapter 4**), the total tunnelled length of the stichosome, including epithelial breaks was estimated by use of AVIZO's "centerline tree" algorithm on embedded portions of stichosome. Centerline tree extracted a non-branching spatial graph from the segmented worm which ran directly through the centre of the worm along the anterior posterior-axis. The proportion of the stichosome which was exposed by breaks in the epithelium overlaying the tunnel was calculated by separating the spatial graph of the embedded stichosome into either "exposed" or "unexposed" lengths which were subsequently measured. The cumulative length of the exposed stichosome was calculated and subtracted from the total tunnelled length to obtain the proportion of the tunnelled region of the stichosome which was exposed by epithelial breaks.

3.5.3 Mucosal thickness measurements

For measurements of mucosal thickness (**chapter 4**), datasets taken using the Zeiss Versa 520 were cropped to a volume of 1500 x 1500 x 1500 µm cube, which included a length of mucosa devoid of worms. The mucosa was labelled using watershed segmentation. The segmented mucosa was subjected to three different approaches to thickness measurement. In the first method, the surface area to volume ratio of the mucosa was calculated. In the second method, distance maps of the mucosa were generated and analysed for thickness in Matlab, using a script used with permission from Dr. Shelley Rawson, University of Manchester (Unpublished script, see **appendix 3**). The script was originally developed to measure foam thickness in titanium aerogel, but was adapted to measuring mucosal thickness by introducing a threshold for thickness measurements and to produce an image of the sampled pixels. In the third method

of thickness measurement, distance maps of the mucosae were generated and thickness was measured by utilising the “influence zones” module of AVIZO (Malachevsky *et al.*, 2019).

Instrument	Manufacture	Objective	Target	Pixel Size (µm)	Voltage (kV)	Sample description	Results in section
Versa 520	Carl Zeiss AG	4X	Tungsten	1.60 - 5.00	50	caecum and proximal colon samples containing *T. muris,* HMDS-dried liver containing *S. mansoni*	4.2.1 - 4.2.5, 6.2.2
Versa 520	Carl Zeiss AG	0.39X	Tungsten	20.00 - 28.44	60	Whole organ (liver, iodine-stained) containing *S. mansoni*	6.2.1
Versa 520	Carl Zeiss AG	10X	Tungsten	1.24	60	Correlative microCT-EM samples	5.2.2
Versa 520	Carl Zeiss AG	20X	Tungsten	0.80	20	caecum and proximal colon samples containing *T. muris*	4.2.1
XTH	Nikon	N/A	Molybdenum	15.00	100	pre-embedded liver lobe containing *S. mansoni*	6.2.1

Table 3.1: Micro-computed tomography parameters for scans in the results chapters. Different machines and objective lenses were used to achieve imaging at a range of resolutions. Additionally, different voltages were required to optimise contrast and signal-to-noise ratio.

Analysis step	Process	Output
1	Filter - non-local means	
2	Thresholding	
3	Fill holes	Segmentation of parenchyma
4	Masking of data with segmented parenchyma	
5	Adaptive thresholding	Segmentation of vasculature
6	Adaptive thresholding	Segmentation of granulomata

Table 3.2: Data analysis workflow for segmentation and measurement of liver pathology

Analysis step	Process	Output
1	crop region of interest	
2	generate gardient image	
3	watershed segmentation	
4	Manual touch-up	Segmented worm and mucosa
5	Generate euclidian distance map of mucosa	
6	Average mucosal thickness calculated in matlab	Average thickness measurement

Table 3.3: Data analysis workflow for segmentation and morphometry of *T. muris* infection of the caecum.

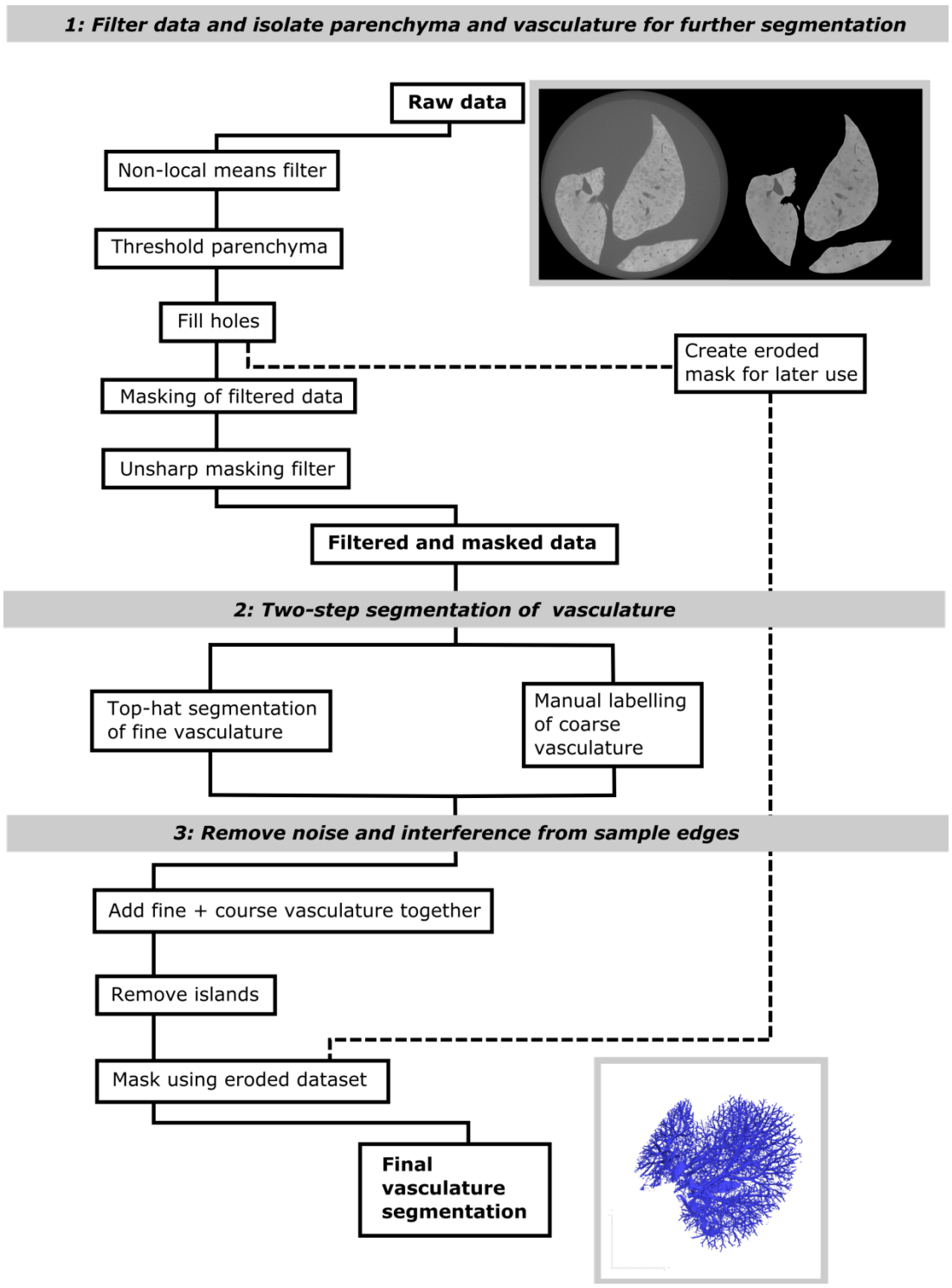

Figure 3.1: Segmentation workflow for whole organ vasculature (liver). 1) Data is filtered and masked in order to increase ease of subsequent thresholding operations. 2) Vasculature is segmented in two stages: firstly, coarse vasculature can be quickly delineated using manual region growing based on greyscale values. Secondly the find vessels can be segmented using a top-hat algorithm which is sensitive to their small size. 3) The coarse and fine vasculature are combined and manually tidied.

3.6 Electron microscopy

3.6.1 Fixation, staining and embedding of samples for SBF-SEM

Larval and adult worms were manually removed from the epithelium using forceps, and added to Karnovsky's fixative solution containing 2.5% Glutaraldehyde and 4% Paraformaldehyde in 0.1M HEPES buffered to pH 7.4. After fixation for 24 hours, the worms were then transferred to a storage solution consisting of 0.5% PFA in 0.1M HEPES pH 7.4 until subsequent use.

T. muris specimens were prepared using the protocol of Deerinck et al. (2010). Samples were washed in ddH_2O before incubation in 1% OsO_4 and 0.1M Potassium ferrocyanide in 0.1M HEPES for 1 hr. Subsequently samples were washed again before 30 minute incubation in 1% Thiocarbohydrazide filtered through a 20 µm pore filter. After washing in ddH_2O, samples were incubated in 1% aqueous OsO_4, before again being washed and transferred to a 1% aqueous solution of Uranyl Acetate stored overnight at 4°C. The samples were washed in ddH_2O and then incubated in a solution of Walton's lead aspartate (Walton, 1979) for 1 hr at 60°C. After dehydration through a graded ethanol series (30%, 50%, 70%, 90%, 100%, 100%, 15 mins each), the samples were incubated in two changes of acetone and then incubated in 25% (Overnight), 50% (Overday), 75% (Overnight), and 100% (6 hr) TAAB 812 Hard resin. Infiltrated samples were then covered in fresh resin in molds and cured for 24 hours at 60°C.

3.6.2 Correlative SBF-SEM and TEM

Backscatter and transmission electron microscopy of relevant experimental areas was carried out in a guided manner by using a correlative MicroCT-EM imaging workflow, as explained in detail by Starborg et al. (Starborg *et al.*, 2019) (**Appendix 2**). Firstly the epoxy-embedded sample was imaged on the Zeiss Versa 520 X-ray microscope. The virtual slices of the MicroCT data were visualised and points of interest identified. Using XRM data as a guide, the resin block was coarsely cut down to size using a hacksaw, and after mounting on a 3View pin the block-face was cut to an appropriate size with a razor blade. Afterwards an ultramicrotome was used to cut to the appropriate position within the tissue block such that the desired region was exposed for the imaging frame.

Serial images of the blockface were recorded at 3kV, a spot size of 2.5 and a pressure of Torr. Pixel size was 15 – 20 nm and slice thickness was 100 nm. Up to 1000 slices were collected for each image set.

TEM was carried out on resin blocks previously imaged by SBF-SEM. Using X-ray data as a guide, the block-face was trimmed to an appropriate depth and polished with an ultramicrotome. Thin slices were cut and without further staining were mounted on grids for TEM imaging. Slices were inspected under a Technai 12 Twin Biotwin transmission electron microscope (Thermo Fisher Scientific, Massachusetts), with a 1 second exposure time at 1 μA current and 100 kV. Image magnification for TEM ranged from 8000X to 11000X magnification.

3.6.3 Scanning Electron Microscopy

Worms were prepared for SEM using an OTO protocol designed to impart the maximum structural support to worms throughout the drying process and reduce shrinkage artefacts (Willingham and Rutherford, 1984). The worms were washed in ddH_2O before incubation in 1% OsO_4 in 0.1M HEPES. Subsequently samples were washed again before a 30 minute incubation in 1% thiocarbohydrazide filtered through a 20 μm pore filter. After washing in ddH_2O, samples were incubated in 1% aqueous OsO_4. At this point samples were dehydrated through a graded ethanol series (30%, 50%, 70%, 90%, 100%, 100%, 15 mins each), incubated in 1:1 ethanol : HMDS mixture and then in pure HMDS for 30 mins each. Immediately afterwards, the samples were transferred to fresh HMDS and left to dry within a dessicator. HMDS drying was used due to its comparative ease and results when compared to critical point drying. After drying, the worms were mounted on round SEM stubs and coated with gold-palladium before SEM imaging.

SEM was carried out using an FEI Quanta (Thermo Fisher Scientific, Massachusetts) scanning electron microscope, at 20 kV with a spot size of 3.5 μm and a chamber pressure of $3.7e^{-6}$ Torr.

3.6.4 Guided Energy Dispersive X-ray Spectroscopy (EDX)

One of the liver samples which had been dried using HMDS and imaged using microCT was selected on the basis of high-density egg being visible in the X-ray data (**chapter 6**). The dried tissue was cut to an appropriate depth to reach a high-density egg using an ultramicrotome. The

sample was then glued to an SEM stub using conductive silver glue. EDX was performed on an FEI Quanta 250 at 10KeV.

3.7 Light microscopy

3.7.1 Fixation, embedding and sectioning of samples

Samples for histology were fixed in either Neutral Buffered Formalin (NBF) (for haematoxylin and eosin) or methacarn (for immunohistochemistry of BrDU treated donors) for 24 hours. Tissues which were fixed in NBF were transferred to 70% ethanol for storage, whereas tissues fixed in methacarn were transferred to 100% methanol and 100% ethanol for one hour each before storage in 70% ethanol. Tissues were processed for histology by transferring up an increasing ethanol gradient, followed by clearing in xylene and further infiltration with paraffin wax. Sections of 5 μm thickness were cut from blocks for all subsequent histological procedures.

3.7.2 Immunohistochemistry

BrDU immunohistochemistry (IHC) was performed by the ABC method using the mouse on mouse kit (vector; Peterborough UK). Antigen retrieval was via 4M HCl method with primary antibody incubation performed at 4^{o}C for 16 hours (1:50). Sections were counterstained with Gills haematoxylin and mounted using DPX.

3.7.3 Morphometry of proliferating cells (pulse chase)

Tissues stained by IHC were analysed in the manner explained by Cliffe et al. (Cliffe *et al.*, 2005). The crypts analyses were divided into discrete regions of 10 cells starting from the base of the crypt. The net change in BrDU-positively labelled cells in each region was quantified between the mice that had been injected 40 minutes and 12 hours before culling. Net gain of cells indicates higher levels of turnover, due to the cells moving up the crypts.

3.7.4 Histochemistry

Paraffin slices of liver and intestine tissue were investigated using Harris' haematoxylin and eosin (H&E), and picrosirius red staining. H&E staining was used in **chapter 6** in order to visualise granulomatous inflammation in the liver, as well as the traversal of the eggs across the

small intestine wall. Picrosirius red staining was used to visualise fibrosis in the liver in **chapter 6**, as well as determine the composition of cuticular inflations in **chapter 5**.

3.8 Polymerase chain reaction

3.8.1 Primer design

Several candidate proteins which may be responsible for formation of cuticular inflations were identified (**chapter 5**), based on sequence similarity to proteins known to be responsible for so-called “blistered cuticle” phenotypes in *Caenorhabditis elegans* (Peters *et al.*, 1991; Stepek *et al.*, 2010). Using Wormbase.org, *Trichuris muris* orthologs with high sequence similarity to *bli-4*, *bli-5* and *dpy-31* proteins were identified (Table 2.3). Exon-spanning primers for these *T. muris* genes were then generated.

T. muris gene	C. elegans ortholog	Putative activity	T. muris Primer	Amplicon length
TMUE_2000009363	*bli-4*	serine-type endopeptidase	F-CGCAGTGTGTAGGACCAAGT	75
			R-TATTCGCCTTCTGATCGGGC	
TMUE_1000003689	*bli-5*	serine-type endopeptidase	F-GAGCCTTTGTGTGCAACCAG	173
			R-AGATTTGCCGCAGAAGGACA	
TMUE_2000008408	*dpy-31*	metalloendopeptidase	F-GTTCAGTACCGCCAACAGGA	245
			R-GACTGCTTGCATTCCTTCGC	

Table 3.4: Forward and reverse primer design for blister-gene homologs in *Trichuris muris*.

3.8.2 Real Time quantitative Polymerase Chain Reaction

Upon manual removal of the worms from the epithelial tunnel at days 21, 23, 25, 28 and 35 post-infection, the worms were stored in RNAlater as per the manufacturer instructions and archived at -80^{o}C. The Qiagen RNeasy Micro Kit was used for RNA extraction, and cDNA was generated from samples of normalised concentration using the TETRO cDNA synthesis kit using random primers. RT-PCR was carried out in triplicate with a reaction volume of 10 µl, using the KAPA SYBR-Green kit optimised for the Lightcycler 480 without ROX reference dye (Roche, Switzerland).

3.9 Statistical Analyses

All statistical tests were performed on Graphpad PRISM 8. Data were tested for normality either by Kolmogorov-Smirnov test. Data were compared either by one way ANOVA, two-sample T-test or linear regression.

Blank page

4: 3D morphology and morphometry of the *Trichuris muris* attachment site using X-ray micro-computed tomography

4.1 Introduction:

Trichuriasis remains a significant public health burden in the developing world (see section 2.4.1) (Pullan *et al.*, 2014). However, the efficacy of existing anthelminthics against *Trichuris* is suboptimal (Keiser and Utzinger, 2008; Speich *et al.*, 2015). Furthermore, there is growing concern that Mass Drug Administration programs used to control trichuriasis in the developing world will be hindered by resistance to anthelminthic drugs (Vercruysse *et al.*, 2011). Much effort has gone into understanding the immune mechanisms underlying resistance and susceptibility to the mouse whipworm *Trichuris muris* as a model for human Trichuriasis (Klementowicz *et al.*, 2012; Hurst and Else, 2013). However, there are still many gaps in our understanding of the relationship between *T. muris* and its host. *Trichuris* uniquely forms a tunnel within the caecum epithelial cells of the host in which it remains at least partly within for its entire life. However, the mechanisms of tunnel maintenance and formation remain poorly understood (Hurst and Else, 2013). A greater understanding of the host-parasite interactions occurring within the tunnel and of how *Trichuris* remodels the surrounding tissue to form the tunnel may inform new targets for drugs. The ability to visualise the niche of *Trichuris* in chronic infection is a basic requirement in achieving this goal. So far, researchers have only been able to visualise the epithelial tunnel of *T. muris* from two positions; by looking down on the surface of the epithelial tunnel from the lumen using SEM (Tilney *et al.*, 2005), and using 2D snapshots of the tunnel interior using sectioning approaches (Sheffield, 1963; Lee and Wright, 1978). Therefore, assumptions about the morphology of the attachment site have continued to be made. These assumptions include the concept that worms only tunnel through the most apical epithelial cells of crypts, which are in direct contact with the luminal contents.

An understanding of the entire niche morphology may provide clues about how surface structures interact with the host. For example, previous researchers have noted the presence of breaks in the epithelium covering the work in scanning electron micrographs (Tilney *et al.*, 2005). The extent to which such breaks in the tunnel reflect the integrity of the niche remains uninvestigated. Furthermore, no quantitative tools for assessing tunnel integrity currently exist, despite the continuing search for novel drugs (Partridge *et al.*, 2017) and vaccines (Shears *et*

al., 2018a; b) for *Trichuris*. Additionally, measurements of inflammatory pathology such as crypt length are generally sampled from a small number of histological slices taken systematically through the tissue. When assessing the nature of chronic infection, it is well-established that *Trichuris* releases immunomodulatory compounds to alter the host immune response (Dige *et al.*, 2017; Bancroft *et al.*, 2019). Yet no quantitative tools exist which specifically allow morphometric measurements to be made at specific locations of interest, such as the epithelial tunnel. The use of micro-computed tomography (microCT), which produces 3D images, could provide a unique solution to these issues, allowing the orientation of the worm within the niche to be visualised *in toto* but also allowing location-specific 3D quantification workflows not possible using conventionally employed microscopic approaches.

In this chapter a *Trichuris*-specific rationale has been presented for developing 1) an effective sample-preparation protocol for visualising intestinal morphology using microCT and 2) morphometric tools for quantifying pathology. We have investigated the morphology of the *T. muris* attachment site in two models of chronic infection: in the C57BL/6 mouse, and the SCID mouse, which lacks the adaptive immune response (Else and Grencis, 1996). Whilst the methodological requirements are determined by current advances in the study of this particular nematode, such tools could also be used more widely to assist in pathology of the variety of other diseases in which evaluation of intestinal inflammation is key in research (Erben *et al.*, 2014).

The aims of this investigation were:

1) To characterise the morphology of the attachment site throughout development of *T. muris* in in C57BL/6 mice

2) To identify key elements of worm morphology such as the stichosome, bacillary band, oesophagus and cuticular inflations and relate the positioning of these to the morphology of the mucosa such as the crypts of Lieberkühn, both in C57BL/6 and SCID mice

3) To develop 3D quantitative measurements of niche integrity and the inflammatory pathology caused by *T. muris*.

4) To investigate mechanisms underlying insights from **2)** in more detail by exploiting models in which the immune response to the parasite is modified.

Micro-computed tomography using osmium tetroxide-staining was used to visualise the attachments site and surrounding caecum morphology in C57BL/6 mice. In the C57BL/6 mice, skeletonisation of worms was used to quantify the integrity of the epithelial tunnel. Additionally, positioning of the worm within the niche was also inspected in SCID mice. Methods for quantifying mucosal thickness was developed and used to compare between SCID mice and C57BL/6 mice. In both C57BL/6 and SCID mice, unusual positioning of the stichosome was observed, which we designated as “head-down” behaviour. In order to test whether head-down behaviour in C57BL/6 mice was due to turnover of epithelial cells, mice were immunosuppressed using corticosterone.

4.2 Results

Experimental protocols, including details of sample acquisition, processing, imaging and analysis are outlines in the methods, **chapter 3**.

4.2.1 Osmium staining of adult worms and surrounding host morphology in C57BL/6 mice

Firstly, we attempted to view the tunnel development and morphology in chronic infection in the caecum. Male C57BL/6 mice were infected orally with a low dose of *T. muris* eggs. At 7, 14, 21 and 35 days post-infection (PI) with *T. muris*, 3-5 mm tubular fragments of caecum were dissected and processed for microCT imaging (**Fig. 4.1**). In caecum fragments taken 35 days PI, we identified an optimal staining protocol utilising Osmium Tetroxide (OsO_4), which allowed superior contrast between the worm and surrounding tissue when compared to worms immersed in aqueous potassium triiodide and PTA (**Fig. 4.2 A-C**). Superior contrast using OsO_4 may have been due to the highly membranous composition of the stichocytes (**Suppl. Fig. 4.1**) which exhibited a high affinity for staining.

In caeca from C57BL/6 mice taken 35 days post-infection, microCT scanning at low resolution (pixel size 3.62 μm) revealed the attachment sites of multiple worms. When magnification was increased in order to visualise regions of interest in more detail (pixel sizes 1.562 μm and 0.596 μm), the resolution of features in 2D slices was comparable to that obtainable by light microscopic histology, and multiple aspects of worm and host morphology were apparent (**Fig. 4.3**). Thus, the crypts of the host mucosa were visible as layers of reduced X-ray attenuation.

The bacillary band, stichocytes and oesophagus of the worm and their orientations were all distinct, and exhibited higher X-ray attenuation than the surrounding host tissue (**Fig. 4.3 A, B**). Cuticular inflations were not visible in the adult worms, either in slices or volume rendering of the worm and attachment site. Larval worms at days 7 and 14 post-infection were not observed in tissue samples taken from these time points. However, one worm was observed in the tissue sample taken 21 days post-infection (**Fig. 4.3 C, D**). In contrast to the situation in the D35 adult worms, the D21 L3 larvae were poorly contrasted against the host mucosa, and instead exhibited poorer attenuation of X-rays than the surrounding tissue.

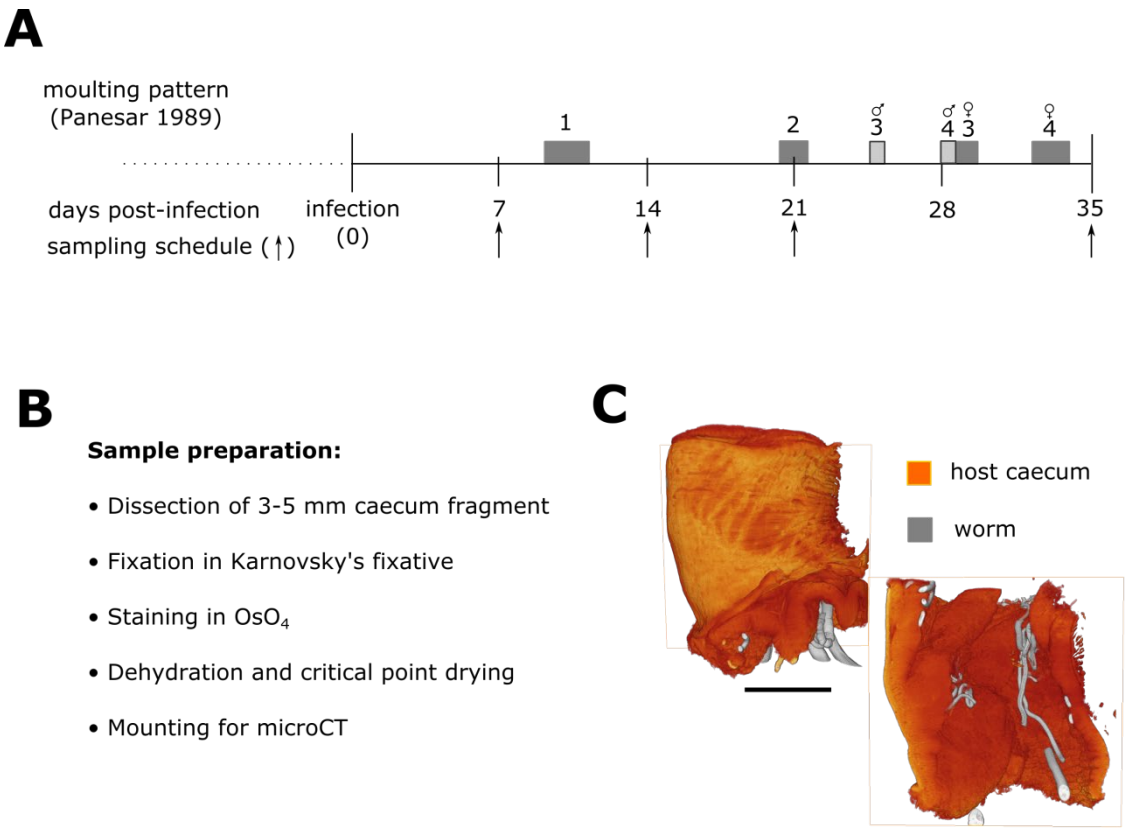

Figure 4.1: Imaging strategy for imaging caeca from C57BL/6 mice infected with *T. muris*. **A**) Timeline showing the sampling schedule at days 7, 14, 21 and 35 post-infection, compared with the occurrence of moulting (upper half of timeline) according to Panesar et al (1989). The final two moults in males occur earlier than the moults in females. **B**) The sample preparation is detailed briefly step-by-step. **C**) The final product is a dataset which shows the organisation of both the host mucosa and the worms within. Scale bar = 1 mm.

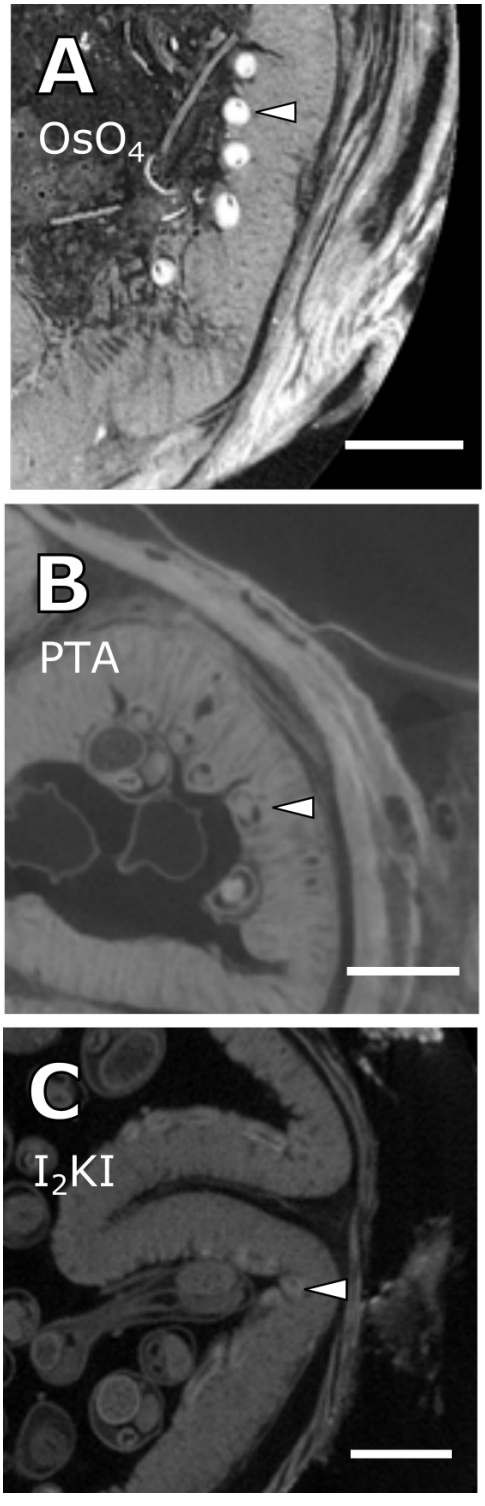

Figure 4.2: Osmium tetroxide (OsO_4) optimally stains the worm within the intra-epithelial niche. Worms were prepared by staining with OsO_4, aqueous Phosphotungstic acid (PTA) or aqueous lugol's iodine (I_2KI). PTA and I_2KI were mounted in liquid for scanning a la Metscher et al. (2009), whereas OsO_4-treated samples were critical point dried and mounted dry. Slices were viewed, in which the minimum greyscale was matched with air. **A**) Superior contrast between worm (white arrowhead) and mucosa was achieved using staining with OsO_4. **B**) PTA staining imparted next to no contrast between worm and mucosa. **C**) I_2KI imparted very little contrast between the worm and mucosa. Scale bars = 300 µm.

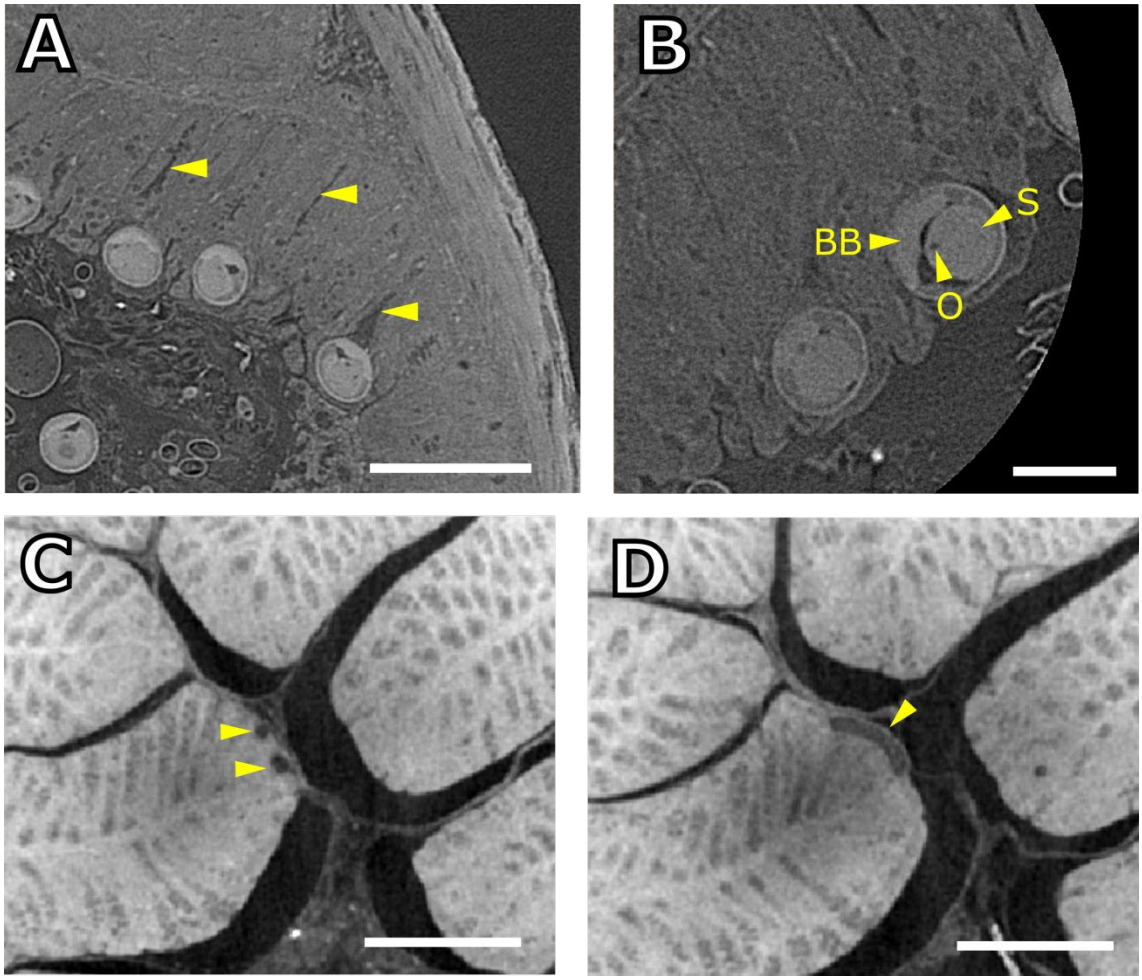

Figure 4.3: Worm and host gut morphology in 2D slices. Fragments of caecum were dissected from male C57BL/6 mice at day 21 and 35 post-infection with <40 *T. muris* eggs. The caecum was OsO_4-stained and critical point dried before being imaged with microCT. **A**) Slice of day 35 PI caecum showing locations of Crypts of Lieberkühn (yellow arrowheads). **B**) High resolution slice of day 35 PI caecum showing the oesophagus (**O**), bacillary band (**BB**) and stichocytes (**S**) of an adult worm. **C**) Slice of a day 21 PI caecum fragment showing two parts of a single L3 worm (yellow arrows), negatively contrasted against the host mucosa. **D**) Slice showing positioning of the single L3 worm (yellow arrow) at the surface of the host mucosa. Scale bars A = 300 µm, B = 100 µm, C and D = 500 µm.

4.2.2 Quantification of the integrity of the epithelial tunnel

In the caecum images from the C57BL/6 mouse at day 35 P.I., worms were assigned a unique ID and subsequently the proportions of the stichosome which were covered and uncovered by the epithelial layer were measured. Only worms for which the whole embedded length of the stichosome was captured within the 3D imaging frame were suitable for subsequent analysis (7out of 10 visible worms, data from a single host). Worms were segmented, and skeletonisation facilitated length measurements of the tortuous stichosome (**Fig. 4.4**). The skeletonised worm was manually fragmented based into “covered” and “uncovered” regions. Therefore, the length of worm covered by the epithelial tunnel could be quantified, and was expressed as a percentage as “epithelial coverage”. Epithelial coverage was measured in seven worms in the caecum of the male C57BL6 mouse (pixel size = 3.619 μm), and was highly variable; the proportion of the exposed stichosome ranged from 0% in worms which were completely covered by the epithelium, to a maximum of 17.44% in one of the worms investigated (**Fig. 4.4**).

The cumulative tunnelled length of the stichosome calculated for seven worms, and was highly variable, ranging from 2959 μm to 8953 μm. Lengths were rounded to the nearest micron sue too the unknown level of error associated with measurements. Furthermore, the number of breaks varied between worms (range: 0 to 5). Importantly, the tunnelled length of the stichosome was not always representative of the total length of the stichosome. Indeed, in all worms, the posterior-most region of the stichosome was positioned outside of the epithelial tunnel within the intestinal lumen.

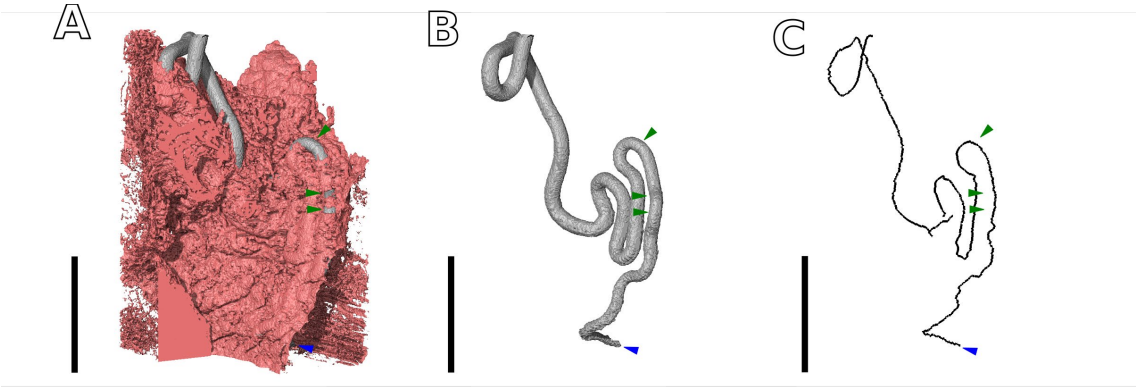

D

Worm ID	total tunneled length including epithelial breaks (µm)	cumulative length of exposed stichosome (µm)	Number of breaks in epithelium	cumulative length of unexposed stichosome (µm)	proportion of stichosome exposed (%)
4-roi2	3141	183	2	2959	5.82
6-roi3	7757	0	0	7757	0.00
9-roi5	3995	697	4	3298	17.44
12-roi6	7414	780	3	6634	10.52
13-roi7	7488	954	2	6534	12.73
14-roi7	9247	284	2	8963	3.07
15-roi7	7413	940	5	6473	12.68

Figure 4.4: Segmented worm and mucosa from a C57BL/6 mouse showing the breaks in the epithelium covering the tunnel. A male C57BL/6 mouse (n = 1) was infected with a low dose of *T. muris,* and the caecum was dissected at day 35 PI. The caecum fragment was prepared for microCT by staining with OsO_4 and critical point drying. After imaging, seven worms and the surrounding mucosa were segmented and skeletonisation was used to analyse the integrity of the epithelial tunnel. **A**) Image showing a worm (grey) and the epithelium (pink) covering the tunnel. Green arrows indicate breaks in the epithelium covering the tunnel, which leave the worm exposed to the lumen. The blue arrow indicates the position of the worm head. **B**) Surface rendering showing a worm in isolation (grey). **C**) Rendering of the skeletonised worm "spatial graph" which was used to estimate the lengths of worms left exposed by breaks in the tunnel covering **D**) Table showing estimated tunnel lengths for seven worms. The lengths of breaks in the epithelium, and thus the proportions of tunnels that were exposed were estimated by using Avizo's centreline tree algorithm to measure segmented worms. All scale bars = 500 µm.

4.2.3 Head morphology and positioning in C57BL/6 mice

In total, two lengths of caecum from a single C57BL/6 mouse were used for qualitative observations of worm and intestinal morphology at day 35 post-infection. In these two lengths of caecum, we found unexpected variation in the positioning of worms within the niche. Six out of the ten worms for which the anterior stichosome was visible were positioned with the anterior-most portion of the stichosome pointed down the crypts of Lieberkühn, with the tip of the head close to the muscularis mucosae (**Fig. 4.5A – D, Supplementary Movie 1**). The three remaining worms were positioned in the conventionally understood manner with the tip of the head lying next to the lumen in the epithelial cells at the apices of the crypts (**Fig. 4.5I – L, Supplementary Movie 2**). In addition, one worm was observed with a "curled" head morphology, where the anterior-most end of the worm was positioned within the crypt, with the tip of the head curled back towards the crypt apex (**Fig. 4.5E – H, Supplementary Movie 3**).

4.2.4 Head morphology and positioning in a SCID mouse

In addition to C57BL/6 mice, we were interested in observing the positioning of worms in Severe Combined Immunodeficient (SCID) mice. These mice lack the adaptive (T- and B-Cell) components of the immune response, and are susceptible to *T. muris* at both high and low doses. In this study, SCID mice were infected with a low dose (<40 eggs) of *T. muris* in order to replicate the infection burden seen in C57BL/6 mice. When microCT of SCID caeca was carried out using the previously established protocol (**Fig. 4.1**), further head-down morphology was observed in the SCID mice similarly to C57BL/6 mice. However, in one SCID mouse we observed one worm which appeared to travel laterally between crypts. Remarkably, closer inspection under higher magnification (pixel size = 1.162 μm) confirmed this lateral movement of the worm through the crypt, and revealed the worm to be traversing the lamina propria (**Fig. 4.6, Supplementary Movie 4**).

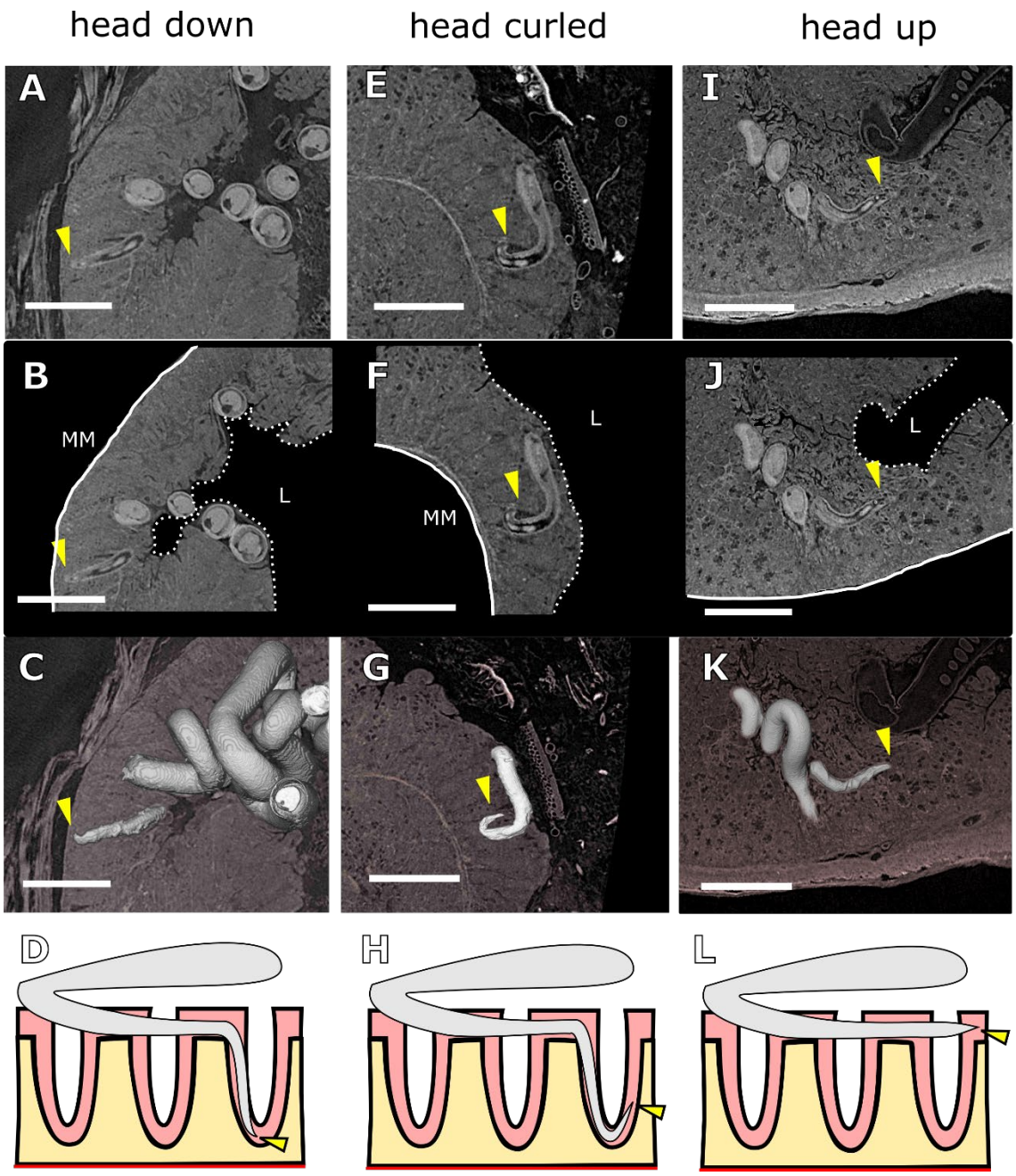

Figure 4.5: Legend overleaf

Figure 4.5: Variable positioning of the anterior stichosome at day 35 post-infection in a C57BL/6 mouse. The caecum from a mouse (n = 1) infected with a low dose of *Trichuris muris* was dissected, OsO_4-stained and imaged at day 35 post-infection. Worm positioning was visualised and is depicted here in slices, volume rendering and diagrammatic format. Three sets of morphologies were revealed among the ten worms investigated. Some worms demonstrated a “head down” behaviour, in which the head is pointed down the crypt towards the muscularis mucosae. This behaviour is shown in a slice (**A**), with the tip of the head indicated by a yellow arrow and in (**B**) is shown in relation to the muscularis mucosae (MM) and lumen (L). **C**) Shows a volume rendering of the worm stichosome (grey) in relation to the host mucosa (pink). **D**) Illustrates the positioning of the worm within the attachment site. One worm within the sample exhibited a “head curled morphology”, in which the head region went down the crypt, and then turned back on itself towards the lumen, shown in slice (**E**) schematic (**F**) volume rendering (**G**), and illustrated (**H**) views. In the “head up” morphology, shown in slice (**I**) schematic (**J**) volume rendering (**K**) and illustrated (**L**) views, worms were positioned as conventionally understood, with the tip of the head within the epithelial cells directly adjacent to the lumen. All scale bars = 600 μm.

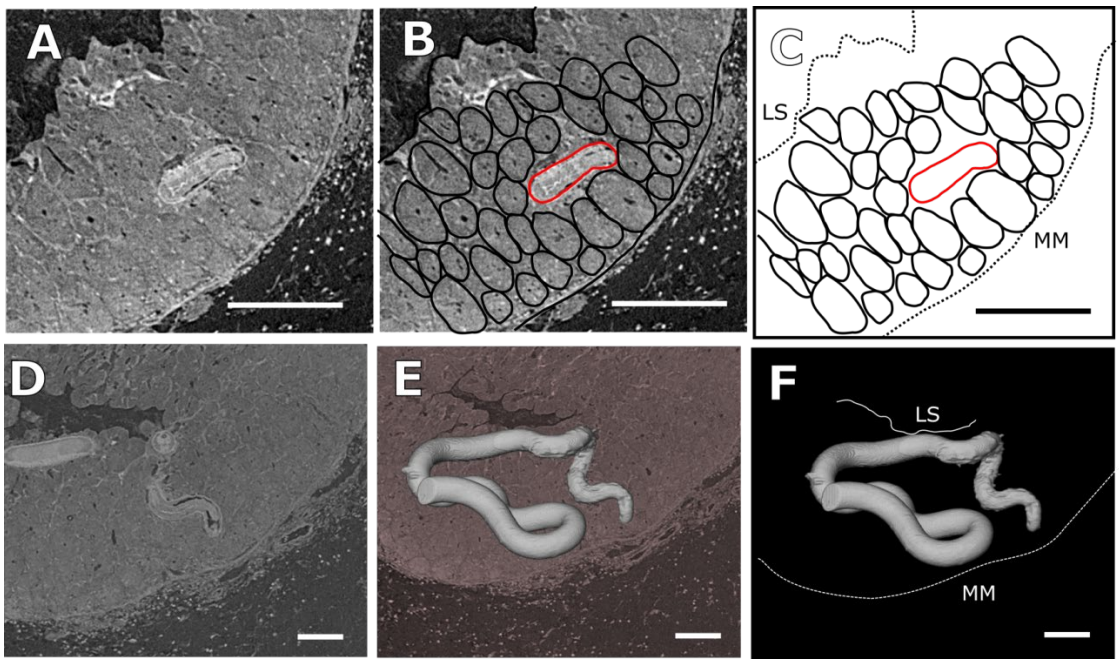

Figure 4.6: Worm head morphology in a SCID mouse reveals a worm traversing a crypt at 35 days post-infection. A SCID mouse (n = 1) caecum dissected at day 35 post-infection and prepared using OsO_4 staining and critical point drying. The caecum contained one worm exhibiting highly unusual positioning. **A**) The worm is travelling laterally across the mucosa, over a distance roughly equivalent to three crypts. **B**) The worm is highlighted in red and the positioning of the crypts is represented by black ovals. **C**) The positioning of the worm (red) is shown in schematic form relative to the lumenal surface of the mucosa (LS) and the muscularis mucosae (MM). **D**) Slice showing the zig-zagging positioning of the worm head. **E**) Volume rendering of the worm showing the positioning of the whole stichosome region compared to the surrounding mucosa (pink, slice). **F**) Schematic showing the spatial relationship between the worm stichosome (grey), the luminal surface of the mucosa (LS) and the muscularis mucosae (MM). Scale bars = 150 µm.

4.2.5 CT measurements of mucosal thickness.

Hypertrophy of the mucosa is a key indicator of its inflammatory status (Erben *et al.*, 2014), with crypt hyperplasia and thickened mucosa indicating the presence of a pro-inflammatory response in chronic *T. muris* infection (Bancroft *et al.*, 2001; Humphreys *et al.*, 2008; Bell and Else, 2011; Hayes *et al.*, 2017). Conventionally crypt hypertrophy is measured in haematoxylin and eosin stained paraffin – embedded histology sections. However, microCT data also presents opportunities to measure the hyperplasia of the mucosal layer of the intestine. Optimising quantitative measurements to ensure accuracy in microCT data is a significant task, which can involve the use of phantoms specifically replicating the sample morphology in known dimensions, and physical probe measurements to quantify the deviation of microCT measurements from true values (Warnett *et al.*, 2016). Here, we lack these tools and are unable to provide reference values for true mucosal thickness with which to compare our measurements. However, we were able to estimate mucosal thickness in microCT data using three different methods (**Fig. 4.7**) and have compared these estimates of mucosal thickness with each other. The first method was a simple calculation of surface are to volume ratio (SAV). The second method utilised Avizo software's "influence zones" module to identify the midline of the mucosa to estimate thickness. The third method used a custom Matlab script to identify the mucosal midline based on local greyscale maxima in a distance map and calculate average thickness. In addition, we also applied one of the methods (Avizo influence zones) to compare differences in average mucosal thickness between C57BL/6 and SCID mice administered with a low dose (<40 eggs) of *T. muris*.

Thickness measurements derived from all three measurement methods were positively correlated when compared by linear regression in a pairwise manner (**Fig. 4.8A-C**) (4 degrees of freedom D.F. for each analysis). Each data set was well fitted to a linear model, and R^2 values, indicating goodness of fit for linear regression, were 0.96, 0.89, and 0.95 respectively for SAV vs Matlab, SAV vs Avizo and Matlab vs Avizo. Whilst all of the methods were highly proportional with each other, the y-intercept and slopes of the linear models differed, reflecting that each method produced different output values. It is unknown which of the methods produced the most accurate output closest to the true value of average mucosal thickness. Applying the Avizo influence zones method to compare the average mucosal thickness between C57BL/6 and SCID caeca revealed no significant difference (unpaired T-test, p=0.59, D.F. = 4).

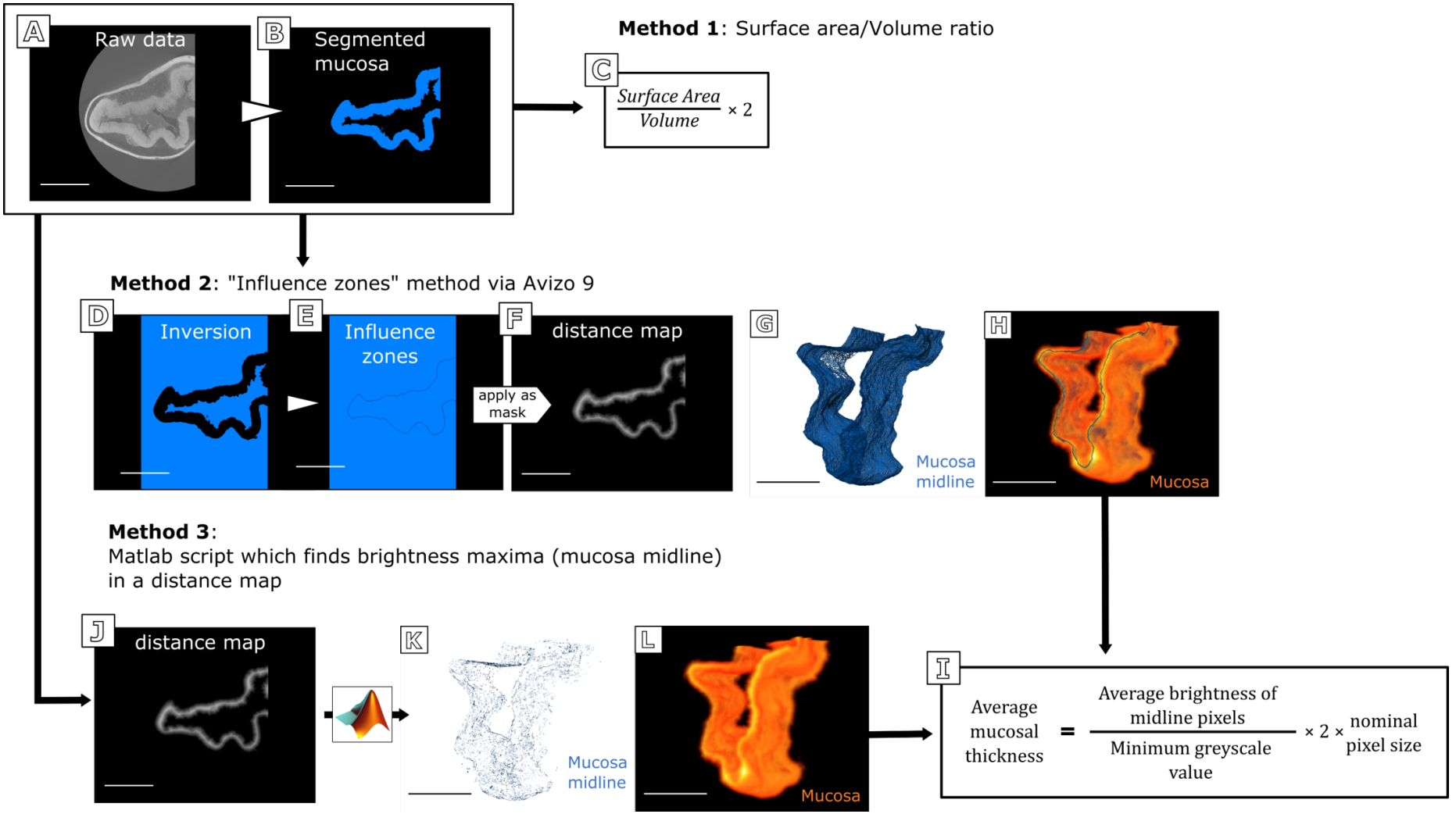

Figure 4.7 Legend overleaf

Figure 4.7: Caeca from mice infected with a low dose of *T. muris* were dissected at d35 PI and prepared for microCT by OsO_4-staining and critical point drying. From the raw microCT data (**A**), the mucosa was labelled using watershed segmentation with manually applied kernels (**B**). **C**) From segmented mucosa, average mucosal thickness could initially be estimated by calculating the surface area to volume ratio based on a parallel sheets model. **D**) In the second method, segmented data was inverted, and Avizo's "influence zones" module was used to find the mucosa midline by identifying pixels equidistant from the mucosal edges (**E**). These midline pixels were used to mask the midline of a mucosal distance map (**F**). These midline pixels are rendered in **G**, and their midline position is shown in **H**. Using the formula in (**I**), the average thickness of the mucosa was calculated from the masked distance map. In the third method, a distance map (**J**) served as the input for a Matlab script which identified pixels on mucosal midline based on their relative brightness. The program then output the average brightness of the pixels on the mucosal midline. **K**) The pixels on the mucosal midline were far sparser than those detected by method 2 when visualised in 3D alongside the mucosa distance map (**L**). The Matlab output of average pixel brightness was input into equation **I** in order to calculate average mucosal thickness. All scale bars = 100 μm.

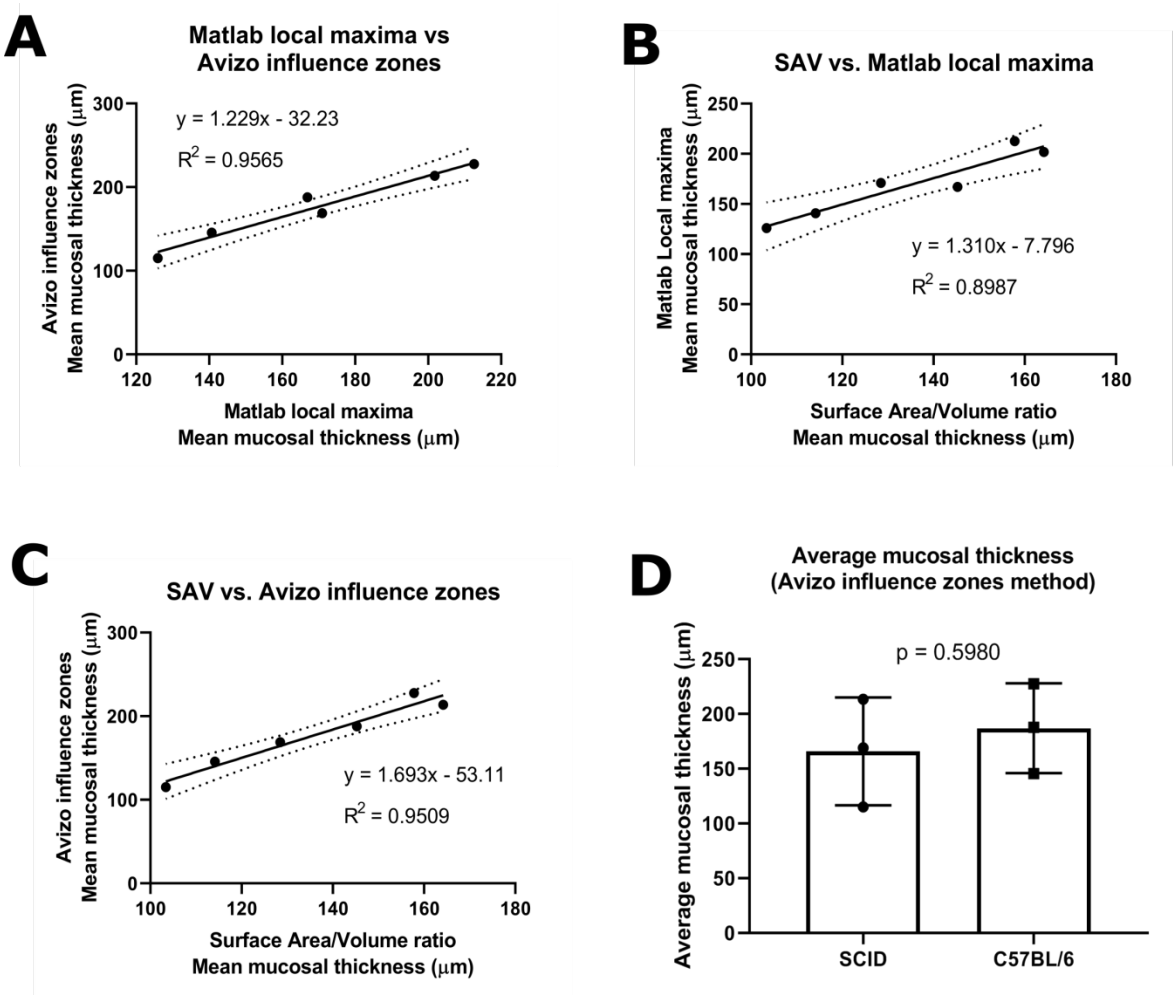

Figure 4.8: Comparison of mucosal thickness measurement models and application of the Avizo influence zones method to compare of mucosal thickness in C57BL/6 and SCID mice. Caeca from three C57BL/6 and three SCID mice infected with a low dose of *T. muris* were dissected at day 35 PI. The caecum fragments were stained with OsO_4, critical point dried and microCT scanned. The average thickness of the mucosa was calculated using three methods which were then compared pairwise by linear regression. Black solid lines indicate the line of best fit, and dotted lines indicate 95% confidence intervals for the linear models. **A)** Matlab Local maxima and Avizo influence zones **B)** Surface area to volume ratio compared to Matlab local intensity. **C**) Surface area to volume ratio compared to Avizo influence zones. Agreement between measurement methods was high. **D)** The Avizo influence zones method was used to compare average mucosal thickness between the mucosae from C57BL/6 and SCID mice, finding no statistically significant difference.

4.2.6 The influence of corticosterone on head-down behaviour and immunopathology

The “head-down” behaviour observed in crypts demonstrates that the *T. muris* accesses compartments of tissue which were not previously considered. Included in the base of the crypts is a compartment of stem cells which are the reservoir for epithelial cell proliferation (Umar, 2010). Previous research has found that expulsion of worms correlates with elevated epithelial cell proliferation and turnover (Cliffe *et al.*, 2005). Interestingly, turnover is also down-modulated during chronic infection (Cliffe *et al.*, 2007). Given the new-found proximity of proliferating cells to worm stichosomes and heads at the base of the crypts, we were interested in the extent to which the head-down behaviour could be correlated with increased intestinal epithelial cell proliferation, and specifically whether it may be a strategy to overcome the “epithelial escalator” model of expulsion suggested by Cliffe et al. (2005). To this end we infected C57BL/6 mice with *T. muris* and administered the immunosuppressant corticosterone and vehicle on days 7, 9 and 13 post-infection (**Fig. 4.9A**). Corticosterone is a murine stress hormone which is physiologically involved in immunosuppression (Pruett, 2000; Cha *et al.*, 2001). In *T. muris* research, corticosteroid injection is conventionally used to sustain chronic infection in otherwise resistant mice (e.g. Caratti *et al.*, 2019). In the context of understanding the *T. muris* “head down” behaviour, our goal in using corticosterone infection was to supress the Th1 IFN-γ-driven epithelial proliferation and turnover. Therefore, any pressure of expulsion on the worm originating from epithelial turnover would be reduced. Our intention was that corticosterone injection would achieve this through its known effects in depleting MHCII+, CD4+ and CD8+ cell number and function while at elevated levels in circulation (DePasquale-Jardieu and Fraker, 1979; Pruett, 1999; Pruett *et al.*, 2000; Schwab, 2004). Either 40 minutes or 12 hours after intraperitoneal injection of BrDU, the caeca were dissected from the mice at day 35 P.I. and prepared for microCT using our optimised sample preparation protocol. Caecum fragments were also taken for BrDU analysis of “pulse-chase” epithelial cell proliferation and crypt length, allowing calculation of epithelial turnover (Cliffe *et al.*, 2005).

Head down behaviour was not observed in any of the mice which were administered corticosterone (n = 4 mice). However, some worms exhibited head-down behaviour in the mice given the vehicle control injection (n = 3 mice) (**Fig. 4.9B**). Interestingly, corticosterone had the opposite effect to what was predicted. Therefore, BrDU pulse-chase, whilst not of sufficient power to be statistically analysed, showed an increased rate of epithelial cell proliferation in corticosterone-treated mice (**Fig. 4.9C - E**). In contrast, the vehicle-treated control group showed reduced epithelial cell turnover (**Fig C - E**). There was also no difference in crypt length between the two treatment groups (**Fig F**). Therefore, surprisingly, corticosterone treatment caused an increase, rather than a decrease in intestinal epithelial turnover, and did not induce head-down behaviour. A summary of the findings is presented in **Fig. 4.9 G**.

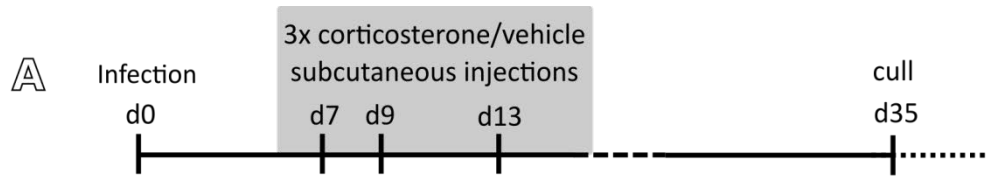

B

Treatment	Number of individual worms		Percentage of worms exhibiting
	head down	head up	head down behaviour
Corticosterone (n=4 mice)	0	14 (n=4)	0.00
Vehicle (n = 3 mice)	3 (n=1)	8 (n=2)	27.27

C

Treatment	Net percent change in BrDU positive cells between 40 min and 12 hours		
	crypt positions 0-10	crypt positions 11-20	crypt positions 21-30
Corticosterone (n=4)	21.92	51.15	37.96
Vehicle (n=4)	-11.13	-13.17	-4.92

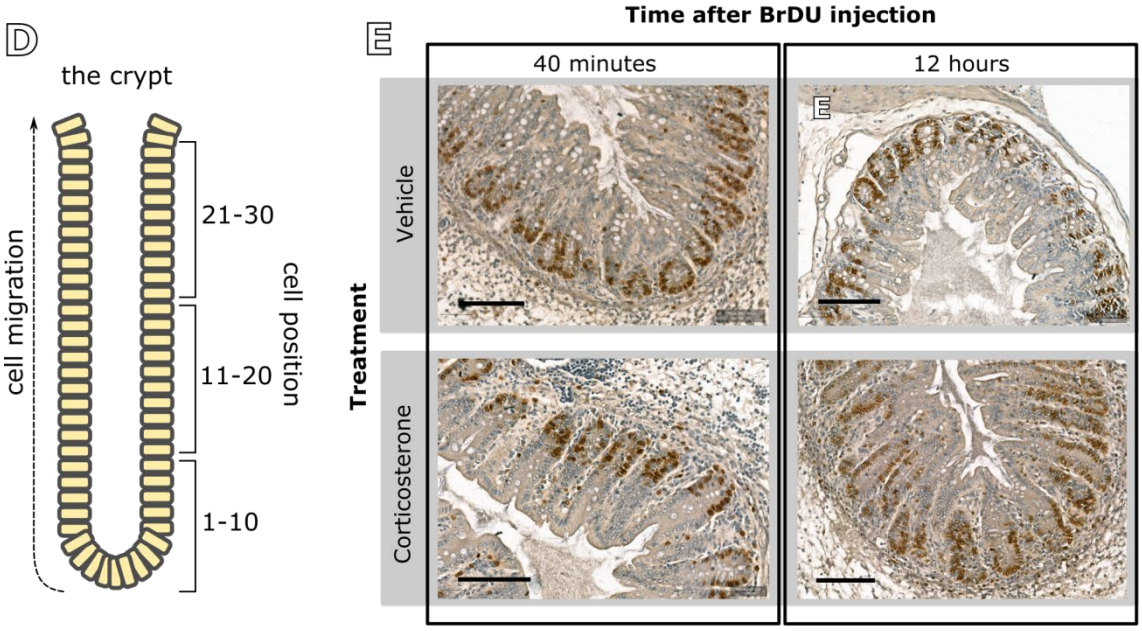

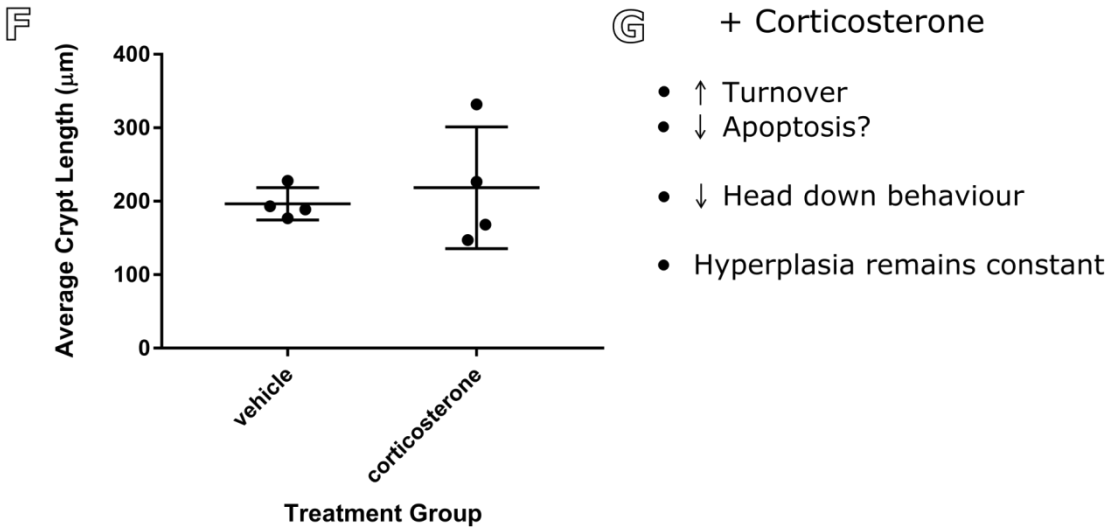

Figure 4.9 legend overleaf

Figure 4.9: Corticosterone-treated mice exhibit accelerated epithelial cell proliferation in comparison to vehicle controls, in conjunction with a reduction in head-down behaviour in parasitizing worms. A) Experimental design: C57BL/6 mice were injected with a low dose of *T. muris* and on days 7, 9, and 13 we injected with either vehicle (n=4) or 50mgkg^{-1} suspension of corticosterone (n=4) subcutaneously. Mice were injected with BrDU and culled on day 35 PI at 40 minute and 12 hour intervals. Caeca were prepared for microCT and histological analyses. **B**) Frequencies of head down behaviour of worms in different treatment groups. None of the worms in the 4 corticosterone treated mice exhibited head-down behaviour, whilst 3 did in the vehicle control mice. **C**) Table showing average net change in BrDU-positive cells in crypt positions within the mucosa between 40 mins and 12 hours after injection with BrDU. A net positive change indicated increased proliferation and movement of cells up the crypts in corticosterone-treated mice. Negative change indicates a reduction in positive cells in vehicle-treated mice, indicating either stasis in proliferation or increased apoptosis**. D**) Schematic illustration showing the location of crypt cell positions as analysed by BrDU. **E**) Illustrative panels showing positions of BrDU-positive cells in treatment groups. **F**) Average crypt length was measured histologically revealing no significant difference in crypt hyperplasia between corticosterone-treated mice and controls. **G**) Summary of outcome of corticosterone treatment.

4.3 Discussion

4.3.1 Efficacy of micro-computed tomography in imaging the niche of *Trichuris muris*

Micro-computed tomography, once sufficiently optimised in terms sample preparation, was effective at imaging the mucosal attachment site in detail at 35 days post-infection. A variety of established staining approaches were trialled, particularly those well-established in previous literature (Metscher, 2009a; de Souza e Silva *et al.*, 2015). PTA and I_2KI are widely-used stains which form the basis of most biological microCT. The use of PTA in particular was of interest, given that it exhibits preferential binding to collagen, the main constituent of the worm cuticle (Handschuh *et al.*, 2017). However, both PTA and I_2KI showed no preferential staining of *T. muris* compared to the host mucosa. Instead, a co-opted SEM sample preparation protocol in which OsO_4-staining was followed by critical point drying provided the best contrast between the worm and surrounding host tissue. The highly preferential staining of the stichosome may have been due to the oxidation of unsaturated lipid chains present within the cell membranes, a well-understood process which is the basis of OsO_4 usage as a fixative (Hayes, 1963; Riemersma, 1968). Indeed backscatter electron microscopic images of the stichosome confirmed that the stichocytes are rich in internal membranes.

Larval worms were far less visible in the gut at day 21 post-infection, and unlike adult worms were negatively contrasted against the host mucosa. At days 7 and 14 post infection, worms could not be seen, although this may have been due to constraints on resolution rather than an absence of preferential staining behaviour. It may also be that the dissection of the caecum missed regions that contained worms. Alternative staining approaches could be required in order to detect the early larval stages at days 7 and 14 post-infection. However, since PTA and I_2KI performed so poorly in adult worms, an approach using immunostaining (Metscher and Müller, 2011) may be preferable. Alternatively, forgoing staining of any kind in favour of phase contrast imaging may be a more productive approach, by which the difference in phase between the worm cuticle and host mucosa could be exploited in order to detect larval worms. Phase contrast imaging using a synchrotron may have been used also in the context of adult worms, in order to avoid any alterations to the tissue introduced by fixation or staining.

4.3.2 Quantitative measurements of mucosal integrity and pathology

The tunnel running through the mucosal epithelium, which forms the intracellular niche for *T. muris*, has been erroneously described as a living syncytium (Lee and Wright, 1978). Histological study has provided a more convincing scenario in which the mucosal tunnel consists of dead epithelial cells (Tilney *et al.*, 2005). Breaks in the epithelium covering the tunnel are revealed by scanning electron microscopy (SEM) (Tilney *et al.*, 2005), but the extent to which they may leave the stichosome exposed to the lumen has not been quantified. We speculate that the poor efficacy of existing anthelminthics (Speich *et al.*, 2015) may be due to their inability to properly penetrate the epithelium covering the metabolically active stichosome, which is also thought to be the source of immunomodulatory proteins (Foth *et al.*, 2014). Therefore, the extent to which the stichosome is exposed by breaks in the epithelium may have important implications for the required pharmacokinetic properties of novel drugs. X-ray tomographic data provides the unique opportunity to estimate length of 3D objects such as the worms and isolated sections of worms in their intracellular niche. Three adult worms were analysed using these tools to determine the extent to which the stichosome is exposed by breaks in the epithelium. The coverage of worms by the epithelium was variable, with exposed proportion of the stichosome ranging from 0.00% to 17.44%. The total tunnelled length of the stichosome was also highly variable between the three worms analysed. Whilst the tunnelled length of the stichosome was for its majority covered by the epithelium in each worm, it is important to note that in all cases the stichosome continued into the lumen, supporting observations made by Lee *et al.* (1978). The extent to which these measurements of epithelial coverage and tunnel length are reflective of the “health” of the epithelial tunnel is unknown. It may be hypothesised that worms exhibit a reduced tunnel length and epithelial coverage prior to expulsion. A potential future area of investigation is therefore the extent to which niche integrity may be altered upon exposure to drug or vaccine candidates.

Drug delivery to at least a part of the stichosome would be unlikely to be limited by epithelial coverage, given that some proportion of the stichosome is always exposed to the lumen. However, potential redundancy in the metabolic and immunomodulatory functionality of stichocytes may allow the worm to continue living in the mucosal tunnel despite drug administration. The observation that there was a maximum of four epithelial breaks observed over all worms analysed seems to conflict with Scanning Electron Microscopic observations by

Tilney et al. (2005), who observe frequent breaks in the epithelium which covers the worms. Whilst more quantitative data is required to properly cross-examine this claim using evidence from μCT, it may be possible that the exposed surface of the epithelium may be damaged during SEM sample preparation. For SEM, the gut must be “opened” so that the worm may be accessible to the scanning beam of electrons, a process which may be responsible for more breaks in the epithelium. MicroCT imaging avoids the exposure of the lumen and associated mechanical stress, perhaps resulting in better preservation of the *in situ* structure of the mucosal tunnel and a reduced number of breaks seen in our images.

Measurement of average mucosal thickness in 3D was attempted in this study using three different methods. Ultimately no significant differences were found between C57BL/6 and SCID mucosal thickness under low-infection doses, despite that SCID mice lacked the CD4 T-cells which are understood to drive IFN-γ during chronic infection. Crypt hyperplasia during low-dose chronic infection of C57BL/6 mice is well established (Bancroft *et al.*, 2001; Hayes *et al.*, 2017). However, whilst crypt hyperplasia has been observed in chronic infection of SCID mice, it has generally been in the context of higher doses (100 eggs) (Humphreys *et al.*, 2008; Bell and Else, 2011). Whilst the true values of mucosal thickness calculated from our approaches remains unknown, the lack of a significant difference in mucosal thickness between SCID and C57BL/6 strains suggests the presence of crypt hyperplasia in SCID mice at a lower infection dose than previously reported. The inclusion of an uninfected C57BL/6 control group would be a useful experimental addition in validating the methodology, in order to verify whether the known increase in crypt hyperplasia of chronically infected relative to naive mice could be detected.

4.3.4 Uncertainty in quantitative measurement

For all of the quantitative microCT measurements presented in this chapter to progress into more common use by other researchers, there are several essential considerations which should be taken into account. Foremost, any quantitative measurement taken from microCT data is primarily subject to the accuracy of the segmentation, in this case the watershed segmentation of the mucosa. Variation in segmentations between researchers, and the consequent variability in quantification has been an issue in diagnostic assessment of CT images by clinicians for years. Indeed, in clinical settings where CT quantification is employed on a variety of tissues (Engelke *et al.*, 2018; Irimia *et al.*, 2019), it is common practice for

specific measurements to be repeated by different individuals, and an inter-observer variation to be calculated (Parkinson *et al.*, 2008). Likewise, for microCT data, potential replicability and inter-observer variation of the segmentation should be kept in mind whilst analysing data (Jensen *et al.*, 2008). Indeed in the case of soft-tissue data, where contrast may be low, segmentations may become more subjective and vulnerable to variation between observers. In our study, watershed segmentation was used to minimise the manual designation of boundaries between tissue phases by the researcher, instead exploiting the greyscale “edges” between phases to generate an automated segmentation. However, some manual alteration of segmentation was required, which is likely to be a source of inter-observer variability in future research.

Aside from inter-observer variability, additional errors in quantitative measurements and their sources in the microCT acquisition process should be considered. Different scanning parameters may represent sources of error in quantitative measurements. For instance, varying pixel sizes provide different outputs for quantitative measurements of the same sample (Kourra *et al.*, 2016), perhaps due to the effect of partially filled pixels on segmentation. Since contrast between phases is important in determining segmentation, the energy of the beam may introduce variation in measurements (Franco *et al.*, 2014). Additionally small variations in temperature and positioning of the sample may also act as additional sources of error. In real life applications, many of these factors combine, such that in fact there is an unknown amount of error associated with any quantitative measurement from microCT. Functionally, error in quantitative measurement has been investigated through several methods. MicroCT measurements may be compared to those from tactile coordinate measurement machines (CMMs), a gold standard for metrology, or a CAD model of the sample (Warnett *et al.*, 2016). Otherwise, phantom samples can be constructed, and microCT measurements can be compared with known dimensions (Zou *et al.*, 2015). In the case of mucosal thickness and the embedded worms, measurements using tactile coordinate measurement methods would be impossible. However, the next step in validating the methods presented in this chapter may be to create and test phantoms which replicate the contrast between mucosal tissue and worm.

4.3.5 Observation of novel head-down behaviour

3D imaging of the *T. muris* attachment site revealed a variety of behavioural features which challenged the existing paradigm of the epithelial niche. Based on our understanding of electron microscopic images (Sheffield, 1963; Lee and Wright, 1978), the worm tunnel niche has always been assumed to be purely epithelial in nature, being positioned inside the cells at the apices of the crypts directly adjacent to the intestinal lumen. This study has found that positioning of the anterior-most portion of the worm exhibits far more positional variation than previously assumed. Specifically, we confirmed that the tip of the head can be positioned at the base of the crypts, a scenario which has been dismissed in previous immunological work (Cliffe *et al.*, 2007). The head may also turn down the crypt before curling back on itself, and most remarkably in one SCID mouse we observed one worm which seemed to be crossing the lamina propria in a zig-zagging pattern. That the worm has access to the tissues in the lamina propria precludes the widespread idea of the tunnel being purely composed of epithelial cells (Lee and Wright, 1978). Moreover, it hearkens back to some of the oldest debates in *Trichuris* biology. In the 20th century there was some debate as to whether *Trichuris* could be a blood feeder (Burrows and Lillis, 1964). Although likely a rare event, our novel data reveals that *Trichuris* does have some degree of access to the vasculature, although we do not imply any connection to blood-feeding.

4.3.6 The effect of corticosterone on C57BL/6 mice and *Trichuris muris*

Corticosterone injection of mice had the opposite physiological effect than expected, and in fact seemed to increase the rate of epithelial turnover in the mouse caecum compared to vehicle controls. In fact, control mice treated with vehicle showed a net loss of BrDU-positive cells between the 40 min and 12 hour timepoints, perhaps indicating elevated cell death. Cell death may have been apoptotic in nature, as elevated apoptosis of cells at the crypt base is associated with chronic *T. muris* chronic infection (Cliffe *et al.*, 2007). Corticosterone was administered as an immunosuppressant, and increased epithelial turnover was not expected. The influence of corticosteroids on intestinal turnover is not clear, and in fact corticosteroids may have opposite effects of proliferation in epithelia located in different anatomical regions. For instance, corticosteroid can induce apoptosis in airway epithelial cells (Dorscheid *et al.*, 2001), yet prevent apoptosis in mammary gland epithelial cells (Harris *et al.*, 1995; Feng *et al.*, 1995).

We might hypothesise that such an action is occurring in the mouse caecum, by which corticosterone modulates both cell death and proliferation in order to increase turnover (Cliffe *et al.*, 2007).

In all four of the corticosterone-treated mice, none of the worms exhibited head-down behaviour. One of the vehicle-treated mice however contained 3 head-down worms. Statistical analyses of behavioural frequency were not possible to carry out on these data, as zero cannot be accepted as an input in a Chi-squared test. However, the presence of head-down worms was not precluded by the very slow rate of epithelial turnover in vehicle-controls. Furthermore, increased epithelial cell turnover did not result in more frequent head-down behaviour, indicating that the behaviour is unlikely to be initiated by rate of epithelial cell turnover. In future investigations, a focus may be on the other factors such as the immune environment. Indeed, since this study revealed that worms can come into contact with the lamina propria and cross crypts, it is conceivable that the worm head can come into contact with both the proliferative compartment of the crypt epithelium, as well as the immune cells and connective tissue resident in the lamina propria.

4.4 Conclusion

Histological analyses of parasitic infection can be made difficult because the unpredictable distribution of parasites within tissues and their complex 3D attachment sites. In this chapter, microCT has been used to locate and visualise the 3D morphology of the *T. muris* attachment site in the mouse caecum. An optimised sample preparation process using OsO_4 staining and critical point drying allowed quantitative measurements of tunnel integrity to be taken, which may have relevance in development of new drugs. Additionally, novel behaviour and positioning of worms was observed, in which the tip of the head was found to either 1) turn towards the base of the crypts directly adjacent to the muscularis mucosae 2) travel down the crypt and turn back on itself, or 3) traverse the crypts in a zig-zagging fashion, crossing the lamina propria. These observations break the existing paradigm in which 1) the *Trichuris* tunnel is assumed to be purely epithelial, and 2) that *Trichuris* only contacts the cells at the apices of the crypts, directly adjacent to the lumen. These findings may have a highly disruptive effect on our understanding of the niche, as adult *Trichuris* may now have access to a variety of immune and proliferative compartments hitherto not thought possible. We have attempted to develop

quantitative measurements for assessing pathology, particularly in calculating mucosal thickness, which now tested should be validated in future. Finally, by injecting mice with corticosterone, we have generated a model of chronic infection with elevated epithelial turnover, associated with a loss of head-down behaviour. The significance of these particular findings should be investigated in future with histochemical analyses of apoptosis and proliferation in tissue.

Supplementary information

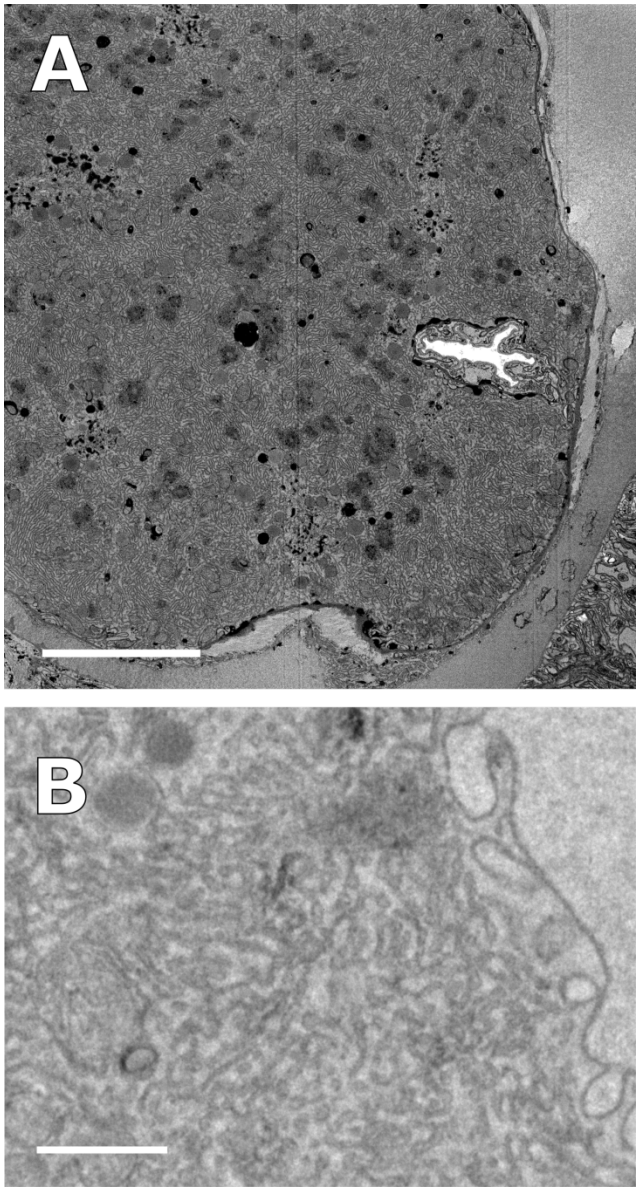

Supplementary Figure 4.1: Backscattered Electron Micrograph (BSEM) of the worm stichocyte reveals a highly membranous composition. A worm was dissected from the caecum of a SCID mouse and prepared for 3D electron microscopy by the protocol of Denk et al. (2003). **A)** The majority of the stichocyte is visible and is packed with membranous structure, likely rough endoplasmic reticulum. **B**) A more highly magnified view of the stichocyte shows the membranes in more detail. Scale bars **A** = 100 µm, **B** = 10 µm.

Blank page

5. Morphology and prospective function of cuticular inflations on the bacillary band of *Trichuris muris*

Contributions:

James O'Sullivan carried out all microCT, SEM, histology and Real Time quantitative Polymerase Chain Reaction (RT-qPCR)

Dr Tobias Starborg assisted in sample preparation and carried out 3D SBF-SEM

Dr Alex Mironov assisted in sample preparation and carried out TEM

5.1 Introduction:

During *Trichuris* infection, the anterior two-thirds of the worm (the stichosome) are embedded within the intestinal epithelium of the host. The stichosome is characterised by the presence of large cylindrical cells filling the body cavity called stichocytes, but also exhibits a variety of other structures along the bacillary band, which covers the ventral side of the anterior stichosome. The functions of structures in the *T. muris* bacillary band still remain enigmatic, despite their highly specialised morphologies and likely roles in the maintenance of the epithelial tunnel niche. Bacillary pores are densely packed throughout the band, and a bacillary cell underlies each pore. Cuticular inflations, which are rounded projections lining the anterior portion of the bacillary band, remain of totally unknown function.

The bacillary cells have received more attention and are suspected to have a role in feeding (Hansen *et al.*, 2016). Research on the function of the bacillary cells and their associated structures has been largely informed by TEM investigations, which revealed the highly folded apical membranes and therefore suggested that they have either absorptive or secretory functions (Wright, 1963, 1968b; Sheffield, 1963; Wright and Chan, 1973; Hüttemann *et al.*, 2007). These ultrastructural observations prompted subsequent functional investigations using fluorescence microscopy (Tilney *et al.*, 2005; Hansen *et al.*, 2016). This body of work demonstrates that a thorough characterisation of the morphology, ultrastructure and composition of the cuticular inflations may be a productive first step for building functional studies in the future.

Studying ultrastructure of the cuticular inflations immediately presents a greater challenge than the bacillary cells. Bacillary cells are densely packed throughout most of the stichosome. In practice this means that as long as the stichosome can be prepared whole, the sectioning plane may be present at any location along its length, at almost any orientation and yet still capture the structure of many bacillary cells. In contrast, the cuticular inflations are present in a smaller section of the stichosome (Lopes Torres *et al.*, 2013), appear less frequently, and must be captured in the correct orientation relative to the plane of sectioning. These difficulties add significant complication to the imaging process, and perhaps for this reason, only one ultrastructural study on the cuticular inflations currently exists and only in the canine whipworm *Trichuris vulpis* (Wright, 1975).

The difficulties in imaging the cuticular inflations may be bypassed by using new correlative imaging workflows. In these cases, microCT imaging of a sample after embedding for EM allows a high-resolution map of the sample interior to be created, which can inform and guide subsequent sectioning attempts (Sengle *et al.*, 2013; Starborg *et al.*, 2019). This approach would allow the cuticular inflations to be located within a resin block and targeted spatially for EM, thus constituting a far more efficient imaging approach than previously possible.

In addition to ultrastructural information, understanding the genetic basis of cuticular inflation development may also be informative in determining their function. Since the early TEM studies, the *T. muris* genome has been sequenced (Foth *et al.*, 2014). Sequencing has revealed a variety of *T. muris* genes which may code for putative drug targets, as well as for secreted proteins involved in host immunomodulation. Comparison of *T. muris* genes with homologs in the highly tractable model nematode *Caenorhabditis elegans* provides a new opportunity to identify and investigate the genetic basis of cuticular inflation development. Strains of *C. elegans* which have mutated “blister” genes display cuticular swellings similar to the cuticular inflations seen in *T. muris*. In particular, the genes *bli-5, bli-4* and *dpy-31* have been well-investigated as blister mutants in *C. elegans* (Stepek *et al.*, 2010; Page *et al.*, 2014), and all have homologs in the *T. muris* genome. Understanding spatiotemporal expression of these blister gene orthologs in *T. muris* represents a novel and intriguing research direction in which the genetic basis for inflation formation could be investigated. A greater understanding of the regulators of inflation development may assist in revealing function.

In this chapter, the goal was to investigate the function of cuticular inflations, by characterising their structure, composition and development in more detail than has previously been attempted. The specific aims were to:

1) To characterise the developmental timeframe for the cuticular inflations.
2) To determine the ultrastructure and composition of the cuticular inflations, and the surrounding tissues.
3) To investigate the expression patterns of blister gene homologs throughout the course of cuticular inflation development.

Worms dissected from the hosts at different time-points post-infection (PI) were inspected with SEM to observe cuticular inflation development. Ultrastructure of the mature cuticular inflations and surrounding structures was investigated using TEM and SBF-SEM at 35 days PI. In order to achieve this, a correlative workflow of microCT-steered EM was developed (**appendix 2**), which allowed efficient imaging of appropriate regions of interest. The composition of cuticular inflations was investigated histochemically. Finally, RT-qPCR was employed to examine patterns of blister gene homolog expression during the window of development as identified by SEM.

5.2 Results:

Experimental Protocols, including details of sample acquisition, processing, imaging and analysis are outlines in the methods, chapter 3.

5.2.1 Cuticular inflations develop between 23 and 28 days post-infection

SEM was used to image worms that had been extracted from the host gut at days 21, 23, 25, and 28 post-infection in order to track the morphological development of the cuticular inflations. At each time-point, worms were extracted an pooled from two murine hosts. Overall, the progress of cuticular inflation development is summarised in **Fig. 5.1**. In this case, partial development of cuticular inflammation was labelled as “immature”, whilst “mature” was the term used to describe when many inflations were spread across the anterior stichosome. The highly-detailed view of the worm surface provided by SEM facilitated a novel characterisation of inflation development. At day 21 and day 23 post-infection, none of the worms imaged (n = 5, 6) exhibited fully formed cuticular inflations with one exception in which one worm out of 5 worms imaged at day 21 PI exhibited a slight swelling of the cuticular surface. This slight swelling may represent a very early stage in cuticular inflation development (**Fig. 5.2 A, B**). Day 25 PI was the first time-point at which worms definitively began to exhibit clear cuticular inflation development (**Fig. 5.2 Ci, ii,** n=9). In three of these worms, several convex cuticular inflations were present on the stichosome (**Fig. 5.3 B - D**). One of the 25 day-old worms analysed exhibited over 30 cuticular inflations in a collapsed aspect along the anterior length of its stichosome (**Fig. 5.3 E**). However, one worm at day 25 PI exhibited no evidence of cuticular inflations (**Fig. 5.3 A**). At day 28 (n = 6), all of the worms imaged exhibited many cuticular inflations (**Fig. 5.2 Di, ii**, n=6). A developmental window was therefore determined, in which the majority of visible cuticular inflation development occurred in worms between days 25 and 28 post-infection.

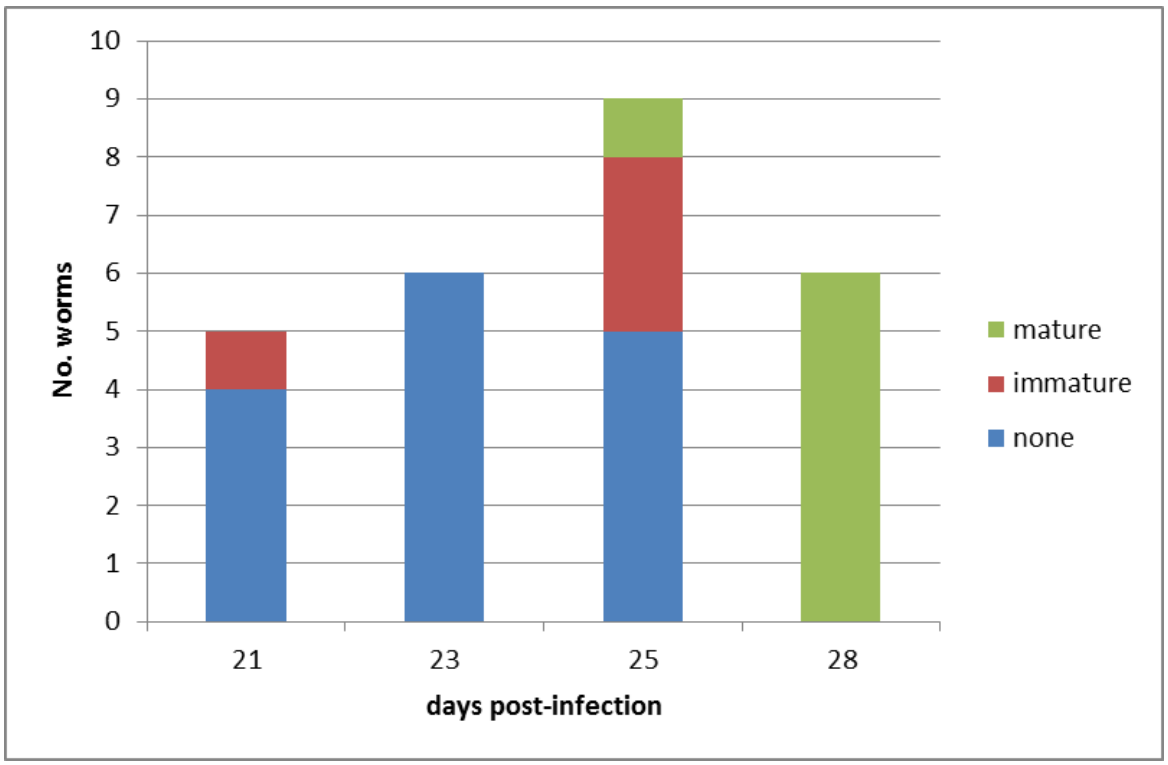

Figure 5.1: Developmental time course of cuticular inflations during days 21 – 28 post - infection. *T. muris* were extracted from the mouse gut (n = 2 - 4 mice) at days 21, 23, 25, 28 and 35 PI and fixed, dried and sputter coated. Worms from each time point PI were pooled. At each time point, we searched for cuticular inflations in immature or mature states. The number of worms displaying either no, immature, or mature inflations are displayed in the graph. At day 21 a small, potentially inflation-related projection was noted on one worm cuticle. At day 25, three worms began to exhibit development of one or two “immature” cuticular projections. At day 28, all worms exhibited cuticular inflations.

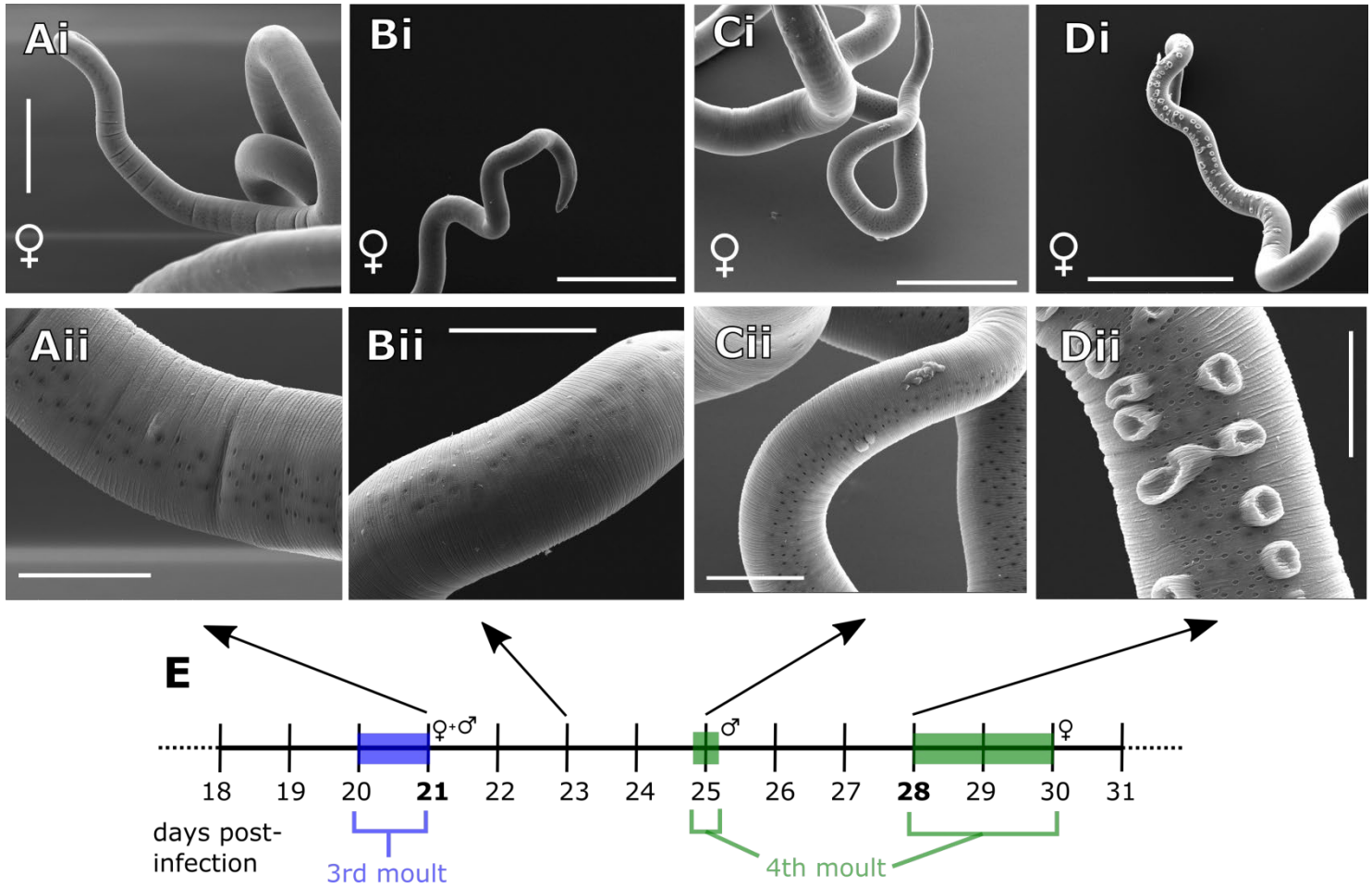

Figure 5.2: Developmental time-course of cuticular inflations in female worms as visualised by SEM

Legend overleaf

Figure 5.2: Developmental time-course of cuticular inflations in female worms as visualised by SEM. *T. muris* were extracted from the mouse gut (n = 2 – 4 mice) at days 21, 23, 25, 28 and 35 PI and fixed, dried and coated for SEM. Worms from each time point PI were pooled. Worms at week 21-postinfection (**Ai, ii**) and week 23 post-infection (**Bi, ii**) lack cuticular inflations. At day 25 post-infection, cuticular inflations become evident (**Ci, ii**). A variety of morphologies can be seen at day 25 (**Fig. 5. 3**), however inflations do not develop simultaneously and instead begin appearing as only one or two at a time. By day 28 post-infection (**Di, ii**), all worms exhibit cuticular inflations. **E**) Timeline indicating the occurrence of moults according to Panesar et al. (1989), alongside the sampling regimen for worms. Scale bars: **Ai** = 100 µm, **Aii** = 30 µm, **Bi** = 100 µm, **Bii** = 20 µm, **Ci** = 100 µm, **Cii** = 30 µm, **Di** = 100 µm, **Dii** = 30 µm.

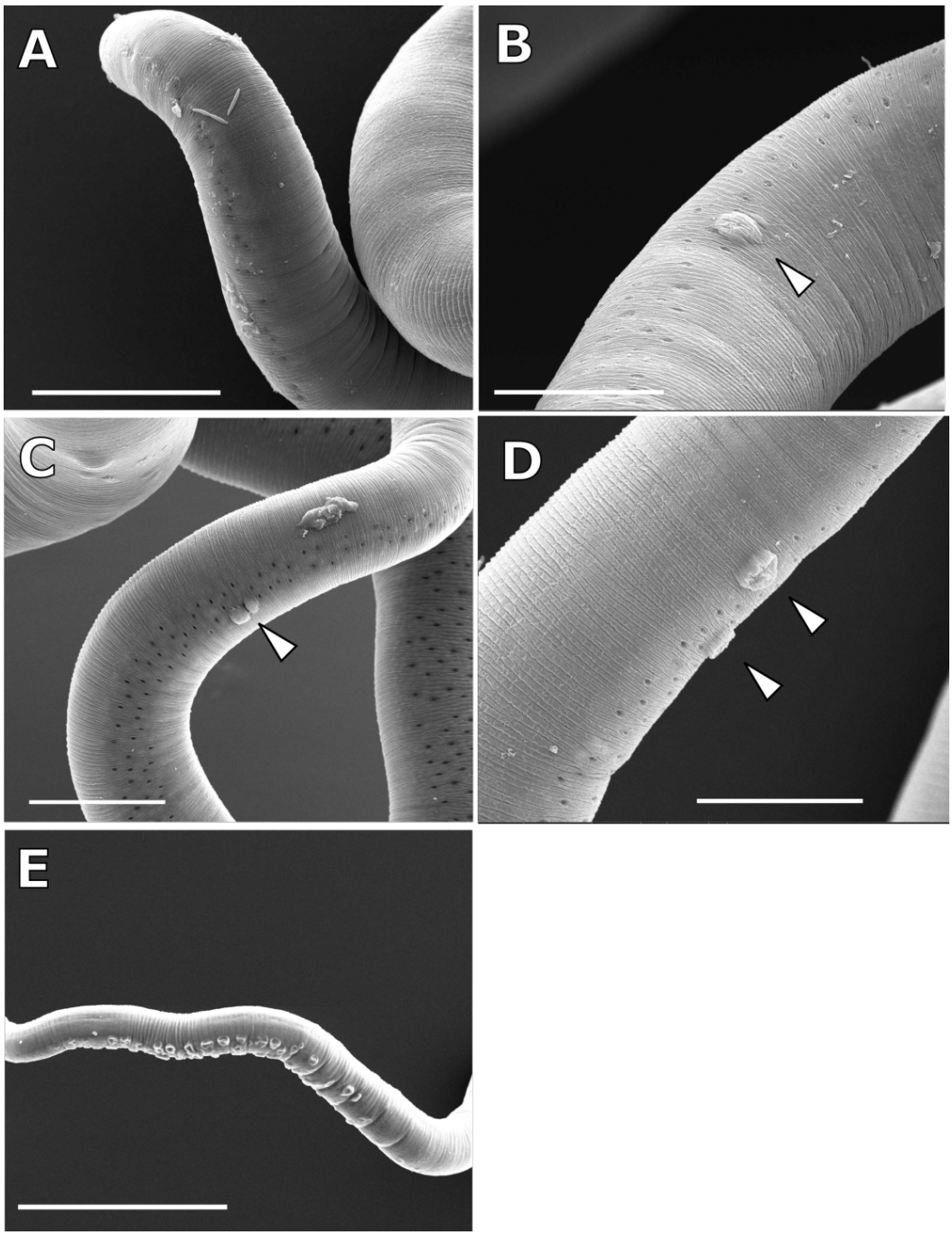

Figure 5.3: A variety of cuticular inflation morphologies are evident at day 25 post-infection. *T. muris* were extracted from the mouse gut (n = 2 mice) at day 25 PI and fixed, dried and coated for SEM. Worms from the 2 mice were pooled before processing. Worms exhibited **A**) no cuticular inflation development. **B**) A single cuticular inflation on the stichosome, and **C, D**) two cuticular inflations on the stichosome. One worm at this time-point was observed to have many cuticular inflations (**E**). Scale bars: **A** = 100 µm, **B** = 30 µm, **C** = 30 µm, **D** = 30 µm, **E** = 100 µm.

5.2.2 Ultrastructure of cuticular inflations from SBF-SEM and TEM

A correlative tomography workflow incorporating microCT guided the SBF-SEM of processed worms (**Fig. 5.4, Appendix paper 2**) (Starborg *et al.*, 2019). In this approach, the microCT data was used to inform the location of the imaging frame, and the sample was accordingly trimmed such that multiple cuticular inflations at different regions of the schistosome were captured and imaged in 3D. In total, two worms were imaged in this way. The cuticular inflations were visible as areas of low attenuation in microCT images (**Fig. 5.5 A, C**). In electron micrographs, the inflations presented as extensions of the cuticle, with the outermost cortical layer of cuticle and epicuticle forming the outer layer of the inflation. Between the cortical and medial layers of cuticle there was a thicker, electron-dense layer of material. Inside the convex inflations to the anterior-most end of the stichosome, empty voids of low electron-density were present (**Fig. 5.5 B**). However, inflations in a more posterior region of the stichosome presented a collapsed aspect (**Fig. 5.5 D**). Similar to the anterior inflations, these collapsed inflations presented a thick, electron-dense layer of material. However, they did not contain a void. The contrast in external morphology seen between the anterior and posterior inflations is highlighted in volume renderings of the entire datasets (**Fig. 5.5 E, F**). This is the first time in which evidence of both collapsed and convex inflations' presence on the same worm but in different regions has been remarked upon. Observation of the cell type directly underlying the cuticular inflation was made possible in an investigation of a separate worm in which better contrast had been achieved during the staining process. In this specimen, directly underlying the cuticular inflations was a cell which, similarly to bacillary cells, exhibited a large quantity of mitochondria (**Fig. 5.6**). However, the cell also lacked a folded apical membrane, which confirmed that it was not a bacillary cell.

At the end of the SBF-SEM acquisition, thin slices were taken from the block-face and mounted on grids. TEM of these slices (**Fig. 5.7**) revealed the ultrastructure of the inflation in greater detail. Specifically, the structure of the inflation was confirmed as an accumulation of material between the cortical and medial layers of the cuticle (**Fig. 5.7 A**). Upon inspection at 11000X magnification, the material filling the inflation was revealed to resemble an anastomosing web-like layer of fibres (**Fig. 5.7 B**). A schematic of the inflation structure is presented in **Fig. 5.7 C** based on the structure as observed by TEM.

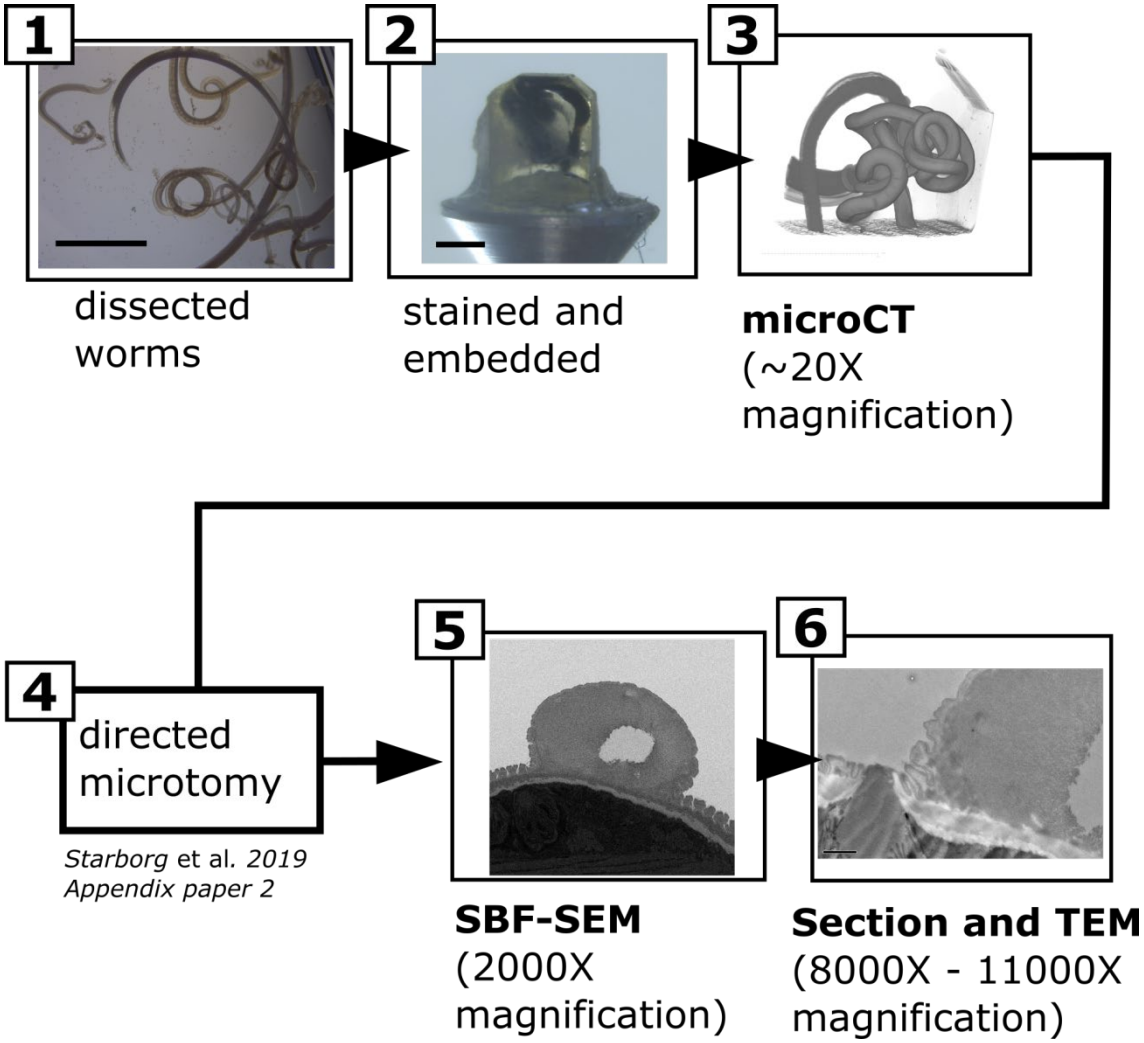

Figure 5.4: Correlative workflow allowing ultrastructural investigation of the cuticular inflations. Worms were removed from the host gut (**1**), stained and embedded for SBF-SEM (**2**) and scanned using microCT to create a map of the sample interior (**3**). Once the cuticular inflations were located, block face was trimmed to the correct shape (trapezoid) and appropriate depth to capture them within the imaging frame (**4**). (**5**) SBF-SEM allowed 3D morphology of the inflations to be inspected at multiple points along the surface of the worm. (**6**) Following SBF-SEM, thin slices were cut from the blockface, mounted on grids and used for TEM in order to visualise ultrastructure at even higher magnification.

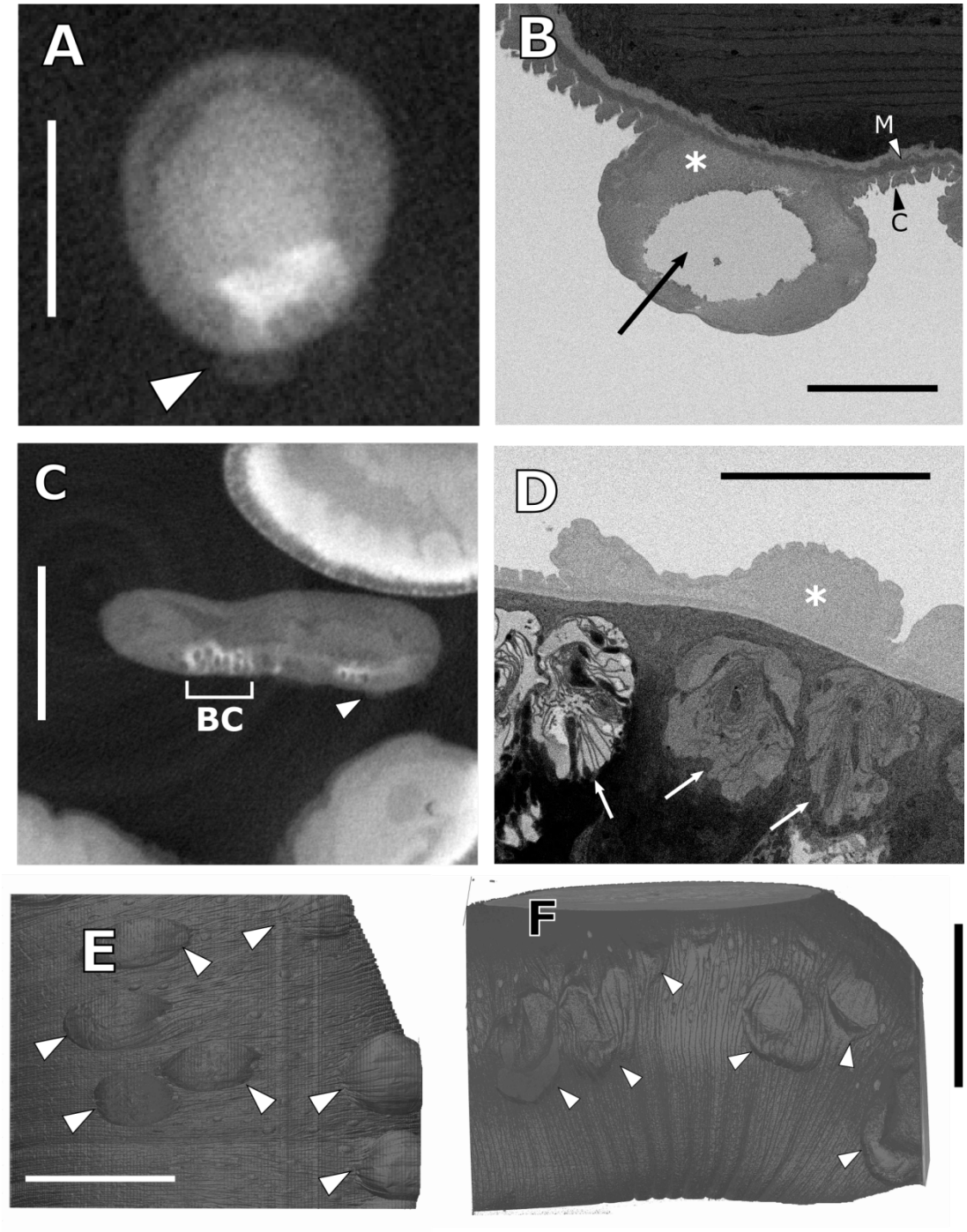

Figure 5.5: SBF-SEM showing the internal morphology of cuticular inflations.

Legend overleaf

Figure 5.5: SBF-SEM showing the internal morphology of cuticular inflations. A worm was removed from the host gut at 35 days PI with *T. muris*, and parasite cuticular inflations were imaged by employing a correlative workflow in which microCT guided the location of the SBF-SEM imaging frame. **A, C)** Cuticular inflations (white arrowheads) from posterior (**A**) and anterior (**C**) regions of the bacillary band were identified using X-ray micro-computed tomography (BC = bacillary cells). SBF-SEM slices revealed that the anterior inflations (**B**) consisted of an interior void (black arrow), surrounded by electron dense material (*) between the median (M) and cortical (C) layers of cuticle. However, the posterior inflations (**D**) lacked the internal void and presented a more collapsed aspect (white arrows = bacillary cells). **E, F)** volume renderings of the SBF-SEM slices make the contrast in inflation shape between the regions more apparent in the (**E**) posterior and (**F)** anterior regions. Scale bars: **A** =100 µm, **B** = 10 µm, **C** = 100 µm, **D** = 10 µm, **E** =50 µm, **F** = 50 µm.

5.2.3 Neural organisation of sensory apparatus as determined by SBF-SEM and TEM

In addition to the structure of the cuticular inflations, carrying out SBF-SEM on the bacillary band structures also provided an unexpected view of the sensory apparatus within the bacillary cells (**Fig. 5.8**). Within the bacillary pores, four sensory processes were present (**Fig. 5.8A, B**). These extended through and beneath the bacillary cell, and converged into a single four-neuron bundle (**Fig. 5.8 C, D**). They then joined further sensory processes in a neuron bundle adjacent to the stichocyte. The identity of these cells as neurons was confirmed by TEM, which revealed a characteristic organisation of microtubules within the processes (**Fig. 5.8E**). For the sake of clarity, a schematic illustration of the neural organisation as observed in SBF-SEM is presented in **Fig. 5.9**. Accompanying SEM images are included to demonstrate the actual ultrastructure at different spatial points within the model (**Fig. 5.9 A –D**).

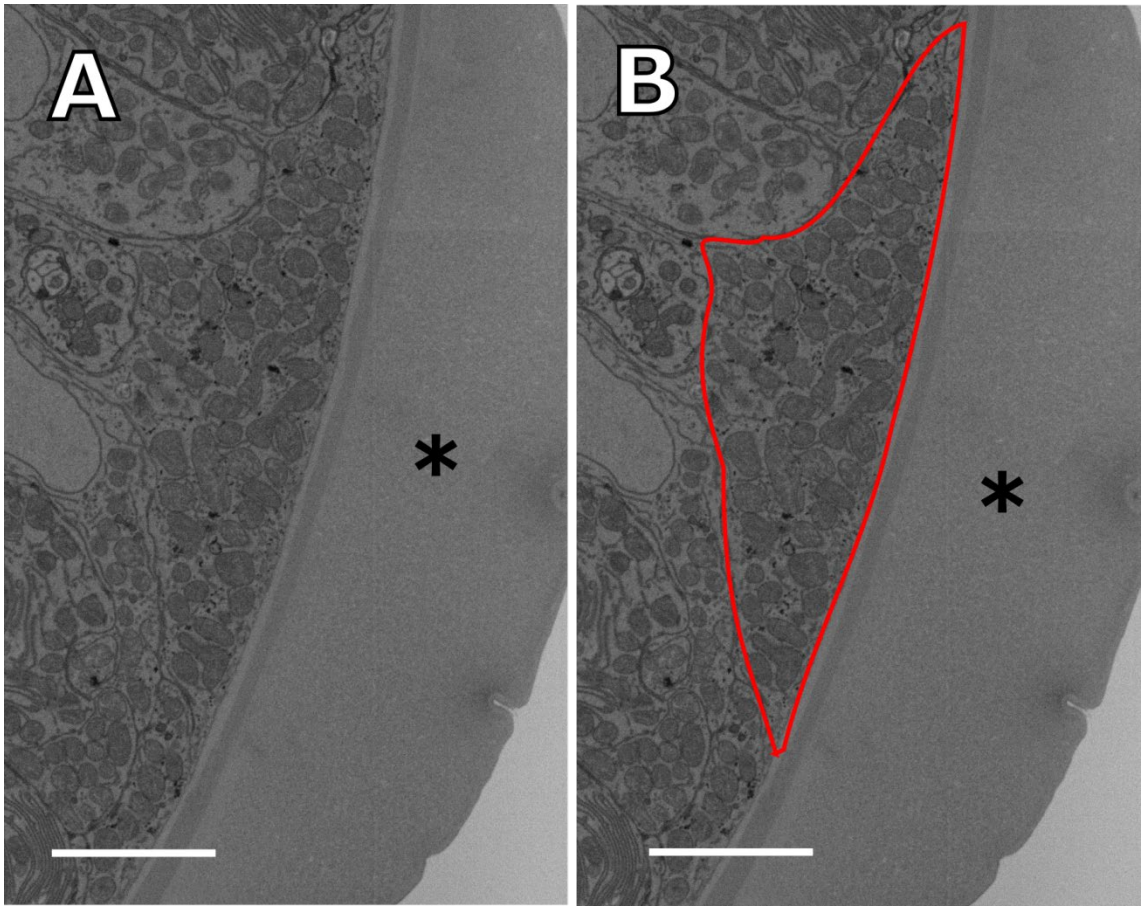

Figure 5.6: A cell under the cuticular inflation has a high concentration of mitochondria. One *T. muris* was extracted at day 35 PI from infected mice and using a correlative imaging workflow, regions of interest were captured using SBF-SEM**.** MicroCT-guided SBF-SEM was carried out on the cuticular inflations in 35 day-old worms extracted from the host gut. **A** and **B** show the ultrastructure beneath the cuticular inflations. In particular, a cell is present with a high number of mitochondria (highlighted in red, **B**), directly underneath the inflation (*). The cell is not bacillary, at it lacks the appropriate folded apical membrane. Scale bars = 800 nm.

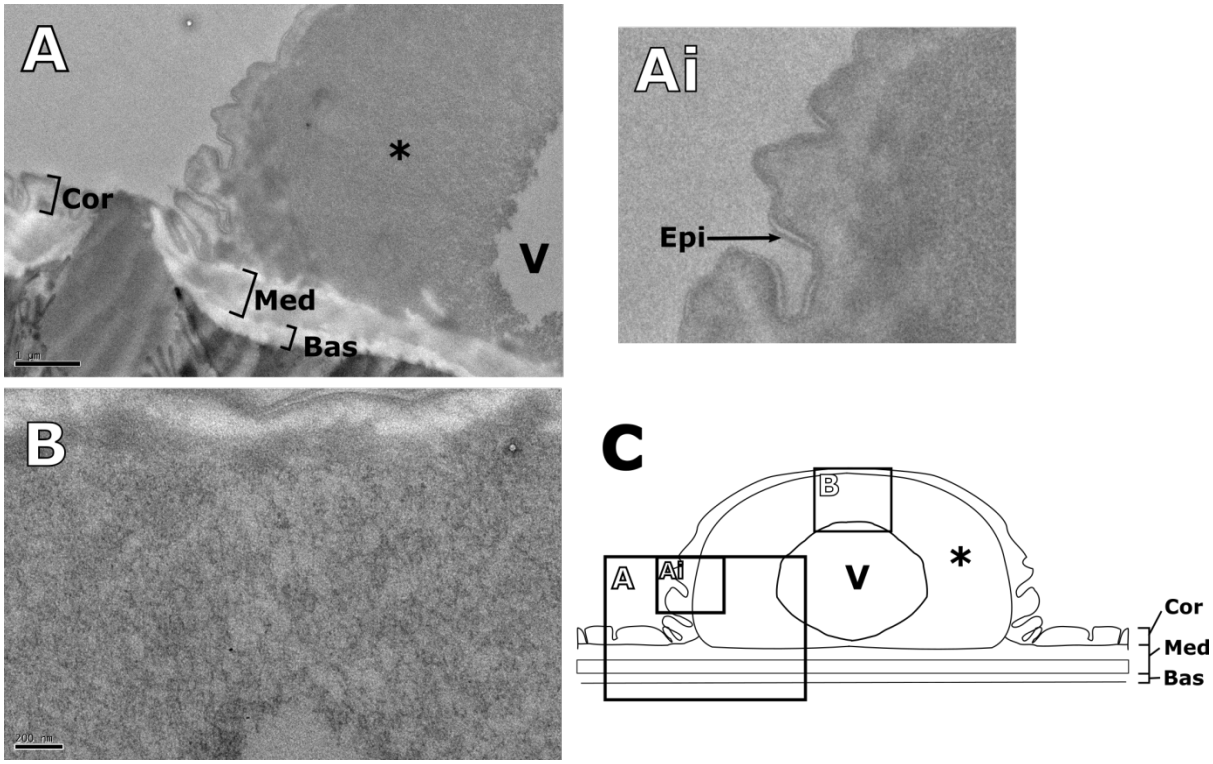

Figure 5.7: Transmission Electron Microscopy (TEM) of the internal composition of the cuticular inflations. One *T. muris* was extracted at day 35 PI from infected mice and using a correlative imaging workflow, regions of interest were captured using TEM (**A)** shows an 8000X magnification image taken from the base of a cuticular inflation. The layers of cuticle were easily discernible, including the cortex (cor), median (med) and basal (bas) layers. We confirm that the inflation originates between the median layer and cortex, and consists of a thickened layer of cuticle-like material (*), as well as a central void (V). The epicuticle can be perceived as a thin layer covering the surface of the cuticle in **Ai)**. **B)** Shows an 11000X magnification image taken from the apex of the inflation. The thick layer of cuticle-like material is revealed to be a web-like network. **C)** A diagram depicting the layout of a cuticular inflation as indicated from the TEM, including the location of the imaging frames in **A** and **B**. Black scale bars: **A** = 500 nm **B** = 200 nm.

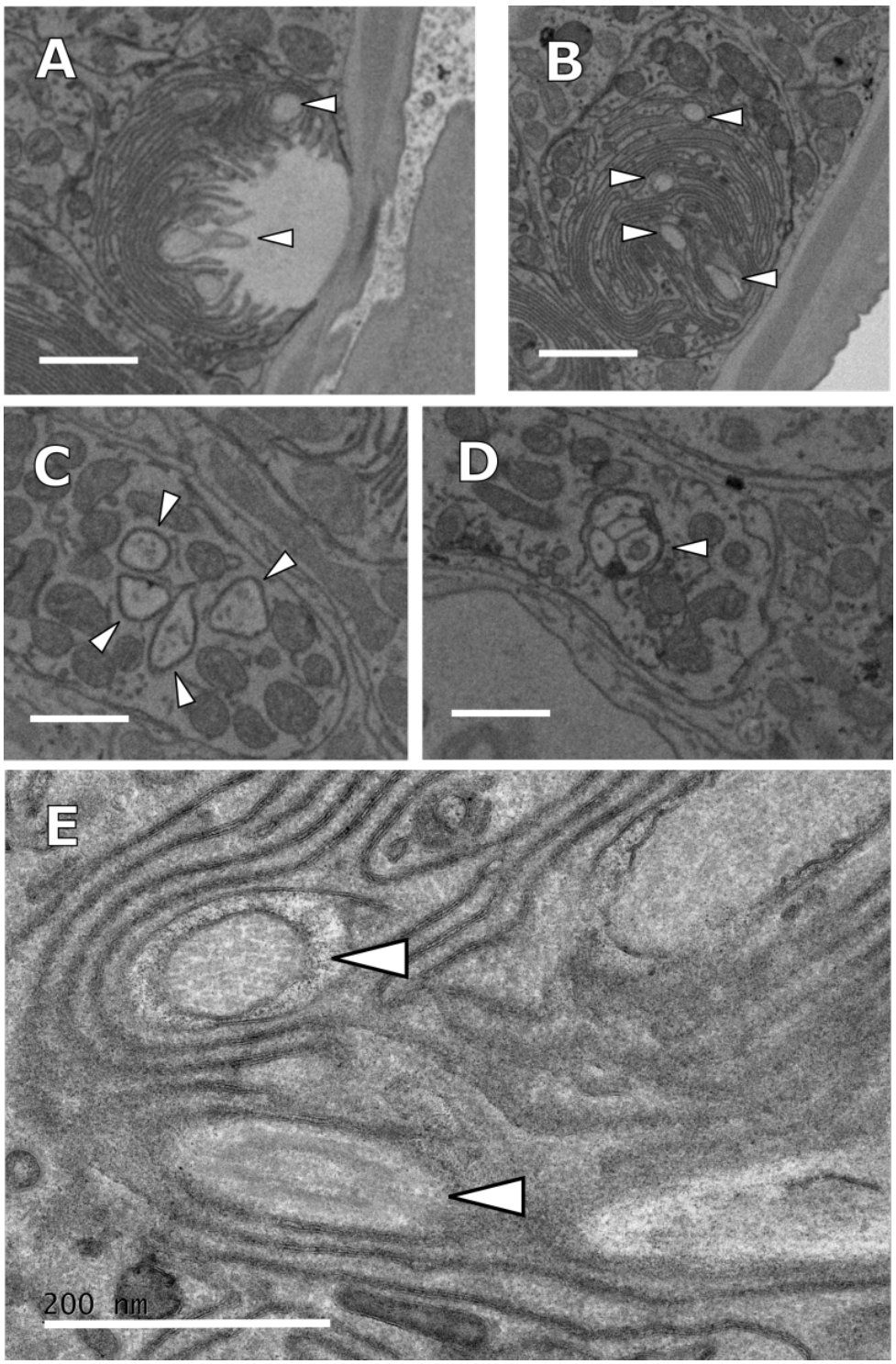

Figure 5.8: SBF-SEM and TEM showing the organisation of sensory cells within the bacillary pores. MicroCT-guided SBF-SEM was carried out on the cuticular inflations in a 35 day-old *Trichuris muris* worm extracted from the host gut. **A, B**) Four sensory processes are present within the bacillary pores (white arrowheads). The processes converge basally to the bacillary cell (**C**), and form a bundle (**D**). **E**) The cells are positively identified as neurons due to the conformation of microtubules within the cell cytoplasm, as visualised in TEM. Scale bars A, B = 1 µm, C, D, E = 500 nm

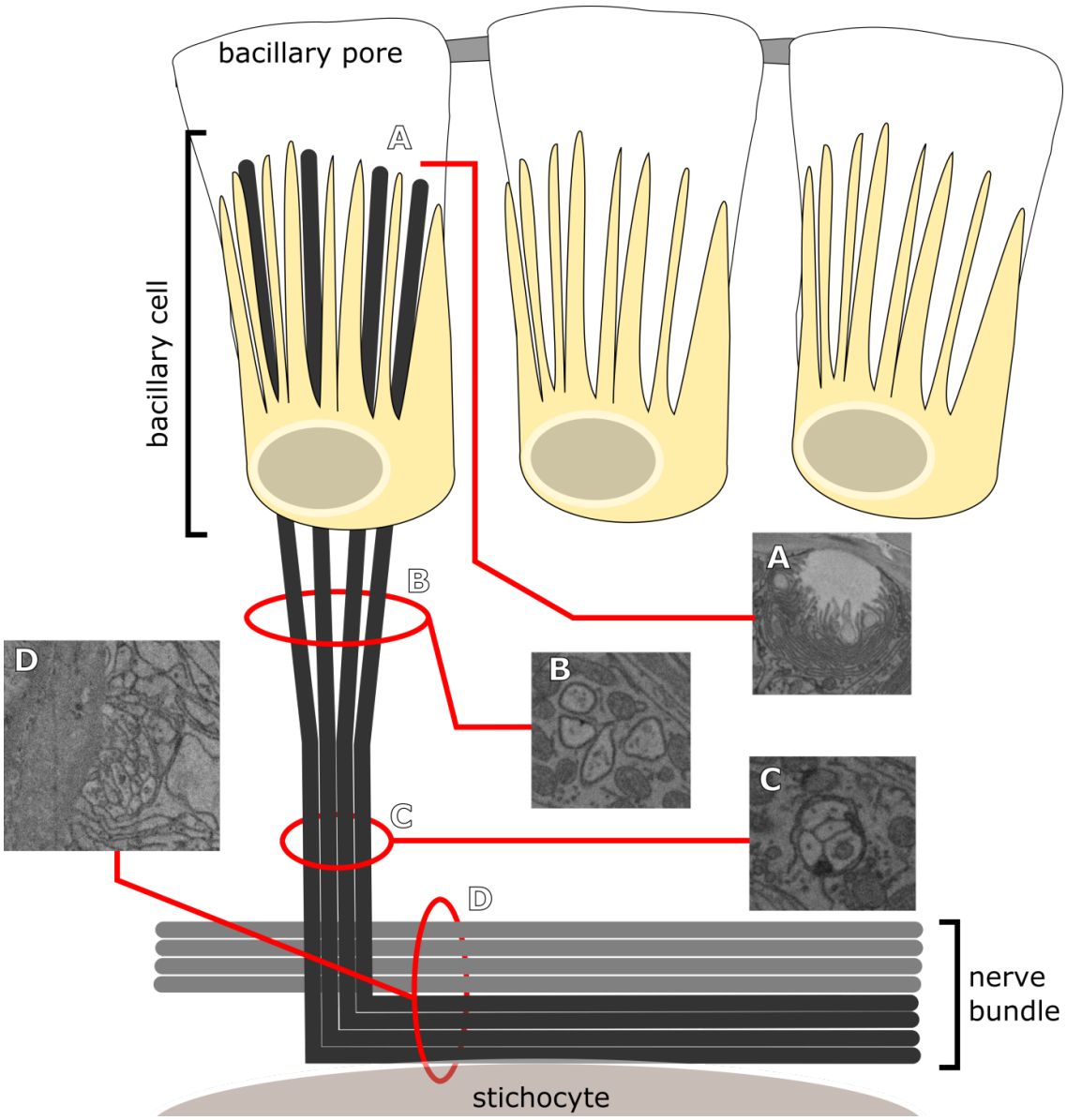

Figure 5.9: Illustration of neural organisation of the sensory processes in bacillary cells as observed by SBF-SEM. SBF-SEM was used to visualise a T. muris worm taken at d35 PI. Based up on the images a schematic can be shown of the likely neural organisation of the sensory processes. Four processes end within the bacillary pore (**A**), and trail back towards the stichocyte (**B**), forming a bundle on their way (**C**). They then join a larger nerve bundle at the surface of the stichocyte (**D**).

5.2.4 Composition of the cuticular inflations

Due to the large sectioning area provided by paraffin embedding tissue, cuticular inflations could be easily found by embedding many worms within a single block and staining sections taken from any depth. Picrosirius red (PSR) staining was used to visualise the tissue and this revealed cuticular inflations in the wax sections. The inflations appeared as surface projections of the correct size (~10 - 20 µm) (**Fig. 5.10 Ai, ii**). Based on TEM and PSR, we predicted that the dense mesh within the inflation was likely collagen fibres. PSR enables collagen fibres to be visualised using polarised light microscopy (**Fig. 5.10 Bi, ii**). The birefringence exhibited in some of the images suggests organised type 1 collagen fibres being present within the inflations. However, birefringence did not account for the entire positively stained region, perhaps due to organisation of collagen fibres perpendicular to the plane of sectioning. Alternatively, type 1 collagen fibres may not be present in these regions.

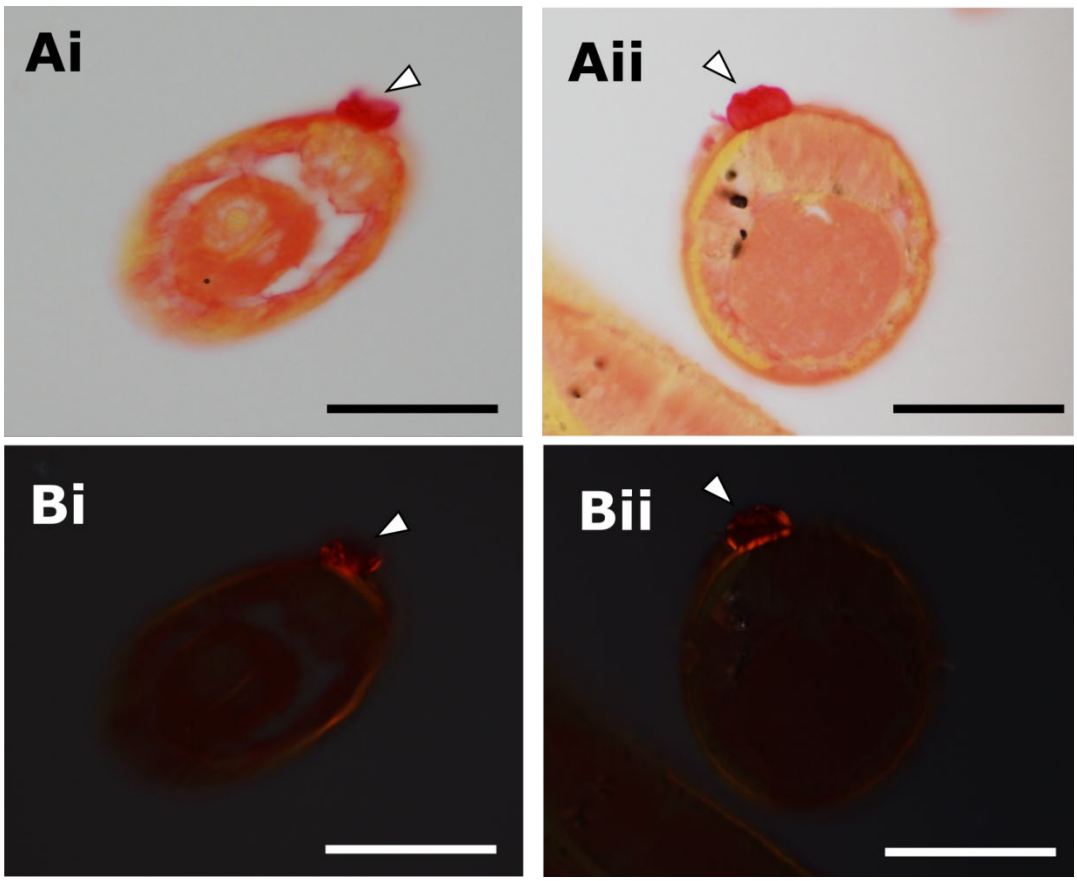

Figure 5.10: Picrosirius red staining of paraffin-embedded worms. Many worms were embedded within a single paraffin block and sectioned in order to locate cuticular inflations. **Ai, ii)** Cuticular inflations show strong, red picrosirius red staining (arrowheads). **Bi, ii)** Polarised light microscopy detects the birefringence of type 1 collagen stained with picrosirius red. Red birefringence around and within the inflation shows the position of type-1 collagen bundles. However, some inflation contents remained poorly birefringent, despite the positive staining seen under brightfield illumination. Scale bars = 50 µm.

5.2.5 Expression of blister protein homologues in the anterior region of the stichosome

T. muris homologs of *C. elegans* blister proteins were identified as potential candidates to have roles in cuticular inflation development, and were targeted for RT-qPCR of their expression. Blister proteins were identified on Wormbase.org (Lee *et al.*, 2018) and *Trichuris* homologs were identified based on high sequence similarity (**Suppl. Table 5.1**). In this way, several *T. muris* homologs were identified to the genes *bli-5, bli-4* and *dpy-31*. The *T. muris* homologs identified were *tmue_1000003689, tmue_2000009363* and *tmue_2000008408*, which were designated as *tm_bli-5*, *tm_bli-4* and *tm_dpy-31*, respectively. We hypothesised that if these homologs were involved in cuticular inflation development, we would expect to see changes in their expression over the course of larval development between days 21 and 28 post-infection. This time window was used because SEM had identified these as key timepoints for the morphological development of inflations.

RT-qPCR was used to examine the expression of blister-protein homologues in *T. muris* at days 21, 23, 25, 28 and 35 post-infection. Expression of *tm_bli-5* and *tm_bli-4* did not change significantly in worms throughout the course of infection (n = 3 per group) (**Fig. 5.11 A, B**). Investigating the balance in expression between *tm_bli-5* and *tm_bli-4* was of interest, due to *tm_bli-5*'s hypothesised role as a *tm_bli-4* inhibitor. Regression analysis of expression of both genes within each sample at all time-points post-infection was carried out, showing a positive correlation between *tm_bli-5* and *tm_bli-4* expression ($y=1.32x – 2.13$, $R^2 = 0.64$, $p > 0.001$, D.F. = 14) (**Fig. 5.11 D**). Expression of *tm_dpy-31* fell as worm age increased (**Fig. 5.11 C**) ($F = 28.96$, $p > 0.001$, D.F. =13), and was significantly lower at 23 and 28 days post-infection compared to 21 days post-infection (d23 $p = 0.048$, d28 $p = 0.029$, D.F. = 9). There was a further reduction in *tm_dpy-31* expression compared to all other time-points at day 35 post-infection ($p > 0.001$, D.F. = 9).

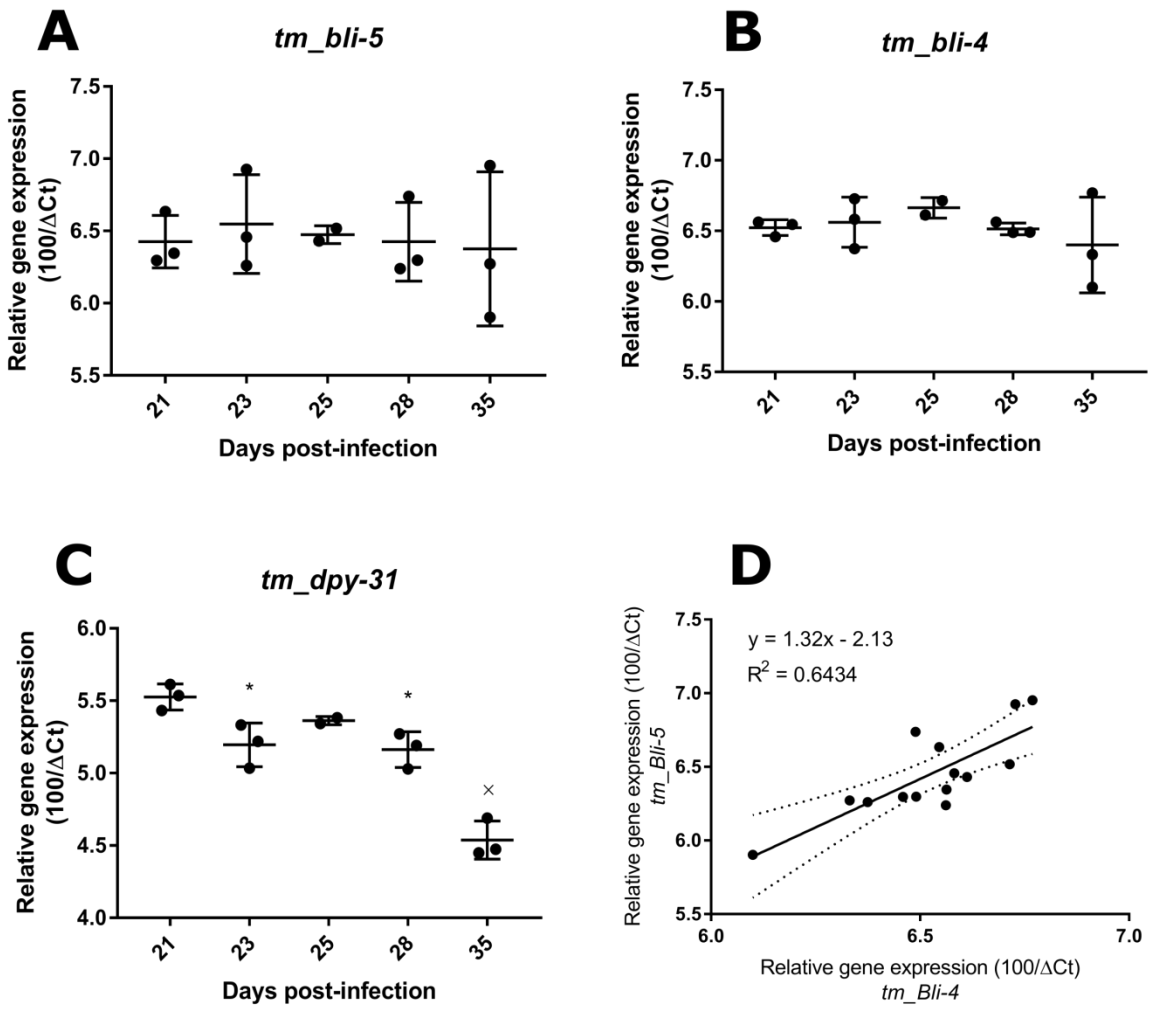

Figure 5.11: RT-qPCR showing expression of collagen-processing genes during the development of cuticular inflations in *T. muris*. Worms were extracted from the host gut at days 21, 23, 25, 28 and 35 post-infection for RT-qPCR. The anterior stichosome was dissected before RNA extraction and further processing. Six worm stichosomes were used for each sample. N = 3 for all days. Both *tm_bli-5* (**A**) and *tm_bli-4* (**B**) expression remain stable from day 21 to adulthood. **C**) *tm_dpy-31* expression dropped slightly at days 23 and 28 when compared to day 21, and was further reduced after the final moult at day 35 post-infection. (* = significantly different to day 21 PI, × = significantly different from all other days). **D**) Expression of *tm_bli-4* and its hypothesised inhibitor *tm_bli-5* were positively correlated ($y=1.32x – 2.13$, $R^2 = 0.64$, $p > 0.001$). Solid line – line of best fit. Dotted lines = 95% confidence interval.

5.3 Discussion

5.3.1 Development of cuticular inflations

SEM allowed characterisation of a coarse developmental time-course for the cuticular inflations. Based on my results it may be surmised that, cuticular inflations may be expected to develop along the stichosome within the course of around 3 days, between days 25 and 28 post-infection. However, the variety of morphologies observed especially in 25 day-old worms suggest that, like moulting, cuticular inflation development is staggered between worms (Panesar, 1989). Cuticular inflations do not appear all at once, and the observation of one or two cuticular inflations on worms taken at day 25 post-infection suggests that cuticular inflations may spread along the surface of the worm by growing individually one at a time. This refutes the supposition that the appearance of the inflations is associated with moulting, as inflation development appeared to occur between the second and third moults and not concurrently with third moult. At day 25, the inflations were found relatively far from the head, suggesting that they may appear and spread both anteriorly and posteriorly from a fixed point.

5.3.2 Ultrastructure of cuticular inflations

The ultrastructure of cuticular inflations in *T. muris* generally conformed to the observations of Wright (1975) in *T. vulpis*. Indeed, the cuticular inflation appeared to occur between the median and cortical layers of cuticle, and contained some fibrous material as seen in TEM. Additionally, the central void of the inflation described in Wright's study was also seen in *T. muris* inflations. However, several differences exist between the two studies. One difference is that in the current study not all observed inflations contained a void, especially those inflations that exhibited a collapsed morphology. In addition, in a single worm, SBF-SEM allowed the identification of both posterior collapsed and anterior convex cuticular inflations. This observation contradicts the suppositions of Wright (1975) and subsequent authors (Lopes Torres *et al.*, 2013) who postulate that the collapsed morphology was purely due to the freeze-drying process required to prepare worms for SEM. A notably absent feature of the inflations in our study was electron-dense granules present in the medial cuticle layer described in the basal region of the inflation by Wright (1975). It is difficult to understand the significance of this particular absence, but one possibility is the age of the worm used for analysis. No age is given for the *T. vulpis* imaged in Wright's study and it is therefore possible it was much older than the 35 day-old worm imaged in

my study. If so, it may be that further changes in morphology develop as the worm gets older. The morphology of worms older than day 35 may therefore be an interesting subject of further study, given that they would be a more accurate model of a worm in the situation of chronic infection which persists past 35 days. Alternately, the differences seen between *T. muris* and *T. vulpis* may simply be species-specific. Ultimately, ultrastructural imaging did not provide much further insight into the function of inflations. However, it did suggest that the mechanism of their formation may be due to changes in the regulation of collagen processing and deposition within the cuticle between moults.

The 3D imaging capabilities of SBF-SEM also unexpectedly allowed revision of the picture of sense cells in the bacillary band as proposed by Wright and Chan (1973) in the closely related trichuroid nematode *Capillaria hepatica*. In *C. hepatica*, between four and six processes are thought to originate from a "receptor cell" body just beneath the bacillary cell and project into the bacillary pores (Wright and Chan, 1973). Much like the situation described in *C. hepatica, T. muris* exhibits four sensory processes which pass through the folded apical membrane of the bacillary cell, and lie just underneath the surface of the bacillary pore. However, instead of being linked to a cell body directly beneath the bacillary cell, the sensory processes reached back from the bacillary pore to the stichocyte, forming a bundle on the way. In fact, the rest of the cells from which the sense receptors originated extended beyond the 3D imaging frame. It is not clear the extent to which our assessment constitutes a revision of nervous structure in the trichuroid nematodes as a clade, or whether the neural organisation detailed here is specific to *Trichuris muris*. Regardless, the finding does illustrate the benefits of employing a 3D EM approach which can capture and track large, dendritic structures on their journey through the tissue.

5.3.3 Composition of cuticular inflations

The cuticular inflations, upon staining with picrosirius red, appeared bright red under brightfield illumination, which is one possible indicator of collagenous composition (Junqueira *et al.*, 1979). Illumination with polarised light, showed the presence of birefringent type 1 collagen bundles within the inflations. However, some regions of the inflations remained dark indicating either an absence of sufficiently organised type 1 collagen, or perhaps that the collagen was in a different orientation relative to the sectioning plane. It may be that these birefringent regions correspond

to changes in ultrastructural organisation not detected in the EM imaging. Alternatively, it may be that collagen IV, which has been reported as red but not birefringent when stained with Picrosirius red (Bhutda *et al.*, 2017) constitutes some of the inflation interior. However, further investigation would be required to verify either situation. Ultimately, 3D imaging of collagen organisation could be attempted using a technique such as light-sheet microscopy of confocal microscopy combined with immunohistochemistry.

5.3.4 A prospective role for Blister genes in cuticular inflation development?

When Wright carried out his observations on the cuticular inflations in *T. vulpis*, he remarked that they appeared strikingly similar to the cuticular bosses present on another intra-epithelial nematode, *Gongylonema pulchrum* (Wright, 1975). His intention was perhaps to imply a shared functional role between these two species. Continuing in the spirit of this insight, I drew upon morphological similarities between, the structure of the *Trichuris* cuticular inflations and features caused by mutation of blister genes in *C. elegans.* These blisters, whilst not regularly dispersed along the surface of *C. elegans* (Peters *et al.*, 1991), nevertheless resemble the transparent convex projections of the *Trichuris* cuticle under brightfield illumination. There are two possible models of the role of blister gene homologs in *T. muris*; firstly that blister gene homologs in *T. muris* would have a direct role in both the formation and function of cuticular inflations. Secondly that blister gene homologs would be involved in only the formation of the inflation, but have no obvious functional role. In order to address either of these scenarios, it was first important assess whether any particular changes in blister gene homolog expression could be observed coinciding with the development of inflations.

Quantitative PCR of the stichosome of worms at 21, 23, 25, 28 and 31 days post-infection revealed the expression patterns of the blister gene homologs in *T. muris* over the course of larval development. No changes were observed in the expression of *tm_bli-5* and *tm_bli-4*. The *tm_dpy-31* gene did decrease slightly over the course of larval development with this most evident in 35 day-old worms compared with young worms. Overall, the decrease in *tm_dpy-31* expression were proportionally quite small compared to the level seen in day 21 and was not sustained at the day 25 time-point, which reflects the first appearance of cuticular inflations in the SEM developmental time course. It seems unlikely therefore that the overall trend for a decrease in in *tm_dpy-31* expression during larval development would be responsible for

inflation development. Ultimately, the research tool most useful in determining the influences of such differentially-expressed genes during development would be transgenic worms, in which the blister gene homologs were knocked out. Whilst not available in the case of *T. muris*, this study provides a hypothetical framework for future investigation, and indeed demonstrates that quantitative analyses of blister-gene expression are indeed possible in *T. muris.*

In light of the results detailed in this chapter, a productive direction of future investigation may be the identification of other *C. elegans* blister gene homologs and analysis of their role in *T. muris* development. Specifically homologs of the blister genes *bli-1*, *bli-2*, *bli-3* and *bli-6* and their regulators could be investigated. These blister genes all have roles in cuticular development. The *bli-1* and *bli-2* genes both encode collagen IV chains (Johnstone, 2000), which are commonly found in the basement membranes surrounding cells. The *bli-3* gene is an NADPH dual oxidase involved in the cross-linkage of collagen within the worm cuticle (Edens *et al.*, 2001; Simmer *et al.*, 2003). The *bli-6* gene hypothetically encodes collagen XXI (The C. elegans Sequencing Consortium, 1998), which interestingly is most well-known as an extracellular matrix component of blood vessel walls, which nematodes lack. The *bli-4* and *bli-5* genes were an attractive choice for preliminary investigation because they encoded both a serine protease and a serine protease inhibitor respectively (Peters *et al.*, 1991; Stepek *et al.*, 2010). Both of these types of protein are highly over-represented in the *T. muris* genome and have been speculated to have immunomodulatory function (Foth *et al.*, 2014). We hypothesised that an imbalance between serine-protease and serine-protease inhibitor activity may be responsible for cuticular inflation formation. However, the expression of both genes changed proportionally throughout development, indicating no changes in balance. Whilst it is possible that no direct functional link between blister genes and cuticular inflations will be identified, their potential regulatory roles may be informative into the nature of the host-parasite interactions occurring at the inflations.

5.4 Conclusions

Using a variety of imaging approaches, this work helped clarify the structure and morphology of cuticular inflations in *Trichuris muris*, and suggested novel mechanisms behind their formation. SEM showed that the majority of cuticular inflations develop between days 25 and 28 PI. The use of microCT-steered SBF-SEM updated our understanding of the structure of cuticular inflations and surrounding structures. Contrary to previous literature, inflations presented both a collapsed and inflated aspect in the same worm, which was determined by the presence or absence of a fluid-filled void. The presence of a fibrous layer between the median and cortical cuticle layers was observed and histology confirmed a collagen component in cuticular inflation composition. In addition, we identified novel organisation of the sensory cells underlying the bacillary band. In future, a much more detailed assessment of cuticular inflation composition is required. Data from SBF-SEM, whilst comprehensive, still provided no obvious clues to function, and the cells underlying the inflations seem to lack extensive RER and are unlikely to be secretory. However, the changes in cuticle structure within the inflations suggest that genes involved in collagen processing maybe involved in inflation formation. Therefore, blister protein homologs remain intriguing genetic targets for future research.

Supplementary information

Gene name *C. elegans*	wormbase URL	*T. muris* homolog	designation in this chapter	wormbase URL	% similarity
bli-4	https://www.wormbase.org/species/c_elegans/gene/WBGene00000254#06-9g5-3	*tmue_2000009363*	*tm_bli-4*	https://www.wormbase.org/species/t_muris/gene/WBGene00286114#06-9g5-3	88.1
bli-5	https://www.wormbase.org/species/c_elegans/gene/WBGene00000255#06-9g5-3	*tmue_1000003689*	*tm_bli-5*	https://www.wormbase.org/species/t_muris/gene/WBGene00287687	80.2
dpy-31	https://www.wormbase.org/species/c_elegans/gene/WBGene00006592#06-9g5-3	*tmue_2000008408*	*tm_dpy-31*	https://www.wormbase.org/species/t_muris/gene/WBGene00300269#06-9g5-3	84.6

Supplementary table 5.1: Names, reference URLs and % similarity of *C. elegans* blister genes and their homologs in *T. muris*. Information taken from wormbase.org

Blank Page

6. 3D characterisation of the hepatic and intestinal granulomas of *Schistosoma mansoni*.

Contributions

James O'Sullivan carried out all microCT, histology and interpretation and analysis of images.

Professor Andrew MacDonald (MCCIR, the University of Manchester) provided feedback and advice on experimental concepts and results.

The University of Manchester Bioimaging core facility imaged histological slides

Dr Teruo Hashimoto sectioned dried samples and carried out Energy Dispersive X-ray Spectroscopy (EDX)

6.1 Introduction

Schistosoma mansoni is the most widespread of the schistosomes (Chitsulo *et al.*, 2000), which as a genus are estimated to infect almost 200 million people worldwide (Vos *et al.*, 2017). The resulting infection, called schistosomiasis, causes significant pathology and mortality (Colley *et al.*, 2014). Adult *S. mansoni* take residence in the portal vein and mesenteric venules and shed eggs that are passed through the vessel and the underlying gut wall. Once in the gut the eggs can be passed out into the faeces where the life cycle will continue. The passage of the eggs through the gut wall is facilitated by the formation of an immune granuloma in the intestinal wall (Costain *et al.*, 2018). Chronic pathology of schistosomiasis is caused by the deposition of eggs within tissues which induce inflammatory granulomas with the eggs as foci. Morbidity in humans infected with *Schistosoma mansoni* can be caused by eggs failing to migrate through the intestinal wall on their way to the intestinal lumen (Lambertucci *et al.*, 2005). However, the greatest source of mortality is hepatic schistosomiasis, in which the eggs which are ectopically deposited within the liver tissue (Wilson *et al.*, 2011). The inflammation and fibrosis characteristic of the liver granuloma causes downstream portal hypertension which can lead to ascites and oesophageal varices (Graham *et al.*, 2010).

Histological assessment of egg-induced granulomas and fibrosis has been important in investigating immunity to schistosomiasis (Villar *et al.*, 2014) and efficacy of drug candidates (Diab *et al.*, 2015; Elhenawy *et al.*, 2017) in mouse models. Quantitative studies of the granuloma have employed stereoscopic methods which extract size and volume information

from 2D slices, assuming spherical granuloma shape as well as their homogeneous distribution throughout tissue (Souza *et al.*, 2011; Sombetzki *et al.*, 2015). *S. mansoni* is one such model which infects and exhibits pathology in both mice and humans (Andrade, 1987), therefore providing a tractable animal model in which to investigate both the migration of eggs through the gut and their contribution to pathology in the liver. In hepatic schistosomiasis, eggs obstruct the blood vessels in which they get trapped (Andrade and Cheever, 1971) and promote angiogenesis in the surrounding tissue (Andrade and Santana, 2010). However, the contribution of this vascular remodelling to the development of downstream pathology is unclear. Whilst studies have assessed the vascular remodelling events qualitatively using corrosion casts of vasculature (Andrade *et al.*, 2006), more quantitative approaches would doubtless be helpful in investigating the contribution of vascular remodelling to pathology. Imaging and quantification of vascular morphology using perfusion of contrast agents to isolate vessel morphology is a well-established technique in microCT (Masyuk *et al.*, 2003; Ananda, 2006; Dunmore-Buyze *et al.*, 2014; Schaad *et al.*, 2017), although it has not yet been used in the context of hepatic or intestinal schistosomiasis. However, contrast of the vasculature in isolation is not just important to achieve; additionally, changes in vascular morphology should be related to the causative inflammation and fibrosis in the surrounding liver parenchyma. Corrosion casting or vascular perfusion with contrast agents such as Microfil would preclude taking this information. Therefore there is a rationale for generating an alternative approach which enables contrast in both the granulomas and the liver vasculature. In addition, the problem of schistosomiasis pathology is truly multiscale in nature, as both the smallest vessels (sinusoids) and the hepatic artery and portal vein experience remodelling. Consequently, effective imaging at multiple scales is required.

Aside from hepatic pathology, microCT provides a novel opportunity to investigate egg traversal through the intestinal wall. In mice, *S. mansoni* preferentially travels through the wall of the small intestine (Saoud, 1965; Tiboldi, 1979). Very little is known about the process of egg migration through the intestinal tissues, perhaps in part due to difficulty in tracking egg location within using histological techniques (Costain *et al.*, 2018). Using microCT represents an excellent opportunity for investigation egg migration in the intestine (and indeed other tissues such as the liver), because a correlative approach may be taken in which the sample is mapped prior histology, thus allowing a guided sectioning process.

The work of this chapter has the following aims:

1) To develop microCT methodology to observe morphological changes within the liver and intestine caused by *S. mansoni* infection, including vascular remodelling and granuloma formation.
2) To exploit the 3D imaging capabilities of microCT to survey egg migration across the small intestine.

In order to observe gross morphological changes in the liver throughout infection, iodine contrast-enhanced microCT was used, alongside a specialised segmentation approach, to visualise changes in granulomatous inflammation and vascular structure at weeks 8 and 14 post-infection (PI). The results of microCT imaging were compared to those from conventional histochemistry to determine the efficacy of the approach. High resolution phase-contrast microCT was used to inspect liver tissue morphology and composition at a higher level of detail at both week 8 and week 14 PI. Finally, correlative microCT was used correlatively to steer histological imaging of the egg traversal through the wall of the small intestine, in order to visualise the cellular surroundings of eggs at different stages in their migrations.

6.2 Results

Experimental Protocols, including details of sample acquisition, processing, imaging and analysis are outlined in the methods, chapter 3.

6.2.1 Visualisation of gross morphology in the *Schistosoma mansoni*-infected liver

In livers taken from animals throughout infection, iodine staining provided sufficient contrast in slices to show differential morphology between naïve animals (**Fig. 6.1A, Supplementary Movie 5**), infected animals at 8 (**Fig. 6.1B, Supplementary Movie 6**) and 14 weeks post-infection (PI, **Fig. 6.1C, Supplementary Movie 7**) (n = 1 for each infection time-point). At 8 weeks PI, granulomas were visible as darker areas of lower attenuation than the surrounding parenchyma (**Fig. 6.1D**). The granulomas were amenable to segmentation using Avizo's Adaptive Thresholding module and could be visualised separately in 3D (**Fig. 6.1E**). In scans of the right lobe at higher magnification, these areas of lower attenuation were confirmed as granulomas because they correlated with both immune cell infiltrates and fibrosis as seen in histological sections (**Fig. 6.2**). At all time-points post-infection, vascular structures were evident

as areas of even lower attenuation than the granulomas. At 8 weeks PI, some areas of high attenuation were present within granulomas; however comparison of X-ray slices with Haematoxylin and Eosin stained tissue slices revealed that eggs observed in tissue slices did not correlate with the areas of high attenuation in X-ray slices (**Fig. 6.2**).

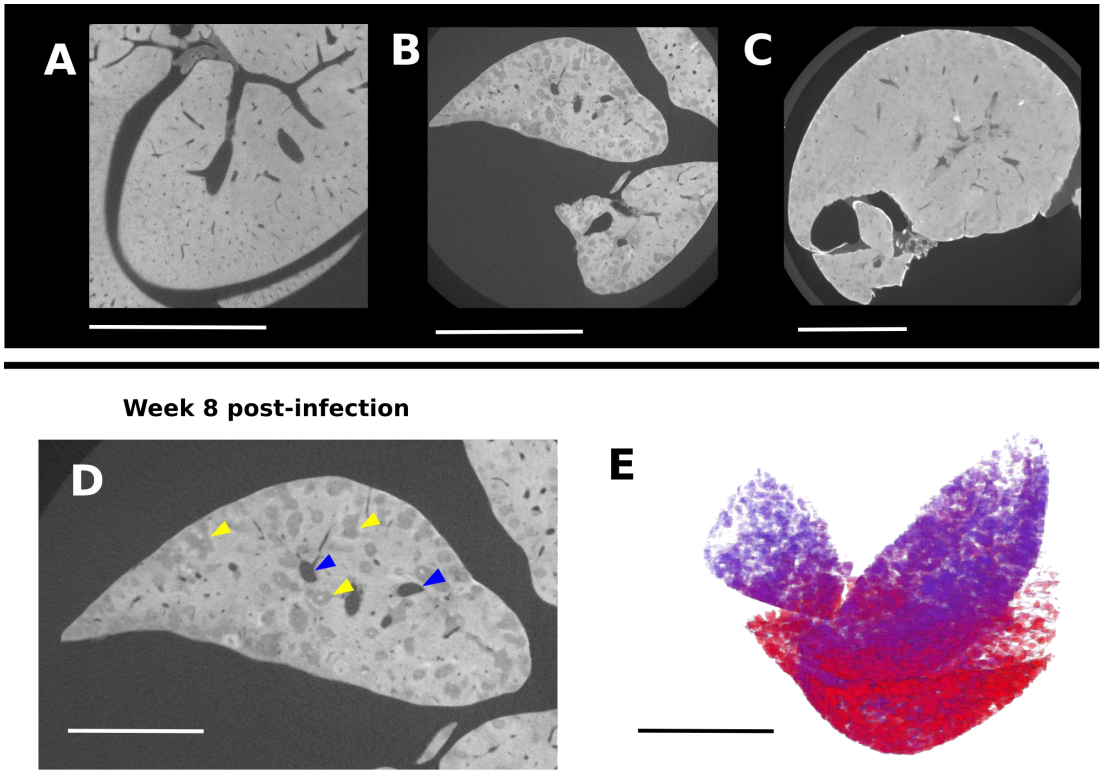

Figure 6.1: Diffusible Iodine Contrast Enhanced MicroCT of the gross morphology and architecture of the liver and lobes. Mice were infected with *S. mansoni* and the livers visualised at weeks 0 **(A)**, 8 **(B)**, and 14 **(C)** post-infection by microCT using diffusible iodine contrast (n = 1 mouse per time-point). **(D)** At week 8 post-infection, granulomas were visible as areas of reduced attenuation compared to the surrounding parenchyma (yellow arrowheads point to granulomas). Vasculature (indicated with blue arrowheads) from which the blood had been drained was the same grayscale value as the empty space surrounding the sample. **(E)** The areas of granulomatous inflammation at week 8 PI were segmented and rendered as a volume. The changing colour of the volume rendering represents a change in greyscale value associated with inconsistent staining. Scale bars (**A-C**) = 1 cm, **(D)** = 500 µm, **(E)** = 1 cm.

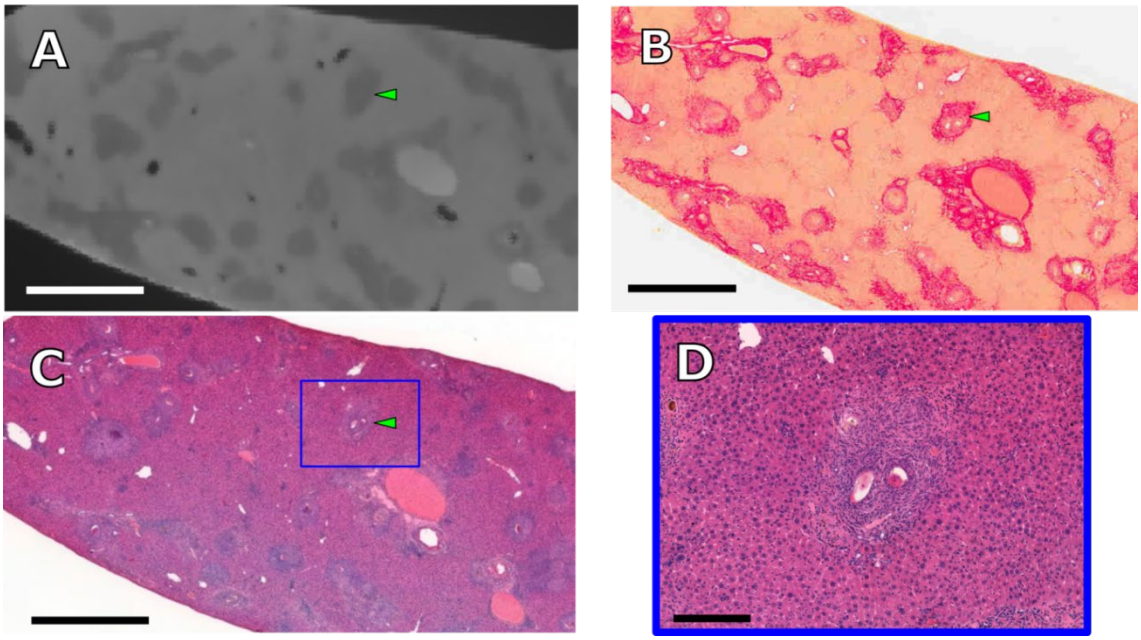

Figure 6.2: Scans of the liver right lobe showing morphology at 8 weeks post-infection with *S. mansoni*. The lower-attenuating regions of the parenchyma in the X-ray data **(A)** were confirmed as the granulomas by using a correlative imaging approach in which the sectioning was guided by microCT data. Picrosirius red staining **(B)** showed that deposition of collagen also correlated with the dark regions. Haematoxylin and Eosin staining **(C)** showed that the granulomas (purple) correlated with dark regions of the microCT image, however, the presence of eggs (green arrow), while obvious in H&E, was not present in the microCT slices. **D)** Magnified panel showing egg as seen in **(C).** Scale bars **(A-C)** = 1 mm, **D** = 400 µm.

In the liver taken at week 14 PI, granulomas were less-well contrasted against the surrounding parenchyma compared with week 8 PI (**Fig. 6.3D**). This weaker attenuation precluded segmentation using the adaptive thresholding technique applied for granulomas at week 8 PI. However, the locations of adult worms were clearly visible in the portal vasculature (**Fig 3D**). Segmentation carried out according to the protocol details in the methods section (**Chapter 3, Figure 1**) allowed the vasculature at 0, 8 and 14 weeks PI to be visualised independently (**Fig. 6.3A-C**). Diminished branching in the vasculature was observed over the course of infection. It was not possible to adequately smooth segmented vasculature images however which precluded quantitative analysis of branching, as rough surfaces produced ectopic branches in the centreline tree algorithm. In addition, the immersion fixation protocol was less able to eliminate blood from the vasculature at 14 weeks PI. Residual blood was identifiable as areas of high attenuation (**Fig. 6.3D**), which resulted in an underestimated segmentation of vasculature in the 14 week PI tissue.

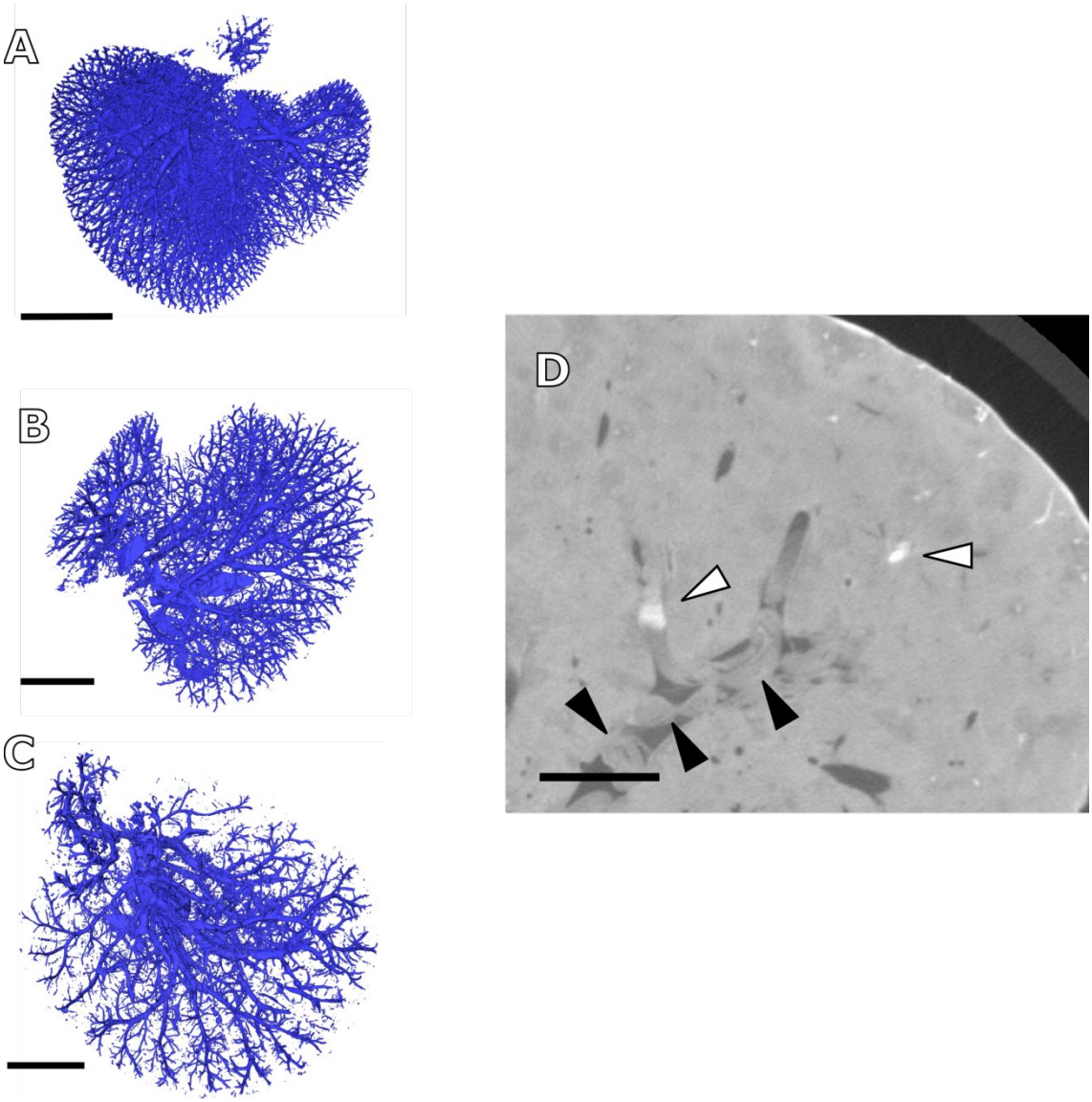

Figure 6.3: Segmentation of vasculature showing reduced vasculature morphology over the course of infection. Mice were infected with *S. mansoni* and the livers visualised at weeks 0 **(A)**, 8 **(B)**, and 14 **(C)** post-infection by microCT using diffusible iodine contrast (n = 1 mouse per time point). **(A)** Volume rendering of vasculature at week 0, showing the highest amount of branching. In comparison there was reduced branching at week 8 post-infection **(B)** and highly reduced branching at week 14 PI **(C)**. Adult worms could be seen in the portal vasculature (black arrowheads, **D**). There are also areas of high attenuation suspected to be blood remaining within the vasculature (white arrowheads), which prevent a complete segmentation of vasculature. The volume rendering in **C)** is therefore an underestimation of the true branching topology. Scale bars A, B, C = 500 μm. D = 100 μm.

6.2.2 High-resolution phase-contrast imaging reveals calcified eggs

In order to visualise vascular and egg morphology in more detail, higher resolution imaging of the liver parenchyma at week 8 post-infection was attempted (**Fig. 6.4A-C**). The liver sinusoids were visible, and individual eggs could be counted within areas of slightly reduced attenuation that corresponded to the granulomas (**Fig. 6.4B**). Whilst the vascular morphology could be observed, resolution at this field of view was too coarse to allow segmentation and mapping of the sinusoids. In livers taken at week 14 post-infection, variation in the X-ray attenuation of eggs was observed which was not present in the sample taken at week 8 PI (**Fig. 6.5**).

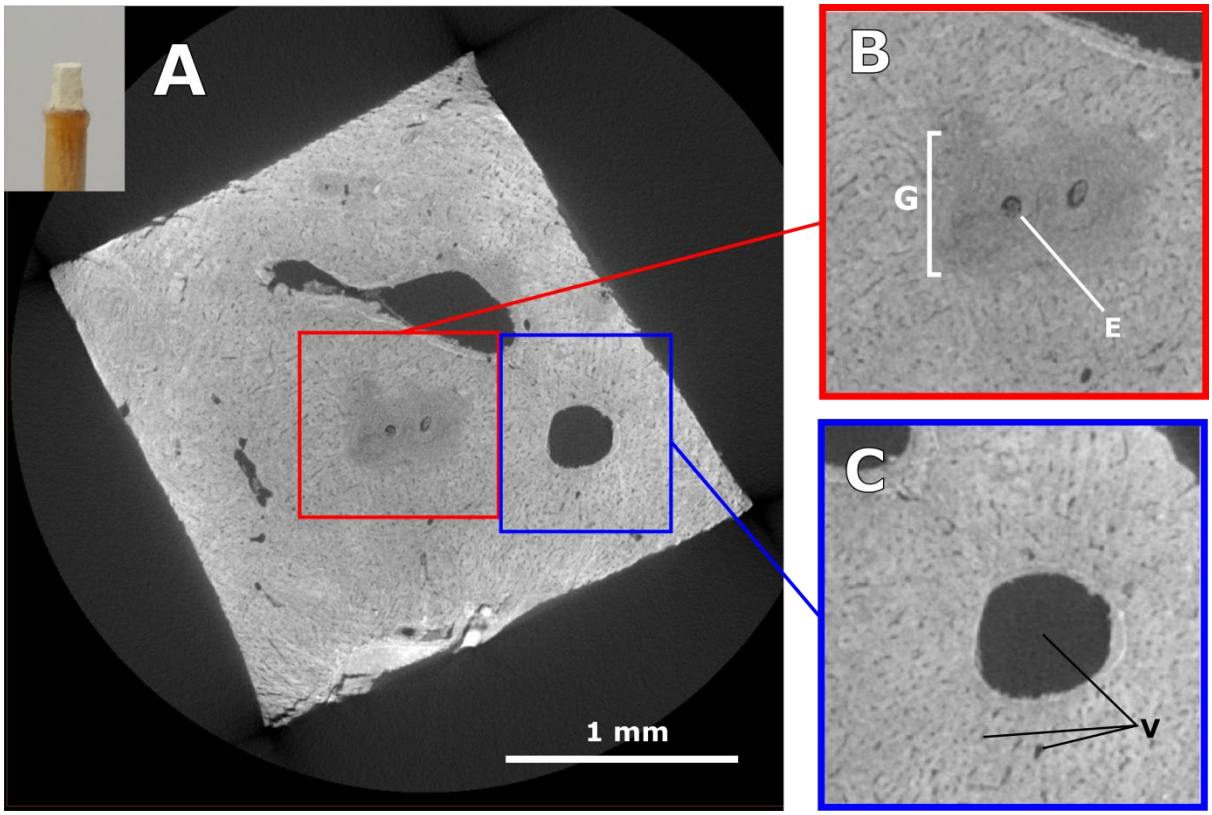

Figure 6.4: High resolution microCT of dried liver tissue showing fine vascular and egg morphology. (A) Ortho-slice of the stained and dried tissue (see inset), showing bright, X-ray-dense parenchyma. Two regions of interest are highlighted (scale bar 1mm). **B**) Region of interest showing a multi-egg granuloma containing two eggs (E) surrounded by the egg granuloma (G), which is slightly less X-ray dense than the healthy parenchyma. **C**) Region of interest showing vasculature (V) including a vein (large dark region) and sinusoids. N = 1 mouse.

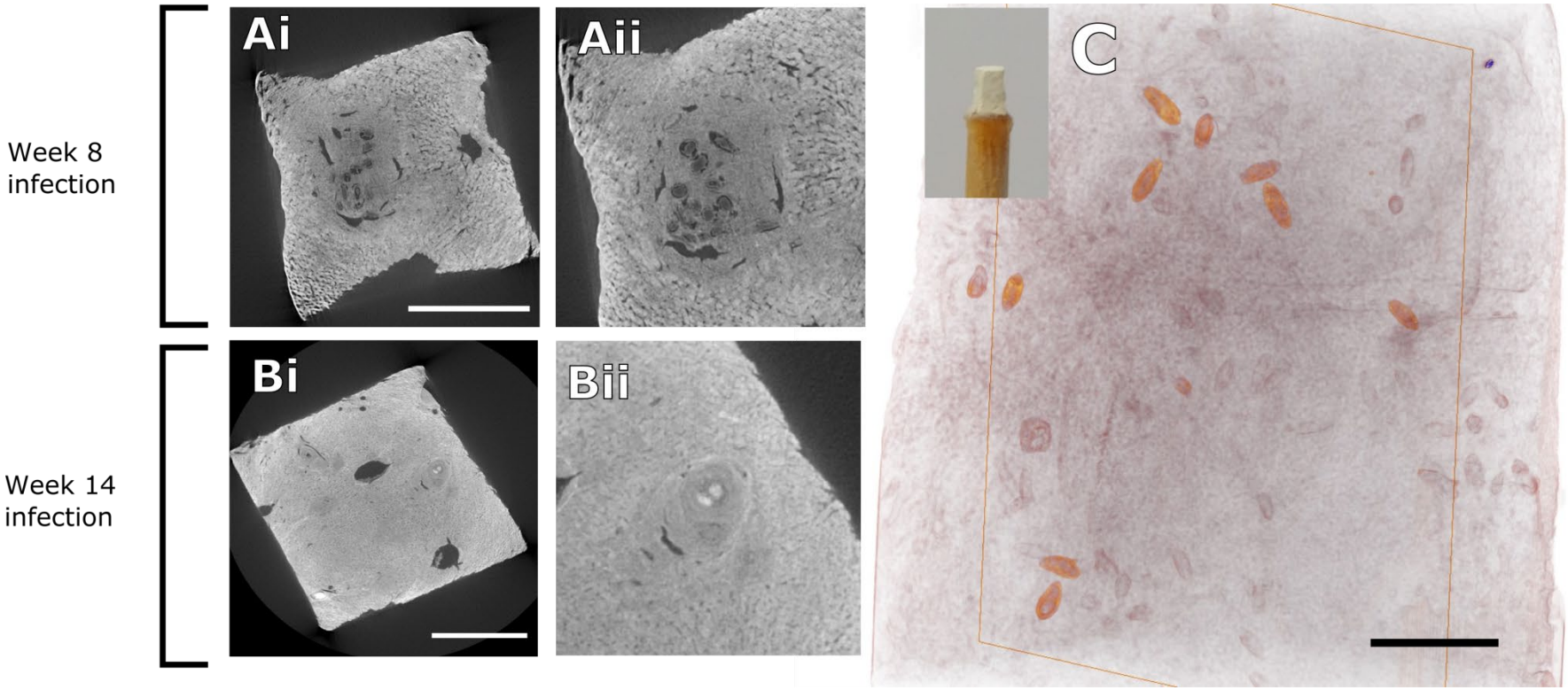

Figure 6.5: High resolution microCT showing differences in egg density in between week 8 and week 14 post-infection. Ai + ii) Slices from chemically dried liver fragments from mice infected with *S. mansoni* show that eggs at week 8 post-infection show a lower X-ray attenuation than the surrounding egg granuloma (n = 1 mouse). **Bi + ii**) Slices show that in tissue taken at week 14 post-infection, a subset of eggs demonstrate a higher level of X-ray attenuation than the surrounding egg granuloma (n = 1 mouse). **C**) Volume rendering of liver tissue taken at week 14 post-infection (inset). Bright orange eggs are those which exhibit a higher X-ray density. Scale bars A and B = 1 mm, C = 500 μm.

In order to investigate whether calcification had occurred in the dense eggs, we used a guided approach which used the microCT data to guide ultramicrotomy to reach an appropriate depth for Energy Dispersive X-ray Spectroscopy (EDX). EDX of the cut sample identified that the dense eggs within the week 14 sample were rich in calcium and phosphorus compared to the surrounding tissue and therefore considered calcified (**Fig. 6.6**). In order to thoroughly determine whether any calcification at all took place in eggs at week 8 post-infection, we analysed eggs from the liver of an infected mice at week 8 PI. Eggs were fractionated based on their density, embedded an agar and analysed by X-ray tomography. In contrast to the eggs seen in the tissue of mice infected with *S. mansoni* at week 14 PI, there was no increase in X-ray attenuation of eggs (**Fig. 6.7**). These data suggest that the eggs from mice at week 8 PI were not calcified. However, a positive control sample of fractionated eggs from a liver taken at week 14 PI would allow additional verification of these results.

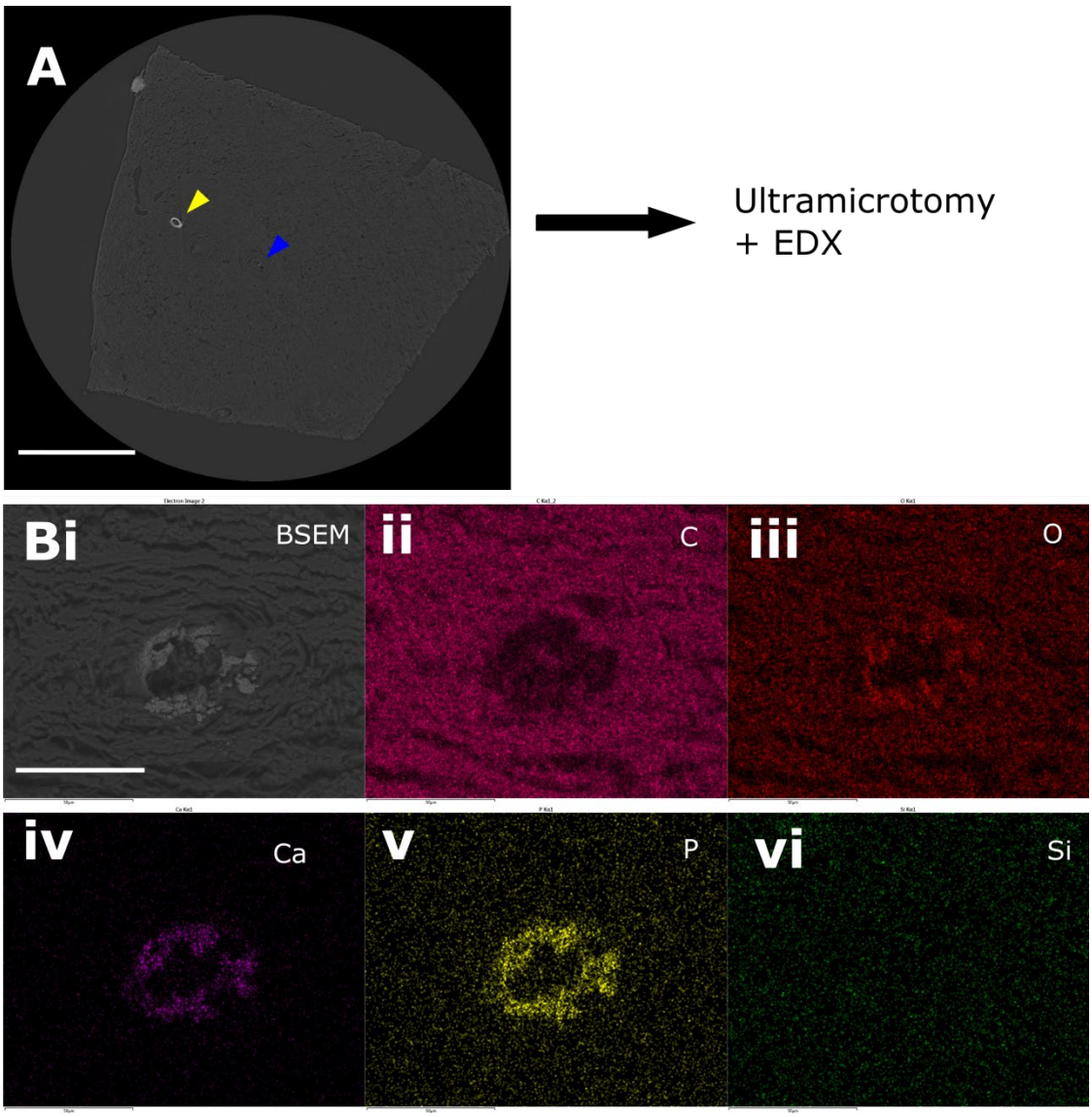

Figure 6.6: X-ray guided BSEM and an EDX analysis confirms calcification of eggs within the liver. A) MicroCT slice showing the location of the high-density egg (yellow arrowhead) and a low density egg (blue arrowhead) (n = 1 mouse). To reach the egg, the top 500 µm of the sample was milled using an ultramicrotome with a diamond knife. **B**) BSEM and EDX analysis of the sample. **Bi)** in agreement with XRM data, the egg corresponds to an area of higher electron density in the BSEM. **Bii – vi)** EDX channels show increased localisation of calcium (**iv**) and phosphorus (**v**) to the electron-dense area, confirming the mineralised composition of the egg. Notably, a small amount of Silicon was detected within the tissue, indicating retention of HMDS within the tissue sample after the drying process. Scale bar A = 500 µm, B = 50 µm.

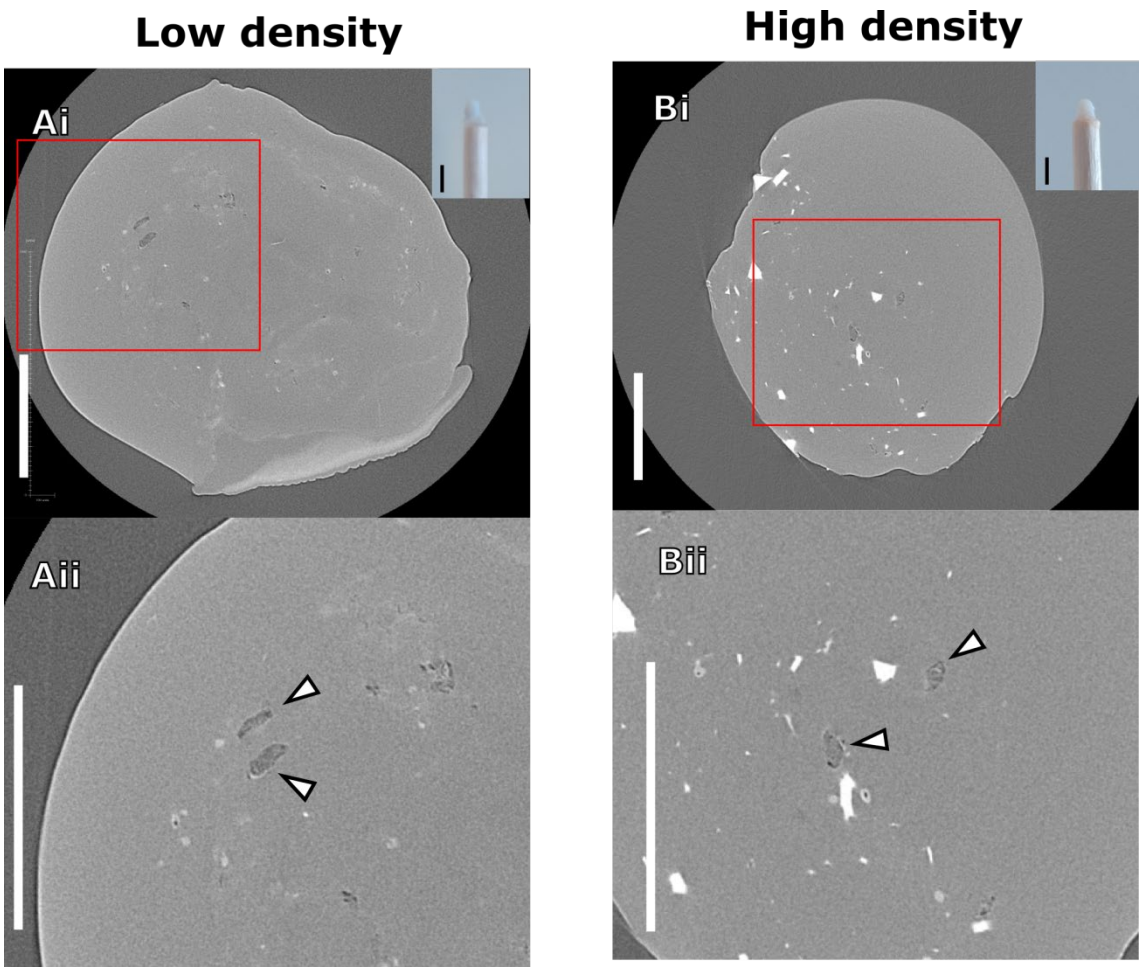

Figure 6.7: MicroCT of agar-embedded eggs from a week 8 post-infection liver of a mouse. **Ai)** transverse slice through the agar-embedded eggs shows their location as areas of slightly reduced attenuation compared to the surrounding agar. **Aii)** Magnified view of low-density eggs (white arrowheads) showing their low attenuation compared to surrounding agar (n=1 mouse). **Bi)** Transverse slice showing high-density embedded eggs, with magnified view in **Bii.** Eggs (white arrowheads) were lower density than surrounding agar, and were surrounded by high-density debris the morphology of which did not correspond to eggs (n = 1 mouse). Scale bars **A** and **B** = 500 μm, insets = 2 mm.

6.2.3 Egg egress from the intestine

Schistosome egg egress through the intestinal wall remains relatively poorly understood. Correlative microCT-histology allowed histological assessment of eggs at different points in their traversal across the intestinal wall (**Fig. 6.8**). Ileum fragments were dissected and embedded in paraffin wax. The edge of the tissue was milled using a microtome to produce a flat surface, which would assist in aligning the histological slices with microCT data upon re-embedding. Excess wax surrounding the tissue was then cut away. Phase contrast (propagation-based) imaging of paraffin-embedded tissue allowed identification of eggs at various stages of egress (**Supplementary Movie 8**), from those located submucosally (**Fig. 6.9A**) to those found within areas closer to the epithelium seemingly including the lamina propria (**Fig. 6.9B**). Expressed as averages (±standard deviation) across n = 3 experimental mice, 28.67 ± 7.76 eggs were found in the ileum muscular layer, 47.00 ± 6.16 in the submcuosa, and 4.67 ± 0.94 in the lamina propria. No eggs were visible in the epithelial layer. The ileum fragments were re-embedded and sectioned in a manner that captured the eggs seen in the microCT data. Haematoxylin and Eosin staining (**Fig. 6.9**) verified the locations of egg granulomas in the submucosa and lamina propria. It was not possible to distinguish granulomatous inflammation from the surrounding healthy tissue in the microCT images. However, while eggs in the submucosa were always observed to be surrounded by granulomas, one egg found to be migrating up through the centre of the villus exhibited greatly reduced granular inflammation (**Fig. 6.9B ii, inset**).

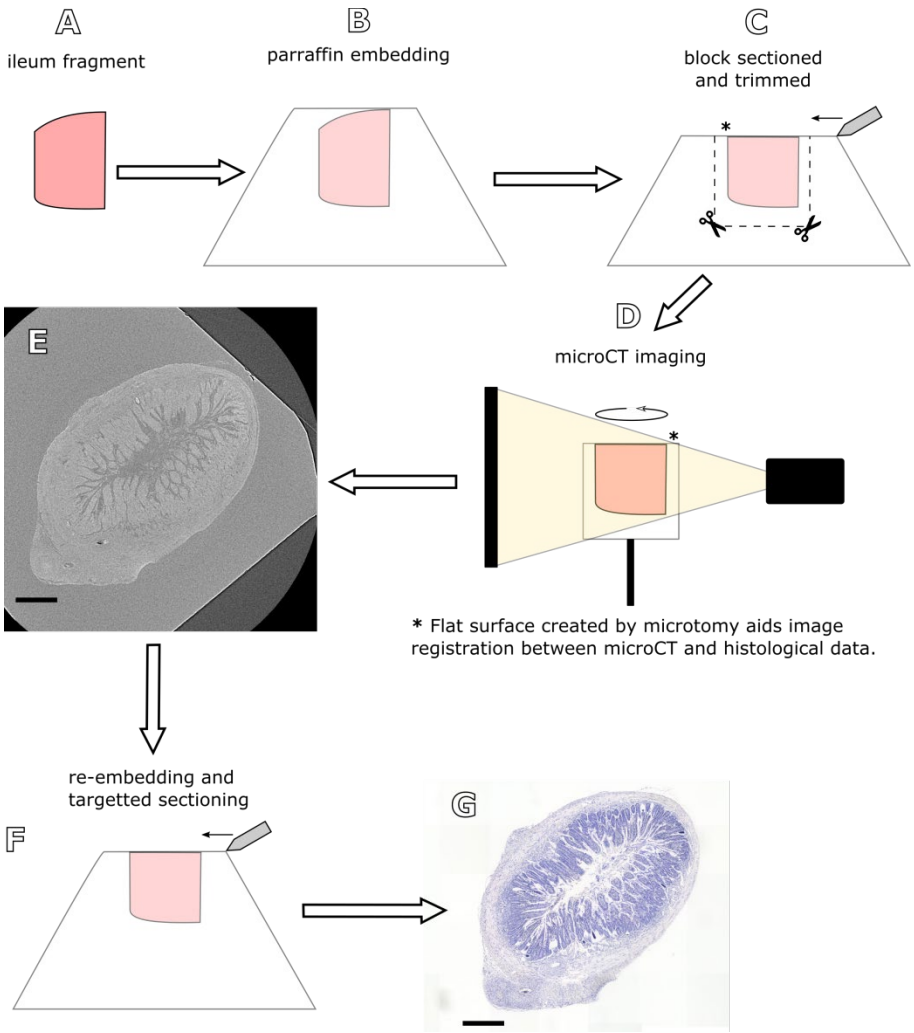

Figure 6.8: Schematic workflow showing the process by which microCT is used to guide histological sectioning targeting *S. mansoni* eggs traversing the mouse ileum. Mouse ileum was dissected and fixed 8 weeks post-infection. The ileum was paraffin embedded ad subjected to a correlative workflow. **A**) A fragment of ileum was dissected. **B**) Embedding in paraffin wax. **C**) A microtome is used to create a flat edge on the sample, which assists in registration of histological and microCT images, and a razor blade is used to remove excess wax from around the tissue. **D**) The block is imaged by microCT. **E**) Regions of interest for subsequent histological investigation are identified in the microCT slices. **F**) The sample is re-embedded and using the X-ray data as a guide, is sectioned to specific regions were eggs of interest are present. **G**) Slices are stained with Haematoxylin and Eosin. Scale bars in E, G = 400 µm

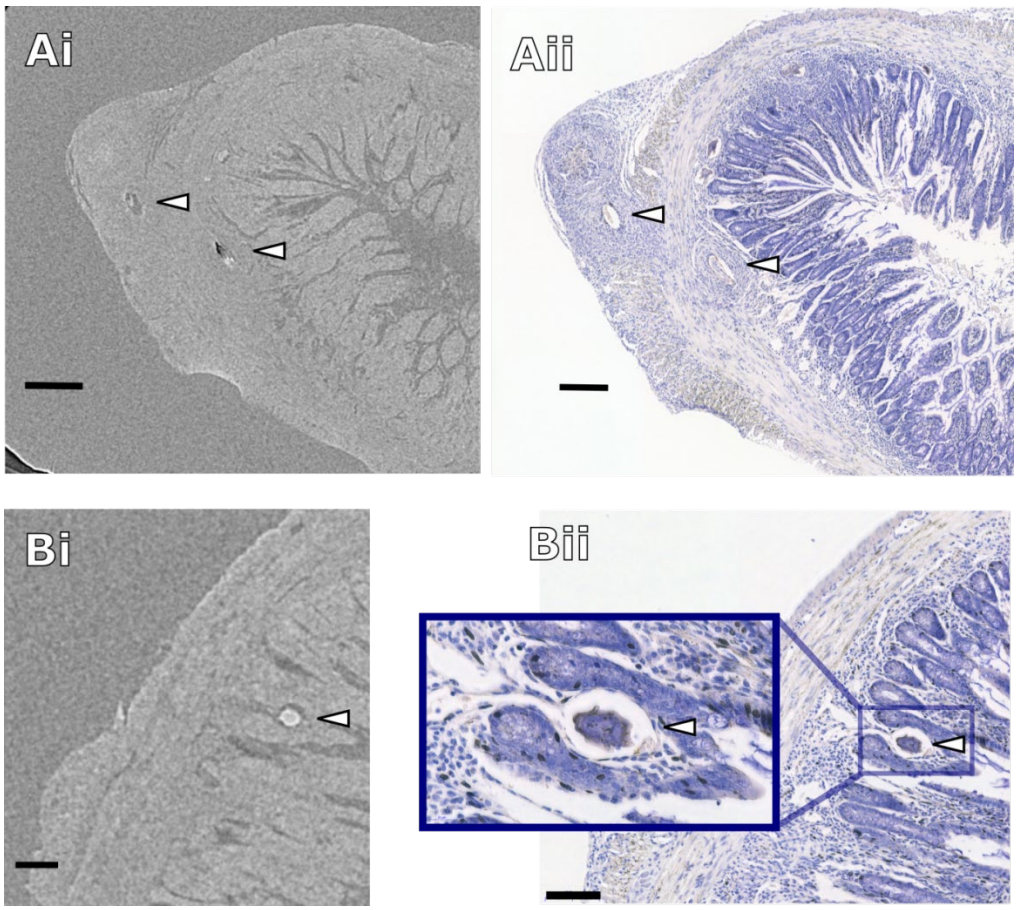

Figure 6.9: Correlative microCT and histology of eggs at various points during their migration across the small intestine wall. Fragments of small intestine taken 8 weeks post-infection were fixed and embedded in paraffin before being prepared for microCT imaging. After microCT, the samples were then re-embedded in paraffin wax and sectioned, with slices being taken at the locations of eggs. H&E revealed the cellular surroundings of the eggs in more detail. **Ai)** Eggs are shown outside the muscular layer of the small intestine, and within the submucosal layer (white arrowheads). **Aii)** When the same eggs are located using guided microtomy, Haematoxylin and Eosin staining shows granulomatous inflammation around eggs in both of these layers (white arrowheads). **Bi)** Only one egg (white arrowhead) was visible in the villi of the small intestine. **Bii)** Haematoxylin and Eosin staining of this egg (white arrowhead) revealed its location in the lamina propria, along with a lack of granulomatous tissue surrounding it (inset). Scale bars A = 200 μm, B = 100 μm.

6.3 Discussion

6.3.1 MicroCT allows visualisation of *Schistosoma mansoni*-induced pathology

Immersion staining with iodine is a commonly used technique in biological microCT (Gignac *et al.*, 2016). Since iodine diffuses quickly and deeply compared to many other stains (Pauwels *et al.*, 2013), it was an obvious choice for imaging whole livers of schistosome-infected mice. In the livers of naïve mice, and those of mice at week 8 and 14 post-infection, the contrast achieved was suitable for visualising some elements of pathology, and ineffective for others. In naïve mice, clear contrast between healthy parenchyma and vasculature allowed for straightforward and complete segmentation of vasculature. Blood had completely drained from the tissue during fixation and immersion staining, and the ability of the vasculature to be seen and segmented was limited only by image resolution. At week 8 post-infection, granulomas were clearly visible alongside vasculature as areas of lower attenuation. These areas of low attenuation correlated well with both granulomas and fibrosis, as observed when compared with paraffin-embedded histology. However, it is not entirely clear the extent to which the reduction in X-ray attenuation is attributable to either fibrosis or cellular infiltrate. Preferential iodine staining of the hepatocytes of the liver parenchyma may perhaps be due to an elevated lipid component of hepatocytes. Indeed, iodine is highly soluble in non-polar solvents (e.g. McDowell, 2000), including lipids. Areas of bright attenuation within the granuloma were of unknown composition. However, the filamentous forms of these bright regions suggest that blood, trapped within the granuloma and stained strongly with iodine, may be responsible.

Using an adaptive thresholding approach, the granulomas could be segmented and visualised in 3D. In future, the extent of granulomatous inflammation in the tissue as a whole could be assessed quantitatively using this method. An analysis of the inflammation in 3D would bypass the need for time-consuming stereological approaches currently used to assess schistosome pathology. These approaches involve randomly sampling tissue, assuming a spherical granuloma shape (Souza *et al.*, 2011), and neglecting multi-egg granulomas (Smith *et al.*, 2009; Souza *et al.*, 2011; Alves *et al.*, 2016). In fact, granuloma diameter is still a common metric for measuring granuloma size, despite their irregular shape (Diab *et al.*, 2015; Elhenawy *et al.*, 2017). At week 14 post-infection, segmentation of granulomas was not possible, due to poor contrast between granulomas and surrounding parenchyma. The reduced contrast may be

associated with reduced granuloma size, reduced necrosis and reduced eosinophilia which occurs later in infection (Andrade and Warren, 1964). Given that fibrosis is still characteristic of granulomas later in infection (Andrade and Cheever, 1993), a reduction in immune cellular infiltrate may indeed be responsible for the reduction in contrast.

The segmentation approach for vasculature detailed in **chapter 3, figure 3.1** proved effective at segmentation of the lower-attenuation regions of vasculature emptied of blood. The effective segmentation of vasculature in the naïve animals highlights that iodine staining, coupled with more sophisticated segmentation approaches than global thresholding effectively facilitates vascular visualisation comparable to levels of those achieved through corrosion casting (Andrade and Santana, 2010). Decreases in vascular branching were observed over the course of infection, however more detailed inspection of slices at week 14 post-infection revealed that blood had likely still remained within the vessels. The remaining blood was brightly stained and was therefore not included in the segmentation as it was outside of the range of selected greyscale values, resulting in an underestimation of branching. Compared to naïve tissue, the retention of blood may in part be attributed to vascular obstruction both by egg granulomas and the adult worms themselves. Therefore, the staining and segmentation techniques used in this chapter are not well-suited to quantifying branching topology of the whole vascular tree over the course of infection. However, retention of blood and reduced branching as detected by the segmentation approach may instead be a useful proxy measurement for the extent of egg-induced vascular blockage events, thus still providing a useful readout of vascular function. If imaging of the full portal vasculature is required, flushing of the vasculature by perfusion of saline solution *post-mortem* may assist future attempts at a complete vascular segmentation. Perfusion with a vascular contrast agent may also increase the appearance of homogeneity in the vasculature for future microCT images. However, this may come at the expense of contrast with the surrounding iodine-stained parenchyma which would constitute a further challenge to vascular segmentation. A solution to this issue may be using dual energy computed tomography approach, such as that taken by Handschuh et al. (Handschuh *et al.*, 2017). Dual energy imaging would facilitate the separation of parenchyma and vasculature based on the elemental composition of staining species, therefore enabling a more accurate segmentation. However, a dual energy CT approach may introduce further challenges, such as morphological artefacts including bubbling introduced by the perfusion stain (Masyuk *et al.*, 2003; Den Buijs *et al.*, 2006;

Mondy *et al.*, 2009). Overall, the challenges encountered in the current study have prevented attempts at quantitative analysis of branching and thickness distribution using tools such as skeletonisation. However, future refinement of the imaging approach could help quantification of granulomatous inflammation alongside gross vascular remodelling in the whole organ.

If sufficiently precise vascular segmentations can be achieved, *in silico* blood flow modelling may also be a useful tool in examining the functional changes to the liver circulation post-infection. However, there are key organ-specific methodological considerations to be taken into account including the mechanical interaction of organs with surrounding tissue (Zagorchev *et al.*, 2010), meaning large work-up would be required. 3D structure of the vascular tree and blood flow modelling are approaches which could be applied to a variety of other schistosomiasis-related questions. For example, treatment with the anthelminthic drug Praziquantel and inhibited Notch signalling both independently reduce the volume of granulomatous tissue in the livers of infected mice (Yepes *et al.*, 2015; Zheng *et al.*, 2016), but little is known regarding the extent to which vascular morphology could return to a pre-infection state in the case of such ameliorative treatments. Quantitative analyses of vascular morphology as attempted here could provide novel insights into such questions.

6.3.2 High-resolution imaging reveals egg calcification in the mouse liver

High-resolution imaging of liver tissue at weeks 8 and 14 post-infection showed the morphology of the egg granuloma in more detail. Whilst sinusoids were visible, resolution was not high enough to allow their segmentation, especially in the granulomatous regions in which no vasculature was evident at all. Lymphatic morphology was also impossible to determine at this resolution. Visualising these finer elements of morphology would be helpful in clarifying the nature of angiogenesis occurring during infection, and would also be helpful in beginning to investigate the lymphatic contribution to schistosomiasis pathology. However, it seems that electron microscopy, and especially 3D approaches to EM may be required in examining these fine morphological elements at sufficient resolution. Correlative tomography may be an absolute necessity in this case, because granulomas must be located before beginning the sectioning workflow. However, the variable size of the egg granuloma may impede such an approach as, some granuloma can reach hundreds of microns in size (Amaral *et al.*, 2017) which would push the limits for field of view of SBF-SEM and FIB-SEM (Peddie and Collinson, 2014). Currently

there is a trend towards developing faster methods of 3D EM sectioning (Burnett *et al.*, 2016) which would facilitate investigations featuring larger fields of view. An EM study would have the added bonus of being able to distinguish immune cell identities and structure, in 3D, alongside measurements of vascular morphology.

Interesting changes in egg density were observed at week 14 PI which were subsequently identified as calcification, due to the high levels of calcium and phosphorus detected by EDX. The EDX results are suggestive of hydroxyapatite deposition. Hydroxyapatite is a compound of calcium and phosphorus which makes up the hard tissue in teeth and bone (Klement and Trömel, 1932). Pathology associated with calcification of helminth eggs is well known in a variety of diseases including schistosomiasis and taeniasis (Nash *et al.*, 2004). In particular, calcification of eggs within the bladder wall is associated with *Schistosoma haematobium* infection (Mostafa *et al.*, 1999), and calcification of eggs in the intestinal wall with *Schistosoma mansoni* infection (Lambertucci *et al.*, 2005). Calcification of eggs within the liver has been reported in *Schistosoma japonicum* (Manzella *et al.*, 2007), but we believe that this may be the first instance in which calcified *S. mansoni* eggs have been identified within the liver of an infected animal. The origin of this unexpected calcification is unknown. The calcification may be dystrophic (originating from necrosis) in nature (Hussmann *et al.*, 1995), due to the necrotic tissue often identified in granulomas (Amaral *et al.*, 2017). It may also be that these calcified eggs are also impossible to clear from the liver. It is known in tuberculosis that calcified granulomas are able to recede after treatment. The cells constituting the granuloma may also be in some way responsible for calcification. Fibroblasts, which are present in the egg granuloma, are stimulated by egg antigen (Wyler and Tracy, 1982), and in humans fibroblasts have been implicated in diseases featuring dysregulation of soft tissue calcification (Ronchetti *et al.*, 2013). The potential effects on calcified tissue on the vasculature are also unknown. Calcification could be host-protective, perhaps because it limits any potentially dangerous inflammatory reaction to dead eggs. Indeed, inflammatory reactions can be particularly dangerous within critical tissues such as the nervous system (Betting *et al.*, 2005), which Schistosome eggs have previously been observed in (Bulantová *et al.*, 2016).

6.3.3 Migration of *S. mansoni* eggs across the small intestine

Migration of *S. mansoni* eggs across the intestinal wall remains very poorly understood (Schwartz and Fallon, 2018; Costain *et al.*, 2018). This is despite the fact that eggs in the gut wall cause a high burden of pathology which happens when they arrest and fail to migrate to reach the lumen (Strickland, 1994; Lambertucci *et al.*, 2005). One potential issue in studying migration of eggs across the gut is the difficulty in finding sparsely distributed eggs in tissue sections for histology. We circumvented this issue by pre-screening paraffin-embedded small intestine using phase contrast microCT to identify the positions of eggs for subsequent haematoxylin and eosin histology. Eggs could be identified in different layers of the intestinal architecture, including outside the muscular layer, and close to the epithelium. Only one egg was found very close to the epithelium, in contrast to the many found in more basal layers, suggesting that the epithelial crossing may be one of the quickest elements of the migration. Interestingly, the egg that was found close to the epithelium appeared to have very little granulomatous inflammation surrounding it, and also seemed to be travelling up the inside of a small intestine villus, through the lamina propria. The lack of inflammation around the egg is especially interesting, since granuloma formation is required to facilitate the traversal of the egg into the lumen (Doenhoff *et al.*, 1981). This raises the question as to whether further regulation, and indeed suppression, of the granuloma is required in order to complete egg egress into the lumen.

6.4 Conclusions

The pathology of Schistosomiasis represents a complex scientific challenge. Multiple tissues are remodelled and multiple cell types interact, including immune cells, vasculature, lymphatics and connective tissue; a catastrophic milieu of factors which can result in a fatal outcome. In this chapter, the potential for 3D imaging to quantify many aspects of pathology at a variety of length scales was investigated. Iodine contrast-enhanced microCT allowed both gross vascular morphology and inflammation to be visualised at the same time within the mouse liver. Ultimately, whilst the approach for vascular segmentation developed here was not quantitative, it showed qualitative reduction in branching throughout infection and, in future, can be built upon to achieve novel and informative quantitative outputs. At higher imaging resolutions, we have revealed calcification of *S. mansoni* eggs within the liver tissue for the first time; the role of

calcification in generating hepatic pathology remains an issue for future investigation. Furthermore, in the intestine correlative microCT and histology has suggested a reduction of granulomatous inflammation in eggs which are traversing the submucosal layers of the small intestine. Indeed, this efficient imaging approach could be further be used to investigate the role that regulation of the granuloma may have in successful egg migration across the intestine. Overall, the data show the potential of microCT as a quantitative and qualitative tool for investigating pathology, and have raised several novel questions regarding the origin and development of schistosomiasis pathology.

Blank Page

7. Conclusions and areas for further research

7.1 Reiteration of dissertation aims

This overall aim of this dissertation was to exploit the 3D imaging capabilities of micro-computed tomography to address unanswered questions in the biology of parasitic diseases, a task which required the development and refinement of new soft tissue imaging methodologies. Within the dissertation, the chapters investigated two murine models of parasitic infection; *Trichuris muris* and *Schistosoma mansoni* in two soft tissues; the liver and gut. In order to investigate the life cycles and pathologies of these parasites, new soft-tissue sample preparation protocols and data analysis routines needed to be developed and optimized. In *T. muris*, the objective was to increase our understanding of the development and maintenance of the intestinal epithelial attachment site. In order to achieve this we exploited 3D imaging to characterize both the morphology of the worm itself and its positioning within host tissue. The specific biological and technical aims of chapters 4 and 5 in this regard were as follows:

> **Chapter 4:** To characterise spatial positioning of *T. muris* within the epithelial tunnel, as well as the ultrastructural features of *Trichuris* at the attachment site. A more comprehensive understanding of tunnel morphology and would inform understanding of tunnel formation and maintenance. **Technical aims:** To develop an optimised staining imaging protocol allowing the attachment site of the worm to be visualised, and to develop 3D measurements of tunnel integrity and mucosal inflammation.
>
> **Chapter 5**: To characterise the morphology, structure and composition of *T. muris* surface structures which interact with the host within the epithelial tunnel, in order to better understand the effector mechanisms by which survival in the host is promoted. **Technical aims:** To develop a correlative imaging approach by which microCT-steered EM allows efficient ultrastructural investigation of the cuticular inflations.

Investigation into *S. mansoni* focused on characterizing the inflammatory pathology caused by deposition of eggs in the liver and gut. We also investigated the effect of egg-induced inflammation in vascular remodelling. Vascular remodelling is involved in the fatal pathology of schistosomiasis and 3D imaging approaches are uniquely suited to characterising vascular morphology (Zagorchev *et al.*, 2010). The aims of chapter 6, therefore, were defined as follows:

Chapter 6: To characterise liver and intestinal pathology of *Schistosoma mansoni*. An understanding of how inflammation leads to change in liver architecture may inform further understanding of how dangerous pathologies are generated. **Technical aims:** To develop optimised staining to visualise changes in egg-induced granulomatous inflammation and vascular pathology throughout infection. To develop a correlative imaging approach by which microCT-steered histology allows efficient investigation of egg traversal across the intestine wall.

7.2 Summary of findings

Between all of the chapters, several new sample preparation protocols and analysis pipelines were developed, as was outlined within each of the chapter aims. Optimized specific soft tissue staining of the *T. muris*-infected gut (**chapter 4**) allowed 3D morphology of the attachment site to be effectively visualized, identifying scientifically novel positioning of the worm. Osmium staining and critical point drying are both established techniques in microCT (Metscher, 2009b). However, this work represents the first time in which both have been combined to provide ideal microCT contrast in the intestine, facilitating quantitative analyses such as epithelial overage and mucosal thickness. Several correlative workflows were developed in which microCT mapping of the sample was used to guide subsequent imaging using modalities providing ultrastructural (**chapter 5**) and compositional (**chapter 6**) information. The correlative workflow employed in chapter 5 and described in appendix 2 allowed efficient imaging of the cuticular inflations and surrounding structures with the assistance of open source software. Ultrastructural findings in chapter 5 represent an update to the body of literature describing *Trichuris* ultrastructure, and lead to establishing a novel hypothesis on the role of blister proteins in inflation formation. In chapter 6, we used a simple and well-established iodine staining protocol to visualise *S. mansoni*-induced inflammatory pathology and vascular morphology. The primary contribution of these data is as a newly-developed methodological basis for future quantitative study. In addition, we identified novel calcification of eggs in infected liver tissue, and using microCT-steered histology we identified eggs undergoing their traversal through the intestinal wall.

7.3 Implications of microCT study of *Trichuris muris*

The investigations of *T. muris* in chapters 4 and 5 succeeded in characterizing novel aspects both in the nature of the parasite-induced epithelial tunnel structure, and in the anatomy of *T. muris* itself. Specifically, new phenomena in *T. muris'* positioning within the gut crypt niche were identified, i.e. the head-down and crypt-traversing behaviour. One of the main findings was that *T. muris* seems to have access to tissue compartments such as the lamina propria and intestinal stem cells which were not previously appreciated. This observation has implications for the development of host immunity and for parasite-driven immunomodulation, given than the worm head is in close proximity to proliferating epithelial cells, tuft cells, and the lymphocytes of the lamina propria.

Despite the advances of this work in understanding of *Trichuris* morphology, there remain many unanswered questions in *Trichuris* biology and many aspects of tunnel formation and maintenance still remain unknown (chapters 4 and 5). However, the successful application of staining protocols that enhanced contrast between worms and the surrounding tissue could be an approach which may be applicable to investigations of other murine trichuroid parasites. *Trichinella* and *Capillaria* nematodes are both embedded within tissues (gut and liver respectively), and possess similarly enigmatic lifestyle and surface structures to *Trichuris* (Wright, 1963, 1968a, 1979; Kim and Ledbetter, 1980). In chapter 4 we demonstrated how parasites can easily be visualised *in toto*, within a whole tissue, in an approach that can surely be replicated in other trichuroid worms to more comprehensively characterise their attachment sites. Likewise, the correlative approach developed in chapter 5 could also be utilised to update the existing ultrastructural literature in these parasites in the way that has been achieved with *T. muris*.

One of the main *Trichuris*-related research questions which this thesis was intended to address was the function of the cuticular inflations underlying the anterio-ventral portion of the worm. The function of the cuticular inflations remains unknown but was speculated to be secretory (Beer, 1976; Hüttemann *et al.*, 2007). However, from the combined work in chapters 4 and 5, it seems unlikely that secretory products do originate from the inflations themselves, or even the cells directly underlying the inflations, as previously speculated (Hüttemann *et al.*, 2007).

Secretory tissues are often characterised by extensive Rough Endoplasmic Reticulum (RER) which is involved in protein production. In chapter 4, electron microscopy showed that stichocytes had a high microCT contrast due to extensive RER, whereas high contrast was not observed in the cuticular inflations in chapter 5. This observation was further confirmed in by BSEM images, in which no particularly high density of RERs were discovered in the immediate vicinity of the inflations. However, it was clear that the structure of the cuticle was disrupted, suggesting altered regulation of collagen deposition and organization at the inflations' locales. It may be hypothesized that this dysregulation is caused by transit of secretory compounds across the cuticle. The overall question of inflation function is thus redefined to whether the inflations represent a route of exit for secretory compounds, rather than production sites. Disturbance in cuticular collagen processing could reasonably be induced by serine proteases or their inhibitors, which are highly over-represented in the *Trichuris muris* genome (Foth *et al.*, 2014). These proteins are involved in cuticle formation during moulting, in which they are responsible for proper processing of collagen precursors (Page *et al.*, 2014), and therefore may reasonably be implicated in inflation development. Investigating the distribution of these proteins near the inflations using techniques such as immunohistochemistry may test this hypothesis.

7.4 Implications of microCT study of *Schistosoma mansoni*

Chapter 6 introduced microCT as a tool for visualizing the egg-induced pathology caused by *S. mansoni* in the liver. It was found that both granuloma and vascular morphology could be delineated using an iodine-based staining protocol, although it was not possible to quantify changes in vascular morphology. By applying a correlative imaging approach incorporating propagation based imaging and EDX, calcification of eggs within the liver tissue was also observed. The relative contributions of calcified and non-calcified eggs to vascular and lymphatic blockage and remodelling represent new areas of investigation. Finally, microCT-steered histology showed reduced inflammation around an egg close to the intestinal epithelium, suggesting that regulation of granuloma size may be important for translocation of the egg into the lumen. This correlative approach overcame the challenge of finding eggs within the tissue, and in future similar microCT-steering based approaches could be used to observe the events surrounding egg traversal across the intestine in more detail. In the chapter a

methodological base was therefore established to investigate inflammatory pathology, allowing segmentation and visualisation in 3D. Whilst examination of vascular structure reached the qualitative levels used by other researchers (Andrade and Santana, 2010), future quantitative observation is subject to optimization of sample preparation. In the discussion of chapter 6 we suggested a number of methodological improvements such as vascular perfusion combined with dual energy imaging, which would help achieve combined quantitative analyses of vascular morphology as set out in the aims of the chapter.

Given the efficacy of iodine staining in delineating granulomatous pathology in chapter 6, it is of interest to consider the extent to which a similar approach could be applied to a variety of other biological questions beyond schistosomiasis. Indeed, microCT imaging of vasculature has already been applied to public health issues such as cirrhosis (Peeters *et al.*, 2018) and cancer (Savai *et al.*, 2009). With respect to the study of granulomas, one interesting study candidate is tuberculosis (TB), a bacterial disease which in 2016 alone was estimated to kill over one million people (Kyu *et al.*, 2018b). Pathology of TB is a multi-stage process (Zumla *et al.*, 2011) involving the formation of granulomas around bacteria (*Mycobacterium tuberculosis*) in the lung. Whilst the human immune response typically succeeds in healing the lesions, the infectious bacteria are not eliminated and remain dormant within the scar tissue (Gengenbacher and Kaufmann, 2012). Between 10-30 years later, the bacteria can emerge from dormancy and produce a “post-primary” infection, which in CT imaging and necropsy has been observed as a mosaic of pathologies including granuloma, necrosis, fibrosis and cavitation (Long *et al.*, 1998; Hunter, 2011). Further downstream pathologies include the development of chronic bronchitis, emphysema, collapsed lung and pulmonary fibrosis (Ravimohan *et al.*, 2018). The pathological progression of tuberculosis remains poorly understood because chronic infection in mice poorly reflects events in humans (Hunter *et al.*, 2007), and so samples for study must largely be taken from human biopsy or necropsy (Hunter, 2016). Such constraints on research have resulted in confusion regarding the basic progression of pathological processes in humans (Lalvani *et al.*, 2013; Nunes-Alves *et al.*, 2014; Andersen and Woodworth, 2014), and new ideas about pathological progression have now been suggested by studies involving thorough re-examination and reproduction of the autopsy-based morphological literature of the 19th and 20th centuries (Hunter, 2016).

TB study is subject to many of the research constraints which we have sought to address in our *T. muris* and *S. mansoni* studies; namely, that the pathogen has a complex life cycle the stages of which are distributed unpredictably throughout the tissue. The lack of suitable animal models for researching chronic disease means that tuberculosis research is perhaps even more constrained than that of the parasites in this thesis. Consequently, there has been a greater reliance on morphological observations to provide insight into disease progression (Hunter, 2016). Likewise, this thesis has represented a research approach which places morphological observations at the centre of experimental investigations into parasite lifestyle and pathology. Examination of granulomatous biopsies using the methods which are fully developed in chapter 6 (iodine staining microCT and correlative histology) could be particularly helpful in maximizing the information gained from valuable human tuberculosis samples. Namely, a correlative approach to histological investigation could aid in identifying regions of interest and could minimize wasting tissue in these valuable samples. Such an approach would supplement the growing immunological research on tuberculosis progression (Rao *et al.*, 2019).

7.5 Advances in microCT contrast enhancement: current challenges and future implications

Light microscopy has been an indispensable tool in determining the structure and composition of tissues, at least in part due to the many histochemical stains which allow specific elements of cellular composition to be highlighted (Horobin, 2002; Nicu *et al.*, 2018). Whilst many staining protocols for microCT exist (O'Sullivan *et al.*, 2018), the two most widely used - iodine and PTA - (Gignac et al. 2016) were found to be unsuited for providing contrast for specific tissue elements, except in the case of dual energy computed tomography (Handschuh *et al.*, 2017). However, work in this thesis has highlighted how specific behaviour of single stains can be used to contrast structures within tissue, allowing clear visualisation and easier subsequent segmentation.

The foremost example of specific staining in this thesis is the use of osmium tetroxide to contrast *T. muris* within the intestinal tissue in chapter 4. Based on electron microscopic data, we believe it likely that the high contrast of the worm was due to the presence of an extensive rough endoplasmic reticulum within the stichocyte. The many carbon-carbon double bonds

within a RER network can bind significantly more OsO_4 than surrounding host mucosal tissue (Riemersma, 1968). High contrast due to densely membranous ultrastructure is a phenomenon which we speculate could also be exploited in microCT imaging of a variety of other tissues. For instance, extensive rough endoplasmic reticulum is prominent in the acinar and beta-cells of the pancreas (Sabatini *et al.*, 1963; Zuber *et al.*, 2004), as well as plasma cells (Martinez-Murillo *et al.*, 2016). Moreover, we predict that the highly extensive and layered outer membranes of Schwann cells surrounding peripheral neurons (Payne *et al.*, 2012) would exhibit similar preference to OsO_4. Therefore, based on the findings of this thesis we would recommend the use of OsO_4 as a first choice in the study of any of these particular cell types.

Another example of specific staining behaviour which was observed but not exploited was the seeming affinity of residual blood within the liver tissue to iodine staining in chapter 6. This was suggested due to the presence of small, filamentous bright areas which were often present around the egg granulomas. Interestingly, iodine may indeed exhibit an affinity for staining blood, because under acidic pH the iodide ion (I^-) binds strongly to haemoglobin, the most abundant protein within red blood cells (Rosenberg, 1959). Although iodide is readily washed out of tissues by water (Pauwels *et al.*, 2013), iodide and haemoglobin in complex are only able to be separated by concentrated ammonia (Rosenberg, 1959). Binding between iodide and haemoglobin has remained unseen and unremarked upon by other microCT researchers. However, we might in future propose a staining protocol which exploits this specific behaviour. Staining an organ with acidified potassium iodide, and then washing out KI that has not bound to haemoglobin using water (Pauwels *et al.*, 2013; Keklikoglou *et al.*, 2019) may be effective in contrasting vascular morphology, and may avoid some of the existing issues with perfusion staining such as bubbling artefacts (Mondy *et al.*, 2013) and incomplete perfusion.

In future, it is likely that a range of new, more specific stains for microCT will be developed. Perhaps one productive way in which this will be achieved is in adapting the currently used histochemical stains for microCT use. For instance, eosin is a common stain used to label the cytoplasm of cells in histological slices. By modifying the fixation of tissue prior to staining and critical point drying samples, Busse et al. (Busse *et al.*, 2018) succeeded in adapting eosin as a cytoplasm-specific microCT stain which allowed observations of nuclear morphology and cell shape, as well as gross organ architecture. Verhoeff's stain, which is used to specifically label endothelial cells and media of arteries, has also been adapted to microCT observation of

vascular morphology (Dunmore-Buyze *et al.*, 2019). The Golgi-Cox staining method has also been employed directly to samples for microCT, in order to visualise morphology of single neurons (Fonseca *et al.*, 2018). There are many other specific histological stains which are potential candidates for microCT staining. For instance picrosirius red and trichrome stains target collagen, and are often used to quantify fibrosis (Junqueira *et al.*, 1979). A protocol adapted for microCT, which exploits the already well-investigated staining behaviour of sirius red (Puchtler *et al.*, 1988; Horobin and Flemming, 1988; Prento, 1993; Nielsen *et al.*, 1998), could be useful in addressing some of the issues regarding what raised in this thesis. For instance, 3D quantification of the fibrotic granulomas late in schistosome infection (Chapter 6) could be attempted, which were unable to be segmented by iodine staining alone. In addition, intestinal disorders such as Inflammatory Bowel Disease (IBD) which can include extensive fibrosis (Rieder and Fiocchi, 2009), may be apt to study using 3D imaging methodology exploiting a specific staining approach.

Existence of specific staining procedures which utilize different elements in order to contrast morphology may be even more useful in future due to the rise of dual energy and hyperspectral imaging (Egan *et al.*, 2015). These approaches are able to identify the elemental composition of various regions of the sample. In the past, this has allowed discrimination between sample regions more greatly stained with PTA or iodine respectively (Handschuh *et al.*, 2017). This approach could be extended to a variety of other multiply-stained systems, given newly uncovered specific staining behaviours of iodine and osmium tetroxide. Such approaches might be used to aid segmentation, and inform the edge detection and morphological approaches to segmentation as presented in chapter 4 and chapter 6 of this thesis.

Whilst not a specific staining protocol, chapter 6 includes the use of HMDS-drying to prepare samples for microCT. Previously, HMDS has been used as a convenient equipment-free substitute for critical point drying SEM (Nation, 1983; Braet *et al.*, 1997). Whilst critical point- and air drying are established as methods for preparing and mounting samples for microCT (Zhang *et al.*, 2015; Busse *et al.*, 2018), HMDS has only very recently been employed for mammalian soft tissue imaging (Pallares Lupon *et al.*, 2019). It is debatable the extent to which HMDS-immersion constitutes staining, as silicon, the highest molecular-weight element in the compound, is still three times lighter than iodine and five times lighter than tungsten and is therefore far less attenuating to X-rays than either. However, EDX in Chapter 6 revealed that

some silicon does remain trapped within tissue following the drying process. Drying samples for microCT may be advantageous to other imaging approaches in which a stained sample is suspended in fluid for scanning, as a dried sample can be glued securely to a sample holder, minimizing the risk of sample movement during a scan and faulty image reconstruction. Moreover, immersing samples in fluid, or embedding in wax or epoxy removes low-energy X-rays from the incoming X-ray beam, whereas in the case of a dried sample, low-energy X-rays are retained and are absorbed by the sample providing contrast, rather than any surrounding material. HMDS treatment of samples may also be more effective in revealing phase information about the sample during phase contrast imaging due to the minimizing the interference from high-Z element absorption. Therefore, we believe that HMDS-drying of samples should be more widely adopted in future microCT studies of soft tissue.

7.6 Correlative imaging in the future

Throughout chapters 5 and 6 of this thesis, the utility of correlative imaging for providing targeted insights into sample interior morphology and composition has been demonstrated. For specific purposes such as targeted EM by MicroCT, proprietary software has been developed to ease registration between datasets (Merkle *et al.*, 2015). However, we have shown that a variety of correlative workflows are possible without the use of proprietary software, albeit with more difficulty, instead only using open source packages such as ImageJ and 3DMOD (Kremer *et al.*, 1996; Schindelin *et al.*, 2012). All of the correlative processes detailed in this thesis have been novel, and have helped obtain the experimental objectives of each chapter, as detailed in the overall thesis aims. In future, correlative methods may expand to include new modalities, for instance those providing greater detail on molecular localisation. Additionally, the volume of the correlated region may be increased due to fewer constraints on throughput.

As mentioned in chapter 6, there is a desire to increase the volumes which can be correlated between microCT and electron microscopy, in order to aid characterization of structures which are larger than the traditional field-of-view offered by both SBF-SEM and FIB-SEM. Increased milling capacity by electron microscopes may be one way to increase volumes inspected, for example as has been enabled by Xenon Plasma-FIB (Burnett *et al.*, 2016). One such method for further increasing inspected volumes is through the use of a laser to mill the sample block-

face faster than can be achieved by existing FIBs. However, as volumes inspected by electron microscopy increase, and as more intense milling of the sample surface is attempted, the risks of both increased charging, as well as damage to the sample surface increase. It may be that new solutions, such as embedding in more conductive resins (Nguyen *et al.*, 2016, 2018), are required in order to facilitate investigation of these larger biological samples.

In chapter 6, microCT data was correlated with paraffin-based histological slices. In future, a key consideration for future efforts may be to create a protocol in which microCT mapping of the sample is achievable in frozen tissue prior to cryosectioning. Samples preserved cryogenically are a staple of biological histology, and many molecules of interest can only be antibody- or probe-labelled in frozen sections of tissue. Scanning of frozen biological samples using modern microfocus X-ray sources has been accomplished through the development of cryogenic sample stages (Hullar *et al.*, 2014; Vasilescu *et al.*, 2017). MicroCT scanning in cryogenic conditions has been used to inspect bone (Maran *et al.*, 2003; Kampschulte *et al.*, 2015) and artery (Kantor *et al.*, 2006) samples. However, whilst the methodological basis therefore exists for microCT, no attempts have been made to correlate microCT data with histochemical analysis of frozen sections. Developing capabilities for cryogenic scanning of microCT samples may not just be useful for correlation with histological techniques. Indeed, the storage of preparation of samples in cryogenic conditions is important for genetic analyses such as RT-qPCR and gene sequencing (Hedegaard *et al.*, 2014; Kuang *et al.*, 2018). MicroCT mapping of a sample prior to these analyses may provide an interesting new avenue to investigate gene expression at highly specific locations within tissue of interest. Relatively new techniques for molecular localisation of many proteins simultaneously, including Imaging Mass Cytometry, also use frozen tissue (Chang *et al.*, 2017). Therefore, more widespread adoption of cryogenic microCT scanning in future may allow for an increased ability for microCT providing information on molecular localisation deep within tissue.

7.7 Towards reliable and accurate biological morphometry by microCT

Throughout the thesis, many useful observations have been qualitative in nature, including characterisation of tunnel morphology and confirmation of the presence of calcified eggs in the livers of *S. mansoni* infected mice. Additionally, use of the correlative microCT-EM workflow

(appendix 2) facilitated further qualitative ultrastructural investigations. Alongside these qualitative observations, we have attempted quantitative morphometric analyses including measuring gut mucosal thickness and *T. muris* tunnel integrity (chapter 4). Quantitative measurement of pathology has been an important aspect of monitoring the status of infection in both *Trichuris* and *Schistosoma* research (e.g Yepes *et al.*, 2015; Hayes *et al.*, 2017). In these cases, measurements are taken from histological slices, usually manually. In this thesis we presented totally new kinds of measurement not possible for 2D histology, for instance the proportion of epithelial coverage of *T. muris*. Other forms of 3D measurement which we attempted are analogous to current standards in the biological literature; for example, both our 3D mucosal thickness measurements in chapter 4 and measurement of crypt length in 2D sections are designed to measure inflammatory pathology. If use of 3D "virtual histology" is to continue to grow in the way asserted by a variety of authors (Dudak *et al.*, 2016; Dullin *et al.*, 2017; Busse *et al.*, 2018; Albers *et al.*, 2018a; b; Saccomano *et al.*, 2018; Martín-Vega *et al.*, 2018; Dunmore-Buyze *et al.*, 2019), a range of questions regarding the accuracy and reliability of 3D measurements as compared to existing 2D standards arise. The ultimate practical concern for researchers is whether 3D methods of measurement are sufficiently, or indeed more accurate or sensitive in detecting real biological differences compared to their 2D counterparts. Importantly, measurements must also be repeatable between researchers.

Central to any 3D measurement by microCT is the segmentation process, by which the tissue phase of interest is labelled. The final value of the segmentation is influenced by both the parameters of scanning and sample preparation process used, as well as the data processing method and segmentation approach selected. Errors introduced by inconsistent segmentation between researchers are already of interest in the medical diagnostic community (Parkinson *et al.*, 2008). For consistent segmentation to be achieved between researchers, systematic errors must be accounted for and ideally a standardised approach developed for a given tissue type. For instance, positional stability (Vogeler *et al.*, 2011), magnification,(Weitkamp and Bleuet, 2004) and beam energy/hardening (Dewulf *et al.*, 2012) represent sources of error in microCT measurements (Franco *et al.*, 2014). In addition, since contrast is important in determining where phase boundaries occur during segmentation, the duration, concentration and species of staining is also important to keep constant. Ideally a staining approach which generates maximum contrast would be selected.

3D measurements are attractive to researchers who are otherwise dependent on 2D quantification and the 2D bias which is perceived to accompany measuring from a specific plane of sectioning. Consequently, some researchers claim that 3D measurements are more accurate than existing 2D techniques (Smith *et al.*, 2016; Masís *et al.*, 2018). However, in these particular cases, the degree to which 2D and 3D measurements agree were not investigated. In fact, the accuracy of the results either remained totally unexamined (Masís *et al.*, 2018), or a "validation" step was carried out in which the measurements of interest were compared by regression analysis with other morphometric measurements from the same microCT dataset (Smith *et al.*, 2016). 3D measurement may indeed be suitable for addressing specific measurement difficulties when a source of systematic error in a specific 2D measurement has been identified (Tapie *et al.*, 2016). However, the accuracy of 3D measurements by microCT in biological samples has not yet been rigorously assessed in the way in which those from industrially manufactured materials have (Warnett *et al.*, 2016). In the case of the studies in this thesis, it may be that 3D measurements could be compared with histological measurements to determine whether different values are obtained. Such an approach may not be suitable for measurements of *T. muris*-induced changes in mucosal thickness in chapter 4, since it is not known the degree to which mucosal thickness fluctuates naturally along the proximal-distal axis of the colon. In such a scenario different thicknesses would be expected from different biopsies. However, such an approach may be applicable in the case of iodine-stained *Schistosoma*-infected liver, which is liable to correlation with histology as we have demonstrated in chapter 6.

Assuming the existence of an idealized sample preparation protocol which provides optimum contrast between phases of interest within a sample, the next step is to assess the accuracy of measurements. As mentioned in chapter 4, physical or optical coordinate measuring machines (CMMs) can be used as a gold standard for distance measurements against which microCT distances can be compared (Warnett *et al.*, 2016). With this information error in CT measurement can be quantified. Alternatively, measurements from CMMs can be used to rescale the voxel size of the microCT dataset to ensure more accurate measurement (Kourra *et al.*, 2016). A similar method could conceivably be applied to measurement of a biological sample, perhaps by the inclusion of a phantom in the scan, from which reference measurements can be taken. Processes such as these would help minimize the effect of any systematic error in distance measurement originating from the microCT image acquisition

process, and more importantly could provide a “true” value for measurements against which traditional 2D approaches could be compared.

As discussed in chapter 4, quantitative measurements are highly dependent on the segmentation obtained, and the reproducibility of scientific findings is dependent on variability in segmentation practices between researchers. I have now discussed controlling sources of systematic error in microCT acquisition to avoid unnecessary variability, as well as assessing the accuracy of a 3D distance measurement. However, differences in segmentation approaches between researchers are also a potential source of error. There is a critical role for edge detection methods in microCT of biological samples, because the greyscale values of phases within a sample may not always be sufficiently different for thresholding methods to discriminate them in segmentation. Therefore, more complex methods to delineate phases based on edge detection have been employed by biologists (Wang *et al.*, 2017). These methods result in boundaries being established between samples. A large range of edge detection methods are available (Ontiveros *et al.*, 2013), all of which may give subtly different results for any segmentation, leading to variation in quantitative methods. Therefore, for each sample type and preparation protocol attempted, there is a requirement by researchers to optimize the method of segmentation and measurement. Using phantoms which mimic the contrast and absorption of the target biological tissue may be one way of accomplishing this.

7.8 General Conclusion

The use of micro-computed tomography has revealed new information about the lifestyles of *Trichuris muris* and *Schistosoma mansoni*. Through the development of a specific staining protocol, our studies on *T. muris* have provided new quantitative tools and methods to facilitate thorough morphological and ultrastructural investigations. We have also shown that the shape of the epithelial tunnel the worm makes in the gut is much more complex than previously assumed, with worms having access to crypt bases, and crossing the lamina propria. These trends in positioning could provide a new basis for future investigations of host-parasite interactions at the epithelial attachment site. In *S. mansoni*, we have demonstrated a method for segmenting inflamed tissue and vascular structure, and have revealed new phenomena such as calcification of eggs in the liver and a seeming reduction in granulomatous inflammation in eggs

traversing the gut. A variety of correlative measurements were developed which were key in attaining these compositional and morphological observations. Overall, we have shown how microCT may be an excellent tool for imaging the complex, and unpredictably distributed attachment sites of parasites from a morphological perspective. We have also demonstrated how, in parasites which are positioned unpredictably, correlative workflows incorporating microCT are highly effective in increasing the efficiency and variety of insights which can be achieved through other modalities. Having contributed a number of novel sample preparation and data analysis protocols, it is clear that microCT of biological samples still has room to develop and provide yet more refined insights on specific types of tissue, and can become increasingly useful in the context of understanding mechanisms of disease.

List of References

Abbe, E. (1873). Beiträge zur Theorie des Mikroskops und der mikroskopischen Wahrnehmung. *Archiv für Mikroskopische Anatomie* **9**, 413–418. doi: 10.1007/BF02956173.

Abd El-Aal, N. F., Hamza, R. S. and Magdy, M. (2017). Anti-angiogenic and anti-lymphangiogenic role of praziquantel and artemether in experimental mansoniasis. *Acta Parasitologica* **62**,. doi: 10.1515/ap-2017-0085.

Adams, R. H. and Alitalo, K. (2007). Molecular regulation of angiogenesis and lymphangiogenesis. *Nature Reviews Molecular Cell Biology*. doi: 10.1038/nrm2183.

Ahmed, A., Al-Mekhlafi, H. M., Azam, M. N., Ithoi, I., Al-Adhroey, A. H., Abdulsalam, A. M. and Surin, J. (2012). Soil-transmitted helminthiasis: a critical but neglected factor influencing school participation of Aboriginal children in rural Malaysia. *Parasitology* **139**, 802–808. doi: 10.1017/S003118201100237X.

Airy, G. B. (1835). On the diffraction of an object-glass with circular aperture. *Transactions of the Cambridge Philosopical Society* **5**, 283.

Akiho, H., Blennerhassett, P., Deng, Y. and Collins, S. M. (2002). Role of IL-4, IL-13, and STAT6 in inflammation-induced hypercontractility of murine smooth muscle cells. *American Journal of Physiology-Gastrointestinal and Liver Physiology* **282**, G226–G232. doi: 10.1152/ajpgi.2002.282.2.G226.

Albers, J., Pacilé, S., Markus, M. A., Wiart, M., Vande Velde, G., Tromba, G. and Dullin, C. (2018a). X-ray-Based 3D Virtual Histology—Adding the Next Dimension to Histological Analysis. *Molecular Imaging and Biology*. doi: 10.1007/s11307-018-1246-3.

Albers, J., Markus, M. A., Alves, F. and Dullin, C. (2018b). X-ray based virtual histology allows guided sectioning of heavy ion stained murine lungs for histological analysis. *Scientific Reports* **8**, 7712. doi: 10.1038/s41598-018-26086-0.

Alves, C. C., Araujo, N., Cassali, G. D. and Fonseca, C. T. (2016). Parasitological, athological, and immunological parameters associated with Schistosoma mansoni infection and reinfection in BALB/c and C57BL/6 mice. *Journal of Parasitology* **102**, 336–341. doi: 10.1645/14-664.

Amaral, K. B., Silva, T. P., Dias, F. F., Malta, K. K., Rosa, F. M., Costa-Neto, S. F., Gentile, R. and Melo, R. C. N. (2017). Histological assessment of granulomas in natural and experimental Schistosoma mansoni infections using whole slide imaging. *PLOS ONE* **12**, e0184696. doi: 10.1371/journal.pone.0184696.

Ananda, S. (2006). The visualization of hepatic vasculature by X-ray micro-computed tomography. *Journal of Electron Microscopy* **55**, 151–155. doi: 10.1093/jmicro/dfl015.

Andersen, P. and Woodworth, J. S. (2014). Tuberculosis vaccines – rethinking the current paradigm. *Trends in Immunology* **35**, 387–395. doi: 10.1016/j.it.2014.04.006.

Andrade, Z. A. (1987). Patogenesis of pipe-stem fibrosis of the liver (experimental observation on murine Schistosomiasis). *Memórias do Instituto Oswaldo Cruz* **82**, 325–334. doi: 10.1590/S0074-02761987000300003.

Andrade, Z. A. and Cheever, A. W. (1971). Alterations of the intrahepatic vasculature in hepatosplenic Schistosomiasis mansoni. *The American Journal of Tropical Medicine and Hygiene* **20**, 425–432. doi: 10.4269/ajtmh.1971.20.425.

Andrade, Z. A. and Cheever, A. W. (1993). Characterization of the murine model of schistosomal hepatic periportal fibrosis (“pipestem” fibrosis). *International Journal of Experimental Pathology* **74**, 195–202.

Andrade, Z. A. and Sadigursky, M. (1982). Pulmonary changes in schistosomal cor pulmonale. *The American Journal of Tropical Medicine and Hygiene* **31**, 779–784. doi: 10.4269/ajtmh.1982.31.779.

Andrade, Z. A. and Santana, T. S. (2010). Angiogenesis and schistosomiasis. *Memórias do Instituto Oswaldo Cruz* **105**, 436–439. doi: 10.1590/S0074-02762010000400013.

Andrade, Z. A. and Warren, K. S. (1964). Mild prolonged schistosomiasis in mice. *Transactions of the Royal Society of Tropical Medicine and Hygiene* **58**, 53–57. doi: 10.1016/0035-9203(64)90068-9.

Andrade, Z. A., Baptista, A. P. and Santana, T. S. (2006). Remodeling of hepatic vascular changes after specific chemotherapy of schistosomal periportal fibrosis. *Memorias do Instituto Oswaldo Cruz* **101**, 267–272. doi: 10.1590/S0074-02762006000900041.

Appleton, I., Brown, N. J., Willis, D., Colville-Nash, P. R., Alam, C., Brown, J. R. and Willoughby, D. A. (1996). The role of vascular endothelial growth factor in a murine chronic granulomatous tissue air pouch model of angiogenesis. *Journal of Pathology*. doi: 10.1002/(SICI)1096-9896(199609)180:1<90::AID-PATH615>3.0.CO;2-D.

Araújo, M. I., de Jesus, A. R., Bacellar, O., Sabin, E., Pearce, E. and Carvalho, E. M. (1996). Evidence of a T helper type 2 activation in human schistosomiasis. *European Journal of Immunology* **26**, 1399–1403. doi: 10.1002/eji.1830260633.

Artis, D., Potten, C. S., Else, K. J., Finkelman, F. D. and Grencis, R. K. (1999). Trichuris muris: host intestinal epithelial cell hyperproliferation during chronic infection is regulated by interferon-γ. *Experimental Parasitology* **92**, 144–153. doi: 10.1006/expr.1999.4407.

Arunsan, P., Ittiprasert, W., Smout, M. J., Cochran, C. J., Mann, V. H., Chaiyadet, S., Karinshak, S. E., Sripa, B., Young, N. D., Sotillo, J., Loukas, A., Brindley, P. J. and Laha, T. (2019). Programmed knockout mutation of liver fluke granulin attenuates virulence of infection-induced hepatobiliary morbidity. *eLife* **8**,. doi: 10.7554/eLife.41463.

Aslanidi, O. V, Nikolaidou, T., Zhao, J., Smaill, B. H., Gilbert, S. H., Holden, A. V, Lowe, T., Withers, P. J., Stephenson, R. S., Jarvis, J. C., Hancox, J. C., Boyett, M. R. and Zhang, H. (2013). Application of micro-computed tomography with iodine staining to cardiac imaging, segmentation, and computational model development. *IEEE transactions on medical imaging* **32**, 8–17. doi: 10.1109/TMI.2012.2209183.

Balint, R., Lowe, T. and Shearer, T. (2016). Optimal contrast agent staining of ligaments and tendons for X-ray computed tomography. *PLoS ONE* **11**,. doi: 10.1371/journal.pone.0153552.

Bancroft, A. J., Else, K. J. and Grencis, R. K. (1994). Low-level infection withTrichuris muris significantly affects the polarization of the CD4 response. *European Journal of Immunology* **24**, 3113–3118. doi: 10.1002/eji.1830241230.

Bancroft, A. J., Else, K. J., Sypek, J. P. and Grencis, R. K. (1997). Interleukin-12 promotes a chronic intestinal nematode infection. *European Journal of Immunology*. doi: 10.1002/eji.1830270410.

Bancroft, A. J., McKenzie, A. N. and Grencis, R. K. (1998). A critical role for IL-13 in resistance to intestinal nematode infection. *Journal of Immunology*.

Bancroft, A. J., Artis, D., Donaldson, D. D., Sypek, J. P. and Grencis, R. K. (2000). Gastrointestinal nematode expulsion in IL-4 knockout mice is IL-13 dependent. *European Journal of Immunology*. doi: 10.1002/1521-4141(200007)30:7<2083::AID-IMMU2083>3.0.CO;2-3.

Bancroft, A. J., Else, K. J., Humphreys, N. E. and Grencis, R. K. (2001). The effect of challenge and trickle Trichuris muris infections on the polarisation of the immune response. *International Journal for Parasitology* **31**, 1627–1637. doi: 10.1016/S0020-7519(01)00281-8.

Bancroft, A. J., Humphreys, N. E., Worthington, J. J., Yoshida, H. and Grencis, R. K. (2004). WSX-1: A key role in induction of chronic intestinal nematode infection. *The Journal of Immunology* **172**, 7635–7641. doi: 10.4049/jimmunol.172.12.7635.

Bancroft, A. J., Levy, C. W., Jowitt, T. A., Hayes, K. S., Thompson, S., Mckenzie, E. A., Ball, M. D., Dubaissi, E., France, A. P., Bellina, B., Sharpe, C., Mironov, A., Brown, S. L., Cook, P. C., S. MacDonald, A., Thornton, D. J. and Grencis, R. K. (2019). The major secreted protein of the whipworm parasite tethers to matrix and inhibits interleukin-13 function. *Nature Communications* **10**, 2344. doi: 10.1038/s41467-019-09996-z.

Barbone, G. E., Bravin, A., Romanelli, P., Mittone, A., Bucci, D., Gaaβ, T., Le Duc, G., Auweter, S., Reiser, M. F., Kraiger, M. J., Hrabě de Angelis, M., Battaglia, G. and Coan, P. (2018). Micro-imaging of brain cancer radiation therapy using phase-contrast computed tomography. *International Journal of Radiation Oncology* **101**, 965–984. doi: 10.1016/j.ijrobp.2018.03.063.

Barsoum, R. S., Esmat, G. and El-Baz, T. (2013). Human schistosomiasis: clinical perspective: review. *Journal of Advanced Research* **4**, 433–444. doi: 10.1016/j.jare.2013.01.005.

Baum, D., Weaver, J. C., Zlotnikov, I., Knötel, D., Tomholt, L. and Dean, M. N. (2019). High-throughput segmentation of tiled biological structures using random walk distance transforms. *Integrative and Comparative Biology*. doi: 10.1093/icb/icz117.

Becker, S. L., Liwanag, H. J., Snyder, J. S., Akogun, O., Belizario., V., Freeman, M. C., Gyorkos, T. W., Imtiaz, R., Keiser, J., Krolewiecki, A., Levecke, B., Mwandawiro, C., Pullan, R. L., Addiss, D. G. and Utzinger, J. (2018). Toward the 2020 goal of soil-transmitted helminthiasis control and elimination. *PLOS Neglected Tropical Diseases* **12**, e0006606. doi: 10.1371/journal.pntd.0006606.

Beer, R. J. (1976). The relationship between Trichuris trichiura (Linnaeus 1758) of man and Trichuris suis (Schrank 1788) of the pig. *Research in Veterinary Science* **20**, 47–54.

Bell, L. V. and Else, K. J. (2011). Regulation of colonic epithelial cell turnover by IDO contributes to the innate susceptibility of SCID mice to Trichuris muris infection. *Parasite Immunology* **33**, 244–249. doi: 10.1111/j.1365-3024.2010.01272.x.

Betting, L. E., Pirani, C., Queiroz, L. de S., Damasceno, B. P. and Cendes, F. (2005). Seizures and cerebral schistosomiasis. *Archives of Neurology* **62**, 1008–1010. doi: 10.1001/archneur.62.6.1008.

Bhutda, S., Surve, M., Anil, A., Kamath, K., Singh, N., Modi, D. and Banerjee, A. (2017). Histochemical staining of collagen and identification of its subtypes by picrosirius red dye in mouse reproductive tissues. *BIO-PROTOCOL* **7**,. doi: 10.21769/BioProtoc.2592.

Bikis, C., Degrugillier, L., Thalmann, P., Schulz, G., Müller, B., Hieber, S. E., Kalbermatten, D. F. and Madduri, S. (2018). Three-dimensional imaging and analysis of entire peripheral nerves after repair and reconstruction. *Journal of Neuroscience Methods* **295**, 37–44. doi: 10.1016/j.jneumeth.2017.11.015.

Blackwell, N. M. and Else, K. J. (2001). B Cells and antibodies are required for resistance to the parasitic gastrointestinal nematode Trichuris muris. *Infection and Immunity* **69**, 3860–3868. doi: 10.1128/IAI.69.6.3860-3868.2001.

Boerckel, J. D., Mason, D. E., McDermott, A. M. and Alsberg, E. (2014). Microcomputed tomography: approaches and applications in bioengineering. *Stem cell research & therapy* **5**, 144. doi: 10.1186/scrt534.

Booth, M., Guyatt, H. L., Li, Y. and Tanner, M. (2007). The morbidity attributable to Schistosoma japonicum infection in 3 villages in Dongting Lake region, Hunan Province, PR China. *Tropical Medicine & International Health* **1**, 646–654. doi: 10.1111/j.1365-3156.1996.tb00090.x.

Boughner, J. C. and Cooper, D. M. L. (2019). Silver-albumin tissue staining protocol to visualize odontogenesis in whole embryos.pp. 197–210. doi: 10.1007/978-1-4939-9012-2_20.

Bradford, B. M., Donaldson, D. S., Forman, R., Else, K. J. and Mabbott, N. A. (2018).

Increased susceptibility to oral Trichuris muris infection in the specific absence of CXCR5 + CD11c + cells. *Parasite Immunology* **40**, e12566. doi: 10.1111/pim.12566.

Braet, F., De Zanger, R. and Wisse, E. (1997). Drying cells for SEM, AFM and TEM by hexamethyldisilazane: a study on hepatic endothelial cells. *Journal of Microscopy* **186**, 84–87. doi: 10.1046/j.1365-2818.1997.1940755.x.

Broglie, L. (1924). XXXV. A tentative theory of light quanta. *Philosophical Magazine* **47**, 446–458.

Brunet, L. R., Finkelman, F. D., Cheever, A. W., Kopf, M. A. and Pearce, E. J. (1997). IL-4 protects against TNF-alpha-mediated cachexia and death during acute schistosomiasis. *Journal of Immunology*.

Bulantová, J., Macháček, T., Panská, L., Krejčí, F., Karch, J., Jährling, N., Saghafi, S., Dodt, H.-U. and Horák, P. (2016). Trichobilharzia regenti (Schistosomatidae): 3D imaging techniques in characterization of larval migration through the CNS of vertebrates. *Micron* **83**, 62–71. doi: 10.1016/j.micron.2016.01.009.

Bullen, T. F., Forrest, S., Campbell, F., Dodson, A. R., Hershman, M. J., Pritchard, D. M., Turner, J. R., Montrose, M. H. and Watson, A. J. M. (2006). Characterization of epithelial cell shedding from human small intestine. *Laboratory Investigation*. doi: 10.1038/labinvest.3700464.

Burnett, T. L., McDonald, S. A., Gholinia, A., Geurts, R., Janus, M., Slater, T., Haigh, S. J., Ornek, C., Almuaili, F., Engelberg, D. L., Thompson, G. E. and Withers, P. J. (2014). Correlative tomography. *Scientific Reports* **4**, 4711. doi: 10.1038/srep04711.

Burnett, T. L., Kelley, R., Winiarski, B., Contreras, L., Daly, M., Gholinia, A., Burke, M. G. and Withers, P. J. (2016). Large volume serial section tomography by Xe Plasma FIB dual beam microscopy. *Ultramicroscopy*. doi: 10.1016/j.ultramic.2015.11.001.

Burrows, R. B. and Lillis, W. G. (1964). The Whipworm as a Blood Sucker. *Journal of Parasitology* **50**, 675. doi: 10.2307/3276127.

Bushby, A. J., P'ng, K. M. Y., Young, R. D., Pinali, C., Knupp, C. and Quantock, A. J. (2011). Imaging three-dimensional tissue architectures by focused ion beam scanning electron microscopy. *Nature protocols* **6**, 845–858. doi: 10.1038/nprot.2011.332.

Busse, M., Müller, M., Kimm, M. A., Ferstl, S., Allner, S., Achterhold, K., Herzen, J. and Pfeiffer, F. (2018). Three-dimensional virtual histology enabled through cytoplasm-specific X-ray stain for microscopic and nanoscopic computed tomography. *Proceedings of the National Academy of Sciences* 201720862. doi: 10.1073/pnas.1720862115.

Caratti, G., Poolman, T., Hurst, R. J., Ince, L., Knight, A., Krakowiak, K., Durrington, H. J., Gibbs, J., Else, K. J., Matthews, L. C. and Ray, D. W. (2019). Caveolin1 interacts with the glucocorticoid receptor in the lung but is dispensable for its anti-inflammatory actions in lung inflammation and Trichuris muris infection. *Scientific Reports* **9**, 8581. doi: 10.1038/s41598-019-44963-0.

Cha, S. W., Lee, H. J., Cho, M. H., Lee, M. H., Koh, W. S., Han, S.-S., Kim, J.-A., Lee, E.-S., Nam, D.-H. and Jeong, T. C. (2001). Role of corticosterone in ethyl carbamate-induced immunosuppression in female BALB/c mice. *Toxicology Letters* **119**, 173–181. doi: 10.1016/S0378-4274(00)00306-4.

Chang, Q., Ornatsky, O. and Hedley, D. (2017). Staining of frozen and formalin-fixed, paraffin-embedded tissues with metal-labeled antibodies for imaging mass cytometry analysis. In *Current Protocols in Cytometry*, pp. 12.47.1-12.47.8. John Wiley & Sons, Inc., Hoboken, NJ, USA doi: 10.1002/cpcy.29.

Cheung, C. Y., Zheng, Y., Hsu, W., Lee, M. L., Lau, Q. P., Mitchell, P., Wang, J. J., Klein, R. and Wong, T. Y. (2011). Retinal vascular tortuosity, blood pressure, and cardiovascular risk factors. *Ophthalmology* **118**, 812–818. doi: 10.1016/j.ophtha.2010.08.045.

Chisty, M. M., Nargis, M., Inaba, T., Ishita, K., Osanai, A. and Kamiya, H. (2004). Transmission electron microscopy of Schistosoma mansoni cercariae treated with hinokitiol (beta-thujaplicin), a compound for potential skin application against cercarial penetration. *Tohoku Journal of Experimental Medicine* **202**, 63–7.

Chitsulo, L., Engels, D., Montresor, A. and Savioli, L. (2000). The global status of schistosomiasis and its control. *Acta tropica* **77**, 41–51. doi: 10.1016/s0001-706x(00)00122-4.

Chofle, A. A., Jaka, H., Koy, M., Smart, L. R., Kabangila, R., Ewings, F. M., Mazigo, H. D., Johnson, W. D., Fitzgerald, D. W., Peck, R. N. and Downs, J. A. (2014). Oesophageal varices, schistosomiasis, and mortality among patients admitted with haematemesis in Mwanza, Tanzania: a prospective cohort study. *BMC Infectious Diseases* **14**, 303. doi: 10.1186/1471-2334-14-303.

Chung, C. and Iwakiri, Y. (2013). The lymphatic vascular system in liver diseases: its role in ascites formation. *Clinical and Molecular Hepatology* **19**, 99. doi: 10.3350/cmh.2013.19.2.99.

Clendenon, S. G., Young, P. A., Ferkowicz, M., Phillips, C. and Dunn, K. W. (2011). Deep tissue fluorescent imaging in scattering specimens using confocal microscopy. *Microscopy and Microanalysis* **17**, 614–617. doi: 10.1017/S1431927611000535.

Cliffe, L. J., Humphreys, N. E., Lane, T. E., Potten, C. S., Booth, C. and Grencis, R. K. (2005). Accelerated intestinal epithelial cell turnover: a new mechanism of parasite expulsion. *Science* **308**, 1463–1465. doi: 10.1126/science.1108661.

Cliffe, L. J., Potten, C. S., Booth, C. E. and Grencis, R. K. (2007). An increase in epithelial cell apoptosis is associated with chronic intestinal nematode infection. *Infection and Immunity* **75**, 1556–1564. doi: 10.1128/IAI.01375-06.

Colley, D. G., Bustinduy, A. L., Secor, W. E. and King, C. H. (2014). Human schistosomiasis. *The Lancet* **383**, 2253–2264. doi: 10.1016/S0140-6736(13)61949-2.

Coons, A. H., Creech, H. J. and Jones, R. N. (1941). Immunological properties of an antibody containing a fluorescent group. *Experimental Biology and Medicine* **47**, 200–202. doi: 10.3181/00379727-47-13084P.

Costain, A. H., MacDonald, A. S. and Smits, H. H. (2018). Schistosome egg migration: mechanisms, pathogenesis and host immune responses. *Frontiers in Immunology* **9**,. doi: 10.3389/fimmu.2018.03042.

Crabtree, J. E. and Wilson, R. A. (1980). Schistosoma mansoni: a scanning electron microscope study of the developing schistosomulum. *Parasitology* **81**, 553–64. doi: 10.1017/S003118200006193X.

Cruickshank, S. M., Deschoolmeester, M. L., Svensson, M., Howell, G., Bazakou, A., Logunova, L., Little, M. C., English, N., Mack, M., Grencis, R. K., Else, K. J. and Carding, S. R. (2009). Rapid dendritic cell mobilization to the large intestinal epithelium is associated with resistance to Trichuris muris infection. *The Journal of Immunology* **182**, 3055–3062. doi: 10.4049/jimmunol.0802749.

Davis, T. L. and Sterling, P. (1979). Microcircuitry of cat visual cortex: classification of neurons in layer IV of area 17, and identification of the patterns of lateral geniculate input. *Journal of Comparative Neurology* **188**, 599–627. doi: 10.1002/cne.901880407.

Davisson, C. J. and Germer, L. H. (1928). Reflection of electrons by a crystal of nickel. *Proceedings of the National Academy of Sciences of the United States of America* **14**, 317–322.

De Clercq, K., Persoons, E., Napso, T., Luyten, C., Parac-Vogt, T. N., Sferruzzi-Perri, A. N., Kerckhofs, G. and Vriens, J. (2019). High-resolution contrast-enhanced microCT reveals the true three-dimensional morphology of the murine placenta. *Proceedings of the National Academy of Sciences* **116**, 13927–13936. doi: 10.1073/pnas.1902688116.

De Cock, K. M. (1986). Hepatosplenic schistosomiasis: A clinical review. *Gut*. doi: 10.1136/gut.27.6.734.

de Menezes, J. P., Saraiva, E. M. and da Rocha-Azevedo, B. (2016). The site of the bite: Leishmania interaction with macrophages, neutrophils and the extracellular matrix in the dermis. *Parasites & Vectors* **9**, 264. doi: 10.1186/s13071-016-1540-3.

de Oliveira, R. N., dos Santos, K. R., Mendes, T. M. F., Garcia, V. L., Santos Oliveira, A. S., de Lourdes Sierpe Jeraldo, V. and Allegretti, S. M. (2017). Sesquiterpenes evaluation on Schistosoma mansoni : Survival, excretory system and membrane integrity. *Biomedicine & Pharmacotherapy* **90**, 813–820. doi: 10.1016/j.biopha.2017.04.058.

de Souza, W. and Attias, M. (2018). New advances in scanning microscopy and its application to study parasitic protozoa. *Experimental Parasitology* **190**, 10–33. doi: 10.1016/j.exppara.2018.04.018.

de Souza e Silva, J. M., Zanette, I., Noël, P. B., Cardoso, M. B., Kimm, M. A. and Pfeiffer, F. (2015). Three-dimensional non-destructive soft-tissue visualization with X-ray staining micro-tomography. *Scientific Reports* **5**, 14088. doi: 10.1038/srep14088.

Deerinck, T., Bushong, E., Lev-Ram, V., Shu, X., Tsien, R. and Ellisman, M. (2010). Enhancing Serial Block-Face Scanning Electron Microscopy to enable high resolution 3-D nanohistology of cells and tissues. *Microscopy and Microanalysis* **16**, 1138–1139. doi: 10.1017/S1431927610055170.

Demiri, M., Müller-Luda, K., Agace, W. W. and Svensson-Frej, M. (2017). Distinct DC subsets regulate adaptive Th1 and 2 responses during Trichuris muris infection. *Parasite Immunology* **39**, e12458. doi: 10.1111/pim.12458.

Den Buijs, J. O., Bajzer, Ž. and Ritman, E. L. (2006). Branching morphology of the rat hepatic portal vein tree: A micro-CT study. *Annals of Biomedical Engineering* **34**, 1420–1428. doi: 10.1007/s10439-006-9150-4.

Denk, W. and Horstmann, H. (2004). Serial block-face scanning electron microscopy to reconstruct three-dimensional tissue nanostructure. *PLoS Biology* **2**, e329. doi: 10.1371/journal.pbio.0020329.

Depannemaecker, D., Santos, L. E. C., de Almeida, A.-C. G., Ferreira, G. B. S., Baraldi, G. L., Miqueles, E. X., de Carvalho, M., Costa, G. S. R., Marques, M. J. G., Scorza, C. A. and Rinkel, J. (2019). Gold nanoparticles for X-ray microtomography of neurons. *ACS Chemical Neuroscience* acschemneuro.9b00290. doi: 10.1021/acschemneuro.9b00290.

DePasquale-Jardieu, P. and Fraker, P. J. (1979). The role of corticosterone in the loss in immune function in the zinc-deficient A/J mouse. *The Journal of Nutrition* **109**, 1847–1855. doi: 10.1093/jn/109.11.1847.

Descamps, E., Sochacka, A., Kegel, B. De, Loo, D. Van, Hoorebeke, V. and Adriaens, D. (2014). Soft tissue discrimination with contrast agents using micro-CT scanning. *Belgium Journal of Zoology* **144**, 20–40.

Dewulf, W., Tan, Y. and Kiekens, K. (2012). Sense and non-sense of beam hardening correction in CT metrology. *CIRP Annals* **61**, 495–498. doi: 10.1016/j.cirp.2012.03.013.

Diab, M., Dkhil, M. A., Bauomy, A. A. and Al-Quraishy, S. (2015). Antioxidant and hepatoprotective role of gold nanoparticles against murine hepatic schistosomiasis. *International Journal of Nanomedicine* 7467. doi: 10.2147/IJN.S97622.

Dige, A., Rasmussen, T. K., Nejsum, P., Hagemann-Madsen, R., Williams, A. R., Agnholt, J., Dahlerup, J. F. and Hvas, C. L. (2017). Mucosal and systemic immune modulation by Trichuris trichiura in a self-infected individual. *Parasite Immunology* **39**, e12394. doi: 10.1111/pim.12394.

Disney, C. M., Madi, K., Bodey, A. J., Lee, P. D., Hoyland, J. A. and Sherratt, M. J. (2017). Visualising the 3D microstructure of stained and native intervertebral discs using X-ray

microtomography. *Scientific Reports* **7**,. doi: 10.1038/s41598-017-16354-w.

Doenhoff, M. J., Pearson, S., Dunne, D. W., Bickle, Q., Lucas, S., Bain, J., Musallam, R. and Hassounah, O. (1981). Immunological control of hepatotoxicity and parasite egg excretion in Schistosoma mansoni infections: stage specificity of the reactivity of immune serum in T-cell deprived mice. *Transactions of the Royal Society of Tropical Medicine and Hygiene* **75**, 41–53. doi: 10.1016/0035-9203(81)90012-2.

Dorscheid, D. R., Wojcik, K. R., Sun, S., Marroquin, B. and White, S. R. (2001). Apoptosis of airway epithelial cells induced by corticosteroids. *American journal of respiratory and critical care medicine* **164**, 1939–47. doi: 10.1164/ajrccm.164.10.2103013.

Du, Z.-W., Chen, R., Utzinger, J., Zhou, X.-N., Wu, F.-W., Steinmann, P., Yap, P., Hattendorf, J. and Jiang, J.-Y. (2013). Rapid re-infection with soil-transmitted helminths after triple-dose albendazole treatment of school-aged children in Yunnan, People's Republic of China. *The American Journal of Tropical Medicine and Hygiene* **89**, 23–31. doi: 10.4269/ajtmh.13-0009.

Dudak, J., Zemlicka, J., Karch, J., Patzelt, M., Mrzilkova, J., Zach, P., Hermanova, Z., Kvacek, J. and Krejci, F. (2016). High-contrast X-ray micro- radiography and micro-CT of ex-vivo soft tissue murine organs utilizing ethanol fixation and large area photon-counting detector. *Nature Publishing Group*. doi: 10.1038/srep30385.

Dullin, C., Ufartes, R., Larsson, E., Martin, S., Lazzarini, M., Tromba, G., Missbach-Guentner, J., Pinkert-Leetsch, D., Katschinski, D. M. and Alves, F. (2017). µCT of ex-vivo stained mouse hearts and embryos enables a precise match between 3D virtual histology, classical histology and immunochemistry. *PLOS ONE* **12**, e0170597. doi: 10.1371/journal.pone.0170597.

Dunmore-Buyze, P. J., Tate, E., Xiang, F. L., Detombe, S. A., Nong, Z., Pickering, J. G. and Drangova, M. (2014). Three-dimensional imaging of the mouse heart and vasculature using micro-CT and whole-body perfusion of iodine or phosphotungstic acid. *Contrast Media and Molecular Imaging* **9**, 383–390. doi: 10.1002/cmmi.1588.

Dunmore-Buyze, P. J., Cruje, C., Nong, Z., Lee, J. J., Kiernan, J. A., Pickering, J. G. and Drangova, M. (2019). 3D vessel-wall virtual histology of whole-body perfused mice using a novel heavy element stain. *Scientific Reports* **9**, 698. doi: 10.1038/s41598-018-36905-z.

Edens, W. A., Sharling, L., Cheng, G., Shapira, R., Kinkade, J. M., Lee, T., Edens, H. A., Tang, X., Sullards, C., Flaherty, D. B., Benian, G. M. and David Lambeth, J. (2001). Tyrosine cross-linking of extracellular matrix is catalyzed by Duox, a multidomain oxidase/peroxidase with homology to the phagocyte oxidase subunit gp91phox. *Journal of Cell Biology* **154**, 879–891. doi: 10.1083/jcb.200103132.

Egan, C. K., Jacques, S. D. M., Wilson, M. D., Veale, M. C., Seller, P., Beale, A. M., Pattrick, R. A. D., Withers, P. J. and Cernik, R. J. (2015). 3D chemical imaging in the laboratory by hyperspectral X-ray computed tomography. *Scientific Reports* **5**, 15979. doi: 10.1038/srep15979.

Egerton, R. F. (2005). TEM Specimens and Images. In *Physical Principles of Electron Microscopy*, pp. 93–124. Springer US, New York.

Eissa, M. M., El Bardicy, S. and Tadros, M. (2011a). Bioactivity of miltefosine against aquatic stages of Schistosoma mansoni, Schistosoma haematobium and their snail hosts, supported by scanning electron microscopy. *Parasites & Vectors* **4**, 73. doi: 10.1186/1756-3305-4-73.

Eissa, M. M., El-Azzouni, M. Z., Amer, E. I. and Baddour, N. M. (2011b). Miltefosine, a promising novel agent for schistosomiasis mansoni. *International Journal for Parasitology* **41**, 235–242. doi: 10.1016/j.ijpara.2010.09.010.

Elhenawy, A. A., Ashour, R. H., Nabih, N., Shalaby, N. M. and Megahed, N. (2017). Possible antifibrotic effect of GDC-0449 (Vismodegib), a hedgehog-pathway inhibitor, in mice model of Schistosoma-induced liver fibrosis. *Parasitology International* **66**, 545–554. doi:

10.1016/j.parint.2017.04.004.

Else, K. J. and Grencis, R. K. (1991). Helper T-cell subsets in mouse trichuriasis. *Parasitology Today*. doi: 10.1016/0169-4758(91)90268-S.

Else, K. J. and Grencis, R. K. (1996). Antibody-independent effector mechanisms in resistance to the intestinal nematode parasite Trichuris muris. *Infection and immunity* **64**, 2950–2954.

Else, K. J., Hültner, L. and Grencis, R. K. (1992). Modulation of cytokine production and response phenotypes in murine trichuriasis. *Parasite Immunology* **14**, 441–449. doi: 10.1111/j.1365-3024.1992.tb00018.x.

Else, K. J., Finkelman, F. D., Maliszewski, C. R. and Grencis, R. K. (1994). Cytokine-mediated regulation of chronic intestinal helminth infection. *Journal of Experimental Medicine* **179**, 347–351. doi: 10.1084/jem.179.1.347.

Engelke, K., Museyko, O., Wang, L. and Laredo, J.-D. (2018). Quantitative analysis of skeletal muscle by computed tomography imaging—State of the art. *Journal of Orthopaedic Translation* **15**, 91–103. doi: 10.1016/j.jot.2018.10.004.

Epah, J., Pálfi, K., Dienst, F. L., Malacarne, P. F., Bremer, R., Salamon, M., Kumar, S., Jo, H., Schürmann, C. and Brandes, R. P. (2018). 3D imaging and quantitative analysis of vascular networks: A comparison of ultramicroscopy and micro-computed tomography. *Theranostics* **8**, 2117–2133. doi: 10.7150/thno.22610.

Erben, U., Loddenkemper, C., Doerfel, K., Spieckermann, S., Haller, D., Heimesaat, M. M., Zeitz, M., Siegmund, B. and Kühl, A. A. (2014). A guide to histomorphological evaluation of intestinal inflammation in mouse models. *International journal of clinical and experimental pathology* **7**, 4557–4576. doi: 25197329.

Eshar, S., Dahan-Pasternak, N., Weiner, A., Dzikowski, R., WHO, Miller, L. H., al., et, Cowman, A. F., Crabb, B. S., Plattner, F., Soldati-Favre, D., Cesbron-Delauw, M. F., al., et, Schermelleh, L., al., et, Toomre, D., Bewersdorf, J., Subramaniam, S., Milne, J. L., Weiner, A., al., et, Riglar, D. T., al., et, Hanssen, E., al., et, Elliott, D. A., al., et, Bakar, N. A., al., et, Aikawa, M., al., et, Ladda, R., al., et, Miller, L. H., al., et, Baum, J., al., et, Schermelleh, L., al., et, Boyle, M. J., al., et, Yeoman, J. A., al., et, Francis, S. E., al., et, Aikawa, M., Aikawa, M., Aikawa, M., Antonovych, T. T., Aikawa, M., Aikawa, M., al., et, Aikawa, M., al., et, Aikawa, M., McEwen, B. F., Marko, M., Slomianny, C., Lazarus, M. D., al., et, Lucic, V., al., et, Larabell, C. A., Gros, M. A. Le, Gros, M. A. Le, al., et, Parkinson, D. Y., al., et, McDermott, G., al., et, Schneider, G., al., et, Hanssen, E., al., et, Dluzewski, A. R., al., et, Lanzer, M., al., et, Bhattacharjee, S., al., et, Crabb, B. S., al., et, Haase, S., Koning-Ward, T. F. de, Wickert, H., Krohne, G., Przyborski, J. M., al., et, Wickert, H., al., et, Spycher, C., al., et, Hanssen, E., al., et, Spycher, C., al., et, Henrich, P., al., et, et al. (2011). *High resolution 3D perspective of Plasmodium biology: Advancing into a new era*. Elsevier doi: 10.1016/j.pt.2011.08.002.

Fallon, P. G. (2000). Immunopathology of schistosomiasis: a cautionary tale of mice and men. *Immunology Today* **21**, 29–35. doi: 10.1016/S0167-5699(99)01551-0.

Faraj, K. A., Cuijpers, V. M. J. I., Wismans, R. G., Walboomers, X. F., Jansen, J. A., van Kuppevelt, T. H. and Daamen, W. F. (2009). Micro-computed tomographical imaging of soft biological materials using contrast techniques. *Tissue Engineering Part C: Methods* **15**, 493–499. doi: 10.1089/ten.tec.2008.0436.

Feliu, C., Spakulová, M., Casanova, J. C., Renaud, F., Morand, S., Hugot, J. P., Santalla, F. and Durand, P. (2000). Genetic and morphological heterogeneity in small rodent whipworms in southwestern Europe: characterization of Trichuris muris and description of Trichuris arvicolae n. sp. (Nematoda: Trichuridae). *Journal of Parasitology* **86**, 442–449. doi: 10.1645/0022-3395(2000)086[0442:GAMHIS]2.0.CO;2.

Feng, Z., Marti, A., Jehn, B., Altermatt, H. J., Chicaiza, G. and Jaggi, R. (1995). Glucocorticoid and progesterone inhibit involution and programmed cell death in the mouse mammary gland. *The Journal of Cell Biology* **131**, 1095–1103. doi:

10.1083/jcb.131.4.1095.

Fetterer, R. H. and Rhoads, M. L. (1993). Biochemistry of the nematode cuticle: relevance to parasitic nematodes of livestock. *Veterinary Parasitology* **46**, 103–111. doi: 10.1016/0304-4017(93)90051-N.

Fonseca, M. de C., Araujo, B. H. S., Dias, C. S. B., Archilha, N. L., Neto, D. P. A., Cavalheiro, E., Westfahl, H., da Silva, A. J. R. and Franchini, K. G. (2018). High-resolution synchrotron-based X-ray microtomography as a tool to unveil the three-dimensional neuronal architecture of the brain. *Scientific Reports* **8**, 12074. doi: 10.1038/s41598-018-30501-x.

Foth, B. J., Tsai, I. J., Reid, A. J., Bancroft, A. J., Nichol, S., Tracey, A., Holroyd, N., Cotton, J. A., Stanley, E. J., Zarowiecki, M., Liu, J. Z., Huckvale, T., Cooper, P. J., Grencis, R. K. and Berriman, M. (2014). Whipworm genome and dual-species transcriptome analyses provide molecular insights into an intimate host-parasite interaction. *Nature Genetics* **46**, 693–700. doi: 10.1038/ng.3010.

Franco, L., Yague-Fabra, J. A., Jimenez, R., Maestro, M. and Ontiveros, S. (2014). Error sources analysis of computed tomography for dimensional metrology: an experimental approach. In *11th European Conference on Non-Destructive Testing (ECNDT 2014)*, .

Friedman, J. F., Kanzaria, H. K. and McGarvey, S. T. (2005). Human schistosomiasis and anemia: the relationship and potential mechanisms. *Trends in Parasitology* **21**, 386–392. doi: 10.1016/j.pt.2005.06.006.

Friedrich, R. W., Genoud, C. and Wanner, A. A. (2013). Analyzing the structure and function of neuronal circuits in zebrafish. *Frontiers in Neural Circuits* **7**, 71. doi: 10.3389/fncir.2013.00071.

Gardner, J. M., Grantham-Mcgregor, S. and Baddeley, A. (1996). Trichuris trichiura infection and cognitive function in Jamaican school children. *Annals of Tropical Medicine & Parasitology* **90**, 55–63. doi: 10.1080/00034983.1996.11813026.

Geary, T. G. (2012). Are new anthelmintics needed to eliminate human helminthiases? *Current Opinion in Infectious Diseases* **25**, 709–717. doi: 10.1097/QCO.0b013e328359f04a.

Gengenbacher, M. and Kaufmann, S. H. E. (2012). Mycobacterium tuberculosis : success through dormancy. *FEMS Microbiology Reviews* **36**, 514–532. doi: 10.1111/j.1574-6976.2012.00331.x.

Georgi, J. R. (1982). Schistosoma mansoni: quantification of skin penetration and early migration by differential external radioassay and autoradiography. *Parasitology* **84**, 263. doi: 10.1017/S0031182000044826.

Georgi, J. R., Dean, D. A. and Mangold, B. L. (1983). Schistosoma mansoni: temporal distribution of radioselenium-labelled schistosomula in lungs of mice during the first two weeks of infection. *Parasitology* **86**, 31–36.

Ghanavati, S., Yu, L. X., Lerch, J. P. and Sled, J. G. (2014). A perfusion procedure for imaging of the mouse cerebral vasculature by X-ray micro-CT. *Journal of Neuroscience Methods* **221**, 70–77. doi: 10.1016/j.jneumeth.2013.09.002.

Gignac, P. M. and Kley, N. J. (2014). Iodine-enhanced micro-CT imaging: Methodological refinements for the study of the soft-tissue anatomy of post-embryonic vertebrates. *Journal of Experimental Zoology Part B: Molecular and Developmental Evolution* **322**, 166–176. doi: 10.1002/jez.b.22561.

Gignac, P. M., Kley, N. J., Clarke, J. A., Colbert, M. W., Morhardt, A. C., Cerio, D., Cost, I. N., Cox, P. G., Daza, J. D., Early, C. M., Echols, M. S., Henkelman, R. M., Herdina, A. N., Holliday, C. M., Li, Z., Mahlow, K., Merchant, S., Müller, J., Orsbon, C. P., Paluh, D. J., Thies, M. L., Tsai, H. P. and Witmer, L. M. (2016). Diffusible iodine-based contrast-enhanced computed tomography (diceCT): an emerging tool for rapid, high-resolution, 3-D imaging of metazoan soft tissues. *Journal of Anatomy* **228**, 889–909. doi:

10.1111/joa.12449.

Gorgas, D., Marreros, N., Rufener, R., Hemphill, A. and Lundstrom-Stadelmann, B. (2017). To see or not to see: non-invasive imaging for improved readout of drug treatment trials in the murine model of secondary alveolar echinococcosis. *Parasitology* **144**, 937–944. doi: 10.1017/S0031182017000051.

Grabherr, S., Hess, A., Karolczak, M., Thali, M. J., Friess, S. D., Kalender, W. A., Dirnhofer, R. and Djonov, V. (2008a). Angiofil®-mediated visualization of the vascular system by microcomputed tomography: A feasibility study. *Microscopy Research and Technique* **71**, 551–556. doi: 10.1002/jemt.20585.

Grabherr, S., Dominietto, M., Yu, L., Djonov, V., Müller, B. and Friess, S. (2008b). Angiofil: a novel radio-contrast agent for post-mortem micro-angiography. In *Proc. SPIE 7078, Developments in X-ray Tomography VI* (ed. Stock, S. R.), p. 70781O. doi: 10.1117/12.792077.

Graham, B. B., Bandeira, A. P., Morrell, N. W., Butrous, G. and Tuder, R. M. (2010). Schistosomiasis-associated pulmonary hypertension. *Chest* **137**, 20S-29S. doi: 10.1378/chest.10-0048.

Greger, K., Swoger, J. and Stelzer, E. H. K. (2007). Basic building units and properties of a fluorescence single plane illumination microscope. *Review of Scientific Instruments* **78**, 023705. doi: 10.1063/1.2428277.

Grimaud, J. A. and Borojevic, R. (1977). Chronic human schistosomiasis mansoni. Pathology of the Disse's space. *Laboratory Investigation* **36**, 268–273.

Gryseels, B., Polman, K., Clerinx, J. and Kestens, L. (2006). Human schistosomiasis. *The Lancet* **368**, 1106–1118. doi: 10.1016/S0140-6736(06)69440-3.

Guidi, A., Lalli, C., Perlas, E., Bolasco, G., Nibbio, M., Monteagudo, E., Bresciani, A. and Ruberti, G. (2016). Discovery and characterization of novel anti-schistosomal properties of the anti-anginal drug, perhexiline and its impact on Schistosoma mansoni male and female reproductive systems. *PLOS Neglected Tropical Diseases* **10**, e0004928. doi: 10.1371/journal.pntd.0004928.

H Salim, O. E., Hamid, H. K. S., Mekki, S. O., Suleiman, S. H. and Ibrahim, S. Z. (2010). Colorectal carcinoma associated with schistosomiasis: a possible causal relationship. *World Journal of Surgical Oncology* **8**, 68. doi: 10.1186/1477-7819-8-68.

Halton, D. W. (2004). Microscopy and the helminth parasite. *Micron* **35**, 361–390. doi: 10.1016/j.micron.2003.12.001.

Hama, H., Kurokawa, H., Kawano, H., Ando, R., Shimogori, T., Noda, H., Fukami, K., Sakaue-Sawano, A. and Miyawaki, A. (2011). Scale: a chemical approach for fluorescence imaging and reconstruction of transparent mouse brain. *Nature Neuroscience* **14**, 1481–1488. doi: 10.1038/nn.2928.

Handschuh, S., Baeumler, N., Schwaha, T. and Ruthensteiner, B. (2013). A correlative approach for combining microCT, light and transmission electron microscopy in a single 3D scenario. *Frontiers in Zoology* **10**, 44. doi: 10.1186/1742-9994-10-44.

Handschuh, S., Beisser, C. J., Ruthensteiner, B. and Metscher, B. D. (2017). Microscopic dual-energy CT (microDECT): a flexible tool for multichannel ex vivo 3D imaging of biological specimens. *Journal of Microscopy*. doi: 10.1111/jmi.12543.

Hansen, T. V. A., Hansen, M., Nejsum, P., Mejer, H., Denwood, M. and Thamsborg, S. M. (2016). Glucose absorption by the bacillary band of Trichuris muris. *PLoS neglected tropical diseases* **10**, e0004971. doi: 10.1371/journal.pntd.0004971.

Harris, R., Hiles, I., Page, M. and O'Hare, M. (1995). The induction of apoptosis in human mammary luminal epithelial cells by expression of activated c-neu and its abrogation by glucocorticoids. *British Journal of Cancer* **72**, 386–392. doi: 10.1038/bjc.1995.343.

Hasnain, S. Z., Evans, C. M., Roy, M., Gallagher, A. L., Kindrachuk, K. N., Barron, L., Dickey, B. F., Wilson, M. S., Wynn, T. A., Grencis, R. K. and Thornton, D. J. (2011). Muc5ac: a critical component mediating the rejection of enteric nematodes. *Journal of Experimental Medicine* **208**, 893–900. doi: 10.1084/jem.20102057.

Hayes, T. L. (1963). A quantitative determination of the osmium tetroxide-lipoprotein interaction. *The Journal of Cell Biology* **19**, 251–255. doi: 10.1083/jcb.19.1.251.

Hayes, K. S., Bancroft, A. J. and Grencis, R. K. (2007). The role of TNF-α in Trichuris muris infection I: Influence of TNF-α receptor usage, gender and IL-13. *Parasite Immunology* **29**, 575–582. doi: 10.1111/j.1365-3024.2007.00979.x.

Hayes, K. S., Cliffe, L. J., Bancroft, A. J., Forman, S. P., Thompson, S., Booth, C. and Grencis, R. K. (2017). Chronic Trichuris muris infection causes neoplastic change in the intestine and exacerbates tumour formation in APC min/+ mice. *PLOS Neglected Tropical Diseases* **11**, e0005708. doi: 10.1371/journal.pntd.0005708.

Hedegaard, J., Thorsen, K., Lund, M. K., Hein, A.-M. K., Hamilton-Dutoit, S. J., Vang, S., Nordentoft, I., Birkenkamp-Demtröder, K., Kruhøffer, M., Hager, H., Knudsen, B., Andersen, C. L., Sørensen, K. D., Pedersen, J. S., Ørntoft, T. F. and Dyrskjøt, L. (2014). Next-generation sequencing of RNA and DNA isolated from paired fresh-frozen and formalin-fixed paraffin-embedded samples of human cancer and normal tissue. *PLoS ONE* **9**, e98187. doi: 10.1371/journal.pone.0098187.

Heimstadt, O. (1911). Das Fluoreszenzmikroskop. *Zeitschrift fur Wissenschaftliche Mikroskopie und Mikroskopische Technik* **28**, 330–337.

Helmby, H., Takeda, K., Akira, S. and Grencis, R. K. (2001). Interleukin (IL)-18 promotes the development of chronic gastrointestinal helminth infection by downregulating IL-13. *The Journal of Experimental Medicine* **194**, 355–364. doi: 10.1084/jem.194.3.355.

Hemphill, A., Stadelmann, B., Rufener, R., Spiliotis, M., Boubaker, G., M?ller, J., M?ller, N., Gorgas, D. and Gottstein, B. (2014). Treatment of echinococcosis: albendazole and mebendazole--what else? *Parasite* **21**, 70. doi: 10.1051/parasite/2014073.

Herman, A. M., Kishe, A., Babu, H., Shilanaiman, H., Tarmohamed, M., Lodhia, J., Amsi, P., Pyuza, J., Mremi, A., Mwasamwaja, A., Nyindo, M., Chilonga, K. and Msuya, D. (2017). Colorectal cancer in a patient with intestinal schistosomiasis: a case report from Kilimanjaro Christian Medical Center Northern Zone Tanzania. *World Journal of Surgical Oncology* **15**, 146. doi: 10.1186/s12957-017-1217-1.

Heude, E., Tesarova, M., Sefton, E. M., Jullian, E., Adachi, N., Grimaldi, A., Zikmund, T., Kaiser, J., Kardon, G., Kelly, R. G. and Tajbakhsh, S. (2018). Unique morphogenetic signatures define mammalian neck muscles and associated connective tissues. *eLife* **7**,. doi: 10.7554/eLife.40179.

Hlushchuk, R., Haberthür, D. and Djonov, V. (2019). Ex vivo microangioCT: Advances in microvascular imaging. *Vascular Pharmacology* **112**, 2–7. doi: 10.1016/j.vph.2018.09.003.

Hoffmann, K. F., Brindley, P. J. and Berriman, M. (2014). Halting harmful helminths. *Science* **346**, 168–169. doi: 10.1126/science.1261139.

Hofman, P., Badoual, C., Henderson, F., Berland, L., Hamila, M., Long-Mira, E., Lassalle, S., Roussel, H., Hofman, V., Tartour, E. and Ilié, M. (2019). Multiplexed immunohistochemistry for molecular and immune profiling in lung cancer—just about ready for prime-time? *Cancers* **11**, 283. doi: 10.3390/cancers11030283.

Horobin, R. W. (2002). Biological staining: mechanisms and theory. *Biotechnic & Histochemistryi* **77**, 3–13.

Horobin, R. W. and Flemming, L. (1988). One-bath trichrome staining: Investigation of a general mechanism based on a structure-staining correlation analysis. *The Histochemical Journal* **20**, 29–34. doi: 10.1007/BF01745966.

Hsu, C., Kalaga, S., Akoma, U., Rasmussen, T. L., Christiansen, A. E. and Dickinson, M. E. (2019). High resolution imaging of mouse embryos and neonates with X-Ray micro-computed tomography. *Current Protocols in Mouse Biology* e63. doi: 10.1002/cpmo.63.

Huang, B., Bates, M. and Zhuang, X. (2009). Super-resolution fluorescence microscopy. *Annual Review of Biochemistry* **78**, 993–1016. doi: 10.1146/annurev.biochem.77.061906.092014.

Hughes, L., Towers, K., Starborg, T., Gull, K. and Vaughan, S. (2013). A cell-body groove housing the new flagellum tip suggests an adaptation of cellular morphogenesis for parasitism in the bloodstream form of Trypanosoma brucei. *Journal of Cell Science* **126**, 5748–5757. doi: 10.1242/jcs.139139.

Hullar, T., Paige, D. F., Rowland, D. J. and Anastasio, C. (2014). Compact cold stage for micro-computerized tomography imaging of chilled or frozen samples. *Review of Scientific Instruments* **85**, 043708. doi: 10.1063/1.4871473.

Humphreys, N. E., Xu, D., Hepworth, M. R., Liew, F. Y. and Grencis, R. K. (2008). IL-33, a potent inducer of adaptive immunity to intestinal nematodes. *Journal of Immunology* **180**, 2443–2449. doi: 10.4049/jimmunol.180.4.2443.

Hunter, R. L. (2011). Pathology of post primary tuberculosis of the lung: An illustrated critical review. *Tuberculosis* **91**, 497–509. doi: 10.1016/j.tube.2011.03.007.

Hunter, R. L. (2016). Tuberculosis as a three-act play: A new paradigm for the pathogenesis of pulmonary tuberculosis. *Tuberculosis* **97**, 8–17. doi: 10.1016/j.tube.2015.11.010.

Hunter, R. L., Jagannath, C. and Actor, J. K. (2007). Pathology of postprimary tuberculosis in humans and mice: Contradiction of long-held beliefs. *Tuberculosis* **87**, 267–278. doi: 10.1016/j.tube.2006.11.003.

Hurst, R. J. M. and Else, K. J. (2013). Trichuris muris research revisited: a journey through time. *Parasitology* **140**, 1325–1339. doi: 10.1017/S0031182013001054.

Hussmann, J., Russell, R. C., Kucan, J. O., Khardori, R. and Steinau, H. U. (1995). Soft-tissue calcifications: differential diagnosis and therapeutic approaches. *Annals of plastic surgery* **34**, 138–147.

Hüttemann, M., Schmahl, G. and Mehlhorn, H. (2007). Light and electron microscopic studies on two nematodes, Angiostrongylus cantonensis and Trichuris muris, differing in their mode of nutrition. *Parasitology Research* **101**, 225–232. doi: 10.1007/s00436-007-0698-1.

Huxley, H. E. (1957). The double array of filaments in cross-striated muscle. *Journal of Biophysical and Biochemical Cytology* **3**, 631–648.

Irimia, A., Maher, A. S., Rostowsky, K. A., Chowdhury, N. F., Hwang, D. H. and Law, E. M. (2019). Brain segmentation from computed tomography of healthy aging and geriatric concussion at variable spatial resolutions. *Frontiers in Neuroinformatics* **13**,. doi: 10.3389/fninf.2019.00009.

Ittiprasert, W., Mann, V. H., Karinshak, S. E., Coghlan, A., Rinaldi, G., Sankaranarayanan, G., Chaidee, A., Tanno, T., Kumkhaek, C., Prangtaworn, P., Mentink-Kane, M. M., Cochran, C. J., Driguez, P., Holroyd, N., Tracey, A., Rodpai, R., Everts, B., Hokke, C. H., Hoffmann, K. F., Berriman, M. and Brindley, P. J. (2019). Programmed genome editing of the omega-1 ribonuclease of the blood fluke, Schistosoma mansoni. *eLife* **8**,. doi: 10.7554/eLife.41337.

Jensen, M. M., Jørgensen, J. T., Binderup, T. and Kjær, A. (2008). Tumor volume in subcutaneous mouse xenografts measured by microCT is more accurate and reproducible than determined by 18F-FDG-microPET or external caliper. *BMC Medical Imaging* **8**, 16. doi: 10.1186/1471-2342-8-16.

Jia, T., Melville, S., Rg Utzinger, J., King, C. H. and Zhou, X. (2012). Soil-transmitted helminth reinfection after drug treatment: a systematic review and meta-analysis. *PLoS*

Neglected Tropical Diseases **6**, e1621. doi: 10.1371/journal.pntd.0001621.

Johnstone, I. L. (1994). The cuticle of the nematode Caenorhabditis elegans: a complex collagen structure. *BioEssays* **16**, 171–178. doi: 10.1002/bies.950160307.

Johnstone, I. L. (2000). Cuticle collagen genes. *Trends in Genetics* **16**, 21–27. doi: 10.1016/S0168-9525(99)01857-0.

Jones, M. V and Calabresi, P. A. (2007). Agar-gelatin for embedding tissues prior to paraffin processing. *BioTechniques* **42**, 569–70.

Jung, H., Medina, L., García, L., Fuentes, I. and Moreno-Esparza, R. (1998). Absorption studies of albendazole and some physicochemical properties of the drug and its metabolite albendazole sulphoxide. *Journal of Pharmacy and Pharmacology* **50**, 43–48.

Junqueira, L. C. U., Bignolas, G. and Brentani, R. R. (1979). Picrosirius staining plus polarization microscopy, a specific method for collagen detection in tissue sections. *The Histochemical Journal* **11**, 447–455. doi: 10.1007/BF01002772.

Kalson, N. S., Starborg, T., Lu, Y., Mironov, A., Humphries, S. M., Holmes, D. F. and Kadler, K. E. (2013). Nonmuscle myosin II powered transport of newly formed collagen fibrils at the plasma membrane. *Proceedings of the National Academy of Sciences of the United States of America* **110**, 4743–4752. doi: 10.1073/pnas.1314348110.

Kamel, R. O. A. and Bayaumy, F. E.-Z. A. (2017). Ultrastructural alterations in Schistosoma mansoni juvenile and adult male worms after in vitro incubation with primaquine. *Memórias do Instituto Oswaldo Cruz* **112**, 247–254. doi: 10.1590/0074-02760160324.

Kaminsky, R. G., Castillo, R. V. and Flores, C. A. (2015). Growth retardation and severe anemia in children with Trichuris dysenteric syndrome. *Asian Pacific Journal of Tropical Biomedicine* **5**, 591–597. doi: 10.1016/j.apjtb.2015.05.005.

Kampschulte, M., Erdmann, G., Sender, J., Martels, G., Böcker, W., ElKhassawna, T., Heiß, C., Langheinrich, A. C., Roeb, E., Roderfeld, M. and Krombach, G. A. (2015). The development and validation of micro-CT of large deep frozen specimens. *Scanning* **37**, 63–72. doi: 10.1002/sca.21180.

Kampschulte, M., Langheinirch, A., Sender, J., Litzlbauer, H., Althöhn, U., Schwab, J., Alejandre-Lafont, E., Martels, G. and Krombach, G. (2016). Nano-computed tomography: technique and applications. *RöFo - Fortschritte auf dem Gebiet der Röntgenstrahlen und der bildgebenden Verfahren* **188**, 146–154. doi: 10.1055/s-0041-106541.

Kantor, B., Jorgensen, S. M., Lund, P. E., Chmelik, M. S., Reyes, D. A. and Ritman, E. L. (2006). Cryostatic micro-computed tomography imaging of arterial wall perfusion. *Scanning* **24**, 186–190. doi: 10.1002/sca.4950240405.

Keiser, J. and Utzinger, J. (2008). Efficacy of current drugs against soil-transmitted helminth infections: systematic review and meta-analysis. *JAMA* **299**, 1937–1948. doi: 10.1001/jama.299.16.1937.

Keiser, J., Tritten, L., Silbereisen, A., Speich, B., Adelfio, R. and Vargas, M. (2013). Activity of oxantel pamoate monotherapy and combination chemotherapy against Trichuris muris and hookworms: revival of an old drug. *PLoS neglected tropical diseases* **7**, e2119. doi: 10.1371/journal.pntd.0002119.

Keisuke Uchida, T. I. (2013). Calcified granulomatous lung lesions contain abundant Mycobacterium tuberculosis components. *Mycobacterial Diseases* **4**,. doi: 10.4172/2161-1068.1000142.

Keklikoglou, K., Faulwetter, S., Chatzinikolaou, E., Wils, P., Brecko, J., Kvaček, J., Metscher, B. and Arvanitidis, C. (2019). Micro-computed tomography for natural history specimens: a handbook of best practice protocols. *European Journal of Taxonomy*. doi: 10.5852/ejt.2019.522.

Khalaf, I., Shokeir, A. and Shalaby, M. (2012). Urologic complications of genitourinary schistosomiasis. *World Journal of Urology* **30**, 31–38. doi: 10.1007/s00345-011-0751-7.

Khan, W. I., Richard, M., Akiho, H., Blennerhasset, P. A., Humphreys, N. E., Grencis, R. K., Van Snick, J. and Collins, S. M. (2003). Modulation of Intestinal Muscle Contraction by Interleukin-9 (IL-9) or IL-9 Neutralization: Correlation with Worm Expulsion in Murine Nematode Infections. *Infection and Immunity* **71**, 2430–2438. doi: 10.1128/IAI.71.5.2430-2438.2003.

Kim, C. W. and Ledbetter, M. C. (1980). Surface Morphology of Trichinella spiralis by Scanning Electron Microscopy. *Journal of Parasitology* **66**, 75. doi: 10.2307/3280593.

King, C. H. and Dangerfield-Cha, M. (2008). The unacknowledged impact of chronic schistosomiasis. *Chronic Illness* **4**, 65–79. doi: 10.1177/1742395307084407.

Klement, R. and Trömel, G. (1932). Hydroxylapatit, der hauptbestandteil der anorganischen knochen- und zahnsubstanz. *Hoppe-Seyler´s Zeitschrift für physiologische Chemie* **213**, 263–269. doi: 10.1515/bchm2.1932.213.5-6.263.

Klementowicz, J. E., Travis, M. A. and Grencis, R. K. (2012). Trichuris muris: a model of gastrointestinal parasite infection. *Seminars in Immunopathology* **34**, 815–828. doi: 10.1007/s00281-012-0348-2.

Knight, R. A. (1984). Morphological differences in Trichuris ovis associated with different host species. *Journal of Parasitology* **70**, 842–843.

Kobat, D., Durst, M. E., Nishimura, N., Wong, A. W., Schaffer, C. B. and Xu, C. (2009). Deep tissue multiphoton microscopy using longer wavelength excitation. *Optics Express* **17**, 13354. doi: 10.1364/OE.17.013354.

Kourra, N., Warnett, J. M., Attridge, A., Dahnel, A., Ascroft, H., Barnes, S. and Williams, M. A. (2016). A metrological inspection method using micro-CT for the analysis of drilled holes in CFRP and titanium stacks. *International Journal of Advanced Manufacturing Technology* **88**, 1417–1427. doi: 10.1007/s00170-016-8691-4.

Kremer, J. R., Mastronarde, D. N. and McIntosh, J. R. (1996). Computer visualization of three-dimensional image data using IMOD. *Journal of Structural Biology* **116**, 71–76. doi: 10.1006/jsbi.1996.0013.

Kuang, J., Yan, X., Genders, A. J., Granata, C. and Bishop, D. J. (2018). An overview of technical considerations when using quantitative real-time PCR analysis of gene expression in human exercise research. *PLOS ONE* **13**, e0196438. doi: 10.1371/journal.pone.0196438.

Kyu, H. H., Abate, D., Abate, K. H., Abay, S. M., Abbafati, C., Abbasi, N., Abbastabar, H., Abd-Allah, F., Abdela, J., Abdelalim, A., Abdollahpour, I., Abdulkader, R. S., Abebe, M., Abebe, Z., Abil, O. Z., Aboyans, V., Abrham, A. R., Abu-Raddad, L. J., Abu-Rmeileh, N. M. E., Accrombessi, M. M. K., Acharya, D., Acharya, P., Ackerman, I. N., Adamu, A. A., Adebayo, O. M., Adekanmbi, V., Ademi, Z., Adetokunboh, O. O., Adib, M. G., Adsuar, J. C., Afanvi, K. A., Afarideh, M., Afshin, A., Agarwal, G., Agesa, K. M., Aggarwal, R., Aghayan, S. A., Agrawal, A., Ahmadi, A., Ahmadi, M., Ahmadieh, H., Ahmed, M. B., Ahmed, S., Aichour, A. N., Aichour, I., Aichour, M. T. E., Akinyemiju, T., Akseer, N., Al-Aly, Z., Al-Eyadhy, A., Al-Mekhlafi, H. M., Al-Raddadi, R. M., Alahdab, F., Alam, K., Alam, T., Alashi, A., Alavian, S. M., Alene, K. A., Alijanzadeh, M., Alizadeh-Navaei, R., Aljunid, S. M., Alkerwi, A., Alla, F., Allebeck, P., Alonso, J., Alsharif, U., Altirkawi, K., Alvis-Guzman, N., Aminde, L. N., Amini, E., Amiresmaili, M., Ammar, W., Amoako, Y. A., Anber, N. H., Andrei, C. L., Androudi, S., Animut, M. D., Anjomshoa, M., Ansha, M. G., Antonio, C. A. T., Anwari, P., Arabloo, J., Aremu, O., Ärnlöv, J., Arora, A., Arora, M., Artaman, A., Aryal, K. K., Asayesh, H., Ataro, Z., Ausloos, M., Avila-Burgos, L., Avokpaho, E. F. G. A., Awasthi, A., Ayala Quintanilla, B. P., Ayer, R., Azzopardi, P. S., Babazadeh, A., et al. (2018a). Global, regional, and national disability-adjusted life-years (DALYs) for 359 diseases and injuries and healthy life expectancy (HALE) for 195 countries and territories, 1990–2017: a systematic analysis for the Global Burden of Disease Study 2017. *The Lancet* **392**, 1859–1922. doi:

10.1016/S0140-6736(18)32335-3.

Kyu, H. H., Maddison, E. R., Henry, N. J., Ledesma, J. R., Wiens, K. E., Reiner, R., Biehl, M. H., Shields, C., Osgood-Zimmerman, A., Ross, J. M., Carter, A., Frank, T. D., Wang, H., Srinivasan, V., Agarwal, S. K., Alahdab, F., Alene, K. A., Ali, B. A., Alvis-Guzman, N., Andrews, J. R., Antonio, C. A. T., Atique, S., Atre, S. R., Awasthi, A., Ayele, H. T., Badali, H., Badawi, A., Barac, A., Bedi, N., Behzadifar, M., Behzadifar, M., Bekele, B. B., Belay, S. A., Bensenor, I. M., Butt, Z. A., Carvalho, F., Cercy, K., Christopher, D. J., Daba, A. K., Dandona, L., Dandona, R., Daryani, A., Demeke, F. M., Deribe, K., Dharmaratne, S. D., Doku, D. T., Dubey, M., Edessa, D., El-Khatib, Z., Enany, S., Fernandes, E., Fischer, F., Garcia-Basteiro, A. L., Gebre, A. K., Gebregergs, G. B., Gebremichael, T. G., Gelano, T. F., Geremew, D., Gona, P. N., Goodridge, A., Gupta, R., Haghparast Bidgoli, H., Hailu, G. B., Hassen, H. Y., Hedayati, M. T. T., Henok, A., Hostiuc, S., Hussen, M. A., Ilesanmi, O. S., Irvani, S. S. N., Jacobsen, K. H., Johnson, S. C., Jonas, J. B., Kahsay, A., Kant, S., Kasaeian, A., Kassa, T. D., Khader, Y. S., Khafaie, M. A., Khalil, I., Khan, E. A., Khang, Y.-H., Kim, Y. J., Kochhar, S., Koyanagi, A., Krohn, K. J., Kumar, G. A., Lakew, A. M., Leshargie, C. T., Lodha, R., Macarayan, E. R. K., Majdzadeh, R., Martins-Melo, F. R., Melese, A., Memish, Z. A., Mendoza, W., Mengistu, D. T., Mengistu, G., et al. (2018b). Global, regional, and national burden of tuberculosis, 1990–2016: results from the Global Burden of Diseases, Injuries, and Risk Factors 2016 Study. *The Lancet Infectious Diseases* **18**, 1329–1349. doi: 10.1016/S1473-3099(18)30625-X.

Lacey, E. (1990). Mode of action of benzimidazoles. *Parasitology Today* **6**, 112–115. doi: 10.1016/0169-4758(90)90227-U.

Lachant, D., Meoli, D. F., Haight, D., Staicu, S., Akers, S., Glickman, S., Ambrosini, R., Champion, H. C. and White, R. J. (2019). Combination therapy improves vascular volume in female rats with pulmonary hypertension. *American Journal of Physiology - Lung Cellular and Molecular Physiology* ajplung.00450.2018. doi: 10.1152/ajplung.00450.2018.

Lalvani, A., Sridhar, S. and von Reyn, C. F. (2013). Tuberculosis vaccines: time to reset the paradigm? *Thorax* **68**, 1092–1094. doi: 10.1136/thoraxjnl-2013-203456.

Lambertucci, J. R., Voieta, I. and Barbosa, A. J. A. (2005). Colonic polyps in hepatosplenic schistosomiasis mansoni. *Revista da Sociedade Brasileira de Medicina Tropical* **38**, 80–81. doi: 10.1590/S0037-86822005000100021.

Lanfredti, R. M. R., Souza, W. D. W. and Gomes, D. C. D. (1995). Comparative study of four species of Trichuris roederer, 1761 (Nematoda, Trichurinae) by scanning electron microscopy. *Memorias do Instituto Oswaldo Cruz* **90**, 489–496. doi: 10.1590/S0074-02761995000400011.

Larson, A. M. (2011). Multiphoton microscopy. *Nature Photonics* **5**, 1–1. doi: 10.1038/nphoton.an.2010.2.

Lee, T. D. G. and Wright, K. A. (1978). The morphology of the attachment and probable feeding site of the nematode Trichuris muris (Schrank, 1788) Hall, 1916. *Canadian Journal of Zoology* **56**, 1889–1905. doi: 10.1139/z78-258.

Lee, R. Y. N., Howe, K. L., Harris, T. W., Arnaboldi, V., Cain, S., Chan, J., Chen, W. J., Davis, P., Gao, S., Grove, C., Kishore, R., Muller, H. M., Nakamura, C., Nuin, P., Paulini, M., Raciti, D., Rodgers, F., Russell, M., Schindelman, G., Tuli, M. A., Van Auken, K., Wang, Q., Williams, G., Wright, A., Yook, K., Berriman, M., Kersey, P., Schedl, T., Stein, L. and Sternberg, P. W. (2018). WormBase 2017: Molting into a new stage. *Nucleic Acids Research*. doi: 10.1093/nar/gkx998.

Liu, Y., Liu, Q., Yang, Z., Lin, J., Wu, X., Huang, Z., Liu, J., Li, R., Huang, Z., Wu, X. and Zhu, Q. (2019). Comparison of three-dimensional micro-CT angiography of cervical spinal cord between two contrast agents. *Contrast Media & Molecular Imaging* 1–8. doi: 10.1155/2019/5215923.

Loker, E. S. (1983). A comparative study of the life-histories of mammalian schistosomes.

Parasitology **87 (Pt 2)**, 343–69. doi: 6359028.

Long, R., Maycher, B., Dhar, A., Manfreda, J., Hershfield, E. and Anthonisen, N. (1998). Pulmonary tuberculosis treated with directly observed therapy: serial changes in lung structure and function. *Chest* **113**, 933–943. doi: 10.1378/chest.113.4.933.

Lopes Torres, E. J., de Souza, W. and Miranda, K. (2013). Comparative analysis of Trichuris muris surface using conventional, low vacuum, environmental and field emission scanning electron microscopy. *Veterinary Parasitology* **196**, 409–416. doi: 10.1016/j.vetpar.2013.02.026.

Lwin, T.-T., Yoneyama, A., Hara, A., Ohbu, M., Maruyama, H., Taguchi, M., Esashi, S., Matsushima, T., Terazaki, K., Hyodo, K. and Takeda, T. (2016). Spontaneous brain tumor imaging of aged rat by crystal X-ray interferometer-based phase-contrast X-ray CT. *Acta Radiologica Open* **5**, 205846011562695. doi: 10.1177/2058460115626958.

Maire, E. and Withers, P. J. (2014). Quantitative X-ray tomography. *International Materials Reviews* **59**, 1–43. doi: 10.1179/1743280413Y.0000000023.

Malachevsky, M. T., Bertolino, G., Oliber, E., D'Ovidio, C., Baruj, A. and Cuscueta, D. (2019). Tomographic characterization of copper cellular bodies fabricated by a powder metallurgy route. *Materials Research Express* **6**, 056531. doi: 10.1088/2053-1591/ab0310.

Manneck, T., Braissant, O., Ellis, W. and Keiser, J. (2011). Schistosoma mansoni: Antischistosomal activity of the four optical isomers and the two racemates of mefloquine on schistosomula and adult worms in vitro and in vivo. *Experimental Parasitology* **127**, 260–269. doi: 10.1016/j.exppara.2010.08.011.

Manzella, A., Ohtomo, K., Monzawa, S. and Hoon Lim, J. (2007). Schistosomiasis of the liver. *Abdominal Imaging* **33**, 144–150.

Maran, A., Khosla, S., Riggs, B. L., Zhang, M., Ritman, E. L. and Turner, R. T. (2003). Measurement of gene expression following cryogenic mu-CT scanning of human iliac crest biopsies. *Journal of musculoskeletal & neuronal interactions* **3**, 83–88.

Martín-Vega, D., Garbout, A., Ahmed, F., Wicklein, M., Goater, C. P., Colwell, D. D. and Hall, M. J. R. (2018). 3D virtual histology at the host/parasite interface: visualisation of the master manipulator, Dicrocoelium dendriticum, in the brain of its ant host. *Scientific Reports* **8**, 8587. doi: 10.1038/s41598-018-26977-2.

Martinez-Murillo, P., Pramanik, L., Sundling, C., Hultenby, K., Wretenberg, P., Spångberg, M. and Karlsson Hedestam, G. B. (2016). CD138 and CD31 double-positive cells comprise the functional antibody-secreting plasma cell compartment in primate bone marrow. *Frontiers in Immunology* **7**, 242. doi: 10.3389/fimmu.2016.00242.

Masís, J., Mankus, D., Wolff, S. B. E., Guitchounts, G., Joesch, M. and Cox, D. D. (2018). A micro-CT-based method for quantitative brain lesion characterization and electrode localization. *Scientific Reports* **8**, 5184. doi: 10.1038/s41598-018-23247-z.

Masyuk, T. V, Ritman, E. L. and LaRusso, N. F. (2003). Hepatic artery and portal vein remodeling in rat liver: vascular response to selective cholangiocyte proliferation. *The American journal of pathology* **162**, 1175–1182. doi: 10.1016/S0002-9440(10)63913-2.

Mathew, R. C. and Boros, D. L. (1986). Anti-L3T4 antibody treatment suppresses hepatic granuloma formation and abrogates antigen-induced interleukin-2 production in Schistosoma mansoni infection. *Infection and Immunity* **54**, 820–826.

Matsuda, K., Masaki, T., Ishii, S., Yamashita, H., Watanabe, T., Nagawa, H., Muto, T., Hirata, Y., Kimura, K. and Kojima, S. (1999). Possible associations of rectal carcinoma with Schistosoma japonicum infection and membranous nephropathy: A case report with a review. *Japanese Journal of Clinical Oncology* **29**, 576–581. doi: 10.1093/jjco/29.11.576.

McDowell, S. A. C. (2000). The distribution constant of iodine between aqueous and organic phases. *Journal of Chemical Education* **77**, 1213. doi: 10.1021/ed077p1213.

McManus, D. P., Dunne, D. W., Sacko, M., Utzinger, J., Vennervald, B. J. and Zhou, X.-N. (2018). Schistosomiasis. *Nature Reviews Disease Primers* **4**, 13. doi: 10.1038/s41572-018-0013-8.

Medina, D. C., Findley, S. E. and Doumbia, S. (2008). State–space forecasting of Schistosoma haematobium time-series in Niono, Mali. *PLoS Neglected Tropical Diseases* **2**, e276. doi: 10.1371/journal.pntd.0000276.

Merkle, A. P., Lechner, L., Steinbach, A., Gelb, J., Perez-Willard, F., Phaneuf, M. W. and Unrau, D. (2015). Mastering the multi-scale challenge: A modern correlation environment. *Microscopy and Microanalysis* **21**, 15–16. doi: 10.1017/S1431927615000872.

Metscher, B. D. (2009a). MicroCT for comparative morphology: simple staining methods allow high-contrast 3D imaging of diverse non-mineralized animal tissues. *BMC Physiology* **9**, 11. doi: 10.1186/1472-6793-9-11.

Metscher, B. D. (2009b). MicroCT for developmental biology: A versatile tool for high-contrast 3D imaging at histological resolutions. *Developmental Dynamics* **238**, 632–640. doi: 10.1002/dvdy.21857.

Metscher, B. D. and Müller, G. B. (2011). MicroCT for molecular imaging: Quantitative visualization of complete three-dimensional distributions of gene products in embryonic limbs. *Developmental Dynamics* **240**, 2301–2308. doi: 10.1002/dvdy.22733.

Michielsen, P. P. (1996). Physiopathology of ascites in portal hypertension. *Acta gastro-enterologica Belgica* **59**, 191–197.

Miller, P. and Wilson, R. A. (1978). Migration of the schistosomula of Schistosoma mansoni from skin to lungs. *Parasitology* **77**, 281–302.

Modha, J., Lambertucci, J. R., Doenhoff, M. J. and McLaren, D. J. (1990). Immune dependence of schistosomicidal chemotherapy: an ultrastructural study of Schistosoma mansoni adult worms exposed to praziquantel and immune serum in vivo. *Parasite Immunology* **12**, 321–334.

Mohamed, A. R., al Karawi, M. and Yasawy, M. I. (1990). Schistosomal colonic disease. *Gut* **31**, 439–442. doi: 10.1136/gut.31.4.439.

Momose, A., Takeda, T., Itai, Y. and Hirano, K. (1996). Phase–contrast X–ray computed tomography for observing biological soft tissues. *Nature Medicine* **2**, 473–475. doi: 10.1038/nm0496-473.

Mondy, W. L., Cameron, D., Timmermans, J.-P., De Clerck, N., Sasov, A., Casteleyn, C. and Piegl, L. a (2009). Micro-CT of corrosion casts for use in the computer-aided design of microvasculature. *Tissue engineering. Part C, Methods* **15**, 729–738. doi: 10.1089/ten.tec.2008.0583.

Mondy, W. L., Casteleyn, C., Loo, D. V, Raja, M., Singleton, C. and Jacot, J. G. (2013). Osmium Tetroxide Labeling of (Poly)Methyl Methacrylate Corrosion Casts for Enhancement of Micro-CT Microvascular Imaging. *Microscopy and microanalysis* **19**, 1416–1427. doi: 10.1017/S1431927613013421.

Morgan, E., Charlier, J., Hendrickx, G., Biggeri, A., Catalan, D., von Samson-Himmelstjerna, G., Demeler, J., Müller, E., van Dijk, J., Kenyon, F., Skuce, P., Höglund, J., O'Kiely, P., van Ranst, B., de Waal, T., Rinaldi, L., Cringoli, G., Hertzberg, H., Torgerson, P., Wolstenholme, A. and Vercruysse, J. (2013). Global change and helminth infections in grazing ruminants in europe: impacts, trends and sustainable solutions. *Agriculture* **3**, 484–502. doi: 10.3390/agriculture3030484.

Mostafa, M. H., Sheweita, S. A. and O'Connor, P. J. (1999). Relationship between schistosomiasis and bladder cancer. *Clinical Microbiology Reviews*.

Mullaly, S. C., Burrows, K., Antignano, F. and Zaph, C. (2011). Assessing the role of CD103 in immunity to an intestinal helminth parasite. *PLoS ONE* **6**, e19580. doi:

10.1371/journal.pone.0019580.

Muntifering, M., Castranova, D., Gibson, G. A., Meyer, E., Kofron, M. and Watson, A. M. (2018). Clearing for deep tissue imaging. *Current Protocols in Cytometry* **86**, e38. doi: 10.1002/cpcy.38.

Murray, C. J. L., Barber, R. M., Foreman, K. J., Ozgoren, A. A., Abd-Allah, F., Abera, S. F., Aboyans, V., Abraham, J. P., Abubakar, I., Abu-Raddad, L. J., Abu-Rmeileh, N. M., Achoki, T., Ackerman, I. N., Ademi, Z., Adou, A. K., Adsuar, J. C., Afshin, A., Agardh, E. E., Alam, S. S., Alasfoor, D., Albittar, M. I., Alegretti, M. A., Alemu, Z. A., Alfonso-Cristancho, R., Alhabib, S., Ali, R., Alla, F., Allebeck, P., Almazroa, M. A., Alsharif, U., Alvarez, E., Alvis-Guzman, N., Amare, A. T., Ameh, E. A., Amini, H., Ammar, W., Anderson, H. R., Anderson, B. O., Antonio, C. A. T., Anwari, P., Arnlöv, J., Arsenijevic, V. S. A., Artaman, A., Asghar, R. J., Assadi, R., Atkins, L. S., Avila, M. A., Awuah, B., Bachman, V. F., Badawi, A., Bahit, M. C., Balakrishnan, K., Banerjee, A., Barker-Collo, S. L., Barquera, S., Barregard, L., Barrero, L. H., Basu, A., Basu, S., Basulaiman, M. O., Beardsley, J., Bedi, N., Beghi, E., Bekele, T., Bell, M. L., Benjet, C., Bennett, D. A., Bensenor, I. M., Benzian, H., Bernabé, E., Bertozzi-Villa, A., Beyene, T. J., Bhala, N., Bhalla, A., Bhutta, Z. A., Bienhoff, K., Bikbov, B., Biryukov, S., Blore, J. D., Blosser, C. D., Blyth, F. M., Bohensky, M. A., Bolliger, I. W., Başara, B. B., Bornstein, N. M., Bose, D., Boufous, S., Bourne, R. R. A., Boyers, L. N., Brainin, M., Brayne, C. E., Brazinova, A., Breitborde, N. J. K., Brenner, H., Briggs, A. D., Brooks, P. M., Brown, J. C., Brugha, T. S., et al. (2015). Global, regional, and national disability-adjusted life years (DALYs) for 306 diseases and injuries and healthy life expectancy (HALE) for 188 countries, 1990–2013: quantifying the epidemiological transition. *The Lancet* **386**, 2145–2191. doi: 10.1016/S0140-6736(15)61340-X.

Naderer, T., Heng, J., Saunders, E. C., Kloehn, J., Rupasinghe, T. W., Brown, T. J. and McConville, M. J. (2015). Intracellular survival of Leishmania major depends on uptake and degradation of extracellular matrix glycosaminoglycans by macrophages. *PLoS Pathogens* **11**, 1–20. doi: 10.1371/journal.ppat.1005136.

Naem, S., Seifi, H. and Simon, G. T. (2000). Scanning Electron Microscopy of Adult Gongylonema pulchrum (Nematoda: Spirurida). *Journal of Veterinary Medicine Series B* **47**, 249–255. doi: 10.1046/j.1439-0450.2000.00347.x.

Nash, T. E., Del Brutto, O. H., Butman, J. A., Corona, T., Delgado-Escueta, A., Duron, R. M., Evans, C. A. W., Gilman, R. H., Gonzalez, A. E., Loeb, J. A., Medina, M. T., Pietsch-Escueta, S., Pretell, E. J., Takayanagui, O. M., Theodore, W., Tsang, V. C. W. and Garcia, H. H. (2004). Calcific neurocysticercosis and epileptogenesis. *Neurology* **62**, 1934–1938. doi: 10.1212/01.wnl.0000129481.12067.06.

Nation, J. L. (1983). A New Method Using Hexamethyldisilazane for Preparation of Soft Insect Tissues for Scanning Electron Microscopy. *Stain Technology* **58**, 347–351. doi: 10.3109/10520298309066811.

Nemetschek, T., Riedl, H. and Jonak, R. (1979). Topochemistry of the binding of phosphotungstic acid to collagen. *Journal of Molecular Biology* **133**, 67–83. doi: 10.1016/0022-2836(79)90251-1.

Nguyen, H. B., Thai, T. Q., Saitoh, S., Wu, B., Saitoh, Y., Shimo, S., Fujitani, H., Otobe, H. and Ohno, N. (2016). Conductive resins improve charging and resolution of acquired images in electron microscopic volume imaging. *Scientific Reports* **6**, 23721. doi: 10.1038/srep23721.

Nguyen, H. B., Thai, T. Q., Sui, Y., Azuma, M., Fujiwara, K. and Ohno, N. (2018). Methodological improvements with conductive materials for volume imaging of neural circuits by electron microscopy. *Frontiers in Neural Circuits* **12**,. doi: 10.3389/fncir.2018.00108.

Nicu, C., Pople, J., Bonsell, L., Bhogal, R., Ansell, D. M. and Paus, R. (2018). A guide to studying human dermal adipocytes in situ. *Experimental Dermatology* **27**, 589–602. doi: 10.1111/exd.13549.

Nielsen, L. F., Moe, D., Kirkeby, S. and Garbarsch, C. (1998). Sirius red and acid fuchsin staining mechanisms. *Biotechnic & histochemistry : official publication of the Biological Stain Commission* **73**, 71–7.

Nierenberger, M., Rémond, Y., Ahzi, S. and Choquet, P. (2015). Assessing the three-dimensional collagen network in soft tissues using contrast agents and high resolution micro-CT: Application to porcine iliac veins. *Comptes Rendus Biologies* **338**, 425–433. doi: 10.1016/j.crvi.2015.04.009.

Nunes-Alves, C., Booty, M. G., Carpenter, S. M., Jayaraman, P., Rothchild, A. C. and Behar, S. M. (2014). In search of a new paradigm for protective immunity to TB. *Nature Reviews Microbiology* **12**, 289–299. doi: 10.1038/nrmicro3230.

O'Sullivan, J. D. B., Behnsen, J., Starborg, T., MacDonald, A. S., Phythian-Adams, A. T., Else, K. J., Cruickshank, S. M. and Withers, P. J. (2018). X-ray micro-computed tomography (μCT): an emerging opportunity in parasite imaging. *Parasitology* **145**, 848–854. doi: 10.1017/S0031182017002074.

Oliveros, R., Cutillas, C., Arias, P. and Guevara, D. (1998). Morphologic, biometric, and isoenzyme characterization of Trichuris suis. *Parasitology Research* **84**, 513–515.

Ontiveros, S., Yagüe, J. A., Jiménez, R. and Brosed, F. (2013). Computer tomography 3D edge detection comparative for metrology applications. *Procedia Engineering* **63**, 710–719. doi: 10.1016/j.proeng.2013.08.263.

Oorschot, V. M. J., Sztal, T. E., Bryson-Richardson, R. J. and Ramm, G. (2014). Immuno correlative light and electron microscopy on tokuyasu cryosections. In *Methods in Cell Biology Volume 124*, pp. 241–258. doi: 10.1016/B978-0-12-801075-4.00011-2.

Page, A. P., Stepek, G., Winter, A. D. and Pertab, D. (2014). Enzymology of the nematode cuticle: A potential drug target? *International Journal for Parasitology: Drugs and Drug Resistance* **4**, 133–141. doi: 10.1016/j.ijpddr.2014.05.003.

Palade, G. E. (1952). The fine structure of mitochondria. *Anatomical Record* **114**, 427–451. doi: 10.1002/ar.1091140304.

Palade, G. E. and Porter, K. R. (1954). Studies on the endoplasmic reticulum. I. Its identification in cells in situ. *Journal of Experimental Medicine* **100**, 641–656. doi: 10.1084/jem.100.6.641.

Pallares Lupon, N., Yessad, L., Hocini, M., Haïssaguerre, M., Bernus, O. and Walton, R. (2019). Optimising micro computed tomography for large mammalian heart imaging at high resolution. *Archives of Cardiovascular Diseases Supplements* **11**, 273. doi: 10.1016/j.acvdsp.2019.02.194.

Panesar, T. S. (1989). The moulting pattern in Trichuris muris (Nematoda: Trichuroidea). *Canadian Journal of Zoology* **67**, 2340–2343. doi: 10.1139/z89-330.

Pang, S., Yeh, A. T., Wang, C. and Meissner, K. E. (2009). Beyond the 1/T[sub p] limit: two-photon-excited fluorescence using pulses as short as sub-10-fs. *Journal of Biomedical Optics* **14**, 054041. doi: 10.1117/1.3253388.

Parkinson, I. H., Badiei, A. and Fazzalari, N. L. (2008). Variation in segmentation of bone from micro-CT imaging: Implications for quantitative morphometric analysis. *Australasian Physical and Engineering Sciences in Medicine* **31**, 160–164. doi: 10.1007/BF03178592.

Partridge, F. A., Murphy, E. A., Willis, N. J., Bataille, C. J. R., Forman, R., Heyer-Chauhan, N., Marinič, B., Sowood, D. J. C., Wynne, G. M., Else, K. J., Russell, A. J. and Sattelle, D. B. (2017). Dihydrobenz[e][1,4]oxazepin-2(3H)-ones, a new anthelmintic chemotype immobilising whipworm and reducing infectivity in vivo. *PLOS Neglected Tropical Diseases* **11**, e0005359. doi: 10.1371/journal.pntd.0005359.

Partridge, F. A., Brown, A. E., Buckingham, S. D., Willis, N. J., Wynne, G. M., Forman, R., Else, K. J., Morrison, A. A., Matthews, J. B., Russell, A. J., Lomas, D. A. and Sattelle,

D. B. (2018). An automated high-throughput system for phenotypic screening of chemical libraries on C. elegans and parasitic nematodes. *International Journal for Parasitology: Drugs and Drug Resistance* **8**, 8–21. doi: 10.1016/j.ijpddr.2017.11.004.

Pascolo, L., Sena, G., Gianoncelli, A., Cernogoraz, A., Kourousias, G., Metscher, B. D., Romano, F., Zito, G., Pacilè, S., Barroso, R., Tromba, G., Zweyer, M. and Ricci, G. (2019). Hard and soft X-ray imaging to resolve human ovarian cortical structures. *Journal of Synchrotron Radiation* **26**, 1322–1329. doi: 10.1107/S1600577519003680.

Patel, C., Hürlimann, E., Keller, L., Hattendorf, J., Sayasone, S., Ali, S. M., Ame, S. M., Coulibaly, J. T. and Keiser, J. (2019). Efficacy and safety of ivermectin and albendazole co-administration in school-aged children and adults infected with Trichuris trichiura: study protocol for a multi-country randomized controlled double-blind trial. *BMC Infectious Diseases* **19**, 262. doi: 10.1186/s12879-019-3882-x.

Pauwels, E., Van Loo, D., Cornillie, P., Brabant, L. and Van Hoorebeke, L. (2013). An exploratory study of contrast agents for soft tissue visualization by means of high resolution X-ray computed tomography imaging. *Journal of Microscopy* **250**, 21–31. doi: 10.1111/jmi.12013.

Payne, S. C., Bartlett, C. A., Harvey, A. R., Dunlop, S. A. and Fitzgerald, M. (2012). Myelin sheath decompaction, axon swelling, and functional loss during chronic secondary degeneration in rat optic nerve. *Investigative Opthalmology & Visual Science* **53**, 6093. doi: 10.1167/iovs.12-10080.

Pearce, E. J. and MacDonald, A. S. (2002). The immunobiology of schistosomiasis. *Nature Reviews Immunology* **2**, 499–511. doi: 10.1038/nri843.

Peddie, C. J. and Collinson, L. M. (2014). Exploring the third dimension: volume electron microscopy comes of age. *Micron* **61**, 9–19. doi: 10.1016/j.micron.2014.01.009.

Peddie, C. J., Domart, M.-C., Snetkov, X., O'Toole, P., Larijani, B., Way, M., Cox, S. and Collinson, L. M. (2017). Correlative super-resolution fluorescence and electron microscopy using conventional fluorescent proteins in vacuo. *Journal of Structural Biology* **199**, 120–131. doi: 10.1016/j.jsb.2017.05.013.

Peeters, G., Debbaut, C., Friebel, A., Cornillie, P., De Vos, W. H., Favere, K., Vander Elst, I., Vandecasteele, T., Johann, T., Van Hoorebeke, L., Monbaliu, D., Drasdo, D., Hoehme, S., Laleman, W. and Segers, P. (2018). Quantitative analysis of hepatic macro- and microvascular alterations during cirrhogenesis in the rat. *Journal of Anatomy* **232**, 485–496. doi: 10.1111/joa.12760.

Perrien, D. S., Saleh, M. A., Takahashi, K., Madhur, M. S., Harrison, D. G., Harris, R. C. and Takahashi, T. (2016). Novel methods for microCT-based analyses of vasculature in the renal cortex reveal a loss of perfusable arterioles and glomeruli in eNOS-/- mice. *BMC Nephrology* **17**, 24. doi: 10.1186/s12882-016-0235-5.

Perrigoue, J. G., Saenz, S. A., Siracusa, M. C., Allenspach, E. J., Taylor, B. C., Giacomin, P. R., Nair, M. G., Du, Y., Zaph, C., van Rooijen, N., Comeau, M. R., Pearce, E. J., Laufer, T. M. and Artis, D. (2009). MHC class II–dependent basophil–CD4+ T cell interactions promote TH2 cytokine–dependent immunity. *Nature Immunology* **10**, 697–705. doi: 10.1038/ni.1740.

Peters, K., McDowall, J. and Rose, A. M. (1991). Mutations in the bli-4 (I) locus of Caenorhabditis elegans disrupt both adult cuticle and early larval development. *Genetics* **129**, 95–102.

Pfaffenberger, G. and Best, T. (1989). Trichuris elatoris sp. n.(Nematoda: Trichuridae) from the Texas kangaroo rat (Dipodomys elator). *Proceedings of the Helminthological Society of Washington* **56**, 76–81.

Phiri, A. M., De Pomerai, D. I., Buttle, D. J. and Behnke, J. M. (2017). A novel assay for the detection of anthelmintic activity mediated by cuticular damage to nematodes: validation on Caenorhabditis elegans exposed to cysteine proteinases. *Parasitology* **144**, 583–593.

doi: 10.1017/S0031182016002353.

Ploem, J. S. (1967). The use of a vertical illuminator with interchangeable dichroic mirrors for fluorescence microscopy with incidental light. *Zeitschrift fur Wissenschaftliche Mikroskopie und Mikroskopische Technik* **68**, 129–142.

Prento, P. (1993). Van Gieson's picrofuchsin. The staining mechanisms for collagen and cytoplasm, and an examination of the dye diffusion rate model of differential staining. *Histochemistry* **99**, 163–174. doi: 10.1007/BF00571877.

Pruett, S. (1999). Quantitative relationships between the suppression of selected immunological parameters and the area under the corticosterone concentration vs. time curve in B6C3F1 mice subjected to exogenous corticosterone or to restraint stress. *Toxicological Sciences* **49**, 272–280. doi: 10.1093/toxsci/49.2.272.

Pruett, S. B. (2000). Modeling and predicting selected immunological effects of a chemical stressor (3,4-Dichloropropionanilide) using the area under the corticosterone concentration versus time curve. *Toxicological Sciences* **58**, 77–87. doi: 10.1093/toxsci/58.1.77.

Pruett, S. B., Fan, R., Myers, L. P., Wu, W.-J. and Collier, S. (2000). Quantitative analysis of the neuroendocrine–immune axis: linear modeling of the effects of exogenous corticosterone and Restraint Stress on lymphocyte subpopulations in the spleen and thymus in female B6C3F1 mice. *Brain, Behavior, and Immunity* **14**, 270–287. doi: 10.1006/brbi.2000.0605.

Puchtler, H. and Isler, H. (1958). The effect of phosphomolybdic acid on the stainability of connective tissues by various dyes. *Journal of Histochemistry and Cytochemistry* **6**, 265–270.

Puchtler, H., Meloan, S. N. and Waldrop, F. S. (1988). Are picro-dye reactions for collagens quantitative? - Chemical and histochemical considerations. *Histochemistry*. doi: 10.1007/BF00570280.

Pullan, R. L., Smith, J. L., Jasrasaria, R. and Brooker, S. J. (2014). Global numbers of infection and disease burden of soil transmitted helminth infections in 2010. *Parasites & Vectors* **7**, 37. doi: 10.1186/1756-3305-7-37.

Quade, F. S. C., Holtzheimer, J., Frohn, J., Töpperwien, M., Salditt, T. and Prpic, N.-M. (2019). Formation and development of the male copulatory organ in the spider Parasteatoda tepidariorum involves a metamorphosis-like process. *Scientific Reports* **9**, 6945. doi: 10.1038/s41598-019-43192-9.

Rao, M., Ippolito, G., Mfinanga, S., Ntoumi, F., Yeboah-Manu, D., Vilaplana, C., Zumla, A. and Maeurer, M. (2019). Latent TB Infection (LTBI) – Mycobacterium tuberculosis pathogenesis and the dynamics of the granuloma battleground. *International Journal of Infectious Diseases* **80**, S58–S61. doi: 10.1016/j.ijid.2019.02.035.

Rasch, L. J., Martin, K. J., Cooper, R. L., Metscher, B. D., Underwood, C. J. and Fraser, G. J. (2016). An ancient dental gene set governs development and continuous regeneration of teeth in sharks. *Developmental Biology* **415**, 347–370. doi: 10.1016/j.ydbio.2016.01.038.

Ravimohan, S., Kornfeld, H., Weissman, D. and Bisson, G. P. (2018). Tuberculosis and lung damage: from epidemiology to pathophysiology. *European Respiratory Review* **27**, 170077. doi: 10.1183/16000617.0077-2017.

Renier, N., Wu, Z., Simon, D. J., Yang, J., Ariel, P. and Tessier-Lavigne, M. (2014). iDISCO: A simple, rapid method to immunolabel large tissue samples for volume imaging. *Cell* **159**, 896–910. doi: 10.1016/j.cell.2014.10.010.

Richardson, D. S. and Lichtman, J. W. (2015). Clarifying tissue clearing. *Cell* **162**, 246–257. doi: 10.1016/j.cell.2015.06.067.

Richter, J., Correia Dacal, A. R., Vergetti Siqueira, J. G., Poggensee, G., Mannsmann, U.,

Deelder, A. and Feldmeier, H. (1998). Sonographic prediction of variceal bleeding in patients with liver fibrosis due to Schistosoma mansoni. *Tropical Medicine & International Health* **3**, 728–735. doi: 10.1046/j.1365-3156.1998.00285.x.

Rieder, F. and Fiocchi, C. (2009). Intestinal fibrosis in IBD—a dynamic, multifactorial process. *Nature Reviews Gastroenterology & Hepatology* **6**, 228–235. doi: 10.1038/nrgastro.2009.31.

Riemersma, J. C. (1968). Osmium tetroxide fixation of lipids for electron microscopy a possible reaction mechanism. *Biochimica et Biophysica Acta (BBA) - Lipids and Lipid Metabolism* **152**, 718–727. doi: 10.1016/0005-2760(68)90118-5.

Robles, M. D. R., Cutillas, C., Panei, C. J. and Callejón, R. (2014). Morphological and molecular characterization of a new Trichuris species (Nematoda- Trichuridae), and phylogenetic relationships of Trichuris species of Cricetid rodents from Argentina. *PloS One* **9**, e112069. doi: 10.1371/journal.pone.0112069.

Rodrigues, F. G., Campos, J. B., Toppa, N. H., Wexner, S. D. and Dasilva, G. (2016). Ultrasonographic diagnosis of Schistosoma mansoni eggs in rectum. *Case Reports in Infectious Diseases* **2016**, 1–3. doi: 10.1155/2016/5438204.

Ronchetti, I., Boraldi, F., Annovi, G., Cianciulli, P. and Quaglino, D. (2013). Fibroblast involvement in soft connective tissue calcification. *Frontiers in Genetics* **4**,. doi: 10.3389/fgene.2013.00022.

Rosenberg, I. N. (1959). Behaviour of iodide in acid solutions of hemoglobin 1. *Endocrinology* **64**, 83–102. doi: 10.1210/endo-64-1-83.

Ross, A. G., Vickers, D., Olds, G. R., Shah, S. M. and McManus, D. P. (2007). Katayama syndrome. *The Lancet Infectious Diseases* **7**, 218–224. doi: 10.1016/S1473-3099(07)70053-1.

Ross, A. G., McManus, D. P., Farrar, J., Hunstman, R. J., Gray, D. J. and Li, Y.-S. (2012). Neuroschistosomiasis. *Journal of Neurology* **259**, 22–32. doi: 10.1007/s00415-011-6133-7.

Roth, G. A., Abate, D., Abate, K. H., Abay, S. M., Abbafati, C., Abbasi, N., Abbastabar, H., Abd-Allah, F., Abdela, J., Abdelalim, A., Abdollahpour, I., Abdulkader, R. S., Abebe, H. T., Abebe, M., Abebe, Z., Abejie, A. N., Abera, S. F., Abil, O. Z., Abraha, H. N., Abrham, A. R., Abu-Raddad, L. J., Accrombessi, M. M. K., Acharya, D., Adamu, A. A., Adebayo, O. M., Adedoyin, R. A., Adekanmbi, V., Adetokunboh, O. O., Adhena, B. M., Adib, M. G., Admasie, A., Afshin, A., Agarwal, G., Agesa, K. M., Agrawal, A., Agrawal, S., Ahmadi, A., Ahmadi, M., Ahmed, M. B., Ahmed, S., Aichour, A. N., Aichour, I., Aichour, M. T. E., Akbari, M. E., Akinyemi, R. O., Akseer, N., Al-Aly, Z., Al-Eyadhy, A., Al-Raddadi, R. M., Alahdab, F., Alam, K., Alam, T., Alebel, A., Alene, K. A., Alijanzadeh, M., Alizadeh-Navaei, R., Aljunid, S. M., Alkerwi, A., Alla, F., Allebeck, P., Alonso, J., Altirkawi, K., Alvis-Guzman, N., Amare, A. T., Aminde, L. N., Amini, E., Ammar, W., Amoako, Y. A., Anber, N. H., Andrei, C. L., Androudi, S., Animut, M. D., Anjomshoa, M., Ansari, H., Ansha, M. G., Antonio, C. A. T., Anwari, P., Aremu, O., Ärnlöv, J., Arora, A., Arora, M., Artaman, A., Aryal, K. K., Asayesh, H., Asfaw, E. T., Ataro, Z., Atique, S., Atre, S. R., Ausloos, M., Avokpaho, E. F. G. A., Awasthi, A., Quintanilla, B. P. A., Ayele, Y., Ayer, R., Azzopardi, P. S., Babazadeh, A., Bacha, U., Badali, H., et al. (2018). Global, regional, and national age-sex-specific mortality for 282 causes of death in 195 countries and territories, 1980–2017: a systematic analysis for the Global Burden of Disease Study 2017. *The Lancet* **392**, 1736–1788. doi: 10.1016/S0140-6736(18)32203-7.

Russell, M. R. G., Lerner, T. R., Burden, J. J., Nkwe, D. O., Pelchen-Matthews, A., Domart, M.-C., Durgan, J., Weston, A., Jones, M. L., Peddie, C. J., Carzaniga, R., Florey, O., Marsh, M., Gutierrez, M. G. and Collinson, L. M. (2017). 3D correlative light and electron microscopy of cultured cells using serial blockface scanning electron microscopy. *Journal of cell science* **130**, 278–291. doi: 10.1242/jcs.188433.

Sabatini, D. D., Bensch, K. and Barnett, R. J. (1963). The preservation of cellular

ultrastructure and enzymatic activity by aldehyde fixation. *The Journal of Cell Biology* **17**, 19–58. doi: 10.1083/jcb.17.1.19.

Saccomano, M., Albers, J., Tromba, G., Dobrivojević Radmilović, M., Gajović, S., Alves, F. and Dullin, C. (2018). Synchrotron inline phase contrast μCT enables detailed virtual histology of embedded soft-tissue samples with and without staining. *Journal of Synchrotron Radiation* **25**, 1153–1161. doi: 10.1107/S1600577518005489.

Sah, V. K., Wang, L., Min, X., Rizal, R., Feng, Z., Ke, Z., Deng, M., Li, L. and Li, H. (2015). Human schistosomiasis: A diagnostic imaging focused review of a neglected disease. *Radiology of Infectious Diseases* **2**, 150–157. doi: 10.1016/j.jrid.2015.11.007.

Saoud, M. F. A. (1965). Comparative studies on the characteristics of some geographical strains of Schistosoma mansoni in mice and hamsters. *Journal of Helminthology* **39**, 101–112. doi: 10.1017/S0022149X00020095.

Saukko, A. E. A., Turunen, M. J., Honkanen, M. K. M., Lovric, G., Tiitu, V., Honkanen, J. T. J., Grinstaff, M. W., Jurvelin, J. S. and Töyräs, J. (2019). Simultaneous quantitation of cationic and non-ionic contrast agents in articular cartilage using synchrotron microCT imaging. *Scientific Reports* **9**, 7118. doi: 10.1038/s41598-019-43276-6.

Savai, R., Langheinrich, A. C., Schermuly, R. T., Pullamsetti, S. S., Dumitrascu, R., Traupe, H., Rau, W. S., Seeger, W., Grimminger, F. and Banat, G. A. (2009). Evaluation of angiogenesis using micro-computed tomography in a xenograft mouse model of lung cancer. *Neoplasia* **11**, 48–56.

Schaad, L., Hlushchuk, R., Barré, S., Gianni-Barrera, R., Haberthür, D., Banfi, A. and Djonov, V. (2017). Correlative imaging of the murine hind limb vasculature and muscle tissue by microCT and light microscopy. *Scientific Reports* **7**, 41842. doi: 10.1038/srep41842.

Schindelin, J., Arganda-Carreras, I., Frise, E., Kaynig, V., Longair, M., Pietzsch, T., Preibisch, S., Rueden, C., Saalfeld, S., Schmid, B., Tinevez, J.-Y., White, D. J., Hartenstein, V., Eliceiri, K., Tomancak, P. and Cardona, A. (2012). Fiji: an open-source platform for biological-image analysis. *Nature Methods* **9**, 676–682. doi: 10.1038/nmeth.2019.

Schopf, L. R., Hoffmann, K. F., Cheever, A. W., Urban, J. F. and Wynn, T. A. (2002). IL-10 Is Critical for Host Resistance and Survival During Gastrointestinal Helminth Infection. *The Journal of Immunology* **168**, 2383–2392. doi: 10.4049/jimmunol.168.5.2383.

Schulz, G., Weitkamp, T., Zanette, I., Pfeiffer, F., Beckmann, F., David, C., Rutishauser, S., Reznikova, E. and Müller, B. (2010). High-resolution tomographic imaging of a human cerebellum: Comparison of absorption and grating-based phase contrast. *Journal of the Royal Society Interface* **7**, 1665–1676. doi: 10.1098/rsif.2010.0281.

Schwab, C. L. (2004). Modeling and predicting stress-Induced immunosuppression in mice using blood parameters. *Toxicological Sciences* **83**, 101–113. doi: 10.1093/toxsci/kfi014.

Schwartz, C. and Fallon, P. G. (2018). Schistosoma “Eggs-Iting” the host: granuloma formation and egg excretion. *Frontiers in Immunology* **9**,. doi: 10.3389/fimmu.2018.02492.

Secor, W. E., Colley, D. G., Nahlen, B. L., Ouma, J. H. and Karanja, D. M. S. (1997). Studies on schistosomiasis in western Kenya: I. evidence for immune-facilitated excretion of schistosome eggs from patients with Schistosoma mansoni and Human immunodeficiency virus coinfections. *The American Journal of Tropical Medicine and Hygiene* **56**, 515–521. doi: 10.4269/ajtmh.1997.56.515.

Sengle, G., Tufa, S. F., Sakai, L. Y., Zulliger, M. A. and Keene, D. R. (2013). A correlative method for imaging identical regions of samples by micro-CT, light microscopy, and electron microscopy. *Journal of Histochemistry & Cytochemistry* **61**, 263–271. doi: 10.1369/0022155412473757.

Sharpe, J., Ahlgren, U., Perry, P., Hill, B., Ross, A., Hecksher-Sørensen, J., Baldock, R.

and Davidson, D. (2002). Optical projection tomography as a tool for 3D microscopy and gene expression studies. *Science* **296**, 541–545. doi: 10.1126/science.1068206.

Shearer, T., Bradley, R. S., Hidalgo-Bastida, L. A., Sherratt, M. J. and Cartmell, S. H. (2016). Three-dimensional visualisation of soft biological structures by X-ray computed micro-tomography. *Journal of Cell Science* **129**, 2483–2492. doi: 10.1242/jcs.179077.

Shears, R. K., Bancroft, A. J., Hughes, G. W., Grencis, R. K. and Thornton, D. J. (2018a). Extracellular vesicles induce protective immunity against Trichuris muris. *Parasite Immunology* **40**, e12536. doi: 10.1111/pim.12536.

Shears, R. K., Bancroft, A. J., Sharpe, C., Grencis, R. K. and Thornton, D. J. (2018b). Vaccination against whipworm: identification of potential immunogenic proteins in Trichuris muris excretory/secretory material. *Scientific Reports* **8**, 4508. doi: 10.1038/s41598-018-22783-y.

Sheffield, H. G. (1963). Electron microscopy of the bacillary band and stichosome of Trichuris muris and T. vulpis. *Journal of Parasitology* **49**, 998. doi: 10.2307/3275740.

Shuhua, X., Binggui, S., Utzinger, J., Chollet, J. and Tanner, M. (2002). Transmission electron microscopic observations on ultrastructural damage in juvenile Schistosoma mansoni caused by artemether. *Acta Tropica* **81**, 53–61. doi: 10.1016/S0001-706X(01)00187-5.

Silva, L. M., Ribeiro-dos-Santos, R., Soares, M. B. P. and Andrade, Z. A. (2006). Characterization of the vascular changes in schistosomal portal (pipestem) fibrosis of mice. *Acta Tropica* **98**, 34–42. doi: 10.1016/j.actatropica.2006.01.011.

Simeon, D. T., Grantham-McGregor, S. M., Callender, J. E. and Wong, M. S. (1995). Treatment of Trichuris trichiura infections improves growth, spelling scores and school attendance in some children. *The Journal of Nutrition* **125**, 1875–1883. doi: 10.1093/jn/125.7.1875.

Simmer, F., Moorman, C., Van Der Linden, A. M., Kuijk, E., Van Den Berghe, P. V. E., Kamath, R. S., Fraser, A. G., Ahringer, J. and Plasterk, R. H. A. (2003). Genome-wide RNAi of C. elegans using the hypersensitive rrf-3 strain reveals novel gene functions. *PLoS Biology* **1**, 77–84. doi: 10.1371/journal.pbio.0000012.

Smith, P. M., Shainheit, M. G., Bazzone, L. E., Rutitzky, L. I., Poltorak, A. and Stadecker, M. J. (2009). Genetic Control of Severe Egg-Induced Immunopathology and IL-17 Production in Murine Schistosomiasis. *The Journal of Immunology* **183**, 3317–3323. doi: 10.4049/jimmunol.0901504.

Smith, D. B., Bernhardt, G., Raine, N. E., Abel, R. L., Sykes, D., Ahmed, F., Pedroso, I. and Gill, R. J. (2016). Exploring miniature insect brains using micro-CT scanning techniques. *Scientific Reports* **6**, 21768. doi: 10.1038/srep21768.

Sombetzki, M., Fuchs, C. D., Fickert, P., Österreicher, C. H., Mueller, M., Claudel, T., Loebermann, M., Engelmann, R., Langner, C., Sahin, E., Schwinge, D., Guenther, N. D., Schramm, C., Mueller-Hilke, B., Reisinger, E. C. and Trauner, M. (2015). 24-nor-ursodeoxycholic acid ameliorates inflammatory response and liver fibrosis in a murine model of hepatic schistosomiasis. *Journal of Hepatology* **62**, 871–878. doi: 10.1016/j.jhep.2014.11.020.

Souza, A. L. S., Souza, P. R. S., Pereira, C. A., Fernandes, A., Guabiraba, R., Russo, R. C., Vieira, L. Q., Corrêa, A., Teixeira, M. M. and Negrão-Corrêa, D. (2011). Experimental Infection with Schistosoma mansoni in CCR5-Deficient Mice Is Associated with Increased Disease Severity, as CCR5 Plays a Role in Controlling Granulomatous Inflammation. *Infection and Immunity* **79**, 1741–1749. doi: 10.1128/IAI.00502-10.

Speich, B., Ali, S. M., Ame, S. M., Bogoch, I. I., Alles, R., Huwyler, J., Albonico, M., Hattendorf, J., Utzinger, J. and Keiser, J. (2015). Efficacy and safety of albendazole plus ivermectin, albendazole plus mebendazole, albendazole plus oxantel pamoate, and mebendazole alone against Trichuris trichiura and concomitant soil-transmitted helminth

infections: a four-arm, randomised controlled t. *The Lancet Infectious Diseases* **15**, 277–284. doi: 10.1016/S1473-3099(14)71050-3.

Starborg, T., O'Sullivan, J. D. B., Carneiro, C. M., Behnsen, J., Else, K. J., Grencis, R. K. and Withers, P. J. (2019). Experimental steering of electron microscopy studies using prior X-ray computed tomography. *Ultramicroscopy* **201**, 58–67. doi: 10.1016/j.ultramic.2019.03.002.

Steinmann, P., Rinaldi, L., Cringoli, G., Du, Z.-W., Marti, H., Jiang, J.-Y., Zhou, H., Zhou, X.-N. and Utzinger, J. (2015). Morphological diversity of Trichuris spp. eggs observed during an anthelminthic drug trial in Yunnan, China, and relative performance of parasitologic diagnostic tools. *Acta Tropica* **141**, 184–189. doi: 10.1016/j.actatropica.2014.08.018.

Stelzer, E. H. K. (2015). Light-sheet fluorescence microscopy for quantitative biology. *Nature Methods* **12**, 23–26. doi: 10.1038/nmeth.3219.

Stepek, G., McCormack, G. and Page, A. P. (2010). The kunitz domain protein BLI-5 plays a functionally conserved role in cuticle formation in a diverse range of nematodes. *Molecular and Biochemical Parasitology* **169**, 1–11. doi: 10.1016/j.molbiopara.2009.08.005.

Stock, S. R. (2008). Recent advances in X-ray microtomography applied to materials. *International Materials Reviews* **53**, 129–181. doi: 10.1179/174328008X277803.

Strickland, G. T. (1994). Gastrointestinal manifestations of schistosomiasis. *Gut* **35**, 1334–1337. doi: 10.1136/gut.35.10.1334.

Svensson, M., Bell, L., Little, M. C., Deschoolmeester, M., Locksley, R. M. and Else, K. J. (2011). Accumulation of eosinophils in intestine-draining mesenteric lymph nodes occurs after Trichuris muris infection. *Parasite Immunology* **33**, 1–11. doi: 10.1111/j.1365-3024.2010.01246.x.

Tapia, J. C., Kasthuri, N., Hayworth, K. J., Schalek, R., Lichtman, J. W., Smith, S. J. and Buchanan, J. (2012). High-contrast en bloc staining of neuronal tissue for field emission scanning electron microscopy. *Nature Protocols* **7**, 193–206. doi: 10.1038/nprot.2011.439.

Tapie, L., Chiche, N., Boitelle, P., Morenton, P., Attal, J.-P., Schmitt, N. and Vennat, E. (2016). Adaptation measurement of CAD/CAM dental crowns with X-Ray Micro-CT: Metrological chain standardization and 3D gap size distribution. *Advances in Materials Science and Engineering* **2016**, 1–13. doi: 10.1155/2016/7963928.

The C. elegans Sequencing Consortium (1998). Genome sequence of the nematode C. elegans: A platform for investigating biology. *Science* **282**, 2012–2018. doi: 10.1126/science.282.5396.2012.

Tiboldi, T. (1979). Intestinal parameters in acute murine schistosomiasis mansoni. *Transactions of the Royal Society of Tropical Medicine and Hygiene* **73**, 81–84. doi: 10.1016/0035-9203(79)90135-4.

Tilney, L. G., Connelly, P. S., Guild, G. M., Vranich, K. a. and Artis, D. (2005). Adaptation of a nematode parasite to living within the mammalian epithelium. *Journal of Experimental Zoology Part A: Comparative Experimental Biology* **303**, 927–945. doi: 10.1002/jez.a.214.

Torres, E. J. L., Nascimento, A. P. F., Menezes, A. O., Garcia, J., dos Santos, M. A. J., Maldonado, A., Miranda, K., Lanfredi, R. M. and de Souza, W. (2011). A new species of Trichuris from Thrichomys apereoides (Rodentia: Echimyidae) in Brazil: Morphological and histological studies. *Veterinary Parasitology* **176**, 226–235. doi: 10.1016/j.vetpar.2010.10.053.

Turkoglu, E., Seckin, H., Gurer, B., Ahmed, A., Uluc, K., Pulfer, K., Arat, A., Niemann, D. and Baskaya, M. (2014). The Cadaveric Perfusion and Angiography as a Teaching Tool: Imaging the Intracranial Vasculature in Cadavers. *Journal of Neurological Surgery Part B: Skull Base* **75**, 435–444. doi: 10.1055/s-0034-1386653.

Umar, S. (2010). Intestinal stem cells. *Current gastroenterology reports* **12**, 340–348. doi:

10.1007/s11894-010-0130-3.

van der Linden, J. C., Waarsing, J. H. and Weinans, H. (2006). The use of micro-CT to study bone architecture dynamics noninvasively. *Drug Discovery Today: Technologies* **3**, 213–219. doi: 10.1016/j.ddtec.2006.06.006.

van Meer, G. (1987). Sorting of sphingolipids in epithelial (Madin-Darby canine kidney) cells. *The Journal of Cell Biology* **105**, 1623–1635. doi: 10.1083/jcb.105.4.1623.

Vasilescu, D. M., Phillion, A. B., Tanabe, N., Kinose, D., Paige, D. F., Kantrowitz, J. J., Liu, G., Liu, H., Fishbane, N., Verleden, S. E., Vanaudenaerde, B. M., Lenburg, M., Stevenson, C. S., Spira, A., Cooper, J. D., Hackett, T.-L. and Hogg, J. C. (2017). Nondestructive cryomicro-CT imaging enables structural and molecular analysis of human lung tissue. *Journal of Applied Physiology* **122**, 161–169. doi: 10.1152/japplphysiol.00838.2016.

Vasquez, S. X., Gao, F., Su, F., Grijalva, V., Pope, J., Martin, B., Stinstra, J., Masner, M., Shah, N., Weinstein, D. M., Farias-Eisner, R. and Reddy, S. T. (2011). Optimization of microCT imaging and blood vessel diameter quantitation of preclinical specimen vasculature with radiopaque polymer injection medium. *PLoS ONE* **6**, e19099. doi: 10.1371/journal.pone.0019099.

Vella, A. T., Hulsebosch, M. D. and Pearce, E. J. (1992). Schistosoma mansoni eggs induce antigen-responsive CD44-hi T helper 2 cells and IL-4-secreting CD44-lo cells. Potential for T helper 2 subset differentiation is evident at the precursor level. *Journal of Immunology*.

Verbrugge, L. M., Rainey, J. J., Reimink, R. L. and Blankespoor, H. D. (2004). Swimmer's itch: Incidence and risk factors. *American Journal of Public Health*. doi: 10.2105/AJPH.94.5.738.

Vercruysse, J., Albonico, M., Behnke, J. M., Kotze, A. C., Prichard, R. K., McCarthy, J. S., Montresor, A. and Levecke, B. (2011). Is anthelmintic resistance a concern for the control of human soil-transmitted helminths? *International Journal for Parasitology* **1**, 14–27. doi: 10.1016/j.ijpddr.2011.09.002.

Vickerton, P., Jarvis, J. and Jeffery, N. (2013). Concentration-dependent specimen shrinkage in iodine-enhanced microCT. *Journal of Anatomy* **223**, 185–193. doi: 10.1111/joa.12068.

Vihinen, H., Belevich, I. and Jokitalo, E. (2013). Three dimensional electron microscopy of cellular organelles by serial block face SEM and ET. *Microscopy and Analysis* **27**, 7–10.

Villar, L., Vicente, B., Blanco-Gómez, A., Castellanos, A., Pérez-Losada, J. and Muro, A. (2014). Identifying phenotypes involved in susceptibility to Schistosoma mansoni infection in F1B6CBA mice. *Acta Parasitologica* **59**,. doi: 10.2478/s11686-014-0277-4.

Vogeler, F., Verheecke, W., Voet, A. and Kruth, J. (2011). Positional stability of 2D X-ray images for computer tomography. *International Symposium on Digital Industrial Radiology and Computed Tomography*.

Vos, T., Abajobir, A. A., Abate, K. H., Abbafati, C., Abbas, K. M., Abd-Allah, F., Abdulkader, R. S., Abdulle, A. M., Abebo, T. A., Abera, S. F., Aboyans, V., Abu-Raddad, L. J., Ackerman, I. N., Adamu, A. A., Adetokunboh, O., Afarideh, M., Afshin, A., Agarwal, S. K., Aggarwal, R., Agrawal, A., Agrawal, S., Ahmadieh, H., Ahmed, M. B., Aichour, M. T. E., Aichour, A. N., Aichour, I., Aiyar, S., Akinyemi, R. O., Akseer, N., Al Lami, F. H., Alahdab, F., Al-Aly, Z., Alam, K., Alam, N., Alam, T., Alasfoor, D., Alene, K. A., Ali, R., Alizadeh-Navaei, R., Alkerwi, A., Alla, F., Allebeck, P., Allen, C., Al-Maskari, F., Al-Raddadi, R., Alsharif, U., Alsowaidi, S., Altirkawi, K. A., Amare, A. T., Amini, E., Ammar, W., Amoako, Y. A., Andersen, H. H., Antonio, C. A. T., Anwari, P., Ärnlöv, J., Artaman, A., Aryal, K. K., Asayesh, H., Asgedom, S. W., Assadi, R., Atey, T. M., Atnafu, N. T., Atre, S. R., Avila-Burgos, L., Avokphako, E. F. G. A., Awasthi, A., Bacha, U., Badawi, A., Balakrishnan, K., Banerjee, A., Bannick, M. S., Barac, A., Barber, R. M., Barker-Collo, S. L., Bärnighausen, T., Barquera, S., Barregard, L., Barrero, L. H., Basu, S., Battista, B., Battle, K. E., Baune, B. T., Bazargan-Hejazi, S., Beardsley, J., Bedi, N., Beghi, E., Béjot, Y., Bekele, B. B., Bell,

M. L., Bennett, D. A., Bensenor, I. M., Benson, J., Berhane, A., Berhe, D. F., Bernabé, E., Betsu, B. D., Beuran, M., et al. (2017). Global, regional, and national incidence, prevalence, and years lived with disability for 328 diseases and injuries for 195 countries, 1990–2016: a systematic analysis for the Global Burden of Disease Study 2016. *The Lancet* **390**, 1211–1259. doi: 10.1016/S0140-6736(17)32154-2.

Walton, J. (1979). Lead asparate, an en bloc contrast stain particularly useful for ultrastructural enzymology. *Journal of Histochemistry & Cytochemistry* **27**, 1337–1342. doi: 10.1177/27.10.512319.

Wang, Z., Verboven, P. and Nicolai, B. (2017). Contrast-enhanced 3D micro-CT of plant tissues using different impregnation techniques. *Plant Methods* **13**, 105. doi: 10.1186/s13007-017-0256-5.

Wangchuk, P., Pearson, M. S., Giacomin, P. R., Becker, L., Sotillo, J., Pickering, D., Smout, M. J., Loukas, A., Panic, G., Duthaler, U., Speich, B., Keiser, J., Morel, M., Vanderstraete, M., Cailliau, K., Lescuyer, A., Lancelot, J., Dissous, C., Pedrique, B., Strub-Wourgaft, N., Some, C., Olliaro, P., Trouiller, P., Ford, N., Pécoul, B., Bradol, J., Keiser, J., Utzinger, J., Wolstenholme, A., Martin, R., Matthews, J., Wang, W., Wang, L., Liang, Y., Mwangi, I., Sanchez, M., Mkoji, G., Agola, L., Runo, S., Cupit, P., Cunningham, C., Stothard, J., Sousa-Figueiredo, J., Betson, M., Bustinduy, A., Reinhard-Rupp, J., Harvey, A., Edrada-Ebel, R., Quinn, R., Lai, H., Sasaki, T., Singh, N., Athanasiadou, S., Githiori, J., Kyriazakis, I., Wangchuk, P., Keller, P., Pyne, S., Taweechotipatr, M., Tonsomboon, A., Rattanajak, R., Kamchonwongpaisan, S., Wangchuk, P., Keller, P., Pyne, S., Willis, A., Kamchonwongpaisan, S., Wangchuk, P., Keller, P., Pyne, S., Lie, W., Willis, A., Rattanajak, R., Kamchonwongpaisan, S., Wangchuk, P., Pyne, S., Keller, P., Taweechotipatr, M., Kamchonwongpaisan, S., Edwards, J., Brown, M., Peak, E., Bartholomew, B., Nash, R., Hoffman, K., Wangchuk, P., Keller, P., Pyne, S., Korth, J., Samten, T. M., Rattanajak, R., Kamchonwongpaisan, S., Ballabh, B., Chaurasa, O., Pareek, A., Suthar, M., Rathore, G., Bansal, V., et al. (2016). Compounds Derived from the Bhutanese Daisy, Ajania nubigena, Demonstrate Dual Anthelmintic Activity against Schistosoma mansoni and Trichuris muris. *PLOS Neglected Tropical Diseases* **10**, e0004908. doi: 10.1371/journal.pntd.0004908.

Warnett, J. M., Titarenko, V., Kiraci, E., Attridge, A., Lionheart, W. R. B., Withers, P. J. and Williams, M. A. (2016). Towards in-process x-ray CT for dimensional metrology. *Measurement Science and Technology* **27**, 035401. doi: 10.1088/0957-0233/27/3/035401.

Warren, K. S. (1972). The immunopathogenesis of schistosomiasis: A multidisciplinary approach. *Transactions of the Royal Society of Tropical Medicine and Hygiene* **66**, 417–432. doi: 10.1016/0035-9203(72)90273-8.

Warren, K. S. (1978). Hepatosplenic schistosomiasis: a great neglected disease of the liver. *Gut* **19**, 572–577. doi: 10.1136/gut.19.6.572.

Webster, J. P., Molyneux, D. H., Hotez, P. J. and Fenwick, A. (2014). The contribution of mass drug administration to global health: past, present and future. *Philosophical Transactions of the Royal Society B: Biological Sciences* **369**, 20130434–20130434. doi: 10.1098/rstb.2013.0434.

Wei, D., Jacobs, S., Modla, S., Zhang, S., Young, C. L., Cirino, R., Caplan, J. and Czymmek, K. (2012). High-resolution three-dimensional reconstruction of a whole yeast cell using focused-ion beam scanning electron microscopy. *BioTechniques* **53**, 41–48. doi: 10.2144/000113850.

Weigert, R., Sramkova, M., Parente, L., Amornphimoltham, P. and Masedunskas, A. (2010). Intravital microscopy: a novel tool to study cell biology in living animals. *Histochemistry and Cell Biology* **133**, 481–491. doi: 10.1007/s00418-010-0692-z.

Weinstock, J. V and Boros, D. L. (1983). Organ-dependent differences in composition and function observed in hepatic and intestinal granulomas isolated from mice with Schistosomiasis mansoni. *Journal of Immunology*.

Weitkamp, T. and Bleuet, P. (2004). Automatic geometrical calibration for x-ray microtomography based on Fourier and Radon analysis. In *Developments in X-ray Tomgography IV* (ed. Bonse, U.), p. 623. doi: 10.1117/12.557094.

Wells, P., Davis, J. ., Suendermann, B., Shadbolt, P. ., Benci, N., Grant, J. ., Davies, D. . and Morgan, M. . (1992). A simple transmission X-ray microtomography instrument. *Nuclear Instruments and Methods in Physics Research Section B: Beam Interactions with Materials and Atoms* **72**, 261–270. doi: 10.1016/0168-583X(92)95242-J.

Wheater, P. R. and Wilson, R. A. (1979). Schistosoma mansoni: a histological study of migration in the laboratory mouse. *Parasitology* **79**, 49–62.

White, J. G. (1987). An evaluation of confocal versus conventional imaging of biological structures by fluorescence light microscopy. *The Journal of Cell Biology* **105**, 41–48. doi: 10.1083/jcb.105.1.41.

White, E. L. and Rock, M. P. (1981). A comparison of thalamocortical and other synaptic inputs to dendrites of two non-spiny neurons in a single barrel of mouse SmI cortex. *Journal of Comparative Neurology* **195**, 265–277. doi: 10.1002/cne.901950207.

White, J. G., Southgate, E., Thomson, J. N. and Brenner, S. (1986). The structure of the nervous system of the nematode Caenorhabditis elegans. *Philosophical Transactions of the Royal Society B: Biological Sciences* **314**, 1–340. doi: 10.1098/rstb.1986.0056.

Williams, M. E., Montenegro, S., Domingues, A. L., Wynn, T. A., Teixeira, K., Mahanty, S., Coutinho, A. and Sher, A. (1994). Leukocytes of patients with Schistosoma mansoni respond with a Th2 pattern of cytokine production to mitogen or egg antigens but with a Th0 pattern to worm antigens. *Journal of Infectious Diseases* **170**, 946–954. doi: 10.1093/infdis/170.4.946.

Willingham, M. C. and Rutherford, A. V (1984). The use of osmium-thiocarbohydrazide-osmium (OTO) and ferrocyanide-reduced osmium methods to enhance membrane contrast and preservation in cultured cells. *The journal of histochemistry and cytochemistry : official journal of the Histochemistry Society* **32**, 455–60. doi: 10.1177/32.4.6323574.

Wilson, R. A. and Barnes, P. E. (1977). The formation and turnover of the membranocalyx on the tegument of Schistosoma mansoni. *Parasitology* **74**, 61–71.

Wilson, R. A. and Lawson, J. R. (1980). An examination of the skin phase of schistosome migration using a hamster cheek pouch preparation. *Parasitology* **80**, 257. doi: 10.1017/S0031182000000731.

Wilson, S., Vennervald, B. J. and Dunne, D. W. (2011). Chronic hepatosplenomegaly in African school children: A common but neglected morbidity associated with schistosomiasis and malaria. *PLoS Neglected Tropical Diseases* **5**, e1149. doi: 10.1371/journal.pntd.0001149.

Withers, P. J. (2007). X-ray nanotomography. *Materials Today* **10**, 26–34. doi: 10.1016/S1369-7021(07)70305-X.

Wright, K. A. (1963). Cytology of the bacillary bands of the nematode Capillaria hepatica (Bancroft, 1893). *Journal of Morphology* **112**, 233–259. doi: 10.1002/jmor.1051120304.

Wright, K. A. (1968a). The fine structure of the cuticle and interchordal hypodermis of the parasitic nematodes, Capillaria hepatica and Trichuris myocastoris. *Canadian Journal of Zoology* **46**, 173–179.

Wright, K. A. (1968b). Structure of the Bacillary Band of Trichuris myocastoris. *Journal of Parasitology* **54**, 1106. doi: 10.2307/3276973.

Wright, K. A. (1975). Cuticular inflations in whipworms, Trichuris spp. *International Journal for Parasitology* **5**, 461–463. doi: 10.1016/0020-7519(75)90014-4.

Wright, K. A. (1979). Trichinella spiralis: an intracellular parasite in the intestinal phase. *Journal of Parasitology* **65**, 441. doi: 10.2307/3280292.

Wright, K. A. and Chan, J. (1973). Sense receptors in the bacillary band of trichuroid nematodes. *Tissue and Cell* **5**, 373–380. doi: 10.1016/S0040-8166(73)80031-X.

Wyler, D. J. and Tracy, J. W. (1982). Direct and indirect effects of soluble extracts of Schistosoma mansoni eggs on fibroblast proliferation in vitro. *Infection and immunity* **38**, 103–108.

Xiong, G., Xiao, Z. R. and Zhang, W. G. (2017). Vascular anatomy of the capitate determined by micro-computed tomography angiography. *Journal of Hand Surgery (European Volume)* **42**, 966–967. doi: 10.1177/1753193417714400.

Yan, L., Liu, S., Qi, J., Zhang, Z., Zhong, J., Li, Q., Liu, X., Zhu, Q., Yao, Z., Lu, Y. and Gu, L. (2019). Three-dimensional reconstruction of internal fascicles and microvascular structures of human peripheral nerves. *International Journal for Numerical Methods in Biomedical Engineering*. doi: 10.1002/cnm.3245.

Yepes, E., Varela-M, R. E., López-Abán, J., Rojas-Caraballo, J., Muro, A. and Mollinedo, F. (2015). Inhibition of granulomatous inflammation and prophylactic treatment of schistosomiasis with a combination of edelfosine and praziquantel. *PLOS Neglected Tropical Diseases* **9**, e0003893. doi: 10.1371/journal.pntd.0003893.

Zaborin, A., Krezalek, M., Hyoju, S., Defazio, J. R., Setia, N., Belogortseva, N., Bindokas, V. P., Guo, Q., Zaborina, O. and Alverdy, J. C. (2017). Critical role of microbiota within cecal crypts on the regenerative capacity of the intestinal epithelium following surgical stress. *American Journal of Physiology-Gastrointestinal and Liver Physiology* **312**, G112–G122. doi: 10.1152/ajpgi.00294.2016.

Zagorchev, L., Oses, P., Zhuang, Z. W., Moodie, K., Mulligan-Kehoe, M., Simons, M. and Couffinhal, T. (2010). Micro computed tomography for vascular exploration. *Journal of Angiogenesis Research* **2**, 7. doi: 10.1186/2040-2384-2-7.

Zamir, A. (2017). Optimization and new applications of edge-illumination based X-ray phase contrast CT.

Zernike, F. (1942). Phase contrast, a new method for the microscopic observation of transparent objects. *Physica*. doi: 10.1016/S0031-8914(42)80035-X.

Zhang, M.-Q., Zhou, L., Deng, Q.-F., Xie, Y.-Y., Xiao, T.-Q., Cao, Y.-Z., Zhang, J.-W., Chen, X.-M., Yin, X.-Z. and Xiao, B. (2015). Ultra-high-resolution 3D digitalized imaging of the cerebral angioarchitecture in rats using synchrotron radiation. *Scientific Reports* **5**, 14982. doi: 10.1038/srep14982.

Zheng, S., Zhang, P., Chen, Y., Zheng, S., Zheng, L. and Weng, Z. (2016). Inhibition of Notch signaling attenuates schistosomiasis hepatic fibrosis via blocking macrophage M2 polarization. *PLOS ONE* **11**, e0166808. doi: 10.1371/journal.pone.0166808.

Zou, J., Hannula, M., Misra, S., Feng, H., Labrador, R. H., Aula, A. S., Hyttinen, J. and Pyykkö, I. (2015). Micro CT visualization of silver nanoparticles in the middle and inner ear of rat and transportation pathway after transtympanic injection. *Journal of nanobiotechnology* **13**, 5. doi: 10.1186/s12951-015-0065-9.

Zuber, C., Fan, J.-Y., Guhl, B. and Roth, J. (2004). Misfolded proinsulin accumulates in expanded pre-Golgi intermediates and endoplasmic reticulum subdomains in pancreatic beta cells of Akita mice. *The FASEB Journal* **18**, 917–919. doi: 10.1096/fj.03-1210fje.

Zumla, A., Atun, R., Maeurer, M., Mwaba, P., Ma, Z., O'Grady, J., Bates, M., Dheda, K., Hoelscher, M. and Grange, J. (2011). Viewpoint: Scientific dogmas, paradoxes and mysteries of latent Mycobacterium tuberculosis infection. *Tropical Medicine & International Health* **16**, 79–83. doi: 10.1111/j.1365-3156.2010.02665.x.

Zumthor, J. P., Cernikova, L., Rout, S., Kaech, A., Faso, C. and Hehl, A. B. (2016). Static

clathrin assemblies at the peripheral vacuole—plasma membrane interface of the parasitic protozoan Giardia lamblia. *PLOS Pathogens* **12**, e1005756. doi: 10.1371/journal.ppat.1005756.

Blank page

Appendices

Apart from the work forming the chapters of the main thesis, I was involved in the authorship of two other relevant publications which have been cited throughout. These publications are presented as final proofs over the following pages. The first (**appendix 1**) is a short review and opinion on the use of microCT in the study of parasites, published in *Parasitology.* The second (**appendix 2**), is a description and set of case studies of the correlative microCT-EM workflow adopted in chapter 5, which was published in *Ultramicroscopy*. **Appendix 3** is the full Matlab code used to measure mucosal thickness in section 4.2.5.

The two papers are presented here in their pre-proof versions, after peer-review comments.

The papers in their published versions are available as follows:

Appendix 1: O'Sullivan J D B, Behnsen J, Starborg T, MacDonald A S, Phythian-Adams A T, Else K J, Cruickshank S M and Withers P J 2018 X-ray micro-computed tomography (CT): an emerging opportunity in parasite imaging *Parasitology* **145** 848-54

Appendix 2: Starborg T, O'Sullivan J D B, Carneiro C M, Behnsen J, Else K J, Grencis R K and Withers P J 2019 Experimental steering of electron microscopy studies using prior X-ray computed tomography *Ultramicroscopy* **201** 58-67

Preface to Appendix 1

I was the main contributor to the following review, *X-ray micro-computed tomography (CT): an emerging opportunity in parasite imaging*.

The Contributions of the other authors were as follows:

PJW, KJE and SMC provided feedback on the manuscript

JB and TS were involved in preparation of the example images involving *T. muris*

ASM and ATP were involved in preparation of the example images involving liver tissue

X-ray micro-computed tomography (μCT): An emerging opportunity in parasite imaging

James D B O'Sullivan[†1], Julia Behnsen[1], Tobias Starborg[2], Andrew S MacDonald[2], Alexander T Phythian-Adams[2], Kathryn J Else[*2], Sheena M Cruickshank[*2], Philip J Withers[*1]

*Senior authors

[†]Correspondence: james.osullivan-4@postgrad.manchester.ac.uk

[1]School of Materials

University of Manchester

Oxford Road

Manchester

M13 9PL

[2]School of Biological Sciences

University of Manchester

Oxford Road

Manchester

M13 9PL

SUMMARY

X-ray micro-computed tomography (μCT) is a technique which can obtain 3D images of a sample, including its internal structure, without the need for destructive sectioning. Here, we review the capability of the technique and examine its potential to provide novel insights into the lifestyles of parasites embedded within host tissue. The current capabilities and limitations of the technology in producing contrast in soft tissues are discussed, as well as the potential solutions for parasitologists looking to apply this technique. We present example images of the mouse whipworm *Trichuris muris* and discuss the application of μCT to provide unique insights into parasite behaviour and pathology which are inaccessible to other imaging modalities.

KEY WORDS**:** X-ray tomography, Helminth, pathology, microscopy

KEY FINDINGS

- X-ray microcomputed tomography (μCT) allows 3D imaging at histological resolution
- μCT is non-destructive, and can image deeper than confocal microscopy over a large field of view
- μCTs capabilities can allow it to address existing limitations in parasite imaging
- 3D μCT data presents exciting opportunities for education and public engagement

INTRODUCTION

Microscopy is a ubiquitous tool for investigating the lifestyles of parasites, and the development of new imaging technologies produces novel insights into how parasites survive in their hosts. For example, electron microscopy captured snapshots of dynamic ultrastructural changes occurring during host invasion by the protozoan *Leishmania donovani* (Loussert *et al.*, 2012), whilst the development of fluorescent and luminescent labelled antibodies, as well as transgenic strains of parasites themselves, allow tracking of a spreading infection within a host (Henriques *et al.*, 2014; Qin *et al.*, 2014; Siciliano and Alano, 2015).

Soil transmitted helminths infect billions of people worldwide and are a significant economic burden (Pullan *et al.*, 2014), yet their lifestyles often remain enigmatic. Complexities surrounding genetic makeup, coupled with difficulties in their maintenance *in vitro*, mean that they lack the potential for genetic tractability which has driven the study of protozoans. An example of these problems is the whipworm *Trichuris* spp., which infects roughly half a billion people worldwide. Existing drugs have limited efficacy (Speich *et al.*, 2015), do not prevent reinfection (Jia *et al.*, 2012) and concerns have grown that existing drugs may become increasingly redundant in the face of increasing anthelminthic resistance (Wolstenholme *et al.*, 2004; Sutherland

and Leathwick, 2011; Vercruysse *et al.*, 2011). Despite this, little is known about invasion patterns, reproduction and feeding and consequently there is a need for novel approaches to studying the lifestyle of parasites such as *Trichuris* to identify novel therapeutic targets.

Here we present *ex vivo* X-ray micro-computed tomography (μCT) as a largely unexploited opportunity which can avoid the limitations of other prominent imaging modalities and provide new insights into parasite lifestyle. Whilst μCT has existed for over 30 years (Elliott and Dover, 1982), relatively recent progress in optimising imaging technology and soft tissue sample preparation has vastly improved the accessibility of the technique for researchers interested in studying parasites. As well as detailing the working principles of μCT, we also summarise aspects of sample preparation which we deem of importance to those looking to visualise samples of soft tissue. Example images of the mouse whipworm *Trichuris muris*, which has an unusual "intracellular" lifestyle embedded within the gut lining of its murine host, are used to illustrate the unique ability of μCT to visualise the spatial positioning of parasites embedded within host tissue *ex vivo*, without any need for sectioning. As well as minimising sectioning-associated artefacts, we also discuss how analysis of virtual slices in 3D data presents unique advantages over other imaging modalities, and how 3D images provide novel opportunities for education and engagement, including via 3D printing.

PRINCIPLES OF X-RAY MICRO-COMPUTED TOMOGRAPHY

X-ray micro-computed tomography (μCT) was developed in the early 1980s (Dover *et al.*, 1981; Elliott *et al.*, 1981; Elliott and Dover, 1982) and could be described as the microscopic cousin of the clinical Computed Tomography (CT) scanners used to examine human patients in hospitals today. However, whereas medical scanners usually have resolutions in the mm range, μCT systems typically achieve resolutions in

the 1-100 μm range. When imaging using X-ray tomography, many (typically between 500 and 3000) 2D projections (digital radiographs) of a sample are collected from many different angles using penetrating X-rays. Following their acquisition, a 3D image of the absorptive power of the sample is reconstructed computationally from the 2D projections (Fig. 1). Tomographic images can also be reconstructed from images produced with gamma rays (Ter-Pogossian *et al.*, 1975), neutrons (Winkler, 2006), electrons (Crowther *et al.*, 1970) or visible light (Sharpe *et al.*, 2002). However, X-rays are often chosen based on the balance between penetration of, and attenuation by, the sample, such that sufficient **contrast** can permit the differentiation of internal features of interest. The contrast results from the differential attenuation of X-rays, as determined by the **attenuation coefficient** of the constituent materials. If a material is dense, or includes heavy elements, more X-rays will be attenuated and **transmittance** will be reduced. Upon acquisition of the data, the 3D volume can be interrogated by examining key virtual cross-sectional images or the whole image stack. In many cases quantification of features in the imaged volume requires the application of 'segmentation' workflows, a process by which domains/features of interest within the sample are virtually distinguished and labelled. Subsequently, visualisation and quantitative analysis of the number, morphology and distribution of the features can then be undertaken (Maire and Withers, 2014).

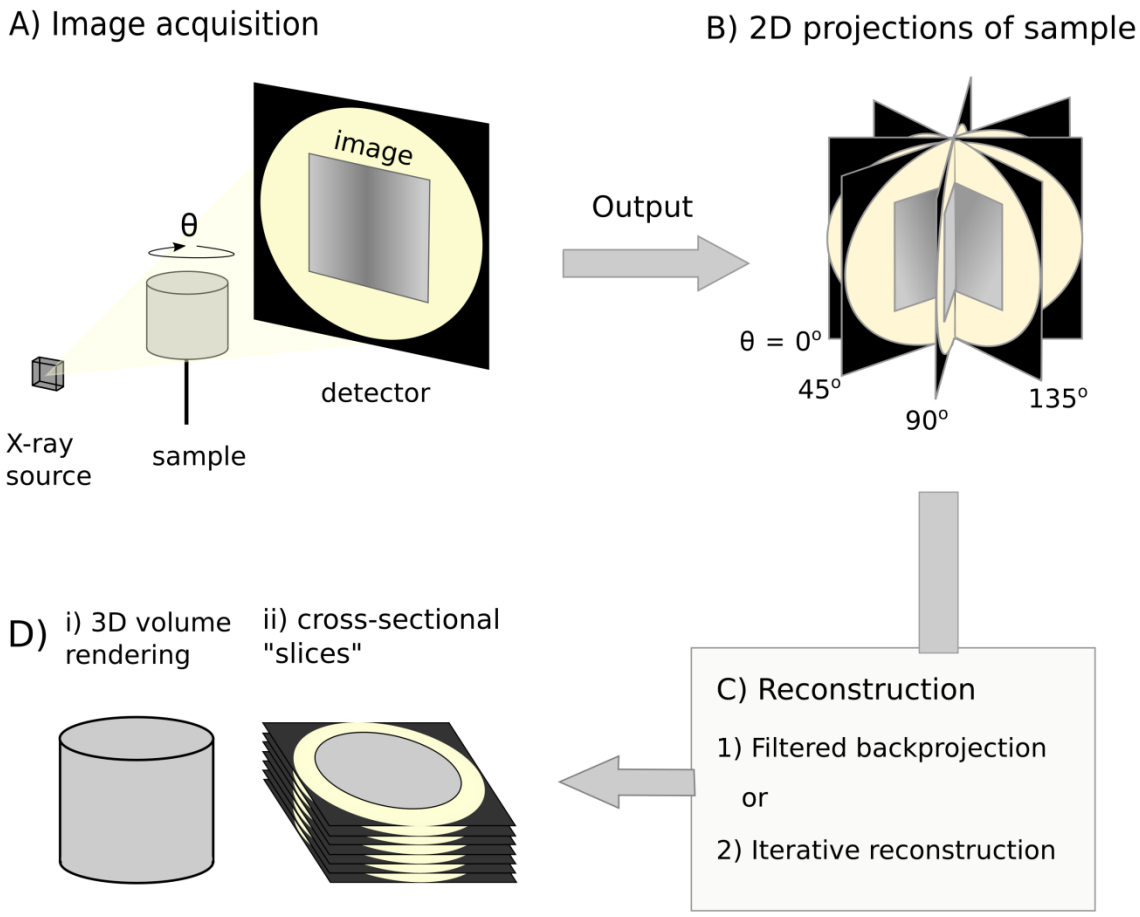

Figure 1: Diagrammatic representation of X-ray micro-computed tomography workflow. A) Basic illustration of tomographic apparatus, including the X-ray source, detector and sample. Projection images are made as the sample is rotated at increments through θ. B) The raw output of the tomogram is a series of projections of the sample taken at different angles C) Projections are digitally "reconstructed"; two commonly used approaches are filtered backprojection and iterative reconstruction. Reconstruction algorithms output a dataset which is suitable for analysis. D) The sample may be viewed in a virtual environment in a variety of ways, including as a 3D rendered volume (i). Alternatively, 2D cross-sections, or “slices”, of the sample may be viewed (ii)

There are at least two scanning arrangements by which the necessary projections are acquired. The first involves rotating a gantry-mounted x-ray source and detector around the object. This method is used in clinical CT scanners and has the advantage for *in vivo* study that the subject is easily stabilised on a flat surface, minimising soft tissue organ movement. The spatial resolution in the gantry-based scanners typically used in preclinical research involving rodents approaches 50 μm (Ritman, 2011). The second scanning arrangement involves rotating the sample on a table whilst keeping the source and detector stationary (see Fig. 1A). Instruments based on the rotating table approach often exploit the use of X-ray lenses and/or variable **geometric magnification** to generate images typically with superior spatial resolutions, which can reach sub-micron levels in certain instruments (Withers, 2007). Rotating table μCT has found usage in a broad range of research areas, including materials (Stock, 2008), geology (Cnudde and Boone, 2013) and life science (Bradley and Withers, 2016).

In vivo preclinical studies have typically used gantry-based scanning arrangements to image whole model organisms such as mice (Cunha *et al.*, 2014). Provided that sufficient contrast can be achieved, *in vivo* studies of parasites offer exciting avenues for future study, particularly for time-lapse monitoring of infection (Lee *et al.*, 2007; Dillon *et al.*, 2013) and assessment of pathology (Ha *et al.*, 2016). Whilst rotating table systems have been used for preclinical *in vivo* studies on rodent models (Paulus *et al.*, 2000; Burstein *et al.*, 2002), they are now commonly used to study inanimate objects and *ex vivo* systems. *Ex vivo* tissue samples are amenable to a range of sample preparation techniques including staining which provide the necessary contrast for viewing histological features. Furthermore, longer image acquisitions facilitating higher spatial resolutions are possible *ex vivo*, as X-ray dose does not need to be limited as with living organisms (Ford *et al.*, 2003). Within the last decade, the ability to retrieve 3D images at close to histological resolution means rotating table μCT has attracted an increasing amount of attention from a broader range of biologists,

notably palaeontologists (Tafforeau *et al.*, 2006), and comparative morphologists (Metscher, 2009a), but largely not yet parasitologists.

In this paper we will consider the opportunities recently opened up by high resolution *ex vivo* µCT with regard to its potential application to parasitological questions. Since its inception, there have been a multitude of methodological developments in µCT technology for biological imaging, exhaustive discussion of which is beyond the scope of this article. However, correlative tomography (Burnett *et al.*, 2014), in which results of multiple imaging modalities are combined, may be of interest to those attempting to integrate functional information in a larger spatial context. In "correlative workflows", µCT datasets have been combined with light microscopic histological observations (Duke *et al.*, 2009; Particelli *et al.*, 2012; Geffre *et al.*, 2015; Bagi *et al.*, 2015) and electron micrographs (Handschuh *et al.*, 2013; Bushong *et al.*, 2015). Such multiscale studies put functional and structural observations on a histological or subcellular scale into the larger spatial context provided by µCT.

CONTRAST ENHANCEMENT FOR PARASITE IMAGING

Use of contrast agents

Imaging parasites within soft tissue introduces challenges for the tomographic process. Because soft tissue is low-density and consists mostly of light elements such as carbon and hydrogen, it attenuates X-rays poorly, resulting in low **contrast** between internal features. Staining with a suitable contrast agent can greatly enhance visibility of tissue structure (Fig. 2). In the case of µCT, ideal stains incorporate heavy elements which bind differentially to internal regions of a sample and provide increased contrast due to higher range of X-ray attenuation. Iodine (as aqueous I_2KI or in ethanol) is a popular choice of stain among researchers looking to visualise soft tissue organisation (Gignac *et al.*, 2016). Stains traditionally used for electron microscopy such as osmium tetroxide and uranyl acetate have also been adopted, as their high electron densities have a

translatable attenuating effect on transmitted X-rays (Descamps *et al.*, 2014), and their common usage between μCT and electron microscopy facilitates correlative workflows. Staining agents must be able to penetrate the whole way into a sample, and therefore staining agents are generally chosen based on fast diffusion rates, rather than specific binding properties. Systematic assessment of a variety of staining species has identified potassium iodide (KI) and mercuric chloride ($Hg(II)Cl_2$) as demonstrating suitably fast diffusion rates (Pauwels *et al.* 2013). However, phosphotungstic acid (PTA) and phosphomolybdenic acid (PMA), which have a slower rate of diffusion, have been highlighted as effective in visualisation of collagenous structures due to their specific binding properties (Metscher, 2009b; Nierenberger *et al.* 2015).

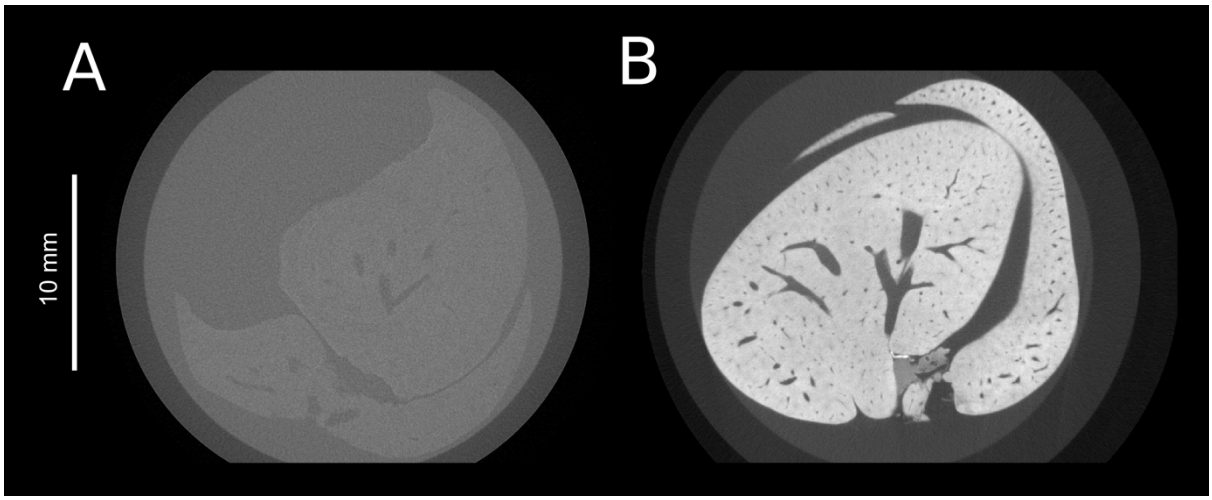

Figure 2. Greyscale slices of two whole mouse livers, acquired under the same X-ray beam energies but differentially prepared. (A) Unstained mouse liver. The outline of the liver is barely visible, and little internal detail can be distinguished. (B) Mouse liver which has been immersed in a mixture containing 1·66% m/v I2 and 3·44% KI for 48 h. Liver tissue appears brighter due to increased attenuation of X-rays from the source, and there is high contrast between the vascular lumen and the surrounding tissue.

It is important to note that the optimal staining time and concentration will be unknown in soft tissues which have not been previously investigated, as differences in tissue composition will result in varying stain binding affinities and rates of stain uptake. A recent meta-analysis of iodine staining includes comprehensive sample preparation information for a large variety of soft tissue samples of different sizes obtained from different species, which authors may refer to in order to ease the amount of guesswork required for previously unstudied samples (Gignac *et al.* 2016). However, no similar meta-analyses are available for other stains, which may require a trial-and-error approach using multiple scans to determine the optimal stain concentration and staining time (Aslanidi *et al.* 2013). An additional consideration is the risk of sample shrinkage during the immersion staining process, with the degree of shrinkage increasing with the concentration of the staining solution (Vickerton *et al.* 2013). However, treatment in graded ethanol before staining is efficient in minimising shrinkage and preserving the native structure of tissue (de Souza e Silva *et al.* 2015).

Phase contrast

Phase contrast is an alternative contrast-enhancement method originally developed for light microscopy, the physical principles of which have since been exploited in μCT instruments. Whilst unstained biological soft tissue is weakly absorbing of the hard energy X-rays produced by laboratory sources, it can produce significant shifts in the phase of transmitted X-rays. Phase contrast is the term used to describe imaging which exploits this effect. For most laboratory μCT systems the illuminating X-rays show little **coherence** and phase gratings must be used to generate phase contrast in the image (Momose *et al.* 2003). However, some laboratory systems do exhibit sufficient coherence for propagation-based imaging (Wu, 2014), edge illumination (Olivo and Speller, 2007) or Zernike phase contrast (Bradley *et al.* 2010). Consequently, phase contrast techniques are now more accessible to researchers trying to image soft tissue

without the use of staining (Bech *et al.* 2009; Zamir *et al.* 2016). Indeed, grating and propagation-based phase contrast have both been investigated as alternatives to serial light microscopic histology (Zanette *et al.*, 2013; Holme *et al.*, 2014).

WHAT PARASITOLOGICAL QUESTIONS COULD µCT ADDRESS?

Until now, a great deal of morphological information about helminths has been gathered by both scanning and transmission electron microscopy, which boast sub-micron resolutions superior to those achievable by µCT systems (Egerton, 2005b; a). However, a sample prepared for µCT does not need to be physically sectioned to view internal structure, so information about the spatial positioning of parasites relative to the host can be gathered without the risk of sectioning-associated artefacts. Furthermore, unusual features are more likely to be found because a volume is interrogated, rather than a cross-sectional area such as a tissue section, which may or may not intersect with the feature of interest. These could be subsequently examined at a higher resolution by electron microscopy within a correlative tomography framework if required. In the case of *Trichuris*, imaging a 3D volume also uniquely allows trajectories of multiple worms to be separated in relation to surrounding host tissue. However, similarly to techniques involving sectioning, rotating-table µCT at histological (i.e. 1 µm) resolution is generally applicable only to *ex vivo* fixed samples for several reasons. Firstly, the time required to acquire all the projections for µCT, typically between two and ten hours using a lab source, precludes imaging of dynamic processes on a similar timescale (although a small number of studies have imaged slow (occurring over several days (Lowe *et al.* 2013)) or cyclical processes (Mokso *et al.* 2015) *in vivo*, albeit in comparatively radiation-tolerant insects). Additionally, the short distance between the X-ray source and sample (in the orders of a few millimetres to tens of millimetres) required to achieve the highest resolutions in a region of interest is only practical for *ex vivo* samples. The low contrast provided by unstained tissue is

also a factor which precludes imaging of soft tissue *in vivo* at histological resolution. Magnetic Resonance Imaging (MRI), which is amenable to *in vivo* imaging, has been used to analyse parasite-induced pathology in whole animals (Voieta *et al.* 2010; Masi *et al.* 2015). However, MRI has a spatial resolution approaching 25-100 μm in the most powerful magnetic fields (Shapiro *et al.* 2004; de Kemp *et al.* 2010), and no meaningful morphological information about tissue structure can be gathered below this threshold.

The first ever published micro-computed **tomogram** depicted the snail *Biomphalaira glabrata*, a vector of the blood fluke *Schistosoma mansoni* (Elliott and Dover, 1982). However, to date, μCT has been applied minimally in parasitological contexts. It has been used to investigate the internal head morphology of *Rhodinus prolixus*, the insect vector for Chagas disease, the imaging of which is facilitated by the relatively high X-ray attenuation of the insect's chitinous cuticle (Sena *et al.* 2014). The unique capabilities of μCT represent an unexploited opportunity to visualise the spatial positioning of helminth endoparasites and their associated pathology. The technique also possesses key advantages over light and electron microscopy in the context of visualising an organism embedded within soft tissue. A key potential application of μCT is that 3D imaging facilitates assessment of accumulation and distribution of parasites within whole organs. This capability has been exploited by two helminth-centric studies to our knowledge, including visualisation of cyst accumulation of the trematode *Paragonimus westermani* in the lung of dogs and an accompanying description of connective channels between the cysts and the surrounding bronchi (Lee *et al.*, 2007). Heterogeneous distribution of Schistosome eggs in the vertebrate central nervous system has also been described (Bulantová *et al.* 2016). Such examples highlight the potential of 3D data to explore phenomena such as migration and invasion of host tissue through the tracking of multiple parasites in relation to the host tissue at once. Higher resolution μCT has also served to highlight interactions between protozoan parasites and host tissues on the nanoscale. In *Plasmodium falciparum*, 3D visualisation of parasite-infected erythrocytes has allowed quantification of their

changing volume and haemoglobin content throughout the course of infection (Hanssen *et al.*, 2012), as well as collapse of membrane integrity before egress of merozoites (Hale *et al.*, 2017).

Apart from requiring a large time investment when investigating a large volume, several other disadvantages also accompany the use of manual sectioning. Samples must often be cut down to a size appropriate for the sectioning equipment, and given a specific orientation so that features of interest identified may be visualised optimally. Such procedures result in a risk of scientifically novel features, which are unaccounted for in the study design, being overlooked. To illustrate how µCT can reduce this risk, we include an example where the µCT workflow captures positioning of the anterior-most portions of *Trichuris* towards the basement membrane of the gut lining (Fig. 3), which is an observation made much more accessible by the capability of µCT to visualise the trajectory of an entire worm. Furthermore, finding parasites within a pre-cut block of tissue is a difficult undertaking with no guarantee of success, as researchers are blind to the internal structure pre-sectioning. In µCT, virtual slices of any orientation within an un-sectioned sample can be visualised, and regions of interest can be determined in a more informed manner once the internal structure is known.

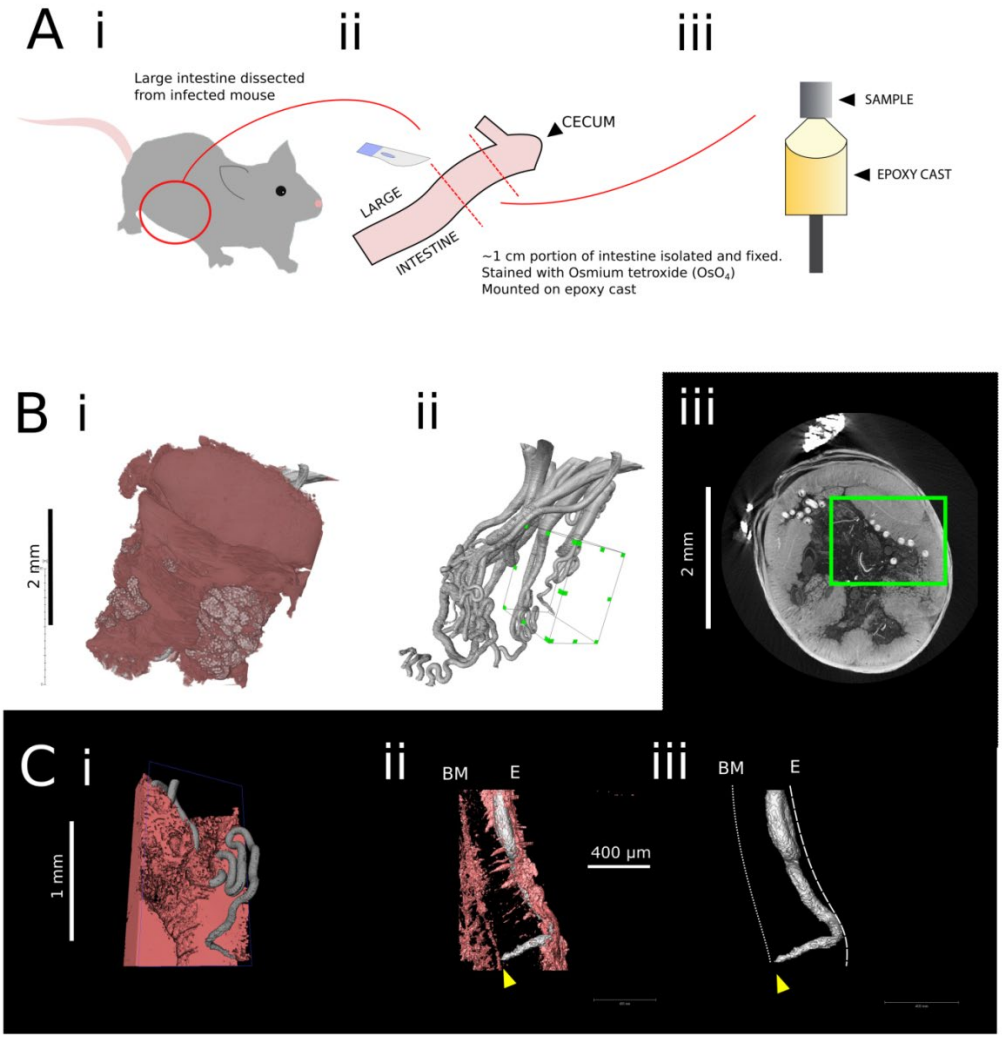

Figure 3: Summary of sample preparation protocol, followed by images acquired on an Xradia Versa XRM 520 tomograph, highlighting positioning of a Trichuris head. (Ai) The large intestine was dissected from a T. muris-infected mouse. (Aii) An approximately 1 cm length of the dissected gut was isolated, fixed in 4% PFA, stained with osmium tetroxide (OsO4) and (Aiii) mounted on an epoxy cast. (Bi) 3D volume rendering of the gut section containing Trichuris and (Bii) 3D surface rendering of the worms that were embedded in that gut section. A green-highlighted cuboid indicates a region of interest which includes the head of a single worm. (Biii) a green square shows the position of the same region of interest in a 2D slice. (Ci) a pseudocoloured volume-rendering of a subsection of the region of interest including Trichuris (grey) embedded within the gut lining (pink). (Cii) Virtual 3D 'surfaces' showing the positioning of the head of Trichuris (grey) in relation to the gut lining (pink). The tip of the head is marked by a yellow arrow. (Ciii) The gut lining is virtually removed from the image, showing the

positioning of the tip of the head in relation to the planes of the basement membrane (BM) and the internal epithelial surface (E), which are indicated by dotted white lines.

The use of μCT also introduces new options for quantitative measurement. Similarly to digitally stored histology slides, 2D distance measurements can be made in virtual slices of a sample. However, existing software and algorithms designed for analysis of non-biological μCT data can be co-opted for the study of parasites. One example of this specific to *Trichuris* is the use of skeletonisation algorithms which estimate the length and topology of filamentous structures. The visualisation and analysis software AVIZO (FEI Visualisation Sciences Group) includes propriety skeletonisation algorithms. However, the Fiji distribution of ImageJ (Schindelin *et al.*, 2012) also includes a skeletonisation extension based on the algorithm of Lee et al. (1994). Skeletons produced in this way can then be analysed using the Analyze Skeleton extension developed for ImageJ (Arganda-Carreras *et al.*, 2010). In the case of *Trichuris*, skeletonisation can be employed to estimate the length of a worm which is embedded within the gut lining (Fig. 4). Furthermore, the length of a given parasite which is covered by the epithelium and the overall integrity of the epithelial niche can be estimated. Such inferences may have importance in determining required pharmacokinetic properties of drugs; if integrity of the epithelial tunnel is high, drugs can be designed to have local epithelial penetrance; in contrast, if large proportions of the worm are exposed to the gut lumen by “breaks” in the epithelial tunnel such novel drug design may not be necessary.

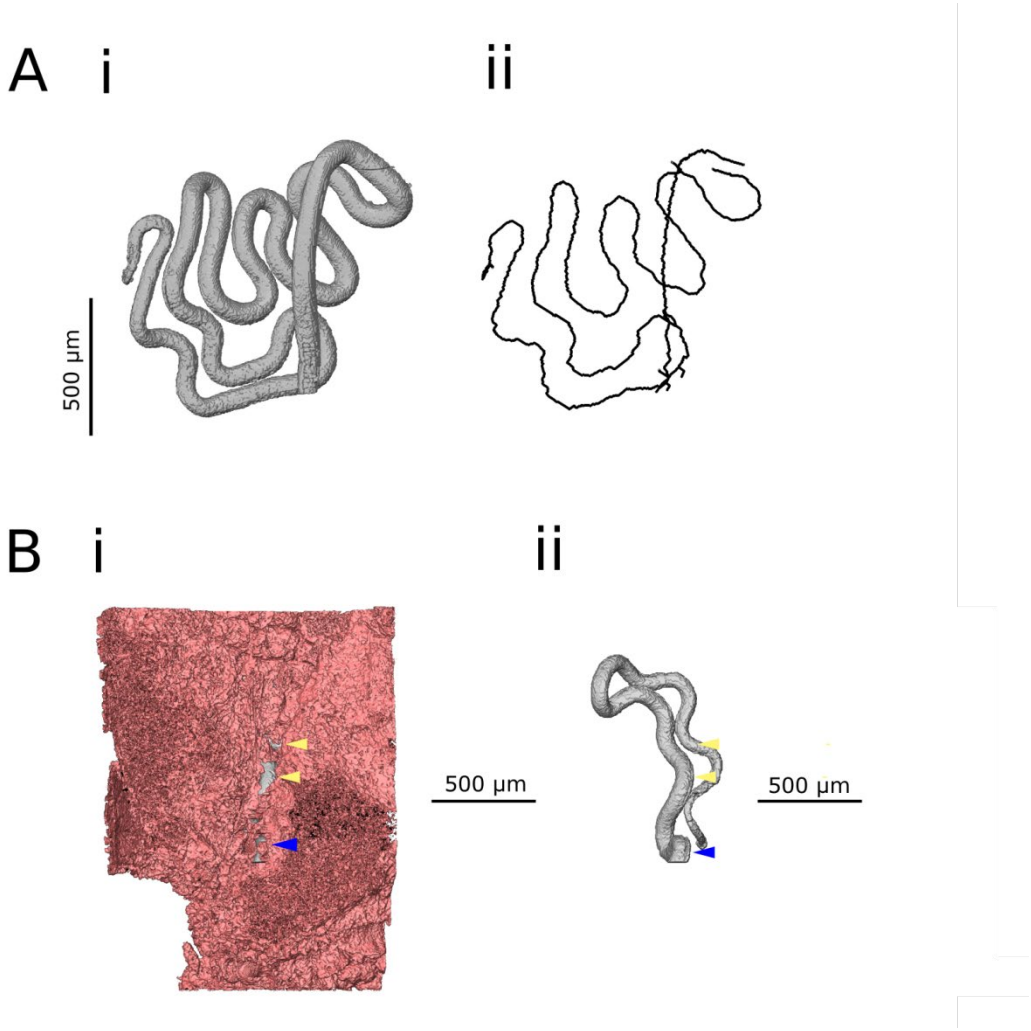

Figure 4: 3D models indicating quantitative measurements possible in 3D datasets. Ai) 3D model of the anterior of Trichuris (grey) which has been 'segmented' (virtually distinguished and labelled, so that it can be visualised independently of surrounding tissue). Aii) A 'spatial graph' is shown, which is produced from an algorithm designed to find and measure the "centreline" of filamentous structures. In this way, the length of a portion of a worm, for instance, that embedded within the gut lining, can be measured. B) 3D models of the anterior of Trichuris (grey) embedded in the epithelium (pink) (i). Bii) is the same image, with the epithelium virtually removed, such that only the embedded worm is visible. Blue arrows indicate the position at which the worm "enters" the gut lining, and yellow arrows indicate breaks or tears in epithelium overlying the embedded worm. The proportion of the embedded worm which is exposed by these breaks can be estimated by using the "centerline tree" algorithm

CONCLUDING REMARKS

Whilst X-ray micro-computed tomography (μCT) has been only minimally used by parasitologists to date, its increasing availability and performance presents a variety of new research opportunities. As a non-destructive method, when coupled with measures taken to enhance image contrast during sample preparation and imaging, the ability to track multiple parasites within intact host tissue particularly provides new opportunities. This technique has already been exploited by a small number of studies for investigating parasite accumulation, distribution and migration, as well as pathology. Qualitative and quantitative analysis of data collected from such efforts is already enabled by a broad array of existing software tools. Additionally, publically archived 3D datasets provide an excellent opportunity to continue data analysis post-publication and can constitute an exciting medium for education and public engagement through the medium of 3D printing.

FINANCIAL SUPPORT AND ETHICS STATEMENT

We acknowledge the University of Manchester for contributing towards the financial support for acquiring example images. The Manchester Henry Moseley X-ray Imaging Facility was funded in part by the EPSRC (grants EP/F007906/1, EP/F001452/1 and EP/I02249X/1) and the HEFCE grant for the Multidisciplinary Characterisation Facility. JDBO is supported by a studentship from Xradia, a division of Carl Zeiss AG. PJW is funded through an Advanced Grant from the European Research Council (CORREL-CT Proj. No. 695638). KJE is funded through a project grant from the Medical Research Council (MR/N022661/1). All animal use was approved by the University of Manchester Animal Welfare and Ethical Review Board and performed under the regulation of the Home Office Scientific Procedures Act (1986) and the Home Office project licence 70/8127.

REFERENCES

Arganda-Carreras, I., Fernández-González, R., Muñoz-Barrutia, A. and Ortiz-De-Solorzano, C. (2010). 3D reconstruction of histological sections: application to mammary gland tissue. *Microscopy Research and Technique* **73**, 1019–1029. doi:10.1002/jemt.20829.

Aslanidi, O. V, Nikolaidou, T., Zhao, J., Smaill, B. H., Gilbert, S. H., Holden, A. V, Lowe, T., Withers, P. J., Stephenson, R. S., Jarvis, J. C., Hancox, J. C., Boyett, M. R. and Zhang, H. (2013). Application of micro-computed tomography with iodine staining to cardiac imaging, segmentation, and computational model development. *IEEE transactions on medical imaging* **32**, 8–17. doi:10.1109/TMI.2012.2209183.

Bagi, C. M., Zakur, D. E., Berryman, E., Andresen, C. J. and Wilkie, D. (2015). Correlation between μCT imaging, histology and functional capacity of the osteoarthritic knee in the rat model of osteoarthritis. *Journal of Translational Medicine* **13**, 276. doi:10.1186/s12967-015-0641-7.

Bech, M., Jensen, T. H., Feidenhans, R., Bunk, O., David, C. and Pfeiffer, F. (2009). Soft-tissue phase-contrast tomography with an x-ray tube source. *Physics in Medicine and Biology* **54**, 2747–2753. doi:10.1088/0031-9155/54/9/010.

Bradley, R. S. and Withers, P. J. (2016). Correlative multiscale tomography of biological materials. *MRS Bulletin* **41**, 549–556. doi:10.1557/mrs.2016.137.

Bradley, R. S., McNeil, A. and Withers, P. J. (2010). An examination of phase retrieval algorithms as applied to phase contrast tomography using laboratory sources. In (ed. Stock, S. R.), p. 780404. doi:10.1117/12.860536.

Bulantová, J., Macháček, T., Panská, L., Krejčí, F., Karch, J., Jährling, N., Saghafi, S., Dodt, H.-U. and Horák, P. (2016). Trichobilharzia regenti (Schistosomatidae):

3D imaging techniques in characterization of larval migration through the CNS of vertebrates. *Micron* **83**, 62–71. doi:10.1016/j.micron.2016.01.009.

Burnett, T. L., McDonald, S. A., Gholinia, A., Geurts, R., Janus, M., Slater, T., Haigh, S. J., Ornek, C., Almuaili, F., Engelberg, D. L., Thompson, G. E. and Withers, P. J. (2014). Correlative tomography. *Scientific Reports* **4**, 4711. doi:10.1038/srep04711.

Burstein, P., Bjorkholm, P. J., Chase, R. C. and Seguin, F. H. (2002). The largest and smallest X-ray computed tomography systems. *Nuclear Instruments and Methods in Physics Research* **221**, 207–212. doi:10.1016/0167-5087(84)90201-1.

Bushong, E. A., Johnson, D. D., Kim, K.-Y., Terada, M., Hatori, M., Peltier, S. T., Panda, S., Merkle, A. and Ellisman, M. H. (2015). X-ray microscopy as an approach to increasing accuracy and efficiency of serial block-face imaging for correlated light and electron microscopy of biological specimens. *Microscopy and Microanalysis* **21**, 231–238. doi:10.1017/S1431927614013579.

Cnudde, V. and Boone, M. N. (2013). High-resolution X-ray computed tomography in geosciences: A review of the current technology and applications. *Earth-Science Reviews* **123**, 1–17. doi:10.1016/j.earscirev.2013.04.003.

Crowther, R. A., DeRosier, D. J. and Klug, A. (1970). The reconstruction of a three-dimensional structure from projections and its application to electron microscopy. *Proceedings of the Royal Society A: Mathematical, Physical and Engineering Sciences* **317**, 319–340. doi:10.1098/rspa.1970.0119.

Cunha, L., Horvath, I., Ferreira, S., Lemos, J., Costa, P., Vieira, D., Veres, D. S., Szigeti, K., Summavielle, T., Máthé, D. and Metello, L. F. (2014). Preclinical imaging: an essential ally in modern biosciences. *Molecular Diagnosis & Therapy* **18**, 153–173. doi:10.1007/s40291-013-0062-3.

de Kemp, R. A., Epstein, F. H., Catana, C., Tsui, B. M. W. and Ritman, E. L. (2010).

Small-animal molecular imaging methods. *Journal of Nuclear Medicine* **51**, 18–32. doi:10.2967/jnumed.109.068148.

de Souza e Silva, J. M., Zanette, I., Noël, P. B., Cardoso, M. B., Kimm, M. A. and Pfeiffer, F. (2015). Three-dimensional non-destructive soft-tissue visualization with X-ray staining micro-tomography. *Scientific Reports* **5**, 14088. doi:10.1038/srep14088.

Descamps, E., Sochacka, A., Kegel, B. De, Loo, D. Van, Hoorebeke, V. and Adriaens, D. (2014). Soft tissue discrimination with contrast agents using micro-CT scanning. *Belgium Journal of Zoology* **144**, 20–40.

Dillon, A. R., Tillson, D. M., Hathcock, J., Brawner, B., Wooldridge, A., Cattley, R., Welles, B., Barney, S., Lee-Fowler, T., Botzman, L., Sermersheim, M. and Garbarino, R. (2013). Lung histopathology, radiography, high-resolution computed tomography, and bronchio-alveolar lavage cytology are altered by Toxocara cati infection in cats and is independent of development of adult intestinal parasites. *Veterinary Parasitology* **193**, 413–426. doi:10.1016/j.vetpar.2012.12.045.

Dover, S. D., Elliott, A. and Kernaghan, A. K. (1981). Three-dimensional reconstruction from images of tilted specimens: the paramyosin filament. *Journal of Microscopy* **122**, 23–33. doi:10.1111/j.1365-2818.1981.tb01239.x.

Duke, P. J., Doan, L., Luong, H., Kelley, C., Leboeuf, W., Diep, Q., Johnson, E. and Cody, D. D. (2009). Correlation between micro-CT sections and histological sections of mouse skull defects implanted with engineered cartilage. *Gravitational and Space Biology Bulletin* **22**, 45–50.

Egerton, R. F. (2005a). The Scanning Electron Microscope. In *Physical Principles of Electron Microscopy*, pp. 129–151. Springer US, New York.

Egerton, R. F. (2005b). TEM Specimens and Images. In *Physical Principles of*

Electron Microscopy, pp. 93–124. Springer US, New York.

Elliott, J. C. and Dover, S. D. (1982). X-ray microtomography. *Journal of Microscopy* **126**, 211–213. doi:10.1111/j.1365-2818.1982.tb00376.x.

Elliott, J. C., Dowker, S. E. P. and Knight, R. D. (1981). Scanning X-ray microradiography of a section of a carious lesion in dental enamel. *Journal of Microscopy* **123**, 89–92. doi:10.1111/j.1365-2818.1981.tb01282.x.

Ford, N. L., Thornton, M. M. and Holdsworth, D. W. (2003). Fundamental image quality limits for microcomputed tomography in small animals. *Medical Physics* **30**, 2869–2877. doi:10.1118/1.1617353.

Geffre, C. P., Pond, E., Pond, G. D., Sroka, I. C., Gard, J. M., Skovan, B. A., Meek, W. E., Landowski, T. H., Nagle, R. B. and Cress, A. E. (2015). Combined micro CT and histopathology for evaluation of skeletal metastasis in live animals. *American Journal of Translational Research* **7**, 348–355.

Gignac, P. M., Kley, N. J., Clarke, J. A., Colbert, M. W., Morhardt, A. C., Cerio, D., Cost, I. N., Cox, P. G., Daza, J. D., Early, C. M., Echols, M. S., Henkelman, R. M., Herdina, A. N., Holliday, C. M., Li, Z., Mahlow, K., Merchant, S., Müller, J., Orsbon, C. P., Paluh, D. J., Thies, M. L., Tsai, H. P. and Witmer, L. M. (2016). Diffusible iodine-based contrast-enhanced computed tomography (diceCT): an emerging tool for rapid, high-resolution, 3-D imaging of metazoan soft tissues. *Journal of Anatomy* **228**, 889–909. doi:10.1111/joa.12449.

Ha, Y. R., Kang, S.-A., Ryu, J., Yeom, E., Kim, M. K. and Lee, S. J. (2016). SPECT/CT analysis of splenic function in genistein-treated malaria-infected mice. *Experimental Parasitology* **170**, 10–15. doi:10.1016/j.exppara.2016.08.008.

Hale, V. L., Watermeyer, J. M., Hackett, F., Vizcay-Barrena, G., van Ooij, C., Thomas, J. A., Spink, M. C., Harkiolaki, M., Duke, E., Fleck, R. A., Blackman, M. J. and Saibil, H. R. (2017). Parasitophorous vacuole poration precedes its

rupture and rapid host erythrocyte cytoskeleton collapse in Plasmodium falciparum egress. *Proceedings of the National Academy of Sciences* **114**, 3439–3444. doi:10.1073/pnas.1619441114.

Handschuh, S., Baeumler, N., Schwaha, T. and Ruthensteiner, B. (2013). A correlative approach for combining microCT, light and transmission electron microscopy in a single 3D scenario. *Frontiers in Zoology* **10**, 44. doi:10.1186/1742-9994-10-44.

Hanssen, E., Knoechel, C., Dearnley, M., Dixon, M. W. A., Le Gros, M., Larabell, C. and Tilley, L. (2012). Soft X-ray microscopy analysis of cell volume and hemoglobin content in erythrocytes infected with asexual and sexual stages of Plasmodium falciparum. *Journal of Structural Biology* **177**, 224–232. doi:10.1016/j.jsb.2011.09.003.

Henriques, C., Henriques-Pons, A., Meuser-Batista, M., Ribeiro, A. and de Souza, W. (2014). In vivo imaging of mice infected with bioluminescent Trypanosoma cruzi unveils novel sites of infection. *Parasites & Vectors* **7**, 89. doi:10.1186/1756-3305-7-89.

Holme, M. N., Schulz, G., Deyhle, H., Weitkamp, T., Beckmann, F., Lobrinus, J. A., Rikhtegar, F., Kurtcuoglu, V., Zanette, I., Saxer, T. and Müller, B. (2014). Complementary X-ray tomography techniques for histology-validated 3D imaging of soft and hard tissues using plaque-containing blood vessels as examples. *Nature Protocols* **9**, 1401–1415. doi:10.1038/nprot.2014.091.

Jia, T., Melville, S., Rg Utzinger, J., King, C. H. and Zhou, X. (2012). Soil-transmitted helminth reinfection after drug treatment: a systematic review and meta-analysis. *PLoS Neglected Tropical Diseases* **6**, e1621. doi:10.1371/journal.pntd.0001621.

Lee, T. C., Kashyap, R. L. and Chu, C. N. (1994). Building skeleton models via 3-D medial surface axis thinning algorithms. *CVGIP: Graphical Models and Image*

Processing **56**, 462–478. doi:10.1006/cgip.1994.1042.

Lee, C. H., Im, J.-G., Goo, J. M., Lee, H. J., Hong, S.-T., Shen, C. H., Chung, D. H., Son, K. R., Chang, J. M. and Eo, H. (2007). Serial CT Findings of Paragonimus Infested Dogs and the Micro-CT Findings of the Worm Cysts. *Korean Journal of Radiology* **8**, 372. doi:10.3348/kjr.2007.8.5.372.

Loussert, C., Forestier, C. and Humbel, B. M. (2012). Correlative light and electron microscopy in parasite research. In *Correlative Light and Electron Microscopy* (ed. Müller-Reichert, T.) and Verkade, P.), pp. 62–73. Elsevier doi:10.1016/B978-0-12-416026-2.00004-2.

Lowe, T., Garwood, R. J., Simonsen, T. J., Bradley, R. S. and Withers, P. J. (2013). Metamorphosis revealed: time-lapse three-dimensional imaging inside a living chrysalis. *Journal of the Royal Society Interface* **10**, 20130304. doi:10.1098/rsif.2013.0304.

Maire, E. and Withers, P. J. (2014). Quantitative X-ray tomography. *International Materials Reviews* **59**, 1–43. doi:10.1179/1743280413Y.0000000023.

Masi, B., Perles-Barbacaru, T.-A., Laprie, C., Dessein, H., Bernard, M., Dessein, A. and Viola, A. (2015). In vivo MRI assessment of hepatic and splenic disease in a murine model of schistosomiasis. *PLoS Neglected Tropical Diseases* **9**, e0004036. doi:10.1371/journal.pntd.0004036.

Metscher, B. D. (2009a). MicroCT for comparative morphology: simple staining methods allow high-contrast 3D imaging of diverse non-mineralized animal tissues. *BMC Physiology* **9**, 11. doi:10.1186/1472-6793-9-11.

Metscher, B. D. (2009b). MicroCT for developmental biology: A versatile tool for high-contrast 3D imaging at histological resolutions. *Developmental Dynamics* **238**, 632–640. doi:10.1002/dvdy.21857.

Mokso, R., Schwyn, D. A., Walker, S. M., Doube, M., Wicklein, M., Müller, T., Stampanoni, M., Taylor, G. K. and Krapp, H. G. (2015). Four-dimensional in vivo X-ray microscopy with projection-guided gating. *Scientific Reports* **5**, 8727. doi:10.1038/srep08727.

Momose, A., Kawamoto, S., Koyama, I., Hamaishi, Y., Takai, K. and Suzuki, Y. (2003). Demonstration of X-Ray Talbot Interferometry. *Japanese Journal of Applied Physics* **42**, 866–868. doi:10.1143/JJAP.42.L866.

Nierenberger, M., Rémond, Y., Ahzi, S. and Choquet, P. (2015). Assessing the three-dimensional collagen network in soft tissues using contrast agents and high resolution micro-CT: Application to porcine iliac veins. *Comptes Rendus Biologies* **338**, 425–433. doi:10.1016/j.crvi.2015.04.009.

Olivo, A. and Speller, R. (2007). A coded-aperture technique allowing x-ray phase contrast imaging with conventional sources. *Applied Physics Letters* **91**, 074106. doi:10.1063/1.2772193.

Particelli, F., Mecozzi, L., Beraudi, A., Montesi, M., Baruffaldi, F. and Viceconti, M. (2012). A comparison between micro-CT and histology for the evaluation of cortical bone: effect of polymethylmethacrylate embedding on structural parameters. *Journal of Microscopy* **245**, 302–310. doi:10.1111/j.1365-2818.2011.03573.x.

Paulus, M. J., Gleason, S. S., Kennel, S. J., Hunsicker, P. R. and Johnson, D. K. (2000). High resolution X-ray computed tomography: An emerging tool for small animal cancer research. *Neoplasia* **2**, 62–70.

Pauwels, E., Van Loo, D., Cornillie, P., Brabant, L. and Van Hoorebeke, L. (2013). An exploratory study of contrast agents for soft tissue visualization by means of high resolution X-ray computed tomography imaging. *Journal of Microscopy* **250**, 21–31. doi:10.1111/jmi.12013.

Pullan, R. L., Smith, J. L., Jasrasaria, R. and Brooker, S. J. (2014). Global numbers of infection and disease burden of soil transmitted helminth infections in 2010. *Parasites & Vectors* **7**, 37. doi:10.1186/1756-3305-7-37.

Qin, C., Feng, J., Zhu, S., Ma, X., Zhong, J., Wu, P., Jin, Z. and Tian, J. (2014). Recent advances in bioluminescence tomography: methodology and system as well as application. *Laser & Photonics Reviews* **8**, 94–114. doi:10.1002/lpor.201280011.

Ritman, E. L. (2011). Current status of developments and applications of micro-CT. *Annual Review of Biomedical Engineering* **13**, 531–552. doi:10.1146/annurev-bioeng-071910-124717.

Schindelin, J., Arganda-Carreras, I., Frise, E., Kaynig, V., Longair, M., Pietzsch, T., Preibisch, S., Rueden, C., Saalfeld, S., Schmid, B., Tinevez, J.-Y., White, D. J., Hartenstein, V., Eliceiri, K., Tomancak, P. and Cardona, A. (2012). Fiji: an open-source platform for biological-image analysis. *Nature Methods* **9**, 676–682. doi:10.1038/nmeth.2019.

Sena, G., Almeida, A. P., Braz, D., Nogueira, L. P., Colaço, M. V, Soares, J., Cardoso, S. C., Garcia, E. S., Azambuja, P., Gonzalez, M. S., Mohammadi, S., Tromba, G. and Barroso, R. C. (2014). Phase contrast X-ray synchrotron microtomography for virtual dissection of the head of Rhodnius prolixus. *Journal of Physics: Conference Series* **499**, 012018. doi:10.1088/1742-6596/499/1/012018.

Shapiro, E. M., Skrtic, S., Sharer, K., Hill, J. M., Dunbar, C. E. and Koretsky, A. P. (2004). MRI detection of single particles for cellular imaging. *Proceedings of the National Academy of Sciences of the United States of America* **101**, 10901–10906. doi:10.1073/pnas.0403918101.

Sharpe, J., Ahlgren, U., Perry, P., Hill, B., Ross, A., Hecksher-Sørensen, J., Baldock, R. and Davidson, D. (2002). Optical projection tomography as a tool for

3D microscopy and gene expression studies. *Science* **296**, 541–545. doi:10.1126/science.1068206.

Siciliano, G. and Alano, P. (2015). Enlightening the malaria parasite life cycle: bioluminescent Plasmodium in fundamental and applied research. *Frontiers in Microbiology* **6**, 391. doi:10.3389/fmicb.2015.00391.

Speich, B., Ali, S. M., Ame, S. M., Bogoch, I. I., Alles, R., Huwyler, J., Albonico, M., Hattendorf, J., Utzinger, J. and Keiser, J. (2015). Efficacy and safety of albendazole plus ivermectin, albendazole plus mebendazole, albendazole plus oxantel pamoate, and mebendazole alone against Trichuris trichiura and concomitant soil-transmitted helminth infections: a four-arm, randomised controlled trial. *The Lancet Infectious Diseases* **15**, 277–284. doi:10.1016/S1473-3099(14)71050-3.

Stock, S. R. (2008). Recent advances in X-ray microtomography applied to materials. *International Materials Reviews* **53**, 129–181. doi:10.1179/174328008X277803.

Sutherland, I. A. and Leathwick, D. M. (2011). Anthelmintic resistance in nematode parasites of cattle: a global issue? *Trends in Parasitology* **27**, 176–181. doi:10.1016/j.pt.2010.11.008.

Tafforeau, P., Boistel, R., Boller, E., Bravin, A., Brunet, M., Chaimanee, Y., Cloetens, P., Feist, M., Hoszowska, J., Jaeger, J.-J., Kay, R. F., Lazzari, V., Marivaux, L., Nel, A., Nemoz, C., Thibault, X., Vignaud, P. and Zabler, S. (2006). Applications of X-ray synchrotron microtomography for non-destructive 3D studies of paleontological specimens. *Applied Physics A* **83**, 195–202. doi:10.1007/s00339-006-3507-2.

Ter-Pogossian, M. M., Phelps, M. E., Hoffman, E. J. and Mullani, N. a (1975). A positron-emission transaxial tomograph for nuclear imaging (PETT). *Radiology* **114**, 89–98. doi:10.1148/114.1.89.

Vercruysse, J., Albonico, M., Behnke, J. M., Kotze, A. C., Prichard, R. K., McCarthy, J. S., Montresor, A. and Levecke, B. (2011). Is anthelmintic resistance a concern for the control of human soil-transmitted helminths? *International Journal for Parasitology* **1**, 14–27. doi:10.1016/j.ijpddr.2011.09.002.

Vickerton, P., Jarvis, J. and Jeffery, N. (2013). Concentration-dependent specimen shrinkage in iodine-enhanced microCT. *Journal of Anatomy* **223**, 185–193. doi:10.1111/joa.12068.

Voieta, I., Queiroz, L. C. de, Andrade, L. M., Silva, L. C. S., Fontes, V. F., Barbosa Jr, A., Resende, V., Petroianu, A., Andrade, Z., Antunes, C. M. and Lambertucci, J. R. (2010). Imaging techniques and histology in the evaluation of liver fibrosis in hepatosplenic schistosomiasis mansoni in Brazil: a comparative study. *Memórias do Instituto Oswaldo Cruz* **105**, 414–421. doi:10.1590/S0074-02762010000400011.

Winkler, B. (2006). Applications of neutron radiography and neutron tomography. *Reviews in Mineralogy and Geochemistry* **63**, 459–471. doi:10.2138/rmg.2006.63.17.

Withers, P. J. (2007). X-ray nanotomography. *Materials Today* **10**, 26–34. doi:10.1016/S1369-7021(07)70305-X.

Wolstenholme, A. J., Fairweather, I., Prichard, R., von Samson-Himmelstjerna, G. and Sangster, N. C. (2004). Drug resistance in veterinary helminths. *Trends in Parasitology* **20**, 469–476. doi:10.1016/j.pt.2004.07.010.

Wu, J. (2014). Propagation based X-ray phase-contrast imaging technique for the microstructure analysis of biological soft tissues. *Optik - International Journal for Light and Electron Optics* **125**, 1062–1064. doi:10.1016/j.ijleo.2013.07.144.

Zamir, A., Endrizzi, M., Hagen, C. K., Vittoria, F. A., Urbani, L., De Coppi, P. and Olivo, A. (2016). Robust phase retrieval for high resolution edge illumination x-ray

phase-contrast computed tomography in non-ideal environments. *Scientific reports* **6**, 31197. doi:10.1038/srep31197.

Zanette, I., Weitkamp, T., Le Duc, G. and Pfeiffer, F. (2013). X-ray grating-based phase tomography for 3D histology. *RSC Advances* **3**, 19816. doi:10.1039/c3ra41372a.

BOX 1: GLOSSARY

Attenuation coefficient: Characterises how easily a volume of a material may be penetrated by a beam of photons

Coherence: A quality of waves on the electromagnetic spectrum, such that highly coherent X-rays have the same phase difference and frequency

Contrast: The difference in intensity between an image and its direct background relative to overall background intensity

Geometric magnification: Magnification which is produced by varying the ratio of distances between the X-ray source, sample and detector. A smaller distance between the source and sample, and larger distance between the sample and detector, increases the magnifying effect

Spatial resolution: The smallest distance between two structures such as they may be distinguished by the observer to be separate

Tomogram: A reconstructed tomographic image

Transmittance: The ratio of light falling on a body which passes through it

Preface to Appendix 2

I contributed as second author to the following work published in the journal *Ultramicroscopy*: *Experimental steering of electron microscopy studies using prior X-ray Computed tomography*.

The nature of my contribution, and those of the other authors may be seen on the following title page of the article.

Experimental steering of electron microscopy studies using prior X-ray Computed Tomography

Tobias Starborg[a], James D. B. O'Sullivan[b], Claudia Martins Carneiro[c], Julia Behnsen[d], Kathryn J. Else[b], Richard K. Grencis[a]. Philip J. Withers[d]

Corresponding author: Tobias Starborg: Tobias.starborg@manchester.ac.uk.

[a] Wellcome Centre for Cell Matrix Research, The University of Manchester, Oxford Road, Manchester M13 9PL, UK

[b] Faculty of Biology Medicine and Health, The University of Manchester, Oxford Road, Manchester M13 9PL, UK

[c] Immunopathology Laboratory, NUPEB, Federal University of Ouro Preto, Campus Universitário Morro do Cruzeiro, 35400-000, Ouro Preto-MG, Brazil

[d] Henry Royce Institute for Advanced Materials, School of Materials, The University of Manchester, Oxford Road, Manchester M13 9PL, UK

Declarations of interest: none

Author contributions: TS Conceived and designed the methodology, collected data and wrote the paper and developed X-ray steering concept

JDBO Performed analysis, improved protocols and wrote the paper, developed concept.

CMC Contributed samples, collected data

JB Setup x-ray tomography and helped design of multiple scanning regimes.

KE Contributed to analysis of data

RG Funded the research

PJW Funded the research, wrote the paper and developed the X-ray steering concept

All authors have approved the final article

Keywords: ultramicrotomy, multiscale imaging, pre-screening, 3View SBF-SEM, IMOD

Highlights:

- Using microCT pre-scans to accurately steer serial block face SEM.
- High throughput screening and mapping samples to reduce time hunting for features of interest.
- Using microCT to optimise specimen preparation and staining
- Using microCT to guide site-specific TEM sample preparation.

Abstract

Transmission electron microscopy (TEM) and scanning electron microscopy (SEM) can provide unrivalled high-resolution images of specific features and volumes of interest. However, the regions interrogated are typically very small, and sample preparation is both time-consuming and destructive. Here we consider how prior X-ray micro-computed tomography (microCT) presents an opportunity to increase the efficiency of biological electron microscopy. We demonstrate how it can be used to; select the most promising samples and target site–specific locations; provide a wider context of the location being interrogated (multiscale correlative imaging); guide sample preparation and 3D imaging schemes; as well as quantify the effects of destructive sample preparation and staining procedures. We present a workflow utilising open source software in which microCT can be used either broadly, or precisely, to experimentally steer and inform subsequent electron microscopy studies. As automated sample registration procedures are developed to enable correlative microscopy, experimental steering by prior CT could be beneficially routinely incorporated into many experimental workflows.

1 Introduction

Transmission (TEM) and scanning (SEM) electron microscopy techniques provide high-resolution images across a range of natural sciences. Through destructive serial sectioning, stacks of 2D images can be collected and aligned in sequence to build up three dimensional (3D) volume images (Zankel *et al.*, 2014; Peddie and Collinson, 2014). Typically, 3D serial block-face scanning electron microscopic (SBF SEM) methods involving focused ion beam (FIB) milling (Heymann *et al.*, 2006) or mechanical sectioning (Denk and Horstmann, 2004) are used to provide high resolution information on very small regions of material, and the volumes interrogated by ultramicrotomy and FIB serial sectioning are typically around $(1mm)^3$ and $(0.03mm)^3$ respectively (Burnett *et al.*, 2016). Therefore, there is a requirement to be able to select the region of interest (ROI) for study with a high degree of site specificity.

It is possible to use information gleaned from inspecting the surface of the sample prior to serial block-face imaging to provide contextual information about the region selected for detailed investigation, thus increasing the chances that the region selected will contain the features of interest prior to embarking on time consuming slicing and imaging workflows. Despite the fact that the volumes interrogated by ion beam methods have been increased somewhat by the advent of plasma FIB microscopes (Burnett *et al.*, 2016) to around $(0.2mm)^3$, capturing the feature of interest is still challenging when the internal morphology of a sample is not known.

In this paper we examine how non-destructive X-ray micro -computed tomography (microCT) can be incorporated into multiscale correlative microscopy workflows to ensure high efficiency and quality of electron microscopy. MicroCT is well suited to the imaging of samples of many millimetre dimensions at resolutions approaching a micron and some nanoCT instruments can image sub-millimeter samples at 50nm resolution (Maire and Withers, 2014). As a non-destructive method, X-ray CT thus provides an opportunity to establish a map of the

sample prior to more detailed, guided investigation by electron microscopy methods (Sengle *et al.*, 2013; Bushong *et al.*, 2015).

In the current work we examine the experimental issues associated with developing a simple correlative workflow. Our approach utilises the freely available and open-source software package IMOD (Kremer *et al.*, 1996) although other software, such as ImageJ/Fiji (Schindelin *et al.*, 2012) could be used following the same principles. This workflow is then applied to a number of case studies where prior microCT could be a useful preliminary step, namely:

- **For high-throughput screening of multiple samples;** in our case to assess staining and fixation quality in samples of heart and enteric fat tissue prior to the beginning of serial sectioning.
- **To steer 3D serial sectioning workflows:** in our case ensure features (Purkinje Fibres in a rabbit heart) are tracked and captured without inefficient wider sampling or, conversely, partially clipping.
- **To identify samples containing specific rare features:** in our case cell clusters in alginate gels.
- **To locate specific features for detailed site-specific investigation:** in our case the head of a whipworm buried within the gut lining of a mouse.

Other potential advantages include using microCT to first generate a coarser scale overview of the sample in order to put into context the regions of interest (ROIs) from which higher resolution electron microscopy images are acquired (multiscale correlative imaging), to orient the sample to optimise subsequent sectioning/excision, or to quantify levels of shrinkage/damage to the sample during sample preparation (fixing, staining or slicing) (Albers *et al.*, 2018b).

Finally we consider future refinements, such as automated sample registration procedures, that would enable correlative imaging or experimental steering by prior CT to be routinely incorporated into experimental workflows.

2 Methods

2.1 Experimental workflow

While every experimental workflow is different, the main steps for microCT steering of serial block-face SEM (SBF-SEM) imaging or site specific TEM are broadly the same as illustrated in Figure 1. Each step is considered in turn below.

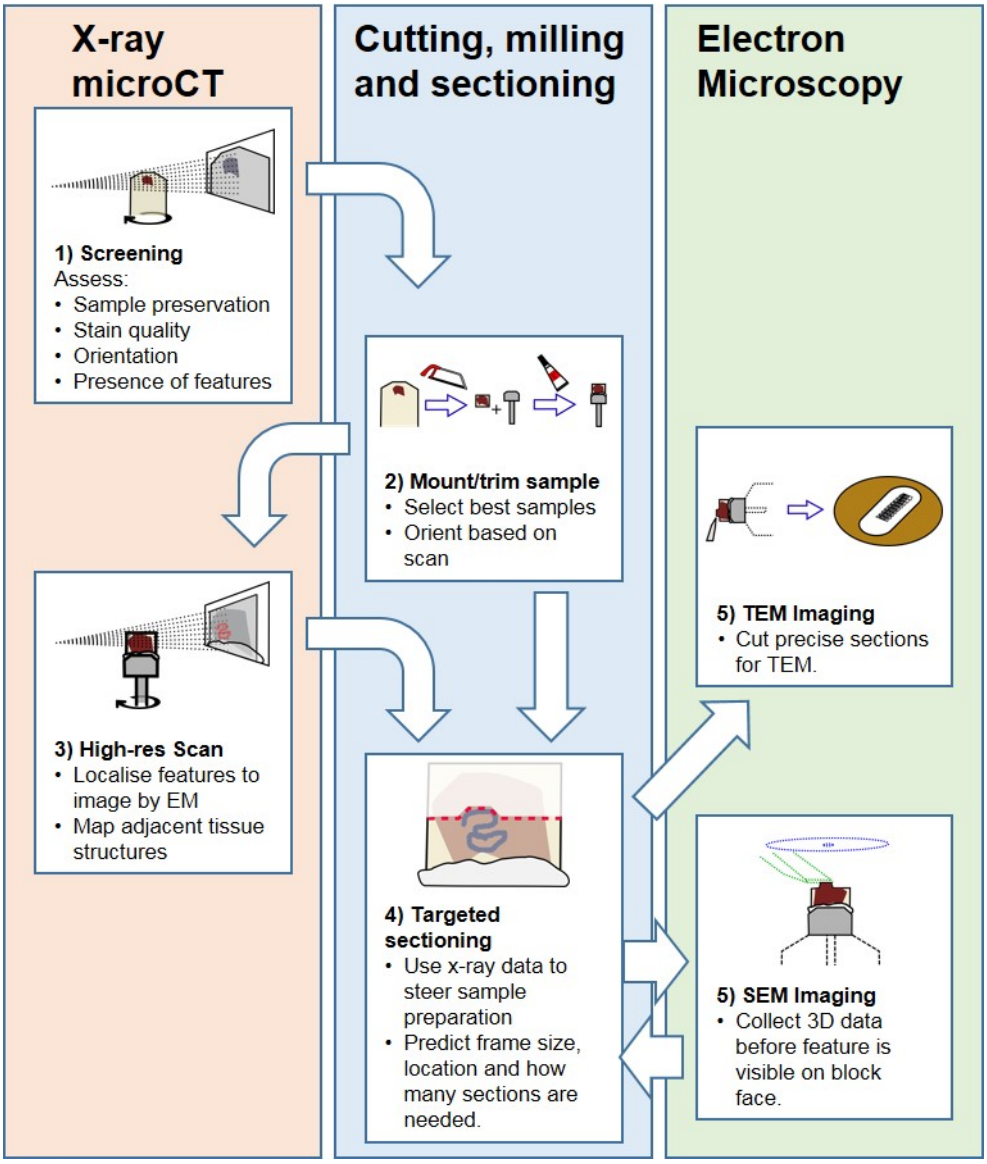

Figure 1. Flow chart for preparing a sample for EM imaging guided by microCT.

2.1.1 MicroCT screening

After samples have been stained and embedded (see section 2.2.2) they are pre-screened by laboratory CT. This reduces the risk of expending a great deal of time, or expense, trimming and imaging samples which lack relevant biological features. By quickly scanning a range of batch-prepared biopsies, it is possible to pick the best samples for further processing, thereby eliminating unfruitful future imaging acquisitions. This is especially relevant for studies aiming to view rare features, which may be distributed heterogeneously throughout biopsies (for examples see sections 3.3 and 3.4). Additionally, once a sample of interest has been selected, an overview of the internal morphology also prevents accidental trimming of important regions. While assessing the screening data it is also possible to examine quality and evenness of sample preparation (see section 3.1) as well the orientation of the feature of interest from the viewpoint of establishing the best sectioning plane. For screening scans, a high-throughput may be more important than maximising resolution, and acquisition settings can be adjusted to collect the data as quickly as possible, for instance by reducing the number of projections,

binning pixels on the detector, as well as using short exposure times. Imaging a number of samples in a single field of view or using a carousel to load scan samples in a sequence are both ways of further increasing throughput of scans.

2.1.2 Mount/trim sample

In the light of the information gathered from the CT scan, one can down-select the most promising samples. For each of these it is possible to orient the sample to optimise subsequent sectioning/excision as well as to aggressively trim the sample to minimise milling/sectioning times. Often this is done fairly coarsely by hand using a razor blade. If it is not the case already, the sample can then be attached to a pin or some other sample stub. This can then be transported directly to the SEM for block-face imaging or sectioned for TEM examination. In cases where reorientation has occurred, and/or a more precise location of a region of interest is required relative to the sample stub before trimming can occur, further CT scanning may be necessary.

2.1.3 High-resolution CT scan

With the sample mounted onto a pin it is now possible to scan at higher resolution in order to more precisely register the location of the features of interest and thereby steer the sample preparation. It is expedient to accommodate the sample within the CT system using the pin/stub which means that the subsequent (horizontal) tomographic slices are oriented normal to the pin. This is especially advantageous for serial block-face SEM because this is parallel to the sectioning plane of the diamond knife. The high-resolution tomographic images can be used as a map that will reveal what lies beneath the surface when the thin sections are removed.

2.1.4 Site specific milling

In order to target a specific region within the sample an ultramicrotome is used to mill a face perpendicular to the pin axis. By controlling the depth of milling and comparing BSEM images of the block-face to the virtual slices in the CT pre-scan/high-res scan it is possible to identify the desired imaging plane. For high-resolution EM imaging the block-face must be accurately trimmed to a size that is compatible with ultra-thin sectioning (<70nm slices). To trim the block-face with sufficient accuracy, the SEM beam may be used to burn fiducial markers onto the surface of the block; the markers can be positioned at points where the ROI box crosses features that are easily identified in the SEM image (see supplementary information). Once markers have been applied, the sample can be further hand-trimmed under a dissecting light microscope. Using this method it is possible to accurately trim a sample face to within 50-100μm of the sample X and Y, and to accurately trim the Z depth to within a micron.

2.1.5 Electron microscope imaging

Once the desired block-face has been exposed and trimmed, electron microscopic imaging can begin. It should be noted that the optimal position of the block-face may vary depending on the modality used; for instance, for TEM imaging the diamond trimming knife should be used to get within a single X-ray slice (approx. 1-2 μm, depending on imaging resolution) of the ROI. Alternatively, for volume imaging using serial block-face, or dual beam SEM machines it is

possible to use the X-ray data volume to target imaging a few micrometres before the feature of interest is revealed so that it is captured in its entirety by the serial sectioning process. The X-ray data can be used to determine how deep the SBF-SEM volume should be, as well as the precise location and size of the imaging frame so that it includes all of the tissue of interest. By restricting the imaging to the exact sizes needed it is possible to accurately control the duration of the scan. Establishing an exactly-sized imaging frame of the region of interest for a high-resolution acquisition also improves throughput, because the scan does not need to be extended over a wide search area in the hope of capturing a feature of interest.

2.2 Experimental procedures

Each of the case studies below highlights a particular opportunity for experimental steering by microCT through the examination of a real world sample. The samples are all biological in nature and have been prepared with the same staining and embedding protocol. There are a number of methods that are common to all of the samples which are as follows:

2.2.1 Experimental Animals:

All procedures involving animals were carried out in accordance with the Animals for Scientific Procedures Act, under the authorities of home office licenses. For the adipose work (section 3.1), murine gut adipose was collected and pieces (<1mm^3) were placed directly into primary fixative. For the heart tissue (section 3.2), a rabbit was euthanized and the heart was quickly removed. The specific regions around the pacemaker cells were carefully dissected and the small pieces (<1mm^3) were placed directly into vials of primary fixative. For the cell culture work (section 3.3), primary murine mammary epithelial cells were cultured in an alginate based hydrogel (Wood *et al.*, 2018). The cells were fixed by replacing the tissue culture media with primary fixative. For the work on *Trichuris muris* (section 3.4), SCID mice were infected by oral gavage with 200 *T. muris* eggs, and euthanised 42 days after infection. Regions of the caecum thought to contain worms were cut into 1 mm^3 and placed into primary fixative.

2.2.2 Staining, Fixing, and Embedding:

All samples were prepared according to a standard SBF-SEM protocol (Deerinck *et al.*, 2010). Sample fragments were fixed in 2.5% Glutaraldehyde, 4% PFA in 0.1M HEPES pH 7.2 before being stained in 1% Osmium tetroxide, 1.5% potassium ferrocyanide in 0.1M HEPES, followed by 1% aqueous filtered Thiocarbohydrazide. After washing, the fragments were incubated in 1% aqueous OsO_4, 1% aqueous Uranyl acetate, and finally in Walton's lead aspartate (Walton, 1979). Samples were dehydrated in graded ethanol and infiltrated with TAAB 812 Hard resin, which was cured in an oven at 60^{o}C for between 24 and 48 hours.

2.2.3 MicroCT imaging:

For the purpose of this study all CT imaging was carried out on a Zeiss Versa 520 X-ray microscope using a 4x objective lens. Due to the high stain content the images gave good contrast at 60kV accelerating voltage with maximum power (5W). A variety of imaging regimes was used depending on the resolution of information required. The scan parameters are detailed in table 1.

Sample	Scan type	Image size (X/Y) in pixels	number of frames	pixel size (µm)	frame time (s)	Total scan time (hour:min)
Acini	Screening (1 sample)	1012 (bin2)	72	2.152	8	00:14
Heart	Screening (1 sample)	1012(bin2)	401	2.966	2.5	00:21
Adipose	Screening (12 samples)	1024 (bin2)	201	15.11	2	00:21
	High-res.(2 samples)	2028	1601	2.264	8	03:37
Trichuris in gut	Screening (1 sample)	1012 (bin2)	72	1.773	10	00:16
	High-res. (1 sample)	2028	1601	1.827	20	08:59

Table1: X-ray scan parameters used to collect the data sets presented in this paper.

CT scans were reconstructed using filtered back-projection. The data were analysed and rendered using Amira 6.4 (Thermo Fischer Scientific). For targeting of EM imaging the MRC file format (Crowther *et al.*, 1996; Cheng *et al.*, 2015) was used. The contrast was inverted in IMOD (Kremer *et al.*, 1996) in order to directly compare the 2D slice images with images collected by EM.

2.2.4 Trimming the sample for serial sectioning:

In each case coarse manual trimming was first applied to reduce the size of the sample. In order to ensure the sample was cut to the minimum size such that the regions of interest were retained, the X-ray data had to be compared with an image of the sample block face. The X-ray data comprises a series of virtual slices through the volume being imaged. The data can be converted into various formats which can be opened using a number of programs. We used IMOD to view the x-ray slices (Kremer *et al.*, 1996) (http://bio3d.colorado.edu) (Fig 7), but other software packages such as Fiji may also be used (Schindelin *et al.*, 2012). A box was then defined to enclose each of the underlying regions of interest in the X-ray data. The individual boxes were then copied onto the X-ray section that mapped to the block-face as seen in the SEM. By comparing the position of the underlying ROIs with the SEM block-face image it is possible to work out how much of the sample could be safely trimmed. The depth of the ROI nearest to the block-face plane is used to decide how much resin can be removed with the trimming knife. The sample was then trimmed using a diamond trimming knife on a standard ultra-microtome (Reichert-Jung Ultracut) counting 500nm thick cuts. Periodically the size of the sample face needed to be reduced in order to reduce strain on the knife. In order to accurately trim the sample a number of fiducial markers were introduced onto the resin surface to guide manual trimming. To do this the sample was placed on the stage of the SEM and fiducial spots introduced by turning the beam to 30kV and magnification 50K and then parking the beam to introduce beam damage onto the resin surface for approximately 20s (this is explained in more detail in the Supplementary information).

2.2.5 Collection of the serial block-face SEM data:

The EM data was collected on a 3View ultra-microtome (Gatan, UK) fitted to an FEI Quanta 250 FEG (Thermo Fischer Scientific). The imaging regimes were tailored to the sample being imaged as summarised in table 2.

Sample	Accelerating voltage (kV)	Chamber pressure (Torr)	Image frame (pixels)	Pixel size (nm)	Dwell time (ms)	Slice thickness (nm)
Acini	3.5	0.28	4000x4000	15	5	60
Heart, Purkinje fibre	3.8	0.45	1) 5000x5000 2) 8192x5000 3) 6750x5000	30	3.5	150
Trichuris, worm head	3.8	0.47	6000x7000	13.47	3.3	60

Table 2: Serial Blockface SEM parameters used to collect the data sets presented in this paper.

3 Results and Discussion

3.1 High-throughput screening; assessing/optimising the quality of sample preparation

In order to collect good quality 3View images it is important that samples are uniformly fixed, so that ultrastructural features are preserved through subsequent processing. In addition, the *en bloc* staining species employed (e.g. Osmium tetroxide, Uranyl acetate) must penetrate the sample sufficiently such that features of interest have enough contrast in the back-scattered electron micrographs. Conventionally, semi-thin sectioning and light microscopic imaging may be employed to determine staining efficacy. Here we instead propose the use of X-ray tomography. Although the use of X-ray imaging will never be able to assess the quality of resin infiltration, nor the formation of fine precipitates, it may be advantageous to use over a sectioning approach, as it avoids cutting away potentially important parts of the sample, and has the potential to achieve a higher throughput by screening many samples at the same time in batches using a quick scan.

Here we consider two case studies in which pre-screening SBF-SEM samples by microCT is used to non-destructively assess the quality of sample preparation, namely samples of murine cardiac muscle and fat from the gut. In the former case insufficient stain penetration is diagnosed by a clear front of increased contrast towards the outer edges of the sample (Fig 2 Ai, ii). The top sample (Ai) shows good stain penetration seen as the uniform absorption across the sample, while the sample on the bottom (Aii) shows poor stain penetration with more X-ray absorption around the periphery. In the second example, many samples are grouped together and imaged in a single run (Fig 2B). In this way the status of multiple samples could be checked at the same time increasing the efficiency (the total time to screen 12 samples was 7 minutes).

This high throughput screening process shows the failure of the fixative (Osmium tetroxide, OsO_4) to sufficiently penetrate the sample leading to partial fixation of the lipids. This has resulted in the extraction of fat cells from the centre of the sample during dehydration in acetone, leaving behind empty portions of extracellular matrix (Fig 2C). This evidence of insufficient penetration of reagents into the tissue facilitates the improvement of the preparation method prior to costly SBF-SEM, either by using longer staining times to increase penetration (Aslanidi *et al.*, 2013; Mikula and Denk, 2015), or by reducing the size of the tissue samples to attain more uniform staining. Alternatively, in some circumstances the outer regions into which stain has penetrated well could serve as a ROI for further electron microscopic examination.

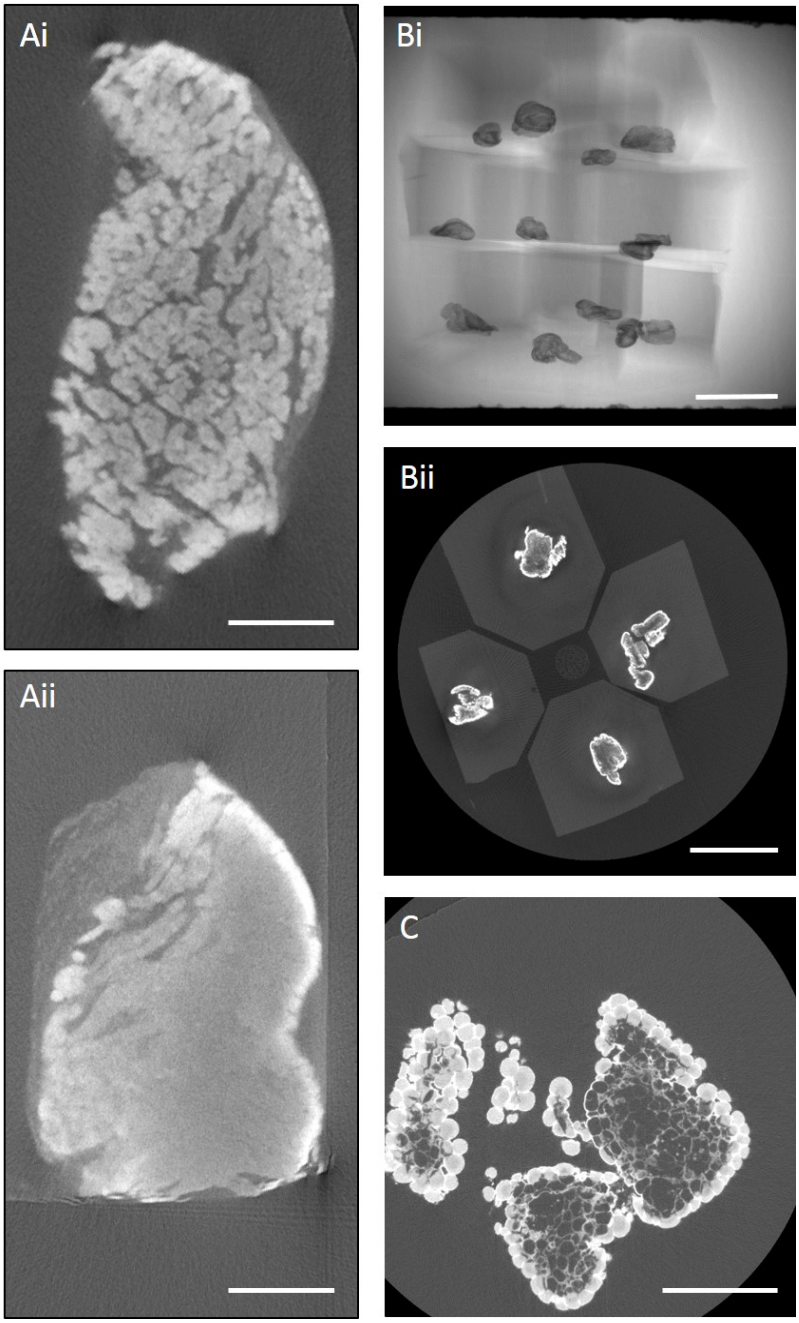

Figure 2 Quick assessment of stain penetration can be supplemented by high throughput screening of samples. Using microCT, stain quality and fixative penetration can be assessed before beginning the time-consuming trimming and sectioning. **A**) microCT virtual slices of two murine heart samples stained for SBF-SEM can be compared. The top sample (**Ai**) shows good stain penetration seen as the uniform absorption across the sample with detail seen in the separation of the individual fibers, while the sample on the bottom (**Aii**) shows poor stain penetration with more X-ray absorption around the periphery and no detail in the centre. Scale bar 25µm. **B**) Radiograph (**Bi**) and virtual slice (**Bii**) of a high-throughput scan of 12 resin-embedded samples of fat. Scale bars 3mm **C**) In a high-resolution scan of a single piece of fat, a clear front of fixative penetration is perceptible. The lipids in the interior of the sample have been extracted by dehydration in acetone leaving only the matrix and cell cytoplasm. Scale bar 500 µm.

3.2 Planning serial block-face imaging campaigns to efficiently track features: Purkinje Fibres in a rabbit heart

In many cases there are morphological, resolution and cost efficiency arguments for orienting the region of interest and carefully planning the extent of sectioned volume before carrying out sectioning. For example, by scoping the region of interest and orienting the sample it is possible to track features in the most time efficient manner while ensuring the region of interest doesn't leave the field of view as sectioning progresses. Secondly, serial sectioning results in anisotropic resolution of the final volume data, because the sectioning thickness (which determines the axial resolution) is, in most cases, significantly larger than the pixel size (which determines the lateral resolution) within each BSEM image (Peddie and Collinson, 2014). Because of this inherent anisotropic resolution, the orientation of samples should be chosen such that features of greatest interest are intersected optimally by the plane of imaging and can be viewed at the superior lateral resolution.

In our case the aim was to examine the cellular morphology of the pacemaker tissue and in particular examining the ultrastructure of the sinoatrial node (SAN) cells and Purkinje fibres (PFs) of the rabbit conduction system. In this case X-ray steering enables the volume to be sectioned to be optimised, without danger of accidentally cropping part of the ROI. From this viewpoint it is desirable for the sample to be oriented such that the fibre runs in the z-orientation so that the 3View field of view can be minimised using a square frame. The X-ray data in Fig 3 shows that at a depth of around 290μm the fibre turns to run near parallel to the image frame. With this prior information we were able to change the 3view sectioning scheme from a square image frame (Fig 3B) to a larger one at the appropriate point to include the whole fibre (Fig 3C). Once we have had passed this point we were able to continue imaging with the standard rectangle frame (Fig 3D). Given that the image acquisition time is based on the total number of pixels per frame we were able to optimise the acquisition sequence and thus acquisition time beforehand without any risk of losing the features of interest from the frame.

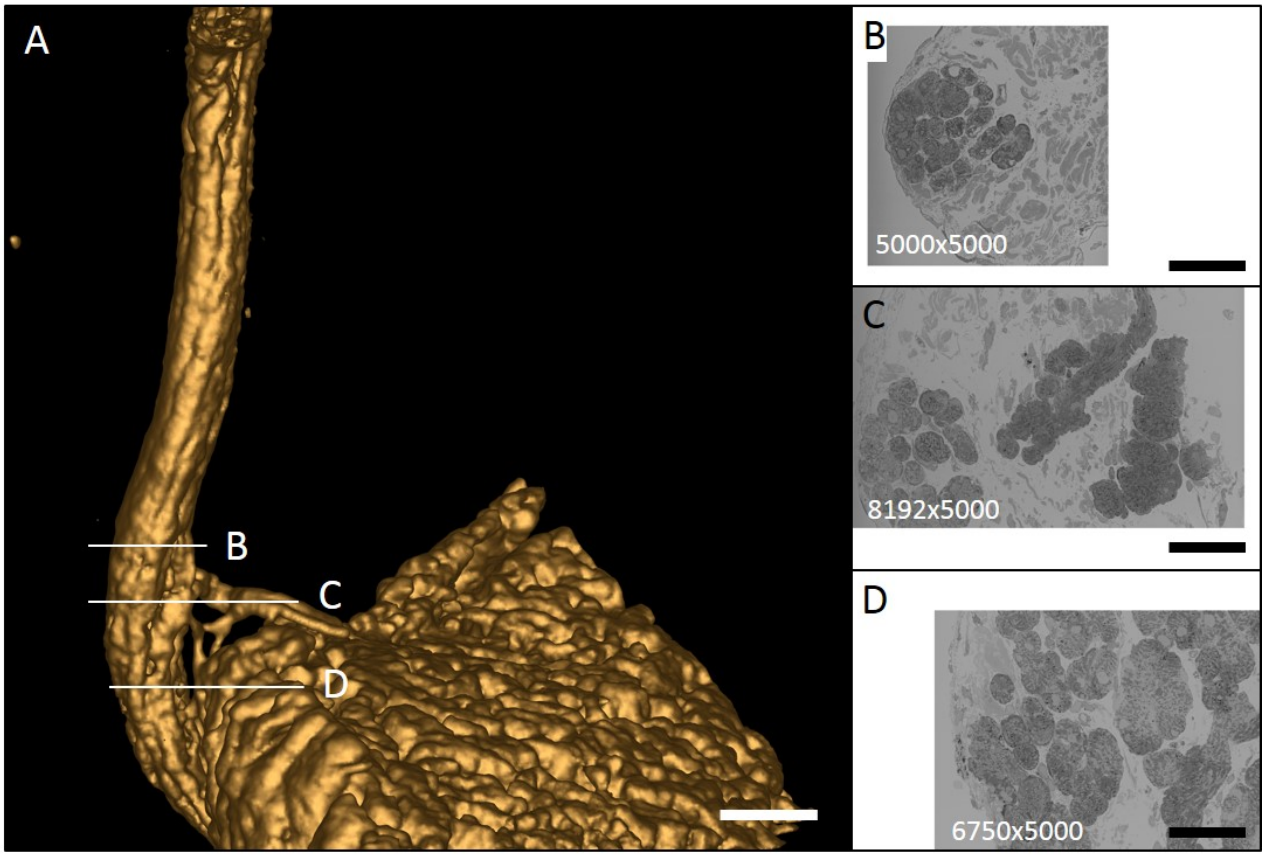

Figure 3. Adjusting SBF-SEM imaging to optimise the acquisition time while retaining the features of interest in the volume. A) Surface rendering of an X-ray tomogram (acquired on a Zeiss Versa 520 tomograph) showing the trajectory of the Purkinje Fibre tracking down to cardiac tissue. Using the microCT data it was possible to orient and define the sectioning scheme so as to image the region where a fibre splits from the main bundle to connect to the cardiac wall. **B-D**) example SEM images collected at different points along the branch as part of an SBF-SEM volume. Scale bars represent 50µm.

3.3 Locating hidden or rare features: cell clusters in alginate gels

Blind SBF-SEM is a very unsatisfactory and inefficient way of locating and imaging rare features. In such cases pre-screening by microCT has clear benefits. Here we consider a 3D cell alginate based cell culture model to examine the role of the extra-cellular matrix environment in the control of cell proliferation and programmed cell death in a model of mammalian milk production (Walker *et al.*, 2014; Wood *et al.*, 2018). In such a sample, a range of fluorescent microscope techniques might be used in order to understand the proteins that are being produced and their localisation. However fluorescent microscopy necessitates the use of specific stains and means that the precise environment cannot be examined. By utilising a non-specific stain and high-resolution of electron microscopy, the cell-matrix interactions across the surface of the acini as well as the polarisation of the cells between the external matrix and the milk filled lumen, can be examined. However, the acini are randomly and sparsely spread throughout the matrix. Pre-scanning by microCT obviates the need to randomly sample large

areas at low magnification in the hope of imaging the acini, or to target cells that are partially exposed on the surface of the block, knowing that we could only collect the portion of the cluster that is left beneath the surface.

A large microCT volume (7.3 mm^3) was acquired prior to destructive SBF-SEM to locate whole acinus (Fig 4A). This screening was undertaken quickly acquiring just 72 radiographs (projections). While this leads to streak artefacts and noise in the X-ray image the resolution and contrast is sufficient to obtain the locations of the acini. With the location identified from the microCT, the ROI was excised and SBF-SEM undertaken confident in the knowledge that the smaller volume was known to contain the whole acinus (Fig 4B).

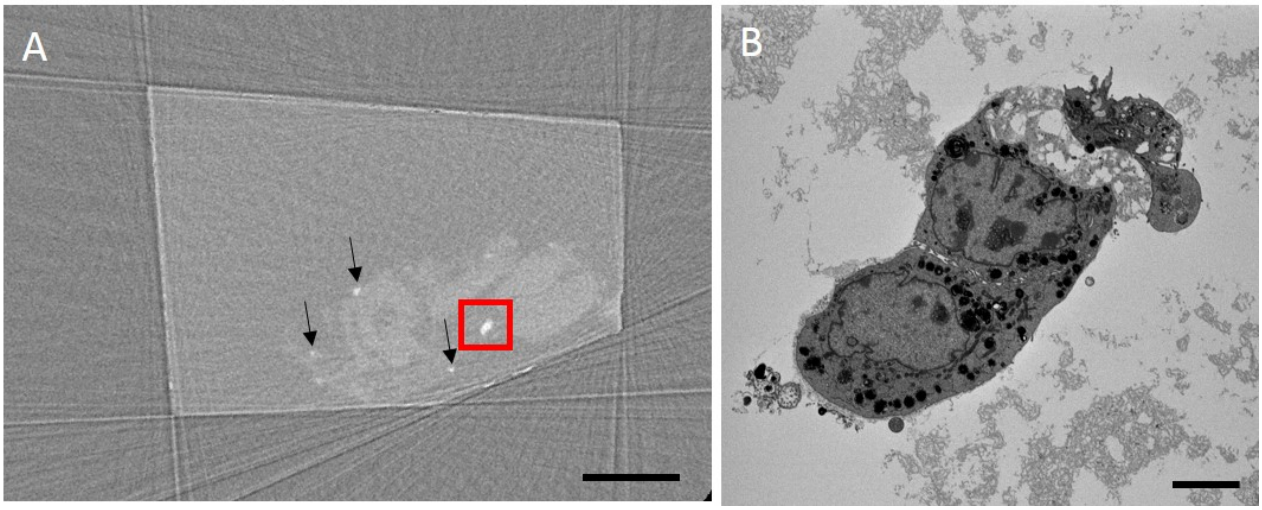

Figure 4. Rare features can be imaged in their entirety. **A**) Using fast (72 projection) X-ray tomogram pre-scanning it is possible to locate rare cell clusters grown in an alginate matrix. The short time and limited projections obtained are evident by the streak artefacts present on the virtual slice. However, resolution and contrast is sufficient to correctly obtain the locations of the cell clusters (arrows and within red box). **B**) Example back-scattered SEM image from the same region boxed in red in **A**.

3.4 Site specific imaging: Locating the head of Trichuris muris within a mouse gut lining

T. muris is a commonly used model of the human endoparasite *Trichuris trichiura* (whipworm), which is responsible for Trichuriasis, one of the most common neglected tropical diseases in the world (Pullan *et al.*, 2014). The *Trichuris* genus is characterised by their unique niche; they live partly embedded within the epithelium of the caecum and proximal colon, in a “tunnel” made by burrowing through adjacent epithelial cells (Lee and Wright, 1978; Tilney *et al.*, 2005). Capturing the anterior, embedded part (‘head’) of the worm *in situ* is important for EM studies attempting to characterise the formation, maintenance and development of the epithelial tunnel. This is because there are many highly specialised, yet poorly understood surface structures such as the bacillary pores which characterise this region and are most likely important in facilitating the worm’s intra-epithelial lifestyle (Hansen *et al.*, 2016). A better understanding of the host-parasite interaction underpins future control strategies targeting this parasite. *In situ* imaging of anterior structures on *Trichuris* within the epithelial tunnel is challenging because 1) in gut biopsies the

orientation of the embedded worm is impossible to determine from external inspection and 2) the bacillary pores, whilst of a consistent appearance on the surface of the worm, are functionally heterogeneous and consist of a variety of cell types distributed beneath the surface (Wright and Chan, 1973; Tilney *et al.*, 2005). The combination of these factors means that the region of worm embedded for sectioning and its orientation are often determined blindly. Perhaps as a result of this, the functions of many *Trichuris* surface structures remain the subject of speculation (e.g. (Hüttemann *et al.*, 2007)).

Here the aim was to target the anterior-most region of the worm and hence identify the pathologically relevant elements of worm and host morphology. Consequently, pre-screening microCT was used firstly to identify a sample worthy of investigation (i.e. one containing a worm) and secondly to steer the SBF-SEM in order to target the embedded anterior most region. Within the opaque resin embedded gut sample (Fig 5A), a length of worm was revealed through inspection of the slices (Fig 5B). Moreover, the presence of the anterior region was confirmed, the tip of which was noted as the desired location for the block-face imaging (Fig 5C).

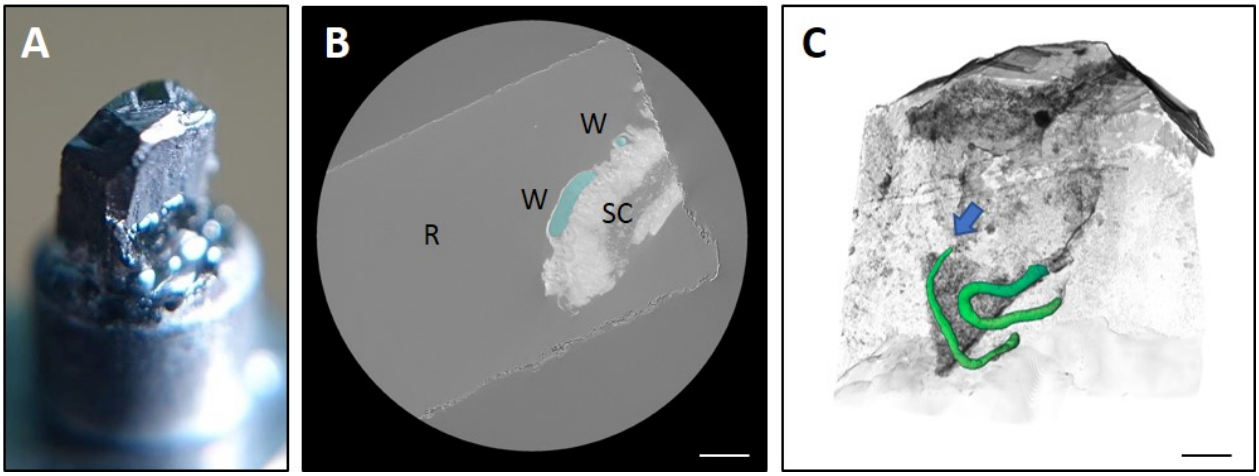

Figure 5. Examining X-ray data reveals hidden sub-surface features. **A**) Photo-micrograph of a mounted 3-view sample coated in gold palladium. **B**) Virtual slice through X-ray volume showing the presence of a *Trichuris* parasite (W) embedded in the stained cecum tissue (SC). The shape of the resin block (R) can be seen as a white outline caused by X-ray absorption from the gold palladium coating. **C**) Volume rendering of *T. muris* (green), showing its positioning within the fragment of gut tissue. The anterior region of the worm, which is the region of interest, is marked by a blue arrow. Scale bars 500 μm.

The microCT reveals that the head lay approximately 980μm from the top of the sample (Fig 6). As well as facilitating the optimal positioning of the block-face before beginning a 3View run, X-ray data can be used to determine the position of features of interest at the end of the data acquisition. In practice small differences in the calibration and alignment between the X-ray and SEM systems mean that there was a slight dis-registry between the two coordinate frames, however the similar appearance of gross morphological features between the two data sets confirms that the SBF-SEM imaging frame was appropriately located (Fig 7). By using IMOD, it

was possible to centre the SEM image acquisition and use CT steering to manage the whole sectioning and image acquisition process.

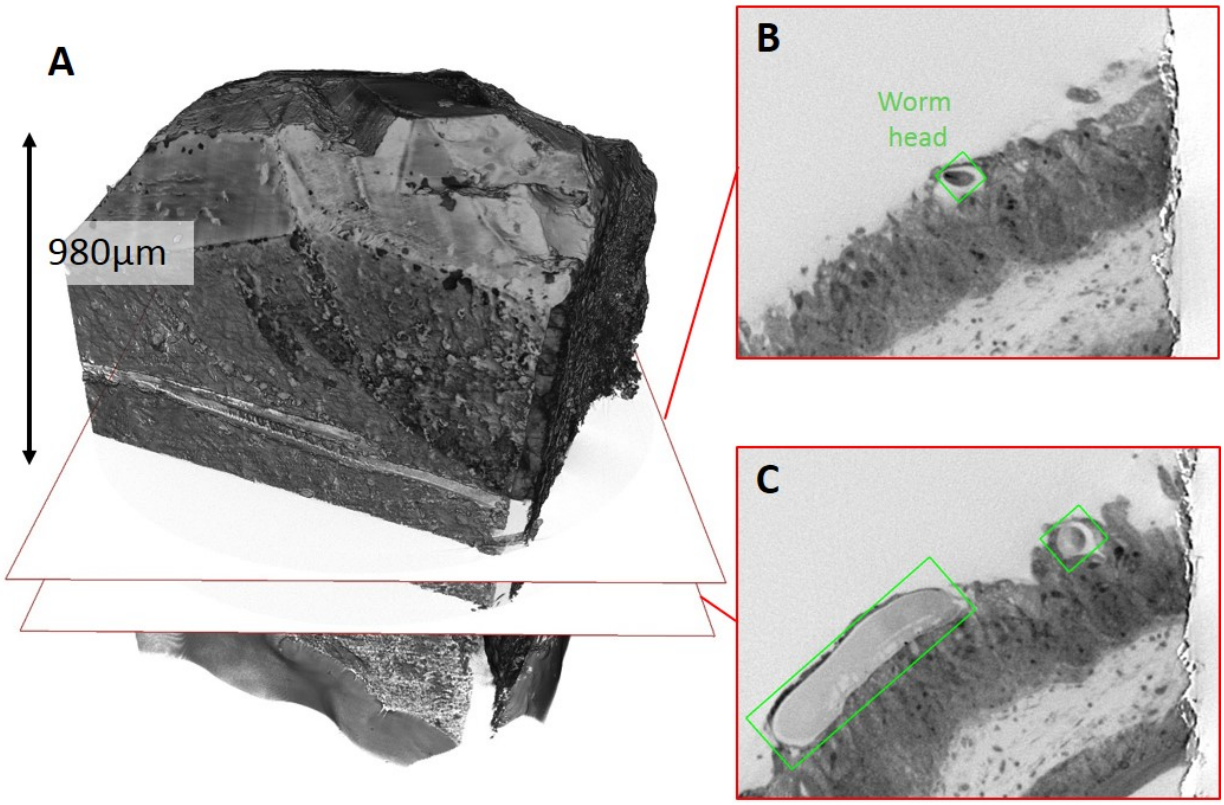

Figure 6. **Identifying regions of interest within the X-ray data set to target subsequent trimming. A**) A magnified volume render of the resin sample generated from the X-ray data. **B**) Virtual XY section showing the worm head buried within the cecum tissue. Analysis of the X-ray tomogram shows that this feature is found 980µm below the current block-face. **C**) A virtual XY CT slice showing the same worm head 180µm deeper into the sample. At this point it is also possible to see part of the body of the whipworm (within the green rectangle, modelled in 3dmod).

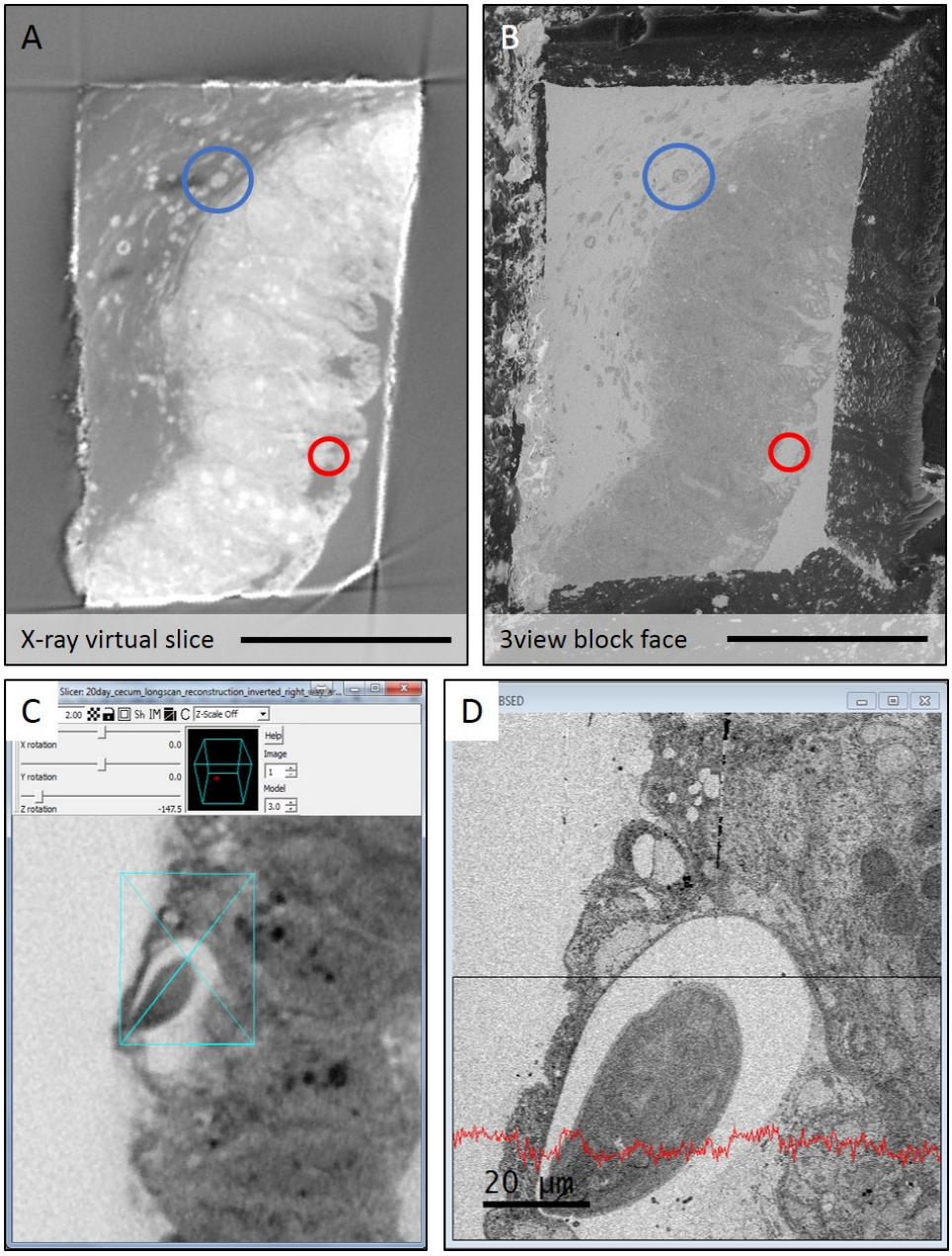

Figure 7. **Side-by-side comparison of a virtual slice from the microCT**. **A**) Virtual slice from the microCT and back scattered SEM image **B**) collected from the block surface revealed by the 3View. Gross morphology such as small capillaries (blue, circled) aid in registering the two datasets. Small differences in registration between the images due to slight miss-registration (circled red). **C**) Virtual section from the microCT of the worm head visualised in IMOD using 'Slicer'. **D**) SBF-SEM image of the same region collected live in Digital Micrograph. Videos of the corresponding stacks of the virtual (CT) and real slices (SEM) side by side are included in the supplementary material.

As a result of X-ray steered SBF-SEM imaging, key aspects of the whipworm morphology have been identified (Fig 8). In the microCT slices, mucosal morphology is evident, including the layers composing the gut wall (muscularis, submucosa, mucosa), as well as features such as the crypts of Lieberkuhn (Fig 8B). The structure of the mucosa itself is important as it contains

goblet cells which secrete mucus and are important in the control of *T. muris* infection (Hasnain *et al.*, 2011). Subsequent higher resolution SBF-SEM images (Fig 8C+D) revealed finer structural elements of the worm itself, including the oesophagus, cuticle, stylet, and bacillary cells. The syncytium which surrounds the worm as it burrows through the host gut lining is also clearly visible, although empty resin between the syncytium and worm suggests that sample shrinkage has occurred.

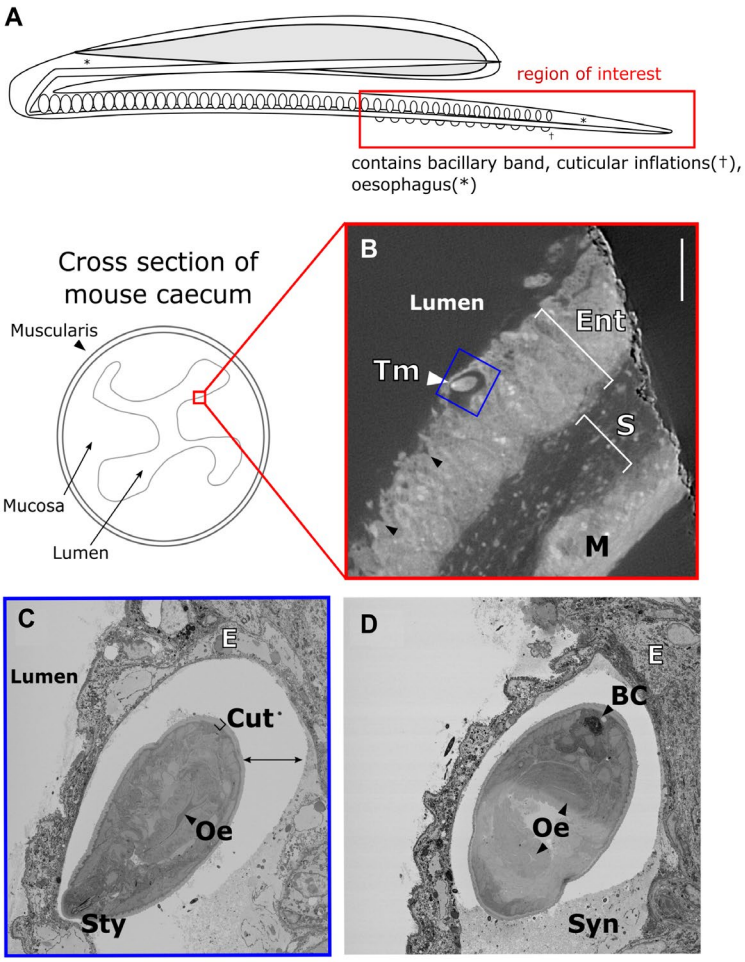

Figure 8: The correlative workflow allows location and identification of key elements of *Trichuris muris* morphology. **A**) Schematic of *T. muris* showing the area of worm relevant to the current study. **B**) X-ray virtual slice of stained, resin-embedded tissue showing the tip of the *T. muris* head (Tm), the enterocytes consisting the mucosa (Ent), sub-mucosa (S) and muscularis (M). Scale bar 100 µm. **C+D**) Backscatter electron micrographs of the block-face showing the morphology of the tip of the worm head (**C**) and the body at a point 300 microns further into the block (**D**) in more detail, including the Stylet (Sty), oesophagus (Oe) and cuticle (Cut, square bracket), as well as the bacillary cell (BC) and syncytium which surrounds the worm (Syn). The worm is surrounded by epithelial cells (E). There is also a gap between the worm and the surrounding syncytium marked by the double-headed arrow, which is likely a shrinkage artefact.

4 Comments on the workflow

A wide range of correlative imaging approaches which draw together diverse imaging and mapping modalities to establish a richer picture of materials are gaining traction (Burnett *et al.*, 2014). Within many of these, X-ray micro-computed tomography features as a first step, to provide temporal (time-lapse) information, to combine different types of data collected using

different modalities, or as a part of multiscale studies. Here, we have looked at the use of micro CT a first step in biological studies, with a particular focus on its use for experimental steering. We have presented a complete workflow which is achievable using open source software, and have provided a number of case studies that illustrate the potential benefits but also some of the experimental issues that must be tackled. During the course of these experiments several areas of improvement and refinement were identified, achievable both in the immediate future and longer timescales, which are discussed in the following paragraphs.

4.1 Extension of the workflow to other EM techniques

Whilst we have described how X-ray screening of samples can be utilised to increase efficacy of SBF-SEM, other EM modalities would also benefit from similar pre-screening and experimental steering. For instance, CT pre-screening allows site-specific excision of TEM slices so as to capture specific features within the sample. Further 50nm serial TEM sectioning campaigns can be planned to collect higher-resolution 3D data than is possible by SBF-SEM. An alternative, higher throughput approach would be to collect a series of thick (300nm) sections to cover the region of interest. Here serial section electron tomography can be used to generate a low magnification volume covering the ROI (Kalson *et al.*, 2013). The sections can then be interrogated at higher magnification once the ROI has been accurately identified.

4.2 Automated registration of datasets

For a variety of reasons, the accurate and automated registration of images between imaging modalities is of increasing interest to researchers utilising correlative approaches. For instance in Correlative Light and Electron Microscopy (CLEM), the registration of fluorescence data is important for matching the detailed ultrastructural information of EM with patterns of gene expression and/or protein localisation (Acosta *et al.*, 2016). In the workflow we describe above, registration of BSEM images with equivalent microCT slices has been carried out manually. However, there are a variety of ways in which future application of automated imaging registration of EM and X-ray data could increase the efficiency of data collection and visualisation. For instance registration of the datasets may not only be useful in validating the correct interpretation of features in both datasets, but also in quantifying any artefacts introduced into the morphology due to the action of the microtome (Albers *et al.*, 2018b).

From a data interpretation point of view, superimposing volume renderings and slices of both SBF-SEM and microCT data aids in putting ultrastructure within the context of the surrounding 3D tissue morphology, thus providing greater clarity to readers interested in the exact position of the imaging window. Automatic registration of CT and BSEM images before the commencement of data collection, that is, during the trimming stage may also assist in speeding up critical elements of the workflow. For instance, when trimming the block-face to achieve the desired starting point, automated registration of the block-face with slices of the CT data could facilitate quick quantification of changes in orientation introduced by the investigator.

4.3 Automation of block-face preparation

Whilst we have discussed how automated image registration may allow the streamlining of the existing workflow as presented above, perhaps the greatest savings of time and effort may be gained from the automation of the block trimming itself. For instance, in correlative microCT and FIB-SEM, X-ray data can be used to guide subsequent automated ion beam milling and acquisition of EM volumes (Daly *et al.*, 2017). In the workflow presented in this paper, the X-ray data has been used to inform manual trimming of the sample resin using razor blades and microtomy. However, coarse trimming by eye takes time and effort, and whilst precise trimming by microtomy is necessary to achieve the correct depth of the imaging frame, other trimming approaches may increase the ease of the trimming process. One easy way to increase accuracy and efficiency of block-face trimming may be to include fiducial markers on the SEM stub/pin prior to microCT scanning, in order that the block-face may be trimmed with quick reference to clear landmarks (Bushong *et al.*, 2015). However using X-ray data as a guide for automated trimming is the ultimate goal for high-throughput and accuracy of block-face localisation. As mentioned, automated FIB milling is one approach to achieving this goal, however, this may be too slow a process for resin blocks larger than a few millimetres; instead laser cutting, or even high-precision Computer Numerical Control (CNC) machining may be best suited to high-throughput applications, or applications where the resin blocks are above several mm^3 in volume. Ultimately, it seems likely that continuing development of correlative imaging will exploit automated sample excision and preparation.

4.4 Logistical considerations associated with the workflow

In addition to the experimental aspects, which we have demonstrated and discussed in detail, those wishing to employ the correlative approach outlined above should be aware of logistical issues associated with accessing and exploiting microCT instruments. The costs of using instrumentation are an important consideration, and as with any modality, experiments must be planned around availability of the instruments themselves. In our experience, survey scans can take of the order of minutes and the data can be retrieved and utilised to its full extent almost immediately following a scan, as virtually no post-processing of the virtual slices is required. Once the data are retrieved, the availability of computational power may affect the speed of data visualisation and manipulation; however, facilities which already have 3D imaging instruments (e.g. an SEM with 3View) should already be sufficiently well equipped in this area.

5 Conclusions

Through a series of diverse case studies we have shown that experimental steering by microCT can significantly reduce the time and increase the cost effectiveness and productivity of 3D and 2D electron microscopy. We were able to use a simple workflow based on open-source software to screen samples and identify those which are fixed and stained appropriately, and contain regions of interest before the beginning of the serial sectioning process. In the case of the Purkinje fibres, microCT was useful in orienting the sample to achieve the best resolution and to track the fibres through an appropriately shaped volume that minimised unnecessary

data collection. The method is able to pre-screen many samples quickly and efficiently both to find the best ones for detailed SEM examination but also to ensure that the staining procedures are optimised for best contrast. One of the key benefits of pre-screening by CT is the ability to precisely locate and examine specific features. In our case by accurately registering high resolution CT images with the proposed serial sectioning process we were able to target the buried anterior region of the parasitic whipworm *Trichuris muris* within the a gut biopsy of its murine host, as well as alginate cell clusters embedded in a matrix. Other potential uses include the quantification of the effects of specimen preparation on the integrity of the sample in terms of quantifying non-uniform deformation (uneven shrinkage) or damage during induced fixing, staining or sectioning.

Finally we see advances in correlative imaging, the development of higher precision sample trimming and excision capabilities, the increased connectivity between instruments and image registration schemes having significant benefits in terms of the ease with which microCT driven experimental steering can be applied. Once this becomes more routine we envisage the application of pre-EM microCT to a wide range of problems.

6 Acknowledgements

We acknowledge the Engineering and Physical Science Research Council (EPSRC) for funding the Henry Moseley X-ray Imaging Facility through grants (EP/F007906/1, EP/F001452/1, EP/I02249X, EP/F028431/1, EP/M022498/1, and platform grant EP/M010619/1) within the Henry Royce Institute. PJW acknowledges support from the European Research Council grant No 695638 CORREL-CT. TS and RKG acknowledge support from the Wellcome Trust thorough a grant (203128/Z/16/Z) and investigator award (WT100290MA).

We wish to thank: Amber Wood, Heuyan Sun and Andrew Gilmore (University of Manchester, UK) for the use of the alginate embedded cell samples; Sophie Saxton, Ashraf Kitmitto and Tony Heagerty (University of Manchester, UK) for the use of the murine fat samples; Shu Nakao, Il-Young Oh and Mark Boyett (University of Manchester, UK) for the use of the heart samples.

Supplementary information

Inspecting the block-face with the assistance of microCT data

In order to accurately trim the EM sample using the X-ray data as a guide we have used our 3view system, but any SEM with a BSED detector will do. We installed the standalone version of 3dmod (the visualization part of the IMOD suite of software (Kremer *et al.*, 1996)), but it should be noted that IMOD may be substituted with any other volumetric viewing software which allows visualisation and marking of virtual slices. The standalone version of 3dmod is available

from the SerialEM website (bio3d.colorado.edu/SerialEM/. Note: SerialEM is free to use software suite for automated collection of data on a TEM (Mastronarde, 2003), the installation of which is not required in order to use 3dmod; instead follow the link for the standalone 3dmod in the “Other Helpful Materials” section (link confirmed 20/11/2018)). Using 3dmod, we directly compared the images of the freshly polished block-face with the X-ray data (in the form of either MRC stacks or 2D/3D Tifs).

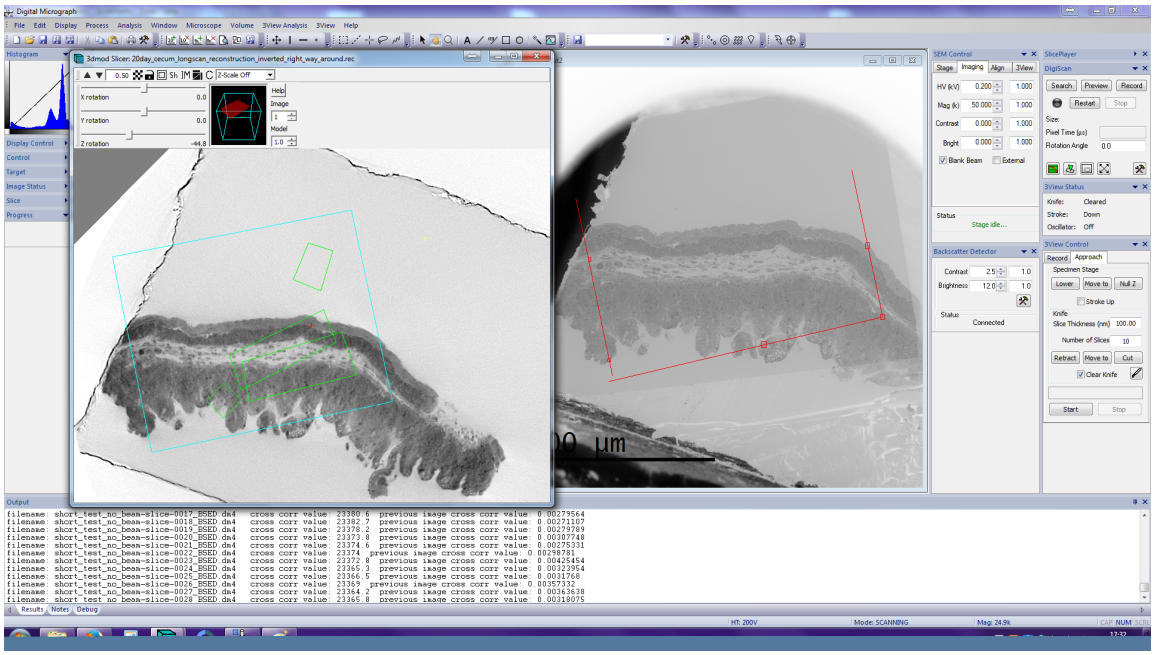

Figure S1: Using X-ray data to trim resin blocks during sample preparation: The inverted X-ray data (left window) is opened in IMOD (http://bio3d.colorado.edu) to compare with live imaging on the SEM. A box (blue) is defined to enclose the underlying regions of interest (green boxes). On the SEM side the cut-out box can be used to define regions to mark for subsequent trimming (smaller squares in this example).

Here we demonstrate opening the inverted contrast X-ray data in the ‘Slicer’ window of 3dmod, while simultaneously imaging the block-face in the SEM (Fig S1). Using the ‘Slicer’ window allows us to rotate the X-ray data so that the orientation matches the orientation of the EM image. We have used 3dmod to model regions of interest at depth (model mode, middle click to place points: See 3dmod guide for more information on how to make a model (http://bio3d.colorado.edu/imod/doc/3dmodguide.html). Once the precise section number of the X-ray data has been identified it is possible to copy the ROI boxes onto the current section (Edit> contour>Copy, then select ‘Copy to section #’ from the pull-down menu). Once the ROIs are plotted on the current section it is possible to draw a box that encloses the hidden ROIs to be used to guide subsequent trimming. Here we have drawn the box in blue in 3dmod (Fig S1,

now contaminated, image. At high magnification there will now be enough contaminants that an accurate stage position can be found, meaning that the line can be marked accurately.

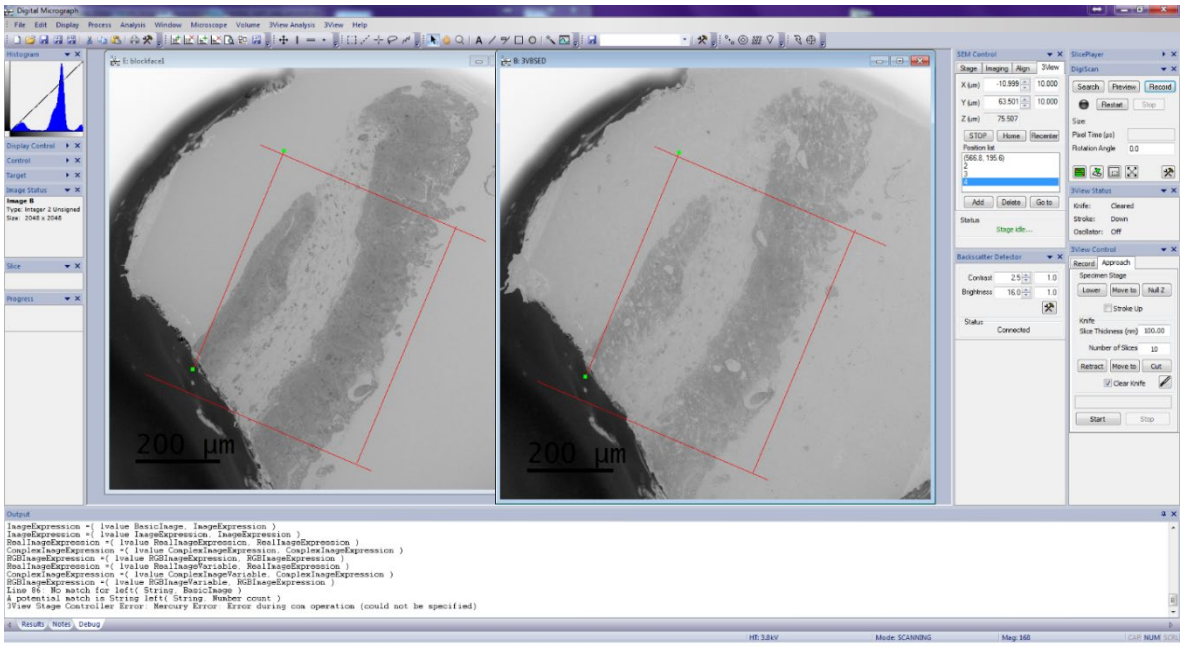

Figure S3: deliberate contamination of the sample surface can be used to improve accuracy of surface marking. Image in the left panel is the freshly trimmed block-face imaged with back-scattered electrons showing sample staining. The image in the right panel is the same sample after it has been contaminated with finger grease. The red rectangles indicate the desired size of the block-face; note that the top left corner of the rectangle is within empty resin, making it difficult to mark its position using the beam. The contamination (right panel) can be seen as some bright and dark spots that appear at random on the surface. The pattern of debris on top of the empty resin now allows specific regions to be identified meaning that the block-face can be accurately marked.

Trimming the sample using markers.

Once all of the markers have been placed it is possible to visualize these under a dissecting microscope in order to accurately trim the sample (Fig S4). Rather than using a ring illumination we have found that it is more beneficial to use a horizontal illumination that is then reflected onto the block surface. In order to see the marks we reflect the light off the back of the razor blade that we will use to trim the sample. By carefully focusing on the block-face we can slowly lower the out of focus razor blade while reflecting the light to allow us to see the marks. As we approach the sample surface the blade will come into focus, which allows us to accurately position the blade for trimming.

In order to reduce stress on the sample it is best to only shave a small amount off the sample with each cut. By slowly advancing towards the fiducial marks you can remove the unwanted material and you can also test the accuracy of you cutting and adjust this accordingly.

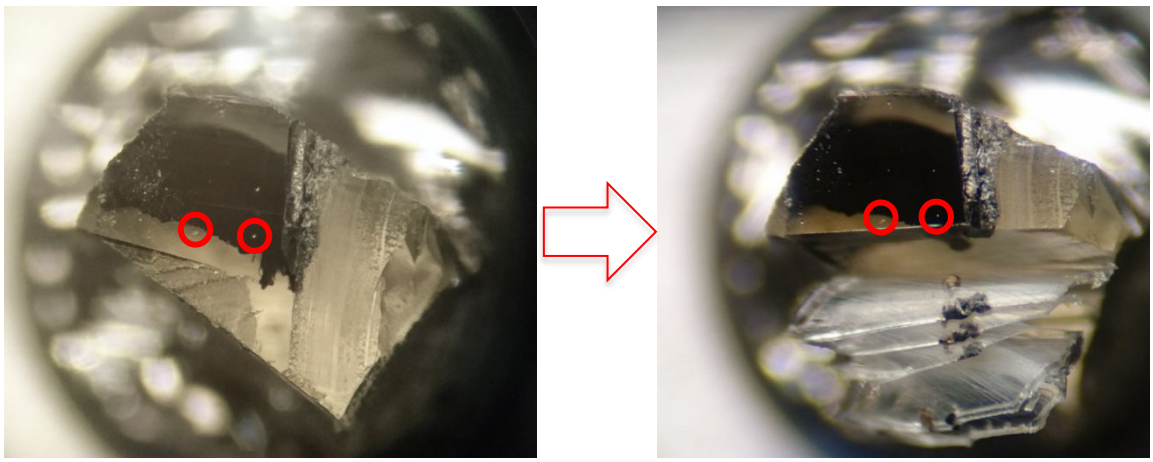

Figure S4: Trimming the marked sample using a razor blade. The sample can be trimmed carefully from the point furthest away from the fiducial marks. Thin slices are taken moving closer to the marks on the surface.

References

[1] A. Zankel, J. Wagner, P. Poelt, Serial sectioning methods for 3D investigations in materials science, Micron. 62 (2014) 66–78. doi:10.1016/j.micron.2014.03.002.

[2] C.J. Peddie, L.M. Collinson, Exploring the third dimension: Volume electron microscopy comes of age, Micron. 61 (2014) 9–19. doi:10.1016/j.micron.2014.01.009.

[3] J.A.W. Heymann, M. Hayles, I. Gestmann, L.A. Giannuzzi, B. Lich, S. Subramaniam, Site-specific 3D imaging of cells and tissues with a dual beam microscope, J. Struct. Biol. 155 (2006) 63–73. doi:10.1016/j.jsb.2006.03.006.

[4] W. Denk, H. Horstmann, Serial block-face scanning electron microscopy to reconstruct three-dimensional tissue nanostructure, PLoS Biol. 2 (2004) e329. doi:10.1371/journal.pbio.0020329.

[5] M. Daly, M.G. Burke, L. Contreras, B. Winiarski, P.J. Withers, T.L. Burnett, R. Kelley, A. Gholinia, Large volume serial section tomography by Xe Plasma FIB dual beam microscopy, Ultramicroscopy. 161 (2015) 119–129. doi:10.1016/j.ultramic.2015.11.001.

[6] E. Maire, P.J. Withers, Quantitative X-ray tomography, Int. Mater. Rev. 59 (2014) 1–43. doi:10.1179/1743280413Y.0000000023.

[7] G. Sengle, S.F. Tufa, L.Y. Sakai, M.A. Zulliger, D.R. Keene, A correlative method for imaging identical regions of samples by micro-CT, light microscopy, and electron microscopy: Imaging adipose tissue in a model system, J. Histochem. Cytochem. 61 (2013) 263–271. doi:10.1369/0022155412473757.

[8] E.A. Bushong, D.D. Johnson, K.Y. Kim, M. Terada, M. Hatori, S.T. Peltier, S. Panda, A. Merkle, M.H. Ellisman, X-Ray Microscopy as an Approach to Increasing Accuracy and Efficiency of Serial Block-Face Imaging for Correlated Light and Electron Microscopy of Biological Specimens, Microsc. Microanal. 21 (2015) 231–238. doi:10.1017/S1431927614013579.

[9] J.R. Kremer, D.N. Mastronarde, J.R. McIntosh, Computer visualization of three-dimensional image data using IMOD, J. Struct. Biol. 116 (1996) 71–76. doi:10.1006/jsbi.1996.0013.

[10] J. Schindelin, I. Arganda-Carreras, E. Frise, V. Kaynig, M. Longair, T. Pietzsch, S. Preibisch, C. Rueden, S. Saalfeld, B. Schmid, J.Y. Tinevez, D.J. White, V. Hartenstein, K. Eliceiri, P. Tomancak, A. Cardona, Fiji: An open-source platform for biological-image analysis, Nat. Methods. 9 (2012) 676–682. doi:10.1038/nmeth.2019.

[11] J. Albers, M.A. Markus, F. Alves, C. Dullin, X-ray based virtual histology allows guided sectioning of heavy ion stained murine lungs for histological analysis, Sci. Rep. 8 (2018) 7712. doi:10.1038/s41598-018-26086-0.

[12] A.M. Wood, H. Sun, J. Williams, K.R. Brennan, A.P. Gilmore, C.H. Streuli, Three-dimensional breast culture models: New culture models for analyzing breast development and function. New culture models for analyzing breast development and function., in: Organoids and Mini-Organs, 2018: pp. 73–88. doi:10.1016/B978-0-12-812636-3.00004-3.

[13] V. Lev-Ram, X. Shu, M. Ellisman, E. Bushong, T. Deerinck, R. Tsien, Enhancing Serial Block-Face Scanning Electron Microscopy to Enable High Resolution 3-D Nanohistology of Cells and Tissues, Microsc. Microanal. 16 (2010) 1138–1139. doi:10.1017/s1431927610055170.

[14] J. Walton, Lead asparate, an en bloc contrast stain particularly useful for ultrastructural enzymology, J. Histochem. Cytochem. 27 (1979) 1337–1342. doi:10.1177/27.10.512319.

[15] R.A. Crowther, R. Henderson, J.M. Smith, MRC image processing programs, J. Struct. Biol. 116 (1996) 9–16. doi:10.1006/jsbi.1996.0003.

[16] A. Cheng, R. Henderson, D. Mastronarde, S.J. Ludtke, R.H.M. Schoenmakers, J. Short, R. Marabini, S. Dallakyan, D. Agard, M. Winn, MRC2014: Extensions to the MRC format header for electron cryo-microscopy and tomography, J. Struct. Biol. 192 (2015) 146–150. doi:10.1016/j.jsb.2015.04.002.

[17] O. V Aslanidi, T. Nikolaidou, J. Zhao, B.H. Smaill, S.H. Gilbert, A. V Holden, T. Lowe, P.J. Withers, R.S. Stephenson, J.C. Jarvis, J.C. Hancox, M.R. Boyett, H. Zhang, Application of micro-computed tomography with iodine staining to cardiac imaging, segmentation, and computational model development, IEEE Trans. Med. Imaging. 32 (2013) 8–17. doi:10.1109/TMI.2012.2209183.

[18] S. Mikula, W. Denk, High-resolution whole-brain staining for electron microscopic circuit reconstruction, Nat. Methods. 12 (2015) 541–546. doi:10.1038/nmeth.3361.

[19] A. Wood, C.H. Streuli, F. Foster, S. Walker, K. Brennan, A.P. Gilmore, T. Owens, Oncogenic activation of FAK drives apoptosis suppression in a 3D-culture model of breast cancer initiation, Oncotarget. 7 (2016). doi:10.18632/oncotarget.11856.

[20] R.L. Pullan, J.L. Smith, R. Jasrasaria, S.J. Brooker, Global numbers of infection and disease burden of soil transmitted helminth infections in 2010, Parasites and Vectors. 7 (2014) 37. doi:10.1186/1756-3305-7-37.

[21] T.D.G. Lee, K.A. Wright, The morphology of the attachment and probable feeding site of the nematode Trichuris muris (Schrank, 1788) Hall, 1916, Can. J. Zool. 56 (2008) 1889–1905. doi:10.1139/z78-258.

[22] L.G. Tilney, P.S. Connelly, G.M. Guild, K. a. Vranich, D. Artis, Adaptation of a nematode parasite to living within the mammalian epithelium, J. Exp. Zool. Part A Comp. Exp. Biol. 303 (2005) 927–945. doi:10.1002/jez.a.214.

[23] T.V.A. Hansen, M. Hansen, P. Nejsum, H. Mejer, M. Denwood, S.M. Thamsborg, Glucose Absorption by the Bacillary Band of Trichuris muris, PLoS Negl. Trop. Dis. 10 (2016) e0004971. doi:10.1371/journal.pntd.0004971.

[24] K.A. Wright, J. Chan, Sense receptors in the bacillary band of trichuroid nematodes, Tissue Cell. 5 (1973) 373–380. doi:10.1016/S0040-8166(73)80031-X.

[25] M. Hüttemann, G. Schmahl, H. Mehlhorn, Light and electron microscopic studies on two nematodes, Angiostrongylus cantonensis and Trichuris muris, differing in their mode of nutrition, in: Parasitol. Res., 2007: pp. 225–232. doi:10.1007/s00436-007-0698-1.

[26] T.A. Wynn, B.F. Dickey, S.Z. Hasnain, D.J. Thornton, M.S. Wilson, A.L. Gallagher, C.M. Evans, K.N. Kindrachuk, M. Roy, R.K. Grencis, L. Barron, Muc5ac: a critical component mediating the rejection of enteric nematodes, J. Exp. Med. 208 (2011) 893–900. doi:10.1084/jem.20102057.

[27] T.L. Burnett, S.A. McDonald, A. Gholinia, R. Geurts, M. Janus, T. Slater, S.J. Haigh, C. Ornek, F. Almuaili, D.L. Engelberg, G.E. Thompson, P.J. Withers, Correlative tomography, Sci. Rep. 4 (2014) 4711. doi:10.1038/srep04711.

[28] Y. Lu, S.M. Humphries, K.E. Kadler, T. Starborg, A. Mironov, D.F. Holmes, N.S. Kalson, Nonmuscle myosin II powered transport of newly formed collagen fibrils at the plasma membrane, Proc. Natl. Acad. Sci. 110 (2013) E4743–E4752. doi:10.1073/pnas.1314348110.

[29] B.M.T. Acosta, P. Bouthemy, C. Kervrann, A common image representation and a patch-based search for correlative light-electron-microscopy (CLEM) registration, in: Proc. - Int.

Symp. Biomed. Imaging, IEEE, 2016: pp. 257–260. doi:10.1109/ISBI.2016.7493258.

[30] R. Kelley, O.C.G. Tuck, E.J. Pickering, F. Léonard, M. Daly, P.J. Withers, A.H. Sherry, T.L. Burnett, A multi-scale correlative investigation of ductile fracture, Acta Mater. 130 (2017) 56–68. doi:10.1016/j.actamat.2017.03.028.

[31] D.N. Mastronarde, SerialEM: A Program for Automated Tilt Series Acquisition on Tecnai Microscopes Using Prediction of Specimen Position, Microsc. Microanal. 9 (2003) 1182–1183. doi:10.1017/s1431927603445911.

Appendix 3: Matlab code used to measure mucosal thickness

The following code was provided for use with permission by Dr. Shelley Rawson, from the University of Manchester. The code was originally developed to measure foam thickness of titanium aerogel, but was modified by the author to estimate mucosal thickness in the mouse intestine in section 4.2.5. The code has not been used in any published work, and is not currently being prepared for publication by Dr. Rawson.

Three modifications were independently made by the author to how the code was used:

1) Generating a Euclidean, rather than Chamfer distance map to input into the Matlab script, in order to provide a more accurate measurement of thickness.

2) Setting an appropriate threshold to the final processed image to reduce noise

3) Producing an output of the final processed images for illustrative purposes. An example output is shown in **Fig. 4.7 K-L**.

Code:

```
%INFO
%   this function cycles through and reads all files in a desired
folder
%   except the first and last ones.
%
%NOTES
%   our input files need to be the distance map stack, not the binary
%   segmented data.
%   to call this function, type:
%   a20180430_3D_NonMaxSup_histogram_properMean2('C:/Users/hmxf/2018-
12-07_test3/*.tif')


%notes on how it works:
%   the function does not include the top and bottom slice of the
stack
%   (these are only used for the search window for the next slice)


function mean_of_full_volume =
a20181130_3D_NonMaxSup_histogram_properMean(file_path)

%below creates a struct array with fields:
%name
%date
%bytes
%isdir
%datenum
%see   help dir   for more info.
%note that you have to enter the full file path, not just the filename
im_list = dir(file_path);
%next we work out the total number of image files in the folder
tot_files = length (im_list);
%subtracts 1 from tot number of files
tot_files_minus1 = tot_files - 1;
tot_files_minus2 = tot_files - 2;
```

```
%creates an empty column matrix the same size as the number of
iterations
%to populate with the mean sheet spacing from each slice
mean_of_all_slices = zeros (tot_files_minus2, 1);

%for plotting histogram; make an array with 20 items. each time a
slice is
%analysed, the bins get added to.
histArray_all_slices = zeros (1,30);
x = 0:5:145;

%create a zero for our sum_sheet_spacing_for_vol variable so we can
add
%these up
sum_sheet_spacing_for_vol = 0;
number_sheet_spacing_measurements_vol = 0;

%cycle through and read all files in the desired folder except the
first and the last
for i_im = 2 : tot_files_minus1

%_____________________________________________________________________
    %reads distance map image number i_im and the two either side as
well

    dist_map = imread (im_list(i_im).name);
    i_im_minus1 = i_im -1;
    dist_map_minus1 = imread (im_list(i_im_minus1).name);
    i_im_plus1 = i_im +1;
    dist_map_plus1 = imread (im_list(i_im_plus1).name);
    %_____________________________________________________________________
    %reads binary image number i_im and the two either side
    %image_mid = imread (im_list(i_im).name);
    %i_im_minus1 = i_im -1;
    %image_minus1 = imread (im_list(i_im_minus1).name);
    %i_im_plus1 = i_im +1;
    %image_plus1 = imread (im_list(i_im_plus1).name);
    %creates 2D dist map from the binary images
    %dist_map = bwdist (image_mid) ;
    %dist_map_minus1 = bwdist (image_minus1) ;
    %dist_map_plus1 = bwdist (image_plus1) ;

    %_____________________________________________________________________

    %finds the max number of entries, rows and columns in
aerogel_slice
    [size_agel]=size (dist_map);
    max_index_agel = numel(dist_map);
    [rowmax_agel,colmax_agel]=ind2sub(size_agel,max_index_agel);

    %create a matrix the same size of aerogel_slice to populate with
the
    %distance transform figures
    non_max_sup = zeros (rowmax_agel, colmax_agel);


    %here we add a 1 pixel wide border of zeros around our
aerogel_slice matrix
    %and call it aerogel_slice_border1
    rowmax_agel_plus1=rowmax_agel+1;
```

```
    colmax_agel_plus1=colmax_agel+1;
    rowmax_agel_plus2=rowmax_agel+2;
    colmax_agel_plus2=colmax_agel+2;
    dist_map_border1=zeros(rowmax_agel_plus2, colmax_agel_plus2);
%creates a matrix populated with zeros

dist_map_border1(2:rowmax_agel_plus1,2:colmax_agel_plus1)=dist_map(1:r
owmax_agel,1:colmax_agel); %puts aerogel_slice within the new zero
populated matrix
    %now we do the same as above but for aerogel_slice_plus1 and
    %aerogel_slice_minus1
    border1_above=zeros(rowmax_agel_plus2, colmax_agel_plus2);
%creates a matrix populated with zeros

border1_above(2:rowmax_agel_plus1,2:colmax_agel_plus1)=dist_map_plus1(
1:rowmax_agel,1:colmax_agel); %puts aerogel_slice within the new zero
populated matrix
    border1_below=zeros(rowmax_agel_plus2, colmax_agel_plus2);
%creates a matrix populated with zeros

border1_below(2:rowmax_agel_plus1,2:colmax_agel_plus1)=dist_map_minus1
(1:rowmax_agel,1:colmax_agel); %puts aerogel_slice within the new zero
populated matrix



    %loop that cycles through each voxel in aerogel_slice
    %crops out a 3x3 matrix from aerogel_slice_border1 with its centre
being
    %the current voxel. Does same in the slices either side of
aerogel_slice
    %sticks the three 3x3 matrices together
    %finds the largest value in the 3x9 matrix and checks to see if
this is the
    %equal to the value in position 2,2 in the 3x3 matrix from
aerogel_slice (the centre of the
    %matrix).
    %if the centre point is the maximum value, we write this value
into the m,n
    %position of the distance_trnasform matrix
    iter_var_pix=1;
    for iter_var_pix = 1: numel(dist_map)
        value_iter_var_pix = dist_map (iter_var_pix);
        [row_agel,col_agel]=ind2sub(size_agel,iter_var_pix);
        %display(['the value in position ' num2str(iter_var_pix) ' is
' num2str(value_iter_var_pix) ' at coordinates ' num2str(row_agel) ',
' num2str(col_agel) ]);
        iter_var_pix = iter_var_pix+1;

        %creates a 3x3 matrix populated with the pixels surrounding
the
        %current slected pixel (assigned to iter_var_pix).
        row_agel_plus2=row_agel+2;
        col_agel_plus2=col_agel+2;
        crop (1:3, 1:3) =
dist_map_border1(row_agel:row_agel_plus2,col_agel:col_agel_plus2);
        % does the same for the slice above and the slice below
        crop_above(1:3, 1:3) = border1_above
(row_agel:row_agel_plus2,col_agel:col_agel_plus2);
        crop_below(1:3, 1:3) = border1_below
(row_agel:row_agel_plus2,col_agel:col_agel_plus2);
        %sticks the three 3x3 matrices we have just created together
        three_nine_matrix = [crop_above, crop, crop_below];
```

```
        % is the centre pixel in the 3 x 3 matrix "crop" the largest
value?
        %if it is, put the value of the centre pixel of the 3x3 martix
"crop"
        %(which is the same as value_iter_var_pix) in the same
position of
        %dist_trans as the position of dist_map that we are currently
looking
        %at. otherwise, set the value in dist_trans to zero.
        crop_max_value = max(three_nine_matrix(:));
        if crop_max_value == value_iter_var_pix
            %display(['the centre voxel is a local maxima, its value
is ' num2str(value_iter_var_pix) ', found in row ' num2str(row_agel)
', column ' num2str(col_agel) ]);
            non_max_sup (row_agel, col_agel) = value_iter_var_pix;
        else
            non_max_sup (row_agel, col_agel) = 0;
        end



    end


    % this next bit tells it to discount any distance map values less
than 2 (this is
    % to try and eliminate the problem whereby we seem to get a very
    % large number of low readings which we think is due to pixels too
    % close to each other, and we think is causing error in the
    % calculation of the mean.) we do this by setting any values less
than
    % 2 in the non_max_sup array to zero

    non_max_sup (non_max_sup < 10) = 0;


    %calculate average sheet spacing for each individual slice
    non_zeros = nonzeros (non_max_sup);
    non_zeros_times2 = non_zeros*2;
    sum_sheet_spacing_measurements_slice = sum(non_zeros_times2);
    number_sheet_spacing_measurements_slice = numel
(non_zeros_times2);
    %summing up sheet spacing measurements and number of measurements
for
    %each slice
    sum_sheet_spacing_for_vol = sum_sheet_spacing_for_vol +
sum_sheet_spacing_measurements_slice;
    number_sheet_spacing_measurements_vol =
number_sheet_spacing_measurements_vol +
number_sheet_spacing_measurements_slice;



    %next try at making the histogram
    %we will have 20 bins (10 poxels in each bin) going from 0 to 200
    %pixels, so the fist bin will be 0-10, next will be 10-20 and so
on up
    %to 200. <note the histogram will be in pixels, not mm distance.
it
    %will need changing to mm later, lets do that and produce proper
graphs
```

```
    %in excel
    histArray_one_slice = zeros (1,30);

    histArray_one_slice(1,1) = numel(non_zeros_times2(
non_zeros_times2(:)>0 & non_zeros_times2(:)<4.9999 ));
    histArray_one_slice(1,2) = numel(non_zeros_times2(
non_zeros_times2(:)>5 & non_zeros_times2(:)<9.9999 ));
    histArray_one_slice(1,3) = numel(non_zeros_times2(
non_zeros_times2(:)>10 & non_zeros_times2(:)<14.9999 ));
    histArray_one_slice(1,4) = numel(non_zeros_times2(
non_zeros_times2(:)>15 & non_zeros_times2(:)<19.9999 ));
    histArray_one_slice(1,5) = numel(non_zeros_times2(
non_zeros_times2(:)>20 & non_zeros_times2(:)<24.9999 ));
    histArray_one_slice(1,6) = numel(non_zeros_times2(
non_zeros_times2(:)>25 & non_zeros_times2(:)<29.9999 ));
    histArray_one_slice(1,7) = numel(non_zeros_times2(
non_zeros_times2(:)>30 & non_zeros_times2(:)<34.9999 ));
    histArray_one_slice(1,8) = numel(non_zeros_times2(
non_zeros_times2(:)>35 & non_zeros_times2(:)<39.9999 ));
    histArray_one_slice(1,9) = numel(non_zeros_times2(
non_zeros_times2(:)>40 & non_zeros_times2(:)<44.9999 ));
    histArray_one_slice(1,10) = numel(non_zeros_times2(
non_zeros_times2(:)>45 & non_zeros_times2(:)<49.9999 ));
    histArray_one_slice(1,11) = numel(non_zeros_times2(
non_zeros_times2(:)>50 & non_zeros_times2(:)<54.9999 ));
    histArray_one_slice(1,12) = numel(non_zeros_times2(
non_zeros_times2(:)>55 & non_zeros_times2(:)<59.9999 ));
    histArray_one_slice(1,13) = numel(non_zeros_times2(
non_zeros_times2(:)>60 & non_zeros_times2(:)<64.9999 ));
    histArray_one_slice(1,14) = numel(non_zeros_times2(
non_zeros_times2(:)>65 & non_zeros_times2(:)<69.9999 ));
    histArray_one_slice(1,15) = numel(non_zeros_times2(
non_zeros_times2(:)>70 & non_zeros_times2(:)<74.9999 ));
    histArray_one_slice(1,16) = numel(non_zeros_times2(
non_zeros_times2(:)>75 & non_zeros_times2(:)<79.9999 ));
    histArray_one_slice(1,17) = numel(non_zeros_times2(
non_zeros_times2(:)>80 & non_zeros_times2(:)<84.9999 ));
    histArray_one_slice(1,18) = numel(non_zeros_times2(
non_zeros_times2(:)>85 & non_zeros_times2(:)<89.9999 ));
    histArray_one_slice(1,19) = numel(non_zeros_times2(
non_zeros_times2(:)>90 & non_zeros_times2(:)<94.9999 ));
    histArray_one_slice(1,20) = numel(non_zeros_times2(
non_zeros_times2(:)>95 & non_zeros_times2(:)<99.9999 ));
    histArray_one_slice(1,21) = numel(non_zeros_times2(
non_zeros_times2(:)>100 & non_zeros_times2(:)<104.9999 ));
    histArray_one_slice(1,22) = numel(non_zeros_times2(
non_zeros_times2(:)>105 & non_zeros_times2(:)<109.9999 ));
    histArray_one_slice(1,23) = numel(non_zeros_times2(
non_zeros_times2(:)>110 & non_zeros_times2(:)<114.9999 ));
    histArray_one_slice(1,24) = numel(non_zeros_times2(
non_zeros_times2(:)>115 & non_zeros_times2(:)<119.9999 ));
    histArray_one_slice(1,25) = numel(non_zeros_times2(
non_zeros_times2(:)>120 & non_zeros_times2(:)<124.9999 ));
    histArray_one_slice(1,26) = numel(non_zeros_times2(
non_zeros_times2(:)>125 & non_zeros_times2(:)<129.9999 ));
    histArray_one_slice(1,27) = numel(non_zeros_times2(
non_zeros_times2(:)>130 & non_zeros_times2(:)<134.9999 ));
    histArray_one_slice(1,28) = numel(non_zeros_times2(
non_zeros_times2(:)>135 & non_zeros_times2(:)<139.9999 ));
    histArray_one_slice(1,29) = numel(non_zeros_times2(
non_zeros_times2(:)>140 & non_zeros_times2(:)<144.9999 ));
    histArray_one_slice(1,30) = numel(non_zeros_times2(
non_zeros_times2(:)>145 & non_zeros_times2(:)<300 ));
```

```
    histArray_all_slices = histArray_all_slices + histArray_one_slice;

end

%calculate the mean
mean_of_full_volume = sum_sheet_spacing_for_vol /
number_sheet_spacing_measurements_vol;

%generate the histogram and print out the histogram values as well
bar(x,histArray_all_slices);
histArray_all_slices

%calculate standard deviation... note that this isnt perfect and will
be
%based on the histArray_all_slices values.
hist_array_indeces = [ 2.5 7.5 12.5 17.5 22.5 27.5 32.5 37.5 42.5 47.5
52.5 57.5 62.5 67.5 72.5 77.5 82.5 87.5 92.5 97.5 102.5 107.5 112.5
117.5 122.5 127.5 132.5 137.5 142.5 147.5];
x_minus_mean_squared = (hist_array_indeces - mean_of_full_volume).^2;
x_minus_mean_squared_all_values = x_minus_mean_squared.*
histArray_all_slices;
top_value = sum(x_minus_mean_squared_all_values);
n_value = sum(histArray_all_slices);
bottom_value = n_value - 1;
division = top_value / bottom_value;
standard_deviation = sqrt(division)
```